



**HAL**  
open science

# Synthesis and characterisation of silicon-based nanoparticles for diagnostic applications

John Ddungu

► **To cite this version:**

John Ddungu. Synthesis and characterisation of silicon-based nanoparticles for diagnostic applications. Other. Université de Strasbourg, 2018. English. NNT : 2018STRAF063 . tel-03270827

**HAL Id: tel-03270827**

**<https://theses.hal.science/tel-03270827>**

Submitted on 25 Jun 2021

**HAL** is a multi-disciplinary open access archive for the deposit and dissemination of scientific research documents, whether they are published or not. The documents may come from teaching and research institutions in France or abroad, or from public or private research centers.

L'archive ouverte pluridisciplinaire **HAL**, est destinée au dépôt et à la diffusion de documents scientifiques de niveau recherche, publiés ou non, émanant des établissements d'enseignement et de recherche français ou étrangers, des laboratoires publics ou privés.

**ÉCOLE DOCTORALE DES SCIENCES CHIMIQUES**  
**Institut de Science et d'Ingénierie Supramoléculaires**

**THÈSE** présentée par :  
**John DDUNGU**

soutenue le : **13 décembre 2018**

pour obtenir le grade de : **Docteur de l'université de Strasbourg**

Discipline/ Spécialité : Chimie

**Synthesis and characterisation of silicon-based  
nanoparticles for diagnostic applications**

**THÈSE dirigée par :**

**M<sup>me</sup> DE COLA Luisa**

Professeur, Université de Strasbourg

**RAPPORTEURS :**

**M<sup>me</sup> ROTHEN-RUTISHAUSER**

**Barbara**

**M LAMMERS Twan**

Professeur, Université de Fribourg (Suisse)

Professeur, Rheinisch-Westfälische Technische Hochschule,  
Aachen (Allemagne)

---

**AUTRES MEMBRES DU JURY :**

**M<sup>me</sup> LICANDRO Emanuela**

**M SAILOR Michael J.**

Professeur, Università degli Studi di Milano (Italie)

Professeur, University of California, San Diego (États-Unis)



**“You can never cross the ocean until you have the courage to lose sight of the shore”**

**– Christopher Columbus**

To my family, my friends, and my brother who inspired me to take this journey in chemistry



# Contents

<b>Abbreviations.....</b>	<b>1</b>
<b>Résumé .....</b>	<b>3</b>
Références .....	16
<b>Introduction .....</b>	<b>17</b>
Abstract .....	17
1.1 Nanoparticles and their applications in medical imaging.....	17
1.1.1 On the design of an optimal imaging probe .....	19
1.1.2 Silicon-based Nanoparticles (Si NPs) .....	27
1.2 Diagnostic imaging methods .....	36
1.2.1 Optical fluorescence imaging .....	37
1.2.2 Magnetic Resonance Imaging (MRI) .....	39
1.2.3 Positron Emission Tomography (PET) .....	39
1.3 Electrochemiluminescence (ECL).....	40
1.3.1 Nanoparticles in ECL .....	41
1.4 Scope of the Thesis.....	44
1.5 References .....	46
<b>Synthesis and characterisation of Silicon-based nanoparticles.....</b>	<b>53</b>
Abstract .....	53
2.1 Introduction .....	53
2.2 Synthesis of amine-terminated Si NPs via microemulsion method .....	54
2.2.1 Synthesis route .....	54
2.2.2 Characterisation.....	56
2.3 Synthesis of amine-terminated Si NPs via hydrothermal method.....	63
2.3.1 Synthesis route .....	63
2.3.2 Characterisation.....	63
2.4 Conclusions .....	70
2.5 Experimental Section .....	70
2.5.1 General information .....	70
2.5.2 Synthetic procedures .....	72
2.6 References .....	74
<b>Silicon or Silica? An in depth analysis and comparison of silicon-based nanoparticles produced via the hydrothermal and microwave methods .....</b>	<b>77</b>
Abstract .....	77
3.1 Introduction .....	77

3.2 Synthesis and characterisation of silicon-based nanoparticles .....	80
3.3 Conclusion.....	88
3.4 Experimental Section .....	89
2.5.1 General information .....	89
2.5.2 Synthetic procedures .....	90
3.5 References .....	92
<b>Silicon-based nanoparticles for Bio-imaging .....</b>	<b>95</b>
Abstract .....	95
4.1 Introduction .....	95
4.2 Si NPs for Positron Emission Tomography (PET).....	96
4.2.1 Surface functionalisation.....	96
4.2.2 In vivo bio-distribution studies.....	98
4.3 Si NPs for PET and optical fluorescence imaging .....	100
4.3.1 Surface functionalisation.....	100
4.3.2 In vivo bio-distribution studies.....	100
4.3 Si NPs for optical fluorescence imaging across the blood brain barrier (BBB).....	105
4.3.1 Surface functionalisation.....	107
4.3.2 In vivo bio-distribution studies.....	123
4.4 Conclusions .....	126
4.5 Experimental Section .....	127
4.5.1 General information .....	127
4.5.2 Synthetic procedures .....	127
4.5.3 <i>In vitro</i> assessment of nanotoxicity .....	131
4.5.4 Animal experiments .....	131
4.5.5 In vivo small animal positron emission tomography (PET).....	133
4.6 References .....	134
<b>Metal complex + silicon-based nanoparticles hybrid systems for Electrochemiluminescence applications .....</b>	<b>137</b>
Abstract .....	137
5.1 Introduction .....	137
5.2 Synthesis of ruthenium complex modified Si NPs.....	139
5.2.1 Synthesis route .....	139
5.2.2 Characterisation.....	140
5.3 Synthesis of iridium complex modified Si NPs .....	146
5.3.1 Synthesis route .....	146
5.3.2 Characterisation.....	147
5.4 ECL performance .....	153

5.4 Conclusion.....	159
5.5 Experimental section .....	159
5.5.1 General information .....	159
5.5.2 Synthetic procedures .....	161
5.6 References .....	163
<b>Instrumental techniques .....</b>	<b>165</b>
Abstract .....	165
6.1 UV-Vis absorption spectroscopy.....	165
6.2 Emission and excitation spectroscopy.....	166
6.3 Photoluminescence quantum yield.....	168
6.4 Time resolved spectroscopy .....	169
6.5 Transmission Electron Microscopy (TEM).....	170
6.6 X-ray Photoelectron Spectroscopy (XPS).....	171
6.7 X-ray diffraction.....	173
6.8 Positron Emission Tomography .....	174
6.9 References .....	175
<b>Summary .....</b>	<b>177</b>
Références .....	188
<b>Acknowledgements.....</b>	<b>191</b>





# Abbreviations

nm – Nanometre

NP(s) – Nanoparticle(s)

CB – Conduction band

VB – Valence band

°C – Degrees celcius

UV – Ultraviolet

NIR – Near Infra-red

MWCO – Molecular weight cut-off

keV – Kiloelectron volt

eV – Electron volt

CPS – Counts per second

a.u. – Arbitrary unit

ns - Nanosecond

mg – Milligram

$\epsilon$  – Molar extinction coefficient

$\mu\text{mol}$  – Micromole

$\lambda$  – Wavelength

kDa – Kilodalton

W – Watts

PSL – Photostimulated luminescence

$\pm\text{SEM}$  –  $\pm$ Standard error of mean

$\mu\text{L}$  – Microlitre



# Résumé

Les nanoparticules ont reçu une attention croissante ces dernières années, due à leur potentiel en tant que nanosondes efficaces pour la bioimagerie<sup>[1]</sup>. En effet, celles basées sur des matériaux semi-conducteurs, tels les points quantiques (PQs) II-VI ou III-V, ont montré un grand potentiel dans le domaine<sup>[2]</sup>. Ceci est dû à leur haut rendement quantique de fluorescence, leur longueur d'onde d'émission accordable, leur haut seuil de photoblanchiment, et leur haute stabilité électrique et chimique, qualités qui contribuent à leur préférence sur les colorants organiques<sup>[3]</sup>.

En dépit de ces propriétés prometteuses, certains désavantages notables des PQs les empêchent de devenir des outils établis dans le domaine de la bioimagerie<sup>[4]</sup>. Par exemple, les PQs les plus importants à base de noyaux dérivés de Cd, In, Pb, Hg, Se, ou Te avec une enveloppe de ZnS ont une chimie de surface compliquée qui les rend insolubles dans l'eau et difficiles à fonctionnaliser avec des biomolécules. De plus, contrôler de la taille de ces PQs durant la synthèse n'est pas simple, ce qui rend difficile l'obtention de petites tailles nécessaires pour une bioimagerie optimale, et dû à la nature chimique de leur noyau, les PQs sont toxiques dans la plupart des cas<sup>[4]</sup>. Alors que de la bioimagerie utilisant ces PQs a déjà été démontrée possible, ces problèmes, spécialement celui de la toxicité à basse concentration, ont empêché tout progrès avec ces matériaux.

Afin d'éliminer ces problèmes, certaines actions ont été proposées: enlever les métaux lourds de la formulation des PQs, utiliser un seul élément inorganique pour simplifier les propriétés du matériau, et par-dessus tout, s'assurer que ce matériau est biodégradable, abondant sur Terre, a une comportement chimique bien compris, a déjà démontré ses applications biologiques, et possède des rôles biologiques mineurs de façon à ce qu'il puisse être métabolisé par le corps<sup>[5]</sup>. Cela a conduit à un intérêt croissant dans la recherche sur les points quantiques ou nanoparticules à base de silicium (NPSis). La grande abondance naturelle du silicium et sa chimie bien comprise a conduit à la reconnaissance de son large potentiel pour les applications s'étendant de l'électronique à la médecine<sup>[6]</sup>. Le Si élémentaire, composant le noyau des NPSis, peut être métabolisé par le corps en acide silicique, qui est facilement éliminé par les reins<sup>[7]</sup>, et des études ont démontré l'utilisation de ces nanoparticules pour des applications d'imagerie *in vivo*, ce qui montre leur promesse envers le design d'une sonde de bioimagerie optimale<sup>[8]-[11]</sup>.

Dans le but d'améliorer davantage la bioimagerie jusqu'aux niveaux requis pour la détection précoce de maladies et pour la chirurgie guidée par imagerie en temps réel, l'utilisation

simultanée de différentes techniques d'imagerie non invasives (imagerie multimodale) a été explorée avec différents systèmes de nanoparticules<sup>[12]-[15]</sup>. Alors qu'il y a de nombreux exemples de bioimagerie avec des NPSis dans la littérature<sup>[3]-[11],[16]</sup> seulement quelques études ont mis l'accent sur l'imagerie multimodale, et souvent cette fonctionnalité multimodale fut réalisée en combinant les NPSis avec des molécules fonctionnelles dans des larges structures telles que des micelles<sup>[6]</sup>. Ceci augmente de la taille de la sonde de bioimagerie et peut avoir pour conséquence la limitation de l'imagerie dans certaines parties du corps. Le manque d'interactions entre les NPSis entre-elles et avec les autres molécules actives peut aussi signifier que l'imagerie de la même exacte partie du corps n'est pas réalisée une fois que le transport re-largue la cargaison d'imagerie.

Dans le travail de cette thèse, intitulée "Synthèse et caractérisation de nanoparticules à base de silicium pour des applications diagnostiques" l'objectif est d'explorer d'abord la synthèse de nanoparticules à base de silicium (Si NP) de très petites tailles (<5 nm) par différentes techniques de synthèse et obtenir une caractérisation approfondie du matériau préparé. Nous visons ensuite à évaluer l'aptitude des nanoparticules à fonctionner comme sondes d'imagerie multimodales *in vitro* et *in vivo* grâce à la fonctionnalisation de surface des NP de Si avec deux marqueurs d'imagerie différents fonctionnant avec deux techniques d'imagerie distinctes. Enfin, notre objectif est d'explorer l'application des NPs Si en électrochimiluminescence (ECL), une technique de diagnostic émergente pour les essais biologiques.

Cette thèse est divisée en six chapitres. Le chapitre 1 présente une introduction au sujet des nanoparticules en médecine, l'accent étant mis sur leurs applications en bio-imagerie. Les SiNP sont présentées comme le matériau de choix et un aperçu de leurs méthodes de préparation, leurs propriétés, leur fonctionnalisation, et leurs applications *in vitro* et *in vivo* est donné. Les techniques de diagnostic courantes d'imagerie par fluorescence optique, d'imagerie par résonance magnétique (IRM) et de tomographie par émission de positrons (TEP) sont introduites et la possibilité d'imager simultanément des nanoparticules avec deux ou plusieurs de ces techniques en imagerie multimodale est brièvement présentée. Différents marqueurs fonctionnels et molécules nécessaires aux techniques d'imagerie et à l'application biologique des nanoparticules sont mis en évidence et, en ce qui concerne l'un de ces marqueurs, à savoir les complexes de métaux de transition, la technique de l'électrochimiluminescence et son utilisation émergente dans les essais biologiques sont brièvement décrites.

Le chapitre 2 couvre la synthèse des NPs Si terminés par une amine par voies différentes et détaille la caractérisation poussée permettant de comparer les différences et de tenter d'identifier la véritable nature chimique du matériau central. NPSis terminées par des amines furent préparées par deux voies de synthèse différentes: les méthodes de microémulsion et hydrothermale, qui sont illustrées dans la Figure 1.

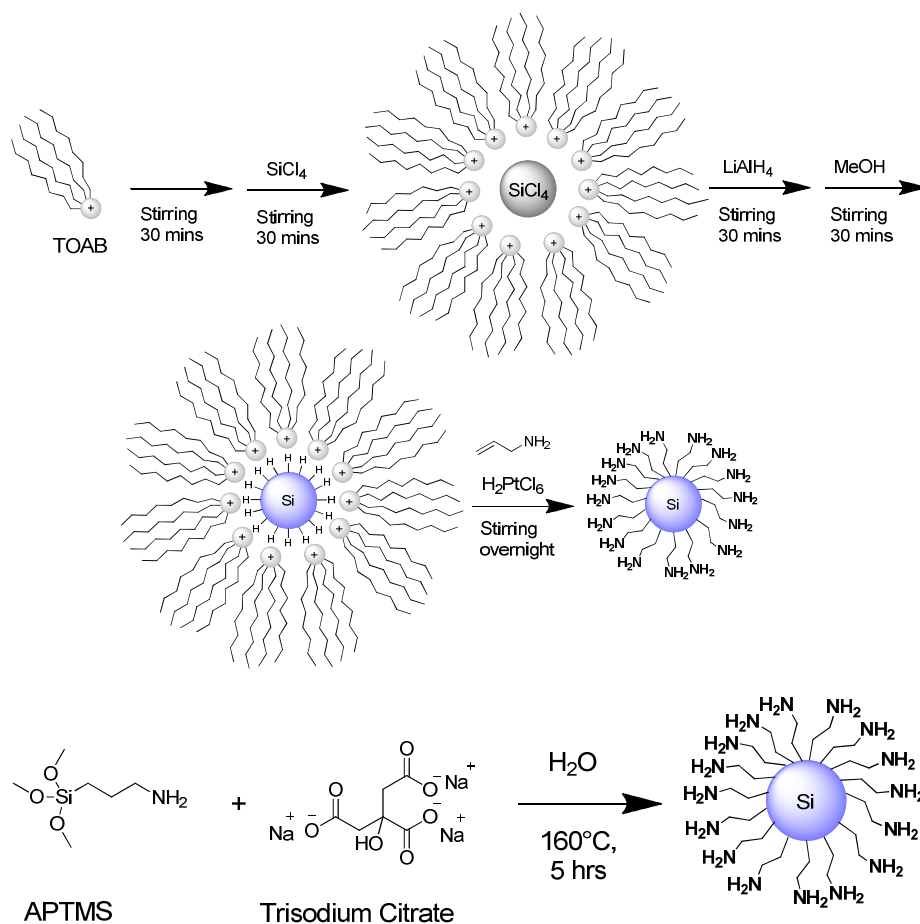


**Figure 1:** Représentations schématiques des synthèses des NPSis. (Haut) NPSis terminées par des amines par la réduction de  $\text{SiCl}_4$  (methode microémulsion)<sup>[10]</sup>. (Bas) NPSis terminées par des amines par réduction hydrothermale de APTMS (methode hydrothermale)<sup>[11]</sup>

Ces méthodes de chimie en solution ascendantes progressent par la réduction d'une source de silicium. Pour la synthèse en microémulsion, le tétrachlorure de silicium est réduit par de l'hydruure d'aluminium et de lithium dans une micelle formée par du bromure de tetraoctylammonium dans le toluene. Les NPSis obtenues sont terminées par des hydruures, qui sont ensuite converti en groupement amine par réaction avec de l'allylamine en utilisant de l'acide hexachloroplatinique comme catalyseur. Pour la synthèse hydrothermale, (3-aminopropyl)triméthoxysilane est réduit par du sel de citrate de trisodium dans l'eau à haute

température en utilisant un récipient scellé sous pression. Caractérisation des NPSis par microscopie électronique à transmission (MET) montre la taille ultra-petite des nanoparticules est réalisée dans les deux cas :  $2.7 \pm 0.9$  nm pour la méthode en microémulsion, et  $3.1 \pm 0.8$  nm pour la méthode hydrothermale.

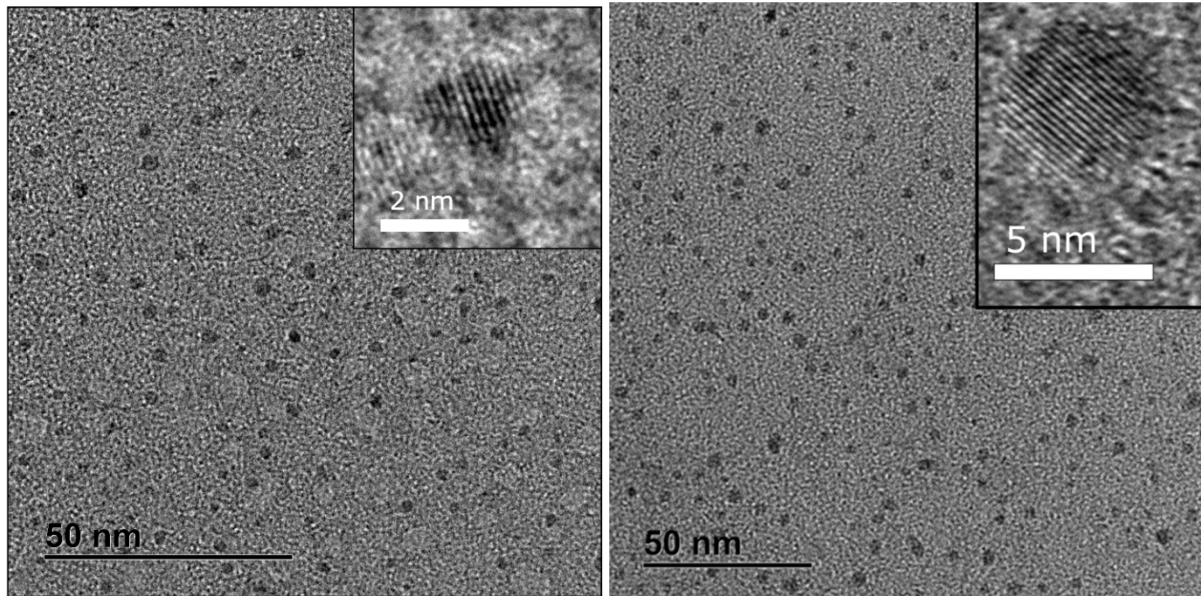


**Figure 2:** Images MET de NPSis à terminaison amine obtenues par la méthode microémulsion (à gauche) et la méthode hydrothermale (à droite). Les franges cristallines appartenant aux NPSis sont clairement visibles en haute résolution

Les propriétés photophysiques des matériaux préparés ont été analysées par spectroscopie UV-Vis, spectroscopie d'émission et d'excitation à l'état d'équilibre, spectroscopie de luminescence résolue dans le temps pour acquérir des données sur les durées de vie des états excités, et des mesures de rendement quantique. Une différence notable entre les deux NPs en Si réside dans le fait que celles de la méthode de la microémulsion affichent un maximum d'émission qui se décale en fonction de la longueur d'onde d'excitation, tandis que ceux de la méthode hydrothermale indiquent un maximum d'émission à une longueur d'onde constante, quelle que soit la longueur d'onde de l'excitation. Dans le cas des nanoparticules de silicium en émulsion, ce comportement serait typique des nanoparticules de silicium élémentaire et serait attribué à la distribution en taille des nanoparticules de silicium ou à la présence de liaisons Si-C à la surface, qui induiraient des états de surface, qui présentent un comportement direct de type bandgap. Les spectres acquis à partir des NP Si hydrothermaux (HT Si NP) sont toutefois plus

similaires à ceux des points de carbone polymériques, ce qui donne une indication initiale que la structure du matériau du noyau pourrait être différente.

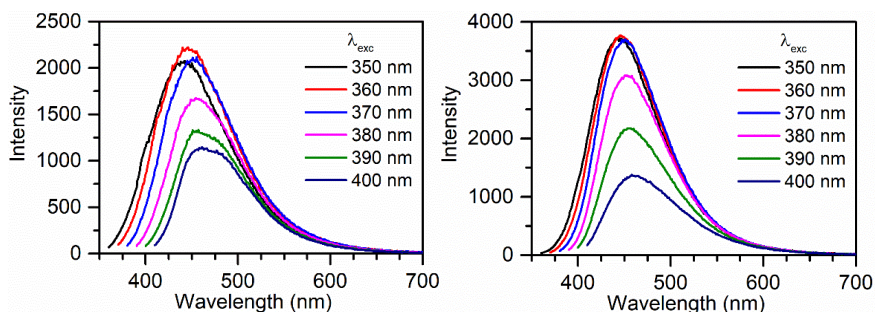


**Figure 3:** Spectres d'émission de NPs Si en microémulsion (à gauche) et hydrothermale (à droite) dans l'eau.

Dans les deux cas, les groupements aminoalkyl de la surface peuvent être identifiés par analyse infrarouge à transformée de Fourier (FT-IR) : les bandes larges centrées à  $3380\text{ cm}^{-1}$  et  $2930\text{ cm}^{-1}$  correspondant à l'élongation des liaisons N–H, les bandes à  $2850\text{ cm}^{-1}$  à l'élongation des liaisons C–H des chaînes alkyl, les bandes à  $1200\text{ cm}^{-1}$  aux vibrations Si–C, et dans le cas des NPSis hydrothermales, une bande intense à  $1026\text{ cm}^{-1}$  correspond aux vibrations Si–O–Si provenant de la présence de silice dans la structure.

Les mesures de spectroscopie photoélectronique par rayons X (XPS) montrent la présence de davantage d'espèces de carbone et de silicium oxydé dans les NP Si comparés à la microémulsion Si NPs, ce qui est une autre forte suggestion que le noyau de la première est plus proche de la silice que du silicium élémentaire dans sa nature et que l'émission peut effectivement provenir d'une source à base de carbone.

Le chapitre 3 se concentre sur les NP Si, pour lesquelles la grande quantité de silice présente dans la structure était au centre d'une enquête sur la véritable structure du matériau central. La procédure expérimentale pour la synthèse hydrothermale fut adaptée d'une méthode décrite où un traitement microonde était utilisé au lieu d'un chauffage dans un récipient scellé sous pression dans un four traditionnel.<sup>9</sup> Les caractéristiques des produits des deux réactions sont presque identiques, cependant l'article original décrit que les nanoparticules de silicium obtenues sont cristallines. Considérant la nature de la réaction, il nous semblait plus plausible que des nanoparticules de silice devraient être formées durant le procédé. Afin d'éprouver l'assertion de l'article original et notre hypothèse, une série de réactions furent réalisées où soit



l'APTMS ou l'acide citrique furent omis du milieu réactionnel avant le traitement, et les différents produits furent sujets aux mêmes techniques de caractérisation.

Il convient de noter les caractéristiques presque identiques trouvées entre les produits des deux réactions, en particulier en ce qui concerne les spectres de silicium Si2p à haute résolution XPS et de carbone C1s, qui montrent le même nombre de pics correspondant aux mêmes types d'environnements de liaison des atomes dans des rapports similaires pour les deux produits.

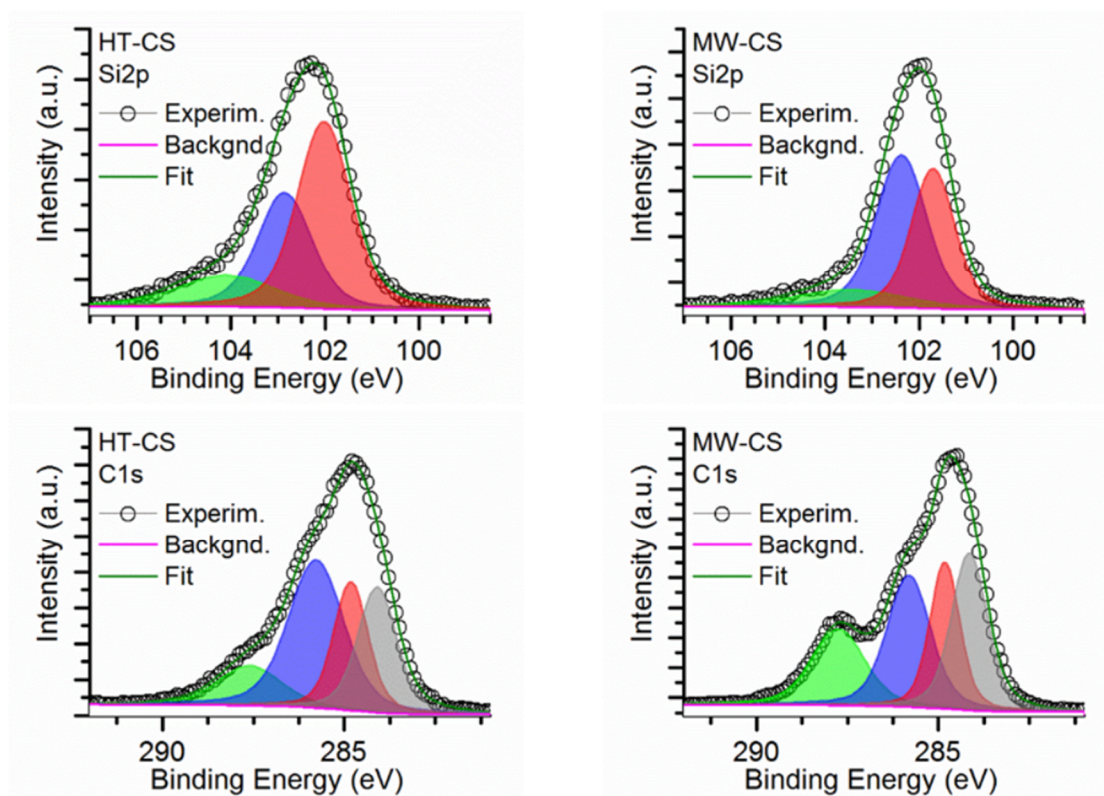


**Figure 4:** Balayages XPS en haute résolution des lignes Si2p (haut) et C1s (bas) des échantillons hydrothermaux (HT-CS (gauche)) et hyperfréquences (MW-CS (droite)).

Les études photophysiques ont montrés que les profils d'absorption des NPSis formés par réaction de l'APTMS et l'acide citrique sont identiques à ceux de l'acide citrique traité seul, indiquant que la composante photoactive des particules est reliée aux points carbone. Les données FT-IR montrent que les particules ont effectivement plus de points communs structurellement avec la silice. Des bandes symétriques et asymétriques d'unités Si-O-Si sont présentes dans les spectres des deux produits, ce qui est rendu très clair par rapport au spectre pour le silsesquioxane polyhédral.

Les données cristallographiques suggèrent également fortement que le silicium cristallin n'est pas présent dans les structures, ce qui indique que des nanoparticules de Si élémentaire ne se sont pas formées dans la réaction. Les deux diffractogrammes de cristallographie par rayons X pour les NP de Si sont caractérisés par deux pics larges. Celui à +/- 22 ° peuvent être attribués à la silice tandis que l'autre aux environs de 11 ° doit résulter d'une deuxième phase amorphe - très probablement du carbone amorphe.

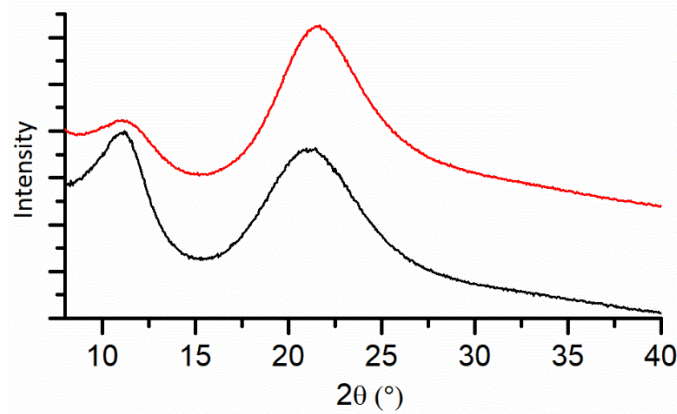


**Figure 5:** Diffractogrammes aux rayons X sur poudre pour les échantillons MW-CS (noir) et HT-CS (rouge).

Enfin, l'imagerie TEM a révélé une transition de phase rapide dans les particules soumises au faisceau d'électrons, passant de amorphe à cristalline, comme le montre la transformée de Fourier de la 6 ci-dessous. Ceci pourrait être causé par le chauffage du faisceau d'électrons, combiné aux conditions de vide poussé à l'intérieur de la chambre d'analyse, ce qui est une preuve supplémentaire de la nature hybride silice-carbone du matériau synthétisé.

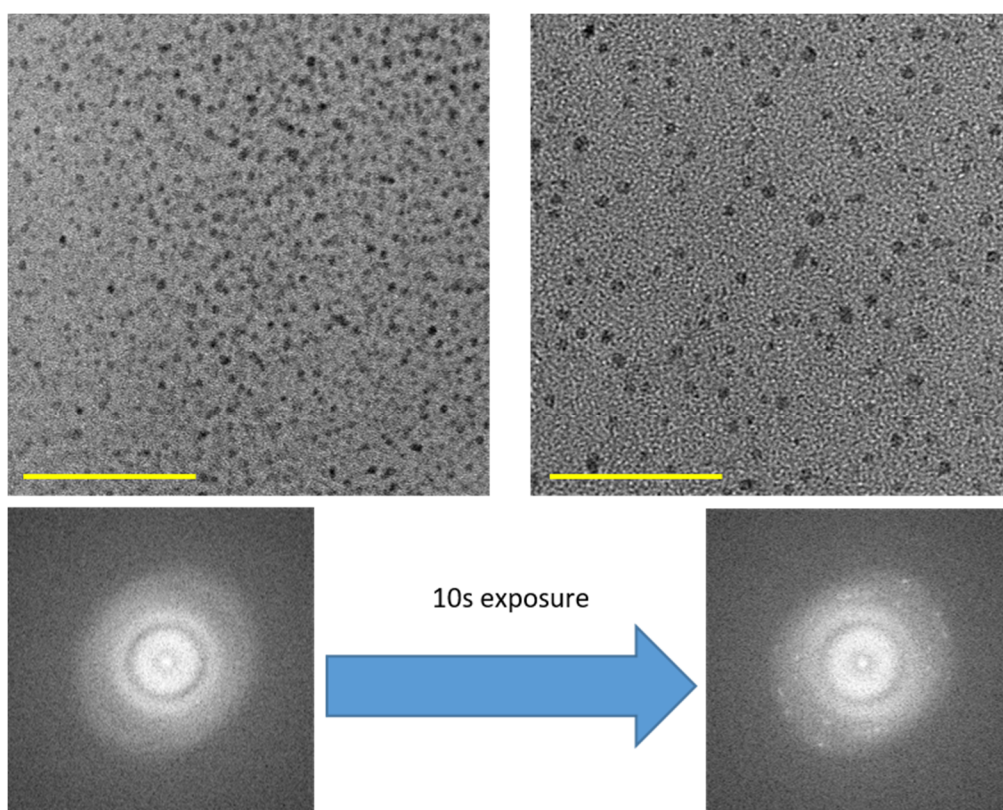


**Figure 6:** (En haut) images TEM représentatives des échantillons HT-CS (à gauche) et MW-CS (à droite) (barres d'échelle = 50 nm). (En bas) Observation en direct de l'évolution de la transformée de Fourier pour une particule dans le temps.

Le chapitre 4 présente les résultats d'investigations en imagerie biologique utilisant les Si NP hydrothermaux et en microémulsion. Avec ces matériaux en main, plusieurs études biologiques ont été réalisées, comme présenté dans notre publication récente<sup>[17]</sup>. Des tests de viabilité cellulaire ont été utilisés pour évaluer la toxicité des NPSis envers les cellules saines. Les NPSis microémulsifiées ont montré une plus grande cytotoxicité en comparaison aux NPSis hydrothermaux, ce qui, si l'on assume que tout le surfactant résiduel a bien été éliminé, peut être attribué à la plus grande concentration de groupement amine. La fonctionnalisation covalente de la surface des NPSis via les amines terminales fut réalisée afin de faciliter leur utilisation pour l'imagerie *in vivo*. Un ester de sulfocyanine 5 fut utilisé pour donner aux NPSis une émission visible *in vivo* dans le rouge, l'attachement de la sulfocyanine 5 confirmé par mesures photophysiques et FT-IR. L'imagerie optique *in vivo* des particules fonctionnalisées dans les souris montrent une fluorescence de tout le corps 20 minutes après injection, et une concentration of the NPSis dans la vessie 50 minutes après injection, démontrant l'élimination rapides des particules via les reins. La possibilité d'utiliser les NPSis pour TEP fut aussi

démontrée. Après greffage de complexes  $^{64}\text{Cu}$ -NOTA sur la surface, des études *in vivo* dans des souris furent réalisées à nouveau, avec de l'imagerie de tout le corps et mouvement vers les reins et la vessie dans les mêmes laps de temps<sup>[17]</sup>.

Ensuite, des sondes d'imagerie multimodales ont été créées en fixant à la fois un colorant fluorescent et un marqueur radioactif à la surface des SiNPs. Celles-ci ont permis de suivre les nanoparticules par imagerie de fluorescence optique et tomographie par émission de positrons (TEP). L'application des NP Si en imagerie *in vitro* et *in vivo* a été évaluée au moyen d'études d'absorption et de viabilité de cellules sur des lignes de cellules humaines ainsi que sur l'imagerie et la clairance rénale chez des souris porteuses de tumeurs.

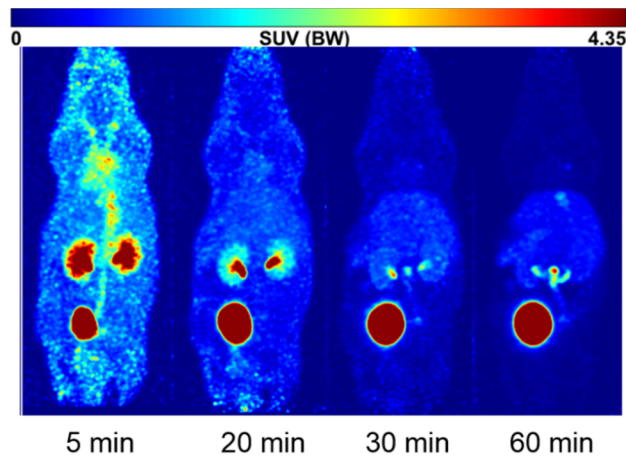


**Figure 7:** Images TEP *in vivo* d'une souris à différents moments après l'injection intraveineuse de  $^{64}\text{Cu}$  Cu-Si NP-IR800-NOTA, montrant la circulation sanguine dans tout le corps et l'élimination rapide subséquente des particules par les reins, la vessie et l'urine

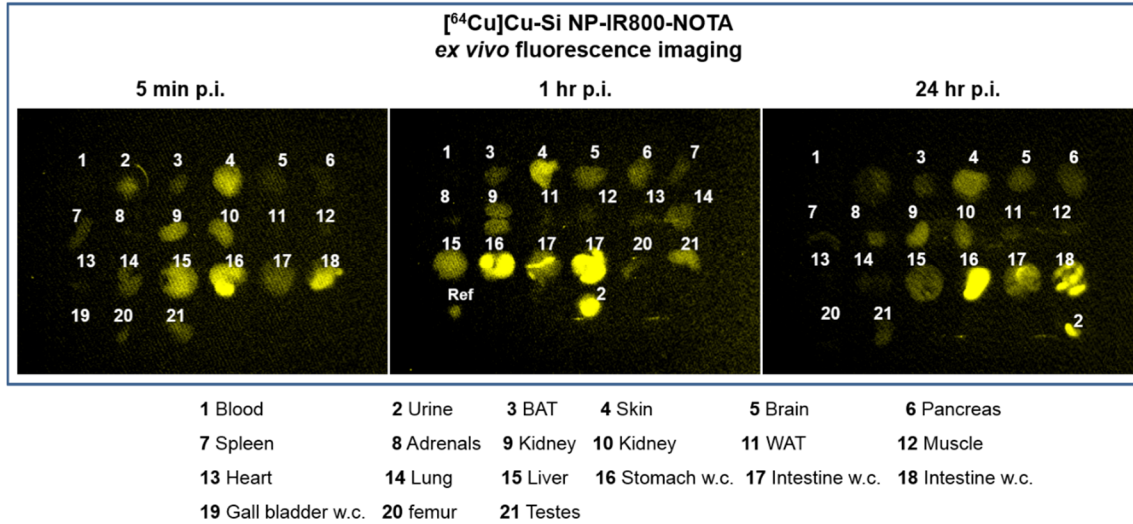


**Figure 8:** Imagerie *ex vivo* par fluorescence d'organes de souris à différents moments après l'injection. Une distribution uniforme est observée dans les 5 premières minutes, puis après 1 heure, la majorité de la fluorescence est observée dans l'intestin et dans les urines. Après 24 heures, des traces de fluorescence restante peuvent être détectées dans l'estomac, l'intestin et l'urine.

Dans une autre étude d'imagerie *in vivo*, la capacité des NPSis à traverser la barrière hémato-encéphalique (BHE) pour l'imagerie des tissus et tumeurs cérébraux, et leur élimination ultérieure furent évaluées. Il est possible pour le glucose du sang d'être transporté à travers la BHE via des protéines de transport spécifiques présentes dans la barrière et il a été montré que des nanoparticules d'or enrobées de glucose sont capables de traverser la barrière *in vitro*<sup>[18]</sup>. En appliquant ceci à notre modèle, des NPSis furent fonctionnalisées avec de la Cyanine 5 pour l'imagerie optique, et de la D-(+)-glucosamine pour aider le transport à travers la BHE. Les efficacités d'absorption, d'imagerie, et d'élimination furent évaluées dans les souris.

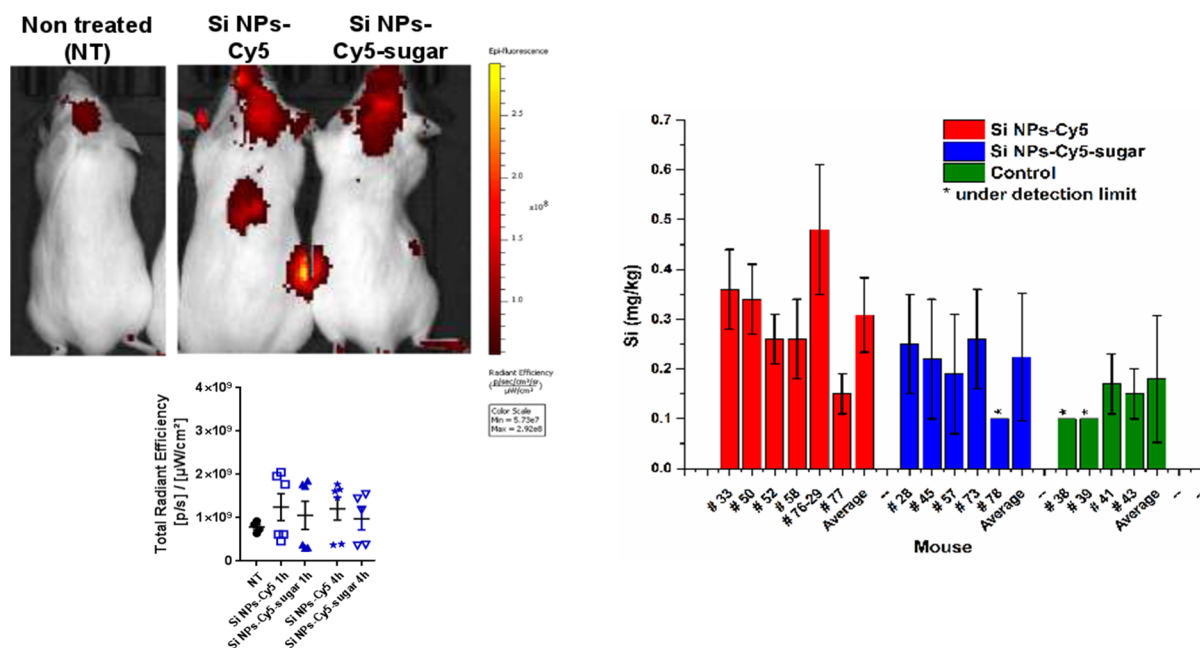


**Figure 9:** (Gauche) Imagerie cérébrale *in vivo* de conjugués SI NP avec un graphique montrant l'efficacité radiante à 1 heure et 4 heures après l'injection intraveineuse. (À droite) Les résultats ICP-AES de différents cerveaux de souris montrent la quantité de Si trouvée dans les tissus cérébraux.

**Une partie du contenu du chapitre 5 est confidentielle au moment de la rédaction.**

Le chapitre 5 traite de la création de nanosystèmes hybrides composés de complexes métalliques de ruthénium et d'iridium couplés à des NP de Si destinés à être utilisés dans des essais biologiques de diagnostic. Les complexes de métaux ont été bien utilisés pour la production d'essais biologiques via l'emploi de l'électrochimiluminescence (ECL). Parmi ceux-ci, les dérivés du complexe de tris(2,2'-bipyridine)Ruthénium(II) ( $[\text{Ru}(\text{bipy})_3]^{2+}$ ) sont devenus la référence absolue après avoir montré une efficacité ECL plus haute que celle de luminophores organiques<sup>[19]</sup>. Des études récentes ont suggéré que l'utilisation de complexes métalliques portant plus d'un centre métallique ou plus d'un complexe sur une espèce pouvant contenir plusieurs complexes à proximité les uns des autres pourrait augmenter encore l'efficacité des ECL. Dans une tentative d'augmenter encore plus l'efficacité ECL, un dérivé de  $[\text{Ru}(\text{bipy})_3]^{2+}$  fut greffé sur les NPSis et l'efficacité ECL fut testé en addition à la caractérisation du matériau par les méthodes employées précédemment. Récemment, il a été rapporté que les complexes d'iridium possédaient une efficacité ECL supérieure à celle des complexes de ruthénium. Par conséquent, un nouveau complexe d'iridium a été couplé à la microémulsion de Si NP dans un système utilisant les plus petits NP de Si disponibles pour tenter d'optimiser la cinétique de diffusion du système.

Les NPs de la microémulsion et du HT Si ont été couplés à un nouveau dérivé de  $[\text{Ru}(\text{bpy})_3]^{2+}$  via les groupes de surface amine et un ester actif de N-hydroxysuccinimide (NHS). Les microémulsions de NP en Si ont également été conjuguées au complexe d'iridium en utilisant une méthode similaire. En utilisant la spectroscopie UV-Vis, les concentrations des systèmes ont été contrôlées à  $10^{-5}$  M en utilisant le profil du complexe libre à la même concentration que la référence. À partir de ces données, des calculs permettant d'estimer le nombre de complexes liés à des NP de Si individuels pourraient être effectués. Les études ECL contredisent les hypothèses initiales. À partir de ces données, des calculs permettant d'estimer le nombre de complexes liés à des NP de Si individuels pourraient être effectués. Les études ECL contredisent les hypothèses initiales, le système HT Si NPs + [Ru] affichant un rendement ECL supérieur à celui de l'équivalent en microémulsion de Si NPs, ce qui est supposé être dû à la présence de davantage de groupes amino sur les NP Si HT, qui sont capable de fonctionner en tant que co-réactifs en plus du TPrA dans la solution. Il convient également de noter le faible rendement ECL calculé pour le système à microémulsion Si NPs + [Ir], ce qui serait dû à une combinaison du rendement plus faible que prévu du complexe lui-même et de la lente diffusion des NP Si vers l'électrode surface.

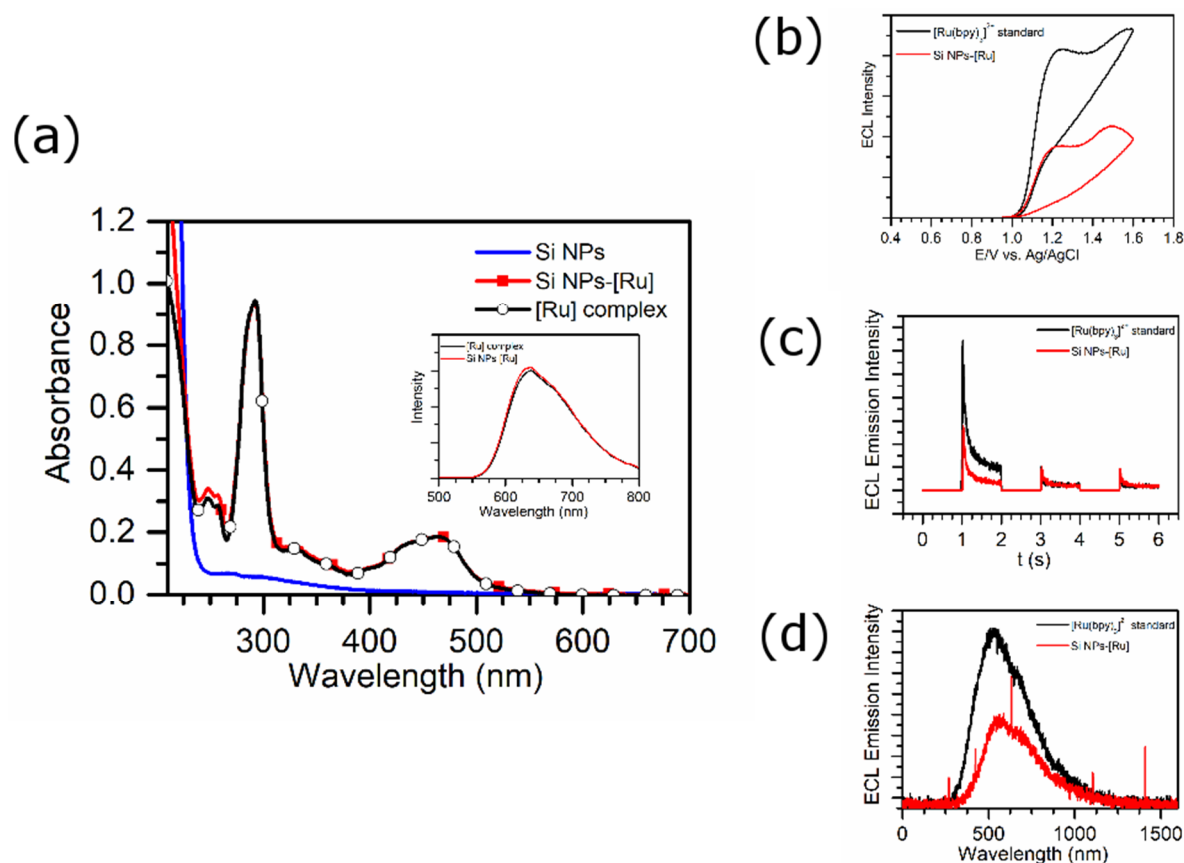


**Figure 10:** a) Spectres UV-visibles de NPs en Si en émulsion, de Si NPs-[Ru] et du nouveau complexe [Ru] dans l'eau (encadré: spectres d'émission du nouveau complexe [Ru] et de Si NPs-[Ru] dans l'eau). b) Parcelles de voltamétrie cyclique de [Ru(bpy)<sub>3</sub>]<sup>2+</sup> et Si NPs-[Ru] à Procell. c) Tracés chronoampérométriques de [Ru(bpy)<sub>3</sub>]<sup>2+</sup> et Si NP-[Ru] dans le Procell. d) Spectre d'émission ECL de [Ru(bpy)<sub>3</sub>]<sup>2+</sup> et Si NPs-[Ru] dans le Procell

Le chapitre 6 donne un bref aperçu des instruments utilisés dans la thèse, ainsi que de brefs détails sur leurs méthodes d'utilisation et leurs principes.

En conclusion, des nanoparticules à base de silicium à terminaison amine ont été synthétisées en utilisant deux méthodes différentes. Les caractéristiques structurelles des deux ont été minutieusement analysées afin de déterminer la véritable nature des matériaux de base. La biocompatibilité et l'application de divers systèmes fonctionnalisés de NPs Si en bioimagerie ont été testées avec succès dans différentes études. Malgré des résultats inattendus, des mesures ont été prises pour mettre au point une sonde efficace pour les essais biologiques et une base pour une optimisation plus poussée a été établie.



## Références

- [1] P. Sharma, S. Brown, G. Walter, S. Santra, B. Moudgil, *Adv. Colloid Interface Sci.* **2006**, *123–126*, 471–485.
- [2] M. Bruchez, M. Moronne, P. Gin, S. Weiss, A. P. Alivisatos, *Science* **1998**, *281*, 2013–2016.
- [3] M. Montalti, A. Cantelli, G. Battistelli, *Chem. Soc. Rev.* **2015**, *44*, 4853–4921.
- [4] R. Bilan, F. Fleury, I. Nabiev, A. Sukhanova, *Bioconjug. Chem.* **2015**, *26*, 609–624.
- [5] J. Liu, F. Erogbogbo, K.-T. Yong, L. Ye, J. Liu, R. Hu, H. Chen, Y. Hu, Y. Yang, J. Yang, et al., *ACS Nano* **2013**, *7*, 7303–7310.
- [6] F. Erogbogbo, K.-T. Yong, I. Roy, R. Hu, W.-C. Law, W. Zhao, H. Ding, F. Wu, R. Kumar, M. T. Swihart, et al., *ACS Nano* **2011**, *5*, 413–423.
- [7] L. T. Canham, *Adv. Mater.* **1995**, *7*, 1033–1037.
- [8] J.-H. Park, L. Gu, G. von Maltzahn, E. Ruoslahti, S. N. Bhatia, M. J. Sailor, *Nat. Mater.* **2009**, *8*, 331–336.
- [9] K. Linehan, H. Doyle, *Small* **2014**, *10*, 584–590.
- [10] J. H. Warner, A. Hoshino, K. Yamamoto, R. D. Tilley, *Angew. Chem. Int. Ed.* **2005**, *44*, 4550–4554.
- [11] Y. Zhong, F. Peng, F. Bao, S. Wang, X. Ji, L. Yang, Y. Su, S.-T. Lee, Y. He, *J. Am. Chem. Soc.* **2013**, *135*, 8350–8356.
- [12] M. Swierczewska, S. Lee, X. Chen, *Mol. Imaging* **2011**, *10*, 3–16.
- [13] S. Y. Lee, S. I. Jeon, S. Jung, I. J. Chung, C.-H. Ahn, *Adv. Drug Deliv. Rev.* **2014**, *76*, 60–78.
- [14] D.-E. Lee, H. Koo, I.-C. Sun, J. H. Ryu, K. Kim, I. C. Kwon, *Chem. Soc. Rev.* **2012**, *41*, 2656–2672.
- [15] A. Louie, *Chem. Rev.* **2010**, *110*, 3146–3195.
- [16] C. Tu, X. Ma, A. House, S. M. Kauzlarich, A. Y. Louie, *ACS Med. Chem. Lett.* **2011**, *2*, 285–288.
- [17] N. Licciardello, S. Hunoldt, R. Bergmann, G. Singh, C. Mamat, A. Faramus, J. L. Z. Ddungu, S. Silvestrini, M. Maggini, L. De Cola, et al., *Nanoscale* **2018**, *10*, 9880–9891.
- [18] R. Gromnicova, H. A. Davies, P. Sreekanthreddy, I. A. Romero, T. Lund, I. M. Roitt, J. B. Phillips, D. K. Male, *PLoS ONE* **2013**, *8*, e81043.
- [19] N. Kebede, P. S. Francis, G. J. Barbante, C. F. Hogan, *The Analyst* **2015**, *140*, 7142–7145.

# Chapter 1

## Introduction

### Abstract

This chapter presents an introduction to the topic of nanoparticles in medicine, with focus placed on their application in bio-imaging. Through this, crystalline silicon-based nanoparticles of very small sizes ( $< 5$  nm) are presented as the material of choice for the thesis work and an overview of their preparation methods, properties, functionalisation, *in vitro* and *in vivo* applications is given. The common diagnostic techniques of optical fluorescence imaging, magnetic resonance imaging (MRI) and positron emission tomography (PET) are introduced. The different functional labels and molecules required for the imaging techniques and their biological applications are highlighted and with regards to one of these labels, namely transition metal complexes, the technique of electrochemiluminescence and its emerging use is briefly covered.

### 1.1 Nanoparticles and their applications in medical imaging

Nanomaterials are defined as objects that possess at least one of their three dimensions in the size range of 1 – 100 nm. Specifically, in the case of nanoparticles (NPs), all three dimensions fall into the aforementioned size range<sup>[1]</sup>.

Nanoparticles have seen usage throughout history thanks to their unique properties. One of their earliest documented uses was purely aesthetic in the form of decoration on the Lycurgus cup<sup>[2]</sup>. From this, it is possible to see the intriguing optical properties of the colloidal silver and gold NPs included in the dichroic glass, which can appear green or red depending on the direction of incident light. Though the Roman artisans probably did not understand the nature of this phenomenon at the time, they remain some of the pioneers of nanotechnology and thanks to this example, a basis was formed for the investigation of the properties of materials at the nanoscale. With the advent of modern-day science, the mechanisms behind this colour change and many other phenomena of NPs have been discovered<sup>[3]</sup> and built upon, leading to the

emergence of a plethora of applications for the material. So numerous are the applications for NPs that they stretch all the way from electronics and photovoltaics to sensing and medicine<sup>[4]</sup>. Among these varied areas, the use of NPs in therapeutic and diagnostic nanomedicine has been a huge influence in increasing the attention on them over the past decades<sup>[5]-[8]</sup>. The wide range of materials available and the possibility to design NPs with a tuned size and functionality is of particular interest in the field on nanomedicine, where NPs see use as both imaging probes<sup>[9]</sup> and drug delivery vehicles<sup>[10]</sup>.

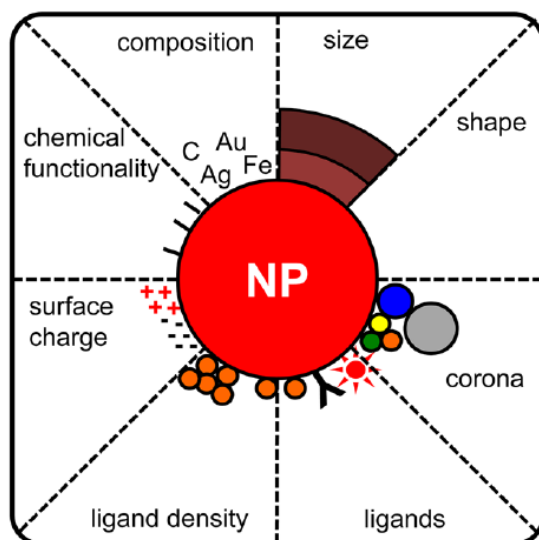


**Figure 1.1:** Designing an optimal imaging probe: Parameters of nanoparticles that need to be considered for biological applications<sup>[11]</sup>. Adapted with permission from J. Rauch, W. Kolch, S. Laurent, M. Mahmoudi, *Chem. Rev.* 113, 3391–3406. Copyright 2013. American Chemical Society

Concerning diagnostic nanomedicine and the use of NPs as imaging probes, NPs composed of an inorganic or crystalline core possessing intriguing properties have received much of the research focus in recent years<sup>[12]</sup>. These include those based on noble metals<sup>[13]</sup>, metal oxides<sup>[14]</sup> and quantum dots containing carbon or semiconductor materials<sup>[15]</sup>. Each of these possess particular properties and characteristics that make them very different from one another and when concerning their application in medical imaging, consideration must be given in order to design an optimal imaging probe to achieve a particular imaging goal.

### 1.1.1 On the design of an optimal imaging probe

#### *Noble metal nanoparticles*

As has been mentioned, the ability of gold nanoparticles to produce different visible colours upon interaction with light has been observed for many years. This is a result of the intrinsic photophysical properties of the nanoparticles, which originate from the size-correlated surface plasmon resonance of electrons on the surface atoms<sup>[16]</sup>. In fact, with gold and other noble metallic nanoparticles such as silver, depending on the size, shape and surface functionalisation of the NPs, it is possible to obtain colours covering the whole visible spectrum of light when irradiating the NPs with UV light<sup>[17]</sup>. Despite this ability to generate a range of colours, this particular property has not seen exploitation in the imaging of noble metal NPs *in vitro* and *in vivo*, most likely due to the need to use UV light as the stimulus, which is damaging to cells and living tissues.

The current visualisation techniques for noble metal NPs, specifically gold NPs, in bioimaging, involve the use of Transmission Electron Microscopy (TEM), Scanning Electron Microscopy (SEM), fluorescence microscopy, confocal microscopy and dark-field microscopy<sup>[18]</sup>. TEM has solely been used for *in vitro* studies, where gold NPs can be used to identify agents that cause infectious diseases (i.e. bacteria) and the different antigens present on their surfaces<sup>[19]</sup>. Examples show that SEM and fluorescence microscopy are also used for similar purposes<sup>[20],[21]</sup>.

In more recent times, imaging of gold NPs in a biological environment using optical microscopy, specifically confocal microscopy, has seen an increase in popularity<sup>[22],[23]</sup>. The most notable method of acquiring images using these imaging tools is by taking advantage of the resonance elastic or two-photon (multiphoton) light scattering that occurs when these plasmonic NPs are placed under the imaging source. Studies have demonstrated the use of this technique in *in vitro* imaging, where it was possible to visualise particular markers on the surface and the inside of cells<sup>[24],[25]</sup>

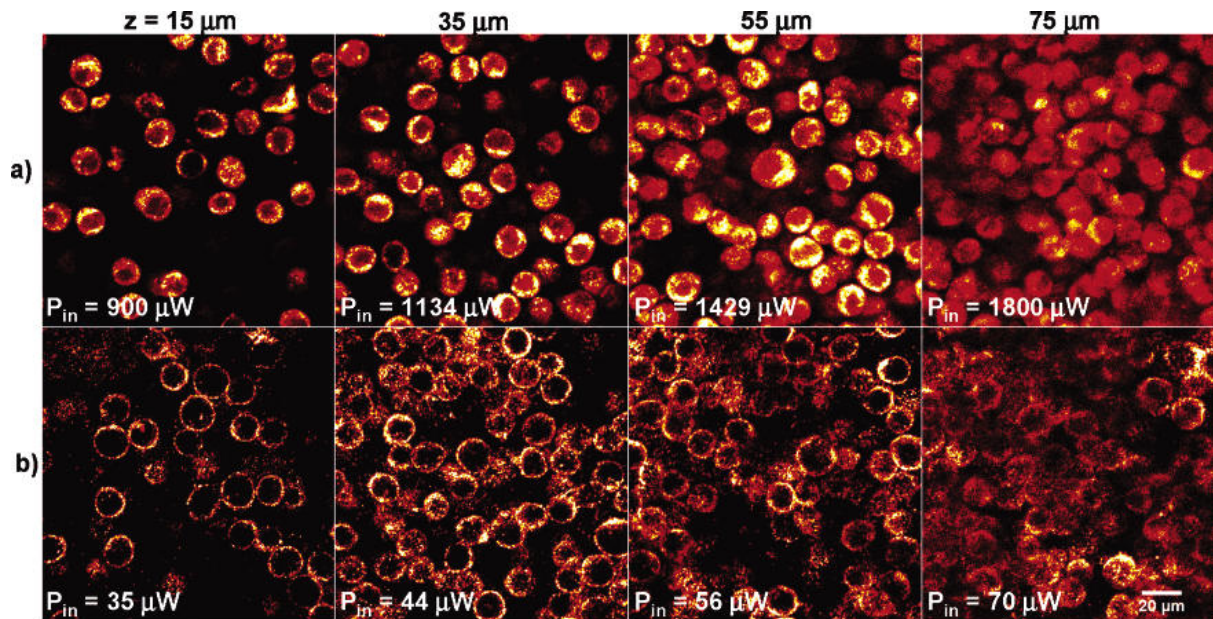


**Figure 1.2:** Two-photon imaging of cancer cells embedded in a collagen matrix at increasing depths. (a) Two-photon autofluorescence (TPAF) imaging of unlabeled cells and (b) Two-photon luminescence (TPL) imaging of nanorod-labeled cells. Both samples required the same excitation power increase of 26% at each 20  $\mu\text{m}$  depth increment to maintain constant emission intensity<sup>[24]</sup>. Reprinted with permission from N. J. Durr, T. Larson, D. K. Smith, B. A. Korgel, K. Sokolov, A. Ben-Yakar, *Nano Lett.*, 7, 941–945 Copyright 2007. American Chemical Society

Dark-field microscopy for the imaging of gold NPs utilises the light scattering capabilities of the NPs to obtain images of objects with a size smaller than the resolution limit of a light microscope. Gold NPs are said to be superior to molecular fluorescence labels in this application<sup>[26]</sup>, due to the higher scattering cross section of an NP compared to a molecule by around  $10^5$  times<sup>[27]</sup>. The capabilities of this technique were demonstrated in a study where gold NPs were conjugated with tumour antigen specific antibodies to facilitate preferential binding to tumour cells over healthy cells. This allowed the authors to map a tumour site with an accuracy down to only several cells using dark-field microscopy to image the resonance scattering of the bound gold NPs<sup>[27]</sup>.

Another more distinct method of using gold NPs in medical imaging is the biophotonic technique of photoacoustic tomography (PAT)<sup>[28]</sup>. With this, gold and other plasmonic noble metal NPs can be used as contrast agents when they absorb pulsed laser light, which causes transient temperature variations that generate acoustic signals<sup>[29]</sup>. These signals can be measured and converted into an image of the selected object<sup>[30]</sup>. Studies have shown the success in using gold NPs as contrast agents with PAT for both *in vitro*<sup>[31]</sup> and more particularly, *in*

*vivo*<sup>[29]</sup> imaging, something that the visualisation techniques mentioned before have not achieved.

Moving onto the size control of synthesised noble metal particles, there are numerous methods that have been established to prepare these species of NPs from sizes of several hundred nanometers<sup>[32]-[35]</sup> all the way down to our target size of < 5 nm<sup>[36],[37]</sup>. Most studies in the literature have seen a focus on gold NPs and possibly the most prominent method for the synthesis of the smaller sizes is that developed by Brust *et al.*<sup>[38]</sup> This makes use of a two-phase system where gold chloride is solvated in toluene by using tetraoctylammonium bromide as a phase transfer reagent and following reduction by sodium borohydride, the resulting small nanoclusters of gold are stabilised in the organic phase by dodecanethiol<sup>[39]</sup>. Although it is possible to obtain these small NPs with a great deal of size control, the reported toxicity<sup>[40]</sup> presents a limitation to their biomedical application. Shape control of gold NPs has also been an objective in the synthesis for a number of years<sup>[39]</sup>. Numerous different shapes have been prepared, with examples including rods<sup>[41]</sup>, shells<sup>[42]</sup>, cages<sup>[43]</sup>, tetrahedra and cubes<sup>[44]</sup>

As is the case for many NP materials, surface functionalisation of gold NPs is necessary in order to access the widest range of imaging applications. Work in this area has largely followed on from an initial study by Bain *et al.* where long-chain alkanethiols were reported to adsorb from solution onto gold surfaces<sup>[45]</sup>. This interaction between the gold and sulphur atom has been established as the cornerstone for the surface functionalisation of gold NPs for biological applications, where a wide variety of useful molecules have been terminated with thiolate groups for successful NP attachment<sup>[39]</sup>. Other functional groups have also proven able to form an interaction with the gold NP surface and anchor different molecules, including amines<sup>[46]</sup>, carboxylates<sup>[46]</sup>, selenides<sup>[47]</sup>, isothiocyanates<sup>[48]</sup> and phosphines<sup>[49]</sup>.

In terms of biocompatibility, gold NPs have been deemed “non-toxic” according to many reports when the size is > 5 nm and they are capped with biocompatible molecules such as citrate, cysteine, glucose, etc. <sup>[50]</sup>. They are believed to be internalised into cells primarily by a receptor mediated endocytosis (RME) mechanism<sup>[51],[52]</sup>. However, reports state that elemental metal NPs including silver NPs and possibly gold NPs can trigger oxidative stress in cells, leading to mitochondrial damage and necrosis<sup>[53],[54]</sup>

Ultimately, despite these good imaging results, range of synthetic strategies, functionalisation possibilities and the numerous non-toxic conclusions, there are drawbacks to gold and other noble metal plasmonic NPs that prevent them having a massive breakthrough into common

clinical bioimaging usage. Firstly, many of the covered promising techniques for the imaging of these NPs are restricted to *in vitro* applications on the microscale only. This is most likely due to the requirement of specialised equipment operating at high energies in order to image the particles themselves, which would be extremely complex to convert from microscopy to whole body *in vivo* imaging. Indeed, although optical fluorescence imaging could possibly be used, owing to the very low luminescence efficiency of noble metal NPs themselves under normal conditions<sup>[55]</sup>, they still seldom find use as optical imaging probes<sup>[56]</sup> when compared to other types of NPs, which show more superior capabilities. Next, the functionalisation of molecules onto the surface of gold NPs can come under scrutiny due to the use of non-covalent interactions. It has been shown that thiols bound to the surface of a gold NP are subject to exchange with those in the surrounding solution in a dynamic process<sup>[57]</sup>. While this can prove extremely useful in other applications such as drug delivery<sup>[58]</sup>, in bioimaging, where labels are targeting moieties must remain on the NP structure, this is a real limitation. Studies that have demonstrated that cell necrosis can be caused by gold and silver NPs, and more importantly, those that have reported toxicity of the smallest sized gold NPs Finally, noble metal NPs are also unable to be naturally degraded inside the body and this has the potential to interfere with their clearance, which could be affected further by the conjugation of additional molecules to the surface.

#### *Metal oxide-based nanoparticles*

Metal oxide NPs are numerous, with those prepared including Iron, Titania, Copper and Zinc to name but a few. However, for medical imaging applications, Iron oxide NPs have seen the most, almost exclusive attention and will therefore be the focus of this section.

For a number of years now, the dominant medical imaging application of Iron oxide NPs has been Magnetic resonance imaging (MRI)<sup>[9]</sup>. This technique takes advantage of the superparamagnetic properties of the iron (II), (III) structure, which allows them to behave as magnetic contrast agents<sup>[59]</sup>. They shorten the spin-spin relaxation time of the surrounding water molecules, and when applied *in vivo*, this can generate high contrast images of the nearby tissues, achieving resolutions much higher than molecular biomarkers<sup>[60]</sup>. With MRI being possible due to an intrinsic property of the core material, some studies have also shown the preparation of a multimodal imaging probe, whereby the iron oxide NPs are functionalised with a fluorescent dye in order to also allow tracking and imaging of the nanoparticles using optical fluorescence imaging<sup>[59]</sup>.

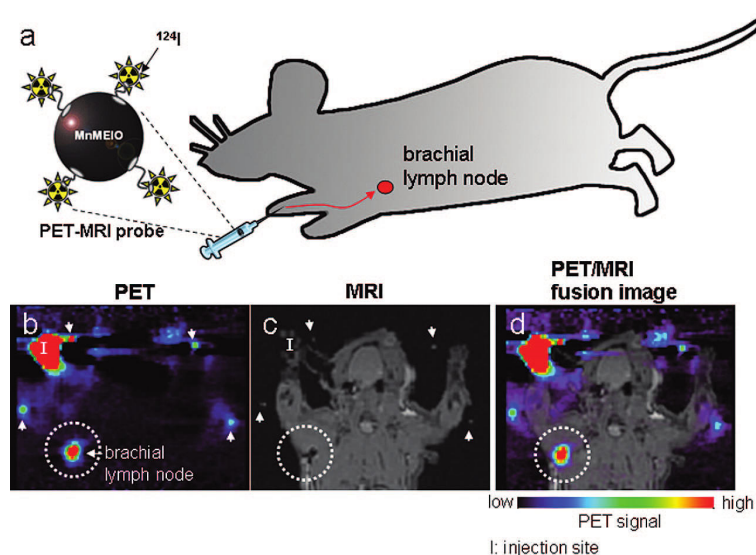


**Figure 1.3:** Two *In vivo* MRI-PET dual-modal imaging: (a) MnMEIO-124I conjugate probes are injected into the forepaw of a rat for the detection of lymph node; (b) PET image; (c) MR image; (d) PET/MR fusion image. The white circle denotes the location of a brachial lymph node<sup>[59]</sup>. Reprinted with permission from J. Cheon, J.-H. Lee, *Acc. Chem. Res.*, *41*, 1630–1640 Copyright 2008. American Chemical Society

A number of different methods exist for the preparation of iron oxide NPs and with this, a wide distribution of sizes of these nanoparticles are accessible<sup>[61]</sup>, ranging from 80 nm and above down to 4 nm. The smallest sizes below 5 nm have been achieved through the classic coprecipitation method from  $\text{FeCl}_3$  and  $\text{FeCl}_2$  to form magnetite ( $\text{Fe}_3\text{O}_4$ )<sup>[60],[62]</sup>, water-in-oil emulsion based syntheses where the NPs are formed in micelles of surfactant, hydrothermal reactions for the high temperature decomposition of organo-iron compounds in the presence of surfactants, and electrochemical methods<sup>[60]</sup>. A high degree of shape control is achieved through these methods with many examples highlighting the uniform spherical NPs synthesised<sup>[60]</sup>.

The lack of functional groups on the surface of pristine iron oxide NPs means that surface functionalisation normally proceeds by coating the NPs in a material that can be functionalised in tandem or thereafter<sup>[14]</sup>. As was stated earlier, dual MRI – fluorescence imaging probes have been prepared by coating the iron oxide NPs in silica doped with a fluorescent dye label<sup>[61]</sup>.

Cytotoxicity is an underlying problem for iron oxide NPs<sup>[63],[64]</sup>. It has been demonstrated that the negative effects of the material can be overcome by coating the NPs in another biocompatible material such as silica without losing the magnetic properties<sup>[65]</sup>, however, this



has the knock-on effect of increasing the overall size of the individual NPs, with no reports showing the achievement of such a system below 5 nm.

### *Quantum dots*

Nanoparticles based on semiconductor materials, such as II-VI or III-V quantum dots (QDs) have shown great potential in the field of imaging<sup>[66]</sup>. This is due to their high quantum yield of fluorescence, tunable emission wavelength, high photo bleaching threshold and high electro- and chemical stability, all of which contribute to their preference over organic dyes<sup>[12]</sup>.

So versatile and well-studied are the II-VI semiconductor QDs that the multitude of species developed possess emission wavelengths that cover the full visible spectrum of light and some regions beyond, as shown in figure 1.4

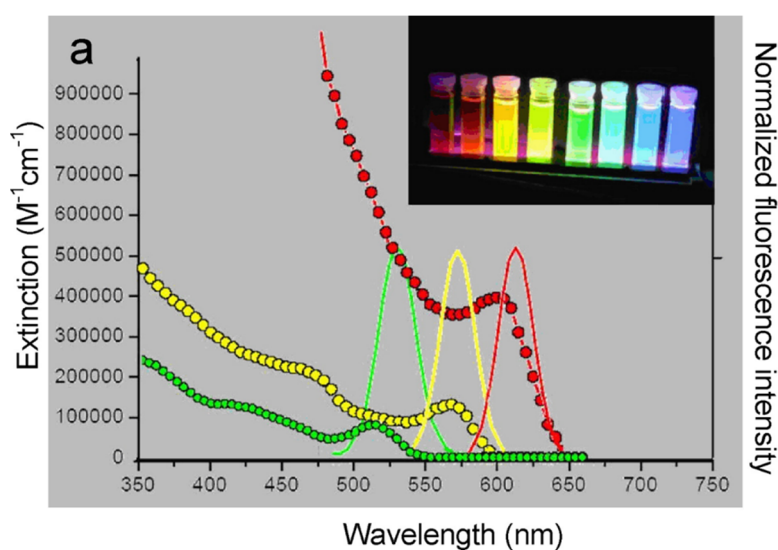


**Figure 1.4:** An example of the spectrum of colours achievable by quantum dots: solutions of CdSe/ZnS nanocrystals of different diameters irradiated under UV light with examples of the emission spectra from green, yellow and red emissive samples<sup>[67]</sup>. Reprinted from *Critical Reviews in Oncology/Hematology*, 68, 39–59., A. Sukhanova, I. Nabiev “Fluorescent nanocrystal-encoded microbeads for multiplexed cancer imaging and diagnosis” Copyright 2008, with permission from Elsevier.

This interesting development is made possible through the quantum confinement effect, a signature feature of quantum dots. Light absorption in bulk semiconductor materials can lead to the excitation of an electron from the valence band to the conducting band, leaving a “hole” in the valence band. The excited electron and hole can bind to each other, which in turn generates an exciton. Upon the return of the electron to its ground state in the valence band, the energy of the exciton is emitted as light of a defined wavelength corresponding to the band gap between the valence and conducting bands. When the dimensions of crystalline semiconductor materials are decreased down to the order of the exciton radius for electrons or holes in the specific material, the electronic structure is modified from that of the bulk material, with the size of the band gap increasing as the size of the crystal decreases. This leads to the formation of quantum dots, where the size of the particle is similar to the wavelength of the electron itself and confinement of motion into the nanoscale dimensions causes electrons to behave according to the “particle in a box” principle. As the size of the band gap is larger for smaller nanoparticles, these tend to emit further to the blue, while larger sized particles normally emit towards the red, as shown in figure 1.5 below.

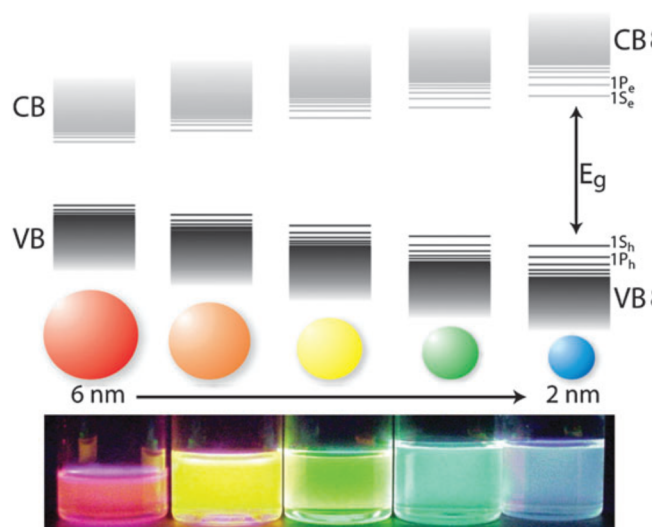


**Figure 1.5:** Schematic representation of the quantum confinement effect occurring in CdSe nanocrystals<sup>[68]</sup>. Republished with permission of The Royal Society of Chemistry from “Synthesis and properties of colloidal heteronanocrystals”, Chem. Soc. Rev., **40**, Copyright 2011; permission conveyed through Copyright Clearance Center, Inc.

This unique feature of achieving specific emission colours through a particular nanoparticle size has provided inspiration for a plethora of bioimaging applications using quantum dots. Particularly useful is that the QDs can be engineered to possess an emission wavelength falling

well within the NIR window for optimal imaging by optical fluorescence techniques. An early demonstration of semiconductor QDs in bioimaging is shown in work by Bruchez et al, where CdSe@CdS core-shell QDs were coated in a layer of silica, which was functionalised thereafter with trimethoxysilylpropyl urea and acetate groups for targeting of the cell nucleus<sup>[69]</sup>. Other examples of work using QDs include the attachment of acetic acid groups to the surface of CdSe@ZnS core-shell QDs via a mercapto-group to increase aqueous solubility and allow the imaging of HeLa cells<sup>[70]</sup>, the cross-linking of streptavidin and immunoglobulin G to CdSe@CdS QDs for imaging cancerous cells<sup>[71]</sup>, and the creation of glyconanospheres containing CdSe@ZnS QDs for studying carbohydrate-protein interactions<sup>[72]</sup>.

Despite these promising properties and applications however, there are some notable drawbacks to QDs that stand to prevent them from becoming established tools in the bio-imaging field<sup>[73]</sup>. For example, the most prominent QDs based on Cd, In, Pb, Hg, Se or Te derived cores with a ZnS shell have complicated surface chemistries that render them water-insoluble without the use of similar organic or silica coatings highlighted above and make functionalisation with biomolecules less straight forward. Existing synthetic procedures are quite harsh, requiring the use of heavy metal powders and high temperatures<sup>[74]</sup>. In addition to this, controlling the size of these QDs during synthesis is not so simple, making very small sizes for optimal bio-imaging applications hard to achieve and due the chemical nature of the core materials, they are non-biodegradable and inherently toxic in most cases<sup>[73]</sup>. Indeed, the possible release of heavy metal ions from the QDs once applied *in vivo* is the largest concern, as this would most likely prove fatal to the host<sup>[75]</sup>. While bio-imaging using these QDs has been demonstrated, these issues, especially the toxicity at low concentrations, have hindered progress with the materials.

In order to eliminate these problems, a number of actions have been suggested including; removing the heavy metals from the QD formulation, using a single inorganic element to simplify the properties of the material and above all, ensuring that this material is biodegradable, earth-abundant, has a well understood chemical behavior, has demonstrated biological applications and possesses minor biological roles such that it can be metabolised in the body<sup>[76]</sup>. This has led to a growing interest into research of silicon quantum dots or silicon-based nanoparticles (Si NPs).

### 1.1.2 Silicon-based Nanoparticles (Si NPs)

As one of the most naturally abundant materials on Earth, the studies and applications of silicon are numerous and wide. Bulk silicon is a well-known semiconductor material that sees usage in electronics and technology, with research into its possibilities on the macro, micro, and nanoscale notably increasing over the recent decades<sup>[77],[78]</sup>. Like other semiconductor materials in the bulk, silicon possesses valence and conducting bands that electrons can pass between. Different in the case of silicon however is the presence of an indirect band gap, which means that only indirect recombination processes of the generated phonon with the “hole” are possible, leading to a loss of energy of the produced photons and causing inefficient emission<sup>[79]-[81]</sup>.

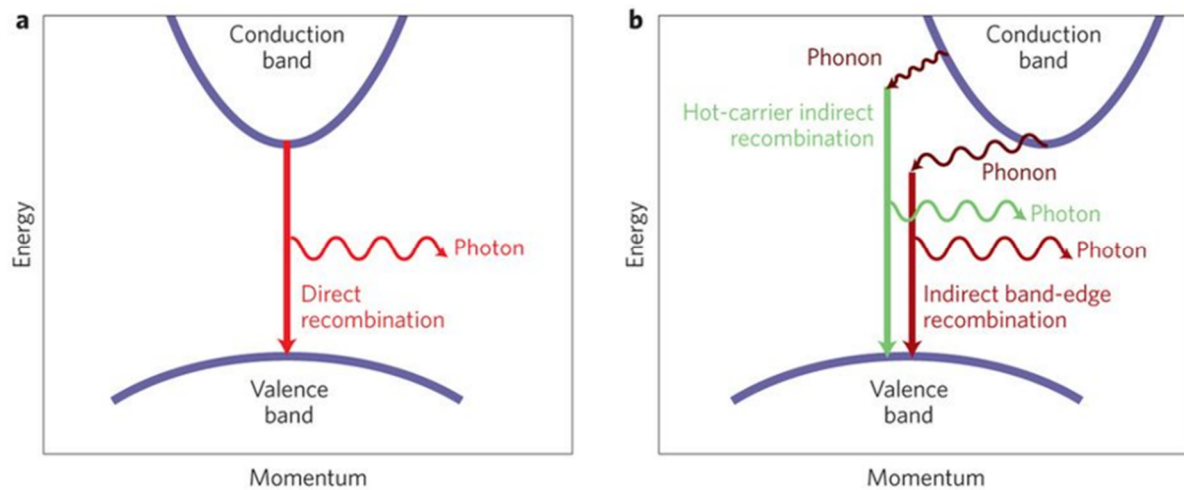


**Figure 1.6:** Schematic representation of a direct band gap and indirect band gap (as is the case for silicon)<sup>[82]</sup>. Reprinted by permission from Springer Nature Customer Service Centre GmbH: Springer Nature, Nature Photonics, “Silicon photonics: Nanocavity brightens silicon” M.Fujita, Copyright 2013.

Nevertheless, similar to the other semiconductor materials highlighted earlier, bulk silicon experiences a change in its optical properties when the size of the crystalline material is reduced to the nanoscale. It is believed that the size reduction is also accompanied by a transformation of the indirect band gap to a direct band gap<sup>[83],[84]</sup>. This causes nanocrystalline silicon to exhibit quantum dot behaviour and show bright emission of different colours depending on size. Photoluminescence of Si NPs remains a complex topic though, and there are a number of other factors that can influence the optical behaviour of the final product, including; structural defects<sup>[85]</sup>, synthetic methodology<sup>[86]</sup> and surface chemistry<sup>[87]</sup>.

### Synthesis of crystalline Si NPs

Numerous different methods exist in the literature for the synthesis of crystalline Si NPs, which can be divided into the groups of top-down and bottom-up approaches<sup>[12]</sup>. As the different methods lead to the production of NPs possessing different sizes, surface chemistries and optical properties, the choice of procedure will be largely governed by the intended application of the final product. A scheme identifying the most notable synthetic methods in the literature is shown below (figure 1.7).

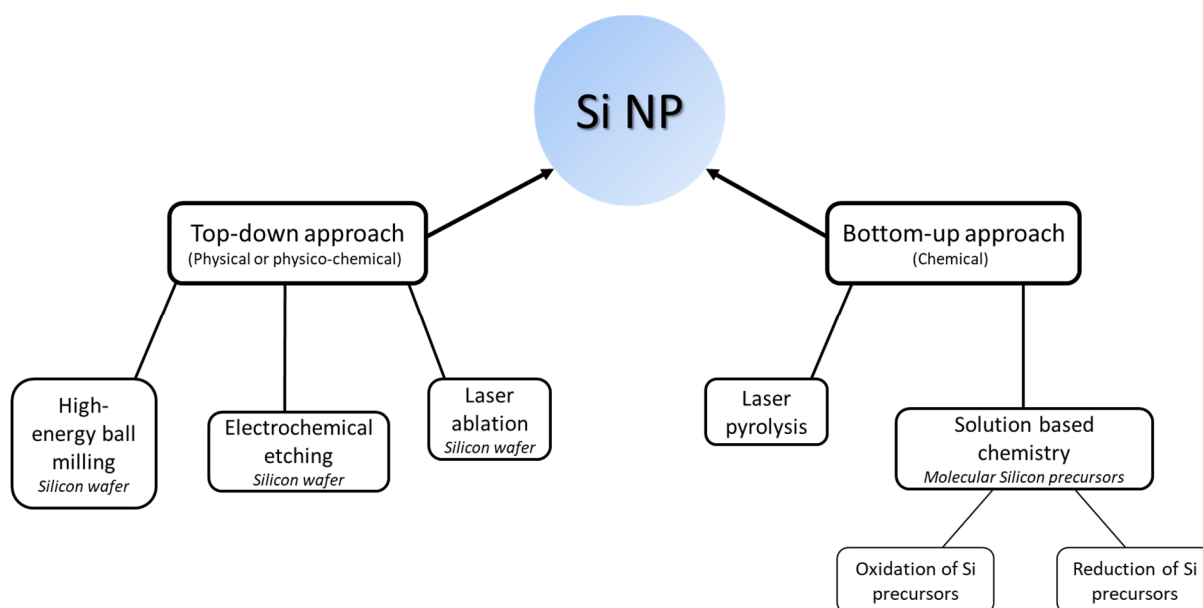


**Figure 1.7:** Scheme showing the most notable methods for the synthesis of Si NPs

Beginning with top-down approaches, these physical or physico-chemical techniques normally produce Si NPs with minimal impurities, but control of size and surface termination is more complex when compared to bottom-up approaches.

High energy ball milling is a physical technique that can be used to break a silicon wafer into nanosized pieces. As shown by Heintz *et al.* pieces of silicon wafer and capping reagents are mixed and processed to produce Si NPs of 4 nm that possessed a blue emission<sup>[88],[89]</sup>. It was noted that the emission wavelength of the Si NPs showed a bathochromic shift dependent on the excitation wavelength, which was hypothesised to be a result of the size distribution of the particles. The region the shift occurs in can be somewhat controlled through the use of different surface capping agents, with more polar molecules such as 1-octanoic acid encouraging a maximum emission further to the red.

Remaining with silicon wafers as the elemental silicon source, treatment by electrochemical etching can also be used to produce colloidal suspensions of luminescent crystalline Si NPs. It is possible to tune the maximum emission of the produced particles by controlling the time of the etching process, as shown in work by Kang et al. where longer etching times produced Si NPs bearing blue emission, and shorter times gave Si NPs with red emission<sup>[90]</sup>.

Laser ablation is a further top-down physico-chemical method. This is shown in work by Yamada et al. who used an ArF laser under a helium atmosphere to ablate a silicon wafer and obtain crystalline Si NPs of sizes from 17 nm down to 3 nm<sup>[91]</sup>.

Moving on to bottom-up approaches, these methods focus on the creation of Si NPs from small molecular precursors and are mainly solution based. As mentioned, they provide a higher degree of size and surface passivation control than top-down approaches, but impurities can be present due to the use of varied reagents.

Another method that makes use of a laser is the laser-induced pyrolysis of silane. It has been shown that using a focused CO<sub>2</sub> laser beam can cause the dissociation of SiH<sub>4</sub> and the subsequent nucleation of Si atoms to form Si NPs of 5 nm diameter<sup>[92]</sup>.

More versatile than the pyrolysis of silanes however, are the solution based wet chemistry methods. These offer arguably the highest degree of control over the formation of Si NPs, which is possible simply through the choice of reagents. Synthetic methods can be divided into those running via the oxidation of a silicon precursor and those running through the reduction of silanes.

Schemes summarising the general oxidation methods are shown in figure 1.8 below.

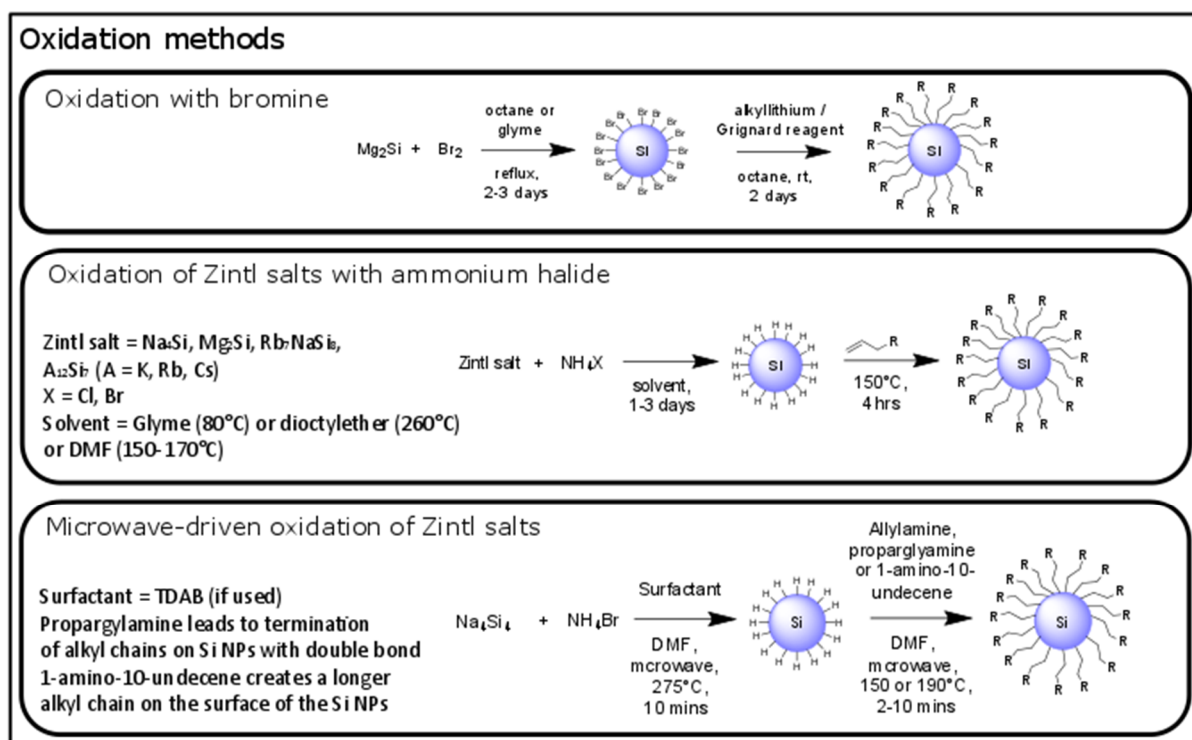


**Figure 1.8:** Methods for the synthesis of Si NPs starting with oxidation of a silicon source<sup>[93]-[96]</sup>

Early examples of many wet chemistry based methods come from the group of Kauzlarich et al. and indeed, they were the first to report a synthesis in the oxidation direction<sup>[93]</sup>. Here,  $Mg_2Si$  is oxidised by  $Br_2$  to obtain Br-terminated Si NPs, which are subsequently treated with lithium aluminium hydride ( $LiAlH_4$ ) in order to obtain H-terminated Si NPs. This group also detailed the synthesis of alkoxy/alkyl-capped Si NPs via oxidation of  $Mg_2Si$  with  $Br_2$ <sup>[94]</sup> Another well explored process by the group was the oxidation of Zintl salts using ammonium halides, which depending on the conditions can yield Si NPs of 5 to 60 nm<sup>[95],[96]</sup>.

A number of varied methods exist for the synthesis of Si NPs through reduction of a silicon source, the most prominent of which are summarised in figure 1.9 below.

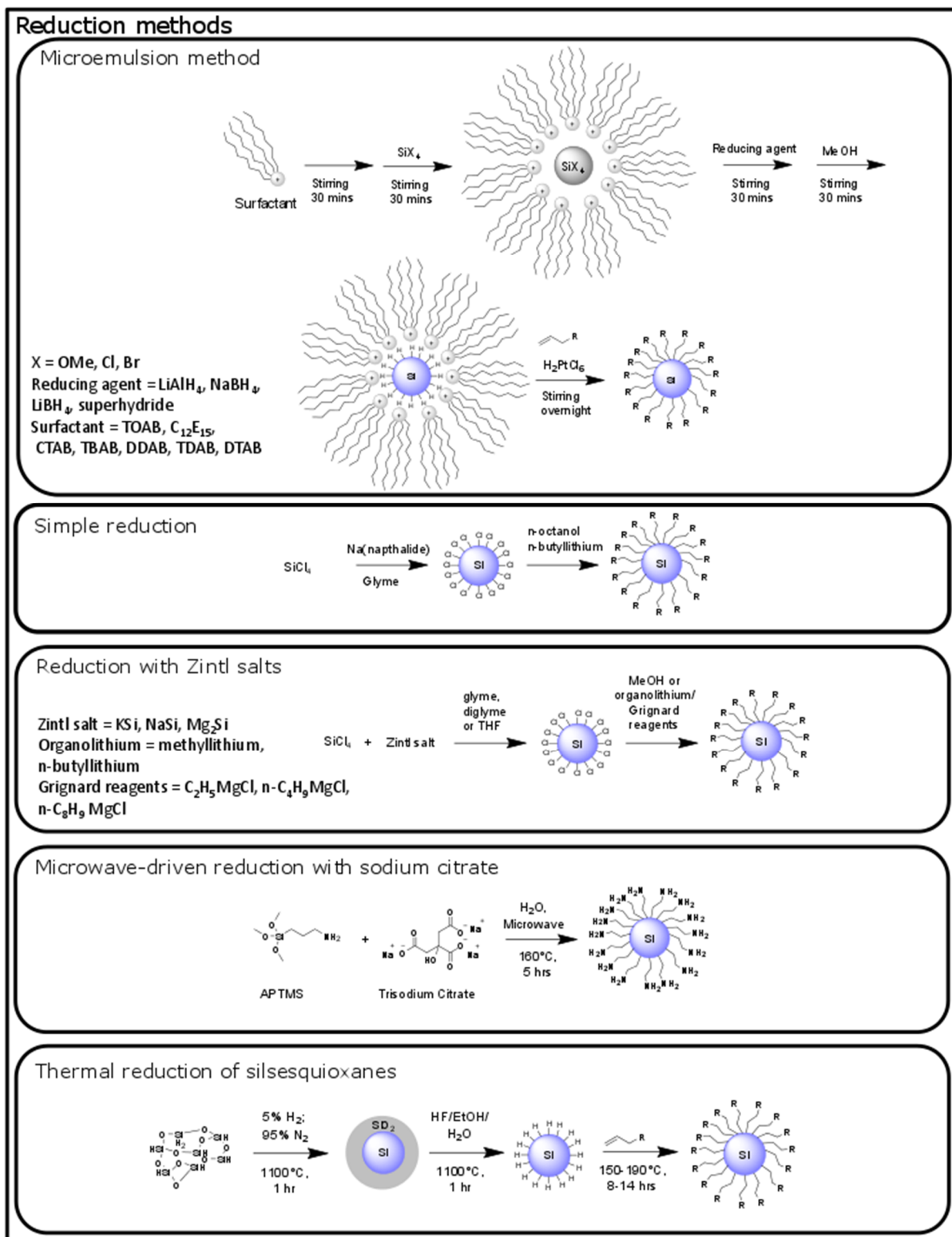


**Figure 1.9:** Methods for the synthesis of Si NPs starting with reduction of a silicon source<sup>[97]-[108]</sup>

An early synthetic method in this direction was reported by Heath in 1992, which involves the reduction of  $\text{SiCl}_4$  and  $\text{RSiCl}_3$  ( $\text{R} = \text{H}$ , octyl alkyl) with sodium in non-polar solvents under



inert atmosphere at high temperature and pressure for extended periods of time. Different R-group chain sizes could control the size of the final Si NPs, with the octyl chain giving a particle size of 5.5 nm<sup>[97]</sup>. The harsh reaction conditions led to studies to synthesise the particles in much milder conditions, such as to achieve better accessibility to the Si NPs and subsequently increase their application. All remain carried out under a strict inert atmosphere.

First is the so called “microemulsion method” where the reduction of the silicon precursor occurs in a reverse micelle “nano-reactor” of surfactants to form H-terminated Si NPs, which can be further functionalised by a hydrosilylation step catalysed using a Pt catalyst or UV irradiation. The reaction inside of the micelles is very advantageous, as it allows for a high degree of size control and maintains a low degree of polydispersion in the final product. The use of this method to produce H-terminated Si NPs was first reported by Wilcoxon et al.<sup>[98]</sup>, with sizes of 1.8 to 10 nm synthesised. The method was taken to the next stage by Tilley et al, who used SiCl<sub>4</sub> or SiBr<sub>4</sub> as precursors and tetraoctyl ammonium bromide (TOAB) or pentaethylene glycol monododecyl ether (C<sub>12</sub>E<sub>5</sub>) as surfactants to study the influence on the properties of the Si NPs, in addition to exploring the use of different reducing agents and methods of capping catalysis with either the Pt catalyst or UV irradiation<sup>[99],[100]</sup>. The strongest reducing agent, LiAlH<sub>4</sub> allowed synthesis of the smallest particles at an average size of 1.6 nm ± 0.4 nm with a blue emission. Other studies have looked more in depth into the use of different surfactants, such as the work by Doyle et al<sup>[101]</sup>, where several surfactants were used in order to change the characteristics of the micelle nano-reactor. TOAB was found to produce the smallest Si NPs (2.0 nm), and depending on the surfactant used, sizes upto 6.0 nm could be achieved.

A “simple reduction” is another method reported by the group of Kauzlarich et al<sup>[102]</sup>. This involves the reduction of SiCl<sub>4</sub> with sodium naphthalide in 1,2-dimethoxyethane (glyme) to produce Cl-terminated Si NPs that could be capped with n-octanol thereafter. The lack of a template means that the size of the particles is not controlled, with the final product being polydisperse Si NPs of 5.2 nm with a blue emission.

Also reported by the same group was the method of reducing SiCl<sub>4</sub> using zintl salts<sup>[103]-[105]</sup>. Si NPs produced here can be surface functionalised either simply by using methanol or by use of Grignard reagents to obtain different alkyl groups. It is the functionalisation that influences the size of the particles, which can be from 2 to 5 nm in diameter and possess emission in the range of 315 to 520 nm.

Another reduction method is the microwave treatment of an aqueous solution containing (3-aminopropyl)trimethoxy silane (APTMS) and trisodium citrate reported by He et al.<sup>[106]</sup>. This one-pot method produces amine-terminated Si NPs with a blue emission and a size in the region of 2.2 nm.

A final reduction method is the thermal decomposition and reduction of silsesquioxanes. In work by Veinot et al.<sup>[107],[108]</sup> the reduction at high temperature leads to the production of Si NPs embedded in silica, which is then etched using hydrofluoric acid to obtain Si NPs with a diameter of around 3.4 nm that possess emission in the visible and near-infrared regions. Further work on this synthesis has explored the synthesis of capped Si NPs possessing organic moieties on the surface using this method<sup>[109],[110]</sup>. The obtained sizes are small (in the region of 2 nm), but despite predictions of a blue emission with the quantum confinement effect, the Si NPs actually show a red emission, proving that size is not the only influential property on emission colour<sup>[86]</sup>.

#### *Photoluminescence of Si NPs*

As has been highlighted, there are a number of different factors that have an effect on the photoluminescence of Si NPs. Of these, the most generally accepted effecting factors are the quantum confinement effect and the influence of surface states.

A proof of the quantum confinement effect came from a study by Kang et al.<sup>[90]</sup>, where red-emissive 3 nm Si NPs produced by electrochemical etching were treated with a H<sub>2</sub>O<sub>2</sub> mixture, which caused the oxidation of the outermost silicon to silica. With increasing treatment time and, subsequently, decreasing diameter of the elemental silicon core, the emission was tuned from red to blue. Etching of the final product with hydrofluoric acid (HF) and the persistence of the blue emission thereafter confirmed that the blue emission originates from the silicon core.

There has also been argument and proof that defects in the silicon structure are the main influence on emission. Sugimoto et al. achieved small, but NIR emissive 3 nm Si NPs that were doped with boron and phosphorous<sup>[111],[112]</sup>. Here, it is suggested that the presence of boron and phosphorous creates donor and acceptor states within the band gap of the silicon, which in turn changes the luminescence of the particles to varying degrees.

Surface states are also an important factor in the photoluminescence and these are in the main influenced and dictated by the synthetic route used to obtain the Si NPs. It has been reported

that the use of nitrogen and oxygen containing chemicals during the synthetic procedure leads to a shift in the emission of Si NPs to blue<sup>[86]</sup>. In this work by the groups of Kauzlarich, Tilley and Veinot, dodecyl-capped Si NPs prepared by three different methods; thermal reduction, oxidation of zintl salts and microemulsion, were compared. Si NPs prepared from thermal reduction possessed a red emission, while the others showed blue emission. To show the influence of the nitrogen and oxygen-containing chemicals on the emission, the red emissive H-terminated Si NPs from the thermal reduction were reacted with TOAB and ammonium bromide. Increasing the concentrations of these reagents shifted the emission of the particles to the blue, however, when the reaction was conducted under an inert atmosphere, no shift in the emission was observed, showing that the initial presence of nitrogen and oxygen is fundamental to the blue emission.

#### *Surface chemistry of Si NPs*

In order to obtain full use of the Si NPs in different applications, appropriate functionalisation of the surface is essential. This becomes even more important at smaller sizes, where an increased percentage of the Si atoms making up the nanoparticle are exposed on the surface, increasing the reactivity and tendency for oxidation to form Si-O bonds in the presence of oxygen and/or water.

One of the most effective ways identified to ensure stability of the silicon core is by passivation of the surface with alkyl chains, which protects the outer Si atoms from oxidation via a stable Si-C covalent bond. Throughout the different synthetic methods, allylamine stands out as a popular ligand for initial surface functionalisation as it terminates the Si NPs with amine groups, granting the surface access to biologically-friendly amide chemistry<sup>[113]</sup>, which can be used for many further functionalisations to couple a variety of molecules to the particles.

#### *Biological imaging applications of Si NPs*

Owing to the highlighted versatility of the material, numerous biological tests and applications with Si NPs have appeared in the literature, evolving from initial in vitro studies conducted by Ruckenstein et al<sup>[114]</sup>, and Tilley et al<sup>[99]</sup>. Some of the contributions to this evolving area of research are highlighted here.

In studies by Zuilhof et al., small (~ 1.57 nm) amine terminated Si NPs with a blue emission bearing different alkylamino chain lengths were synthesised and tested in vitro to assess their bioimaging capabilities<sup>[115]</sup>. The Si NPs were shown to localise in the cytosol of the cells and

were said to not show any notable signs of toxicity. Zuillhof et al. also reported on the synthesis of carboxylic acid terminated Si NPs, which were conjugated to single stranded DNA, providing a prospective base for a biosensing probe.

Si NPs synthesised through the hydrothermal and UV irradiation treatment of (3-aminopropyl)trimethoxysilane have been coupled with the goat anti-mouse IgG antibody in studies by He et al<sup>[106],[116]</sup>. It was shown that the particles are able to stain the nuclei of cells and be imaged over a long term period, while maintaining a very low toxicity.

Internalisation and localisation of Si NPs in cells was demonstrated to be dependent on size and surface functionalisation in a study by Yamaguchi et al<sup>[117]</sup>. Si NPs terminated with either allylamine or block copolymer Pluronic 127 were used in aggregated forms of various sizes (controlled from ca. 30 nm to 270 nm) for studying the interaction with human umbilical vein endothelial cells (HUVECs). Organelle-specific labelling was found to be different with each functionalisation and size group.

Using Si NPs produced through the electrochemical etching procedure, Sailor et al. showed how the versatile model of red emissive porous Si NPs can be used as a theranostic device<sup>[118]</sup>. The particles were loaded with doxorubicin, for which the release of the drug could be correlated with the appearance of silicic acid from natural degradation of the Si NPs. Moreover, whole-body fluorescence imaging in tumour bearing mice showed successful NIR fluorescence imaging of the tumour where Si NPs accumulated passively and subsequently degraded into their nontoxic products.

*In vivo* PET and biodistribution studies using Si NPs were performed by Kauzlarich et al<sup>[119]</sup>. Here, they showed that dextran coated manganese doped Si NPs that are functionalized with a <sup>64</sup>Cu complex are rapidly excreted by renal filtration when small in size (< 7 nm), while larger particles show some localisation in the liver, spleen, and lymphatic system, where after after hepatobiliary processing, they would enter the gall bladder and intestine.

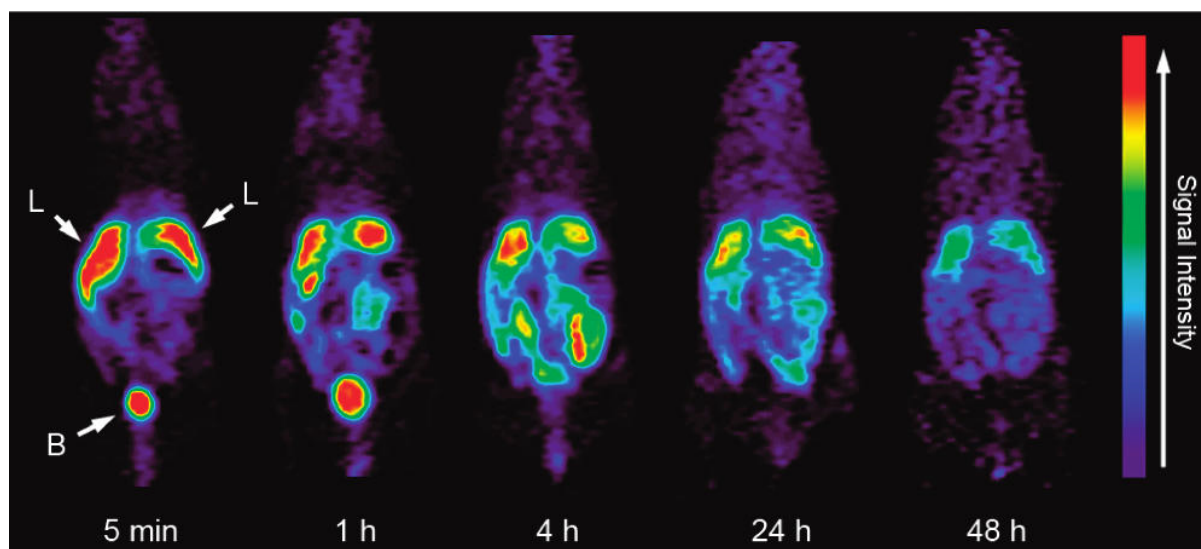


**Figure 1.10:** In vivo PET images of mice ( $n = 4$ ) at 5 min, 1 h, 4 h, 24 h, and 48 h postinjection of  $^{64}\text{Cu}$ -DO3A conjugated dextran SiMn QDs 6: L, liver; B, bladder<sup>[119]</sup> Reprinted with permission from C. Tu, X. Ma, A. House, S. M. Kauzlarich, A. Y. Louie, *ACS Med. Chem. Lett.*, 2, 285–288.

Copyright 2011. American Chemical Society

## 1.2 Diagnostic imaging methods

With the prevalence of cancer in the world, the development of imaging technologies needed to understand its complex and diverse nature in *in vivo* settings has been accelerated over the past few decades. A representation of this is given below in figure 1.11. The techniques of Magnetic Resonance Imaging (MRI) and Positron Emission Tomography (PET) are already well established in clinical practice, while optical fluorescence imaging is the subject of a large amount of research and development in both a clinical and laboratory setting.

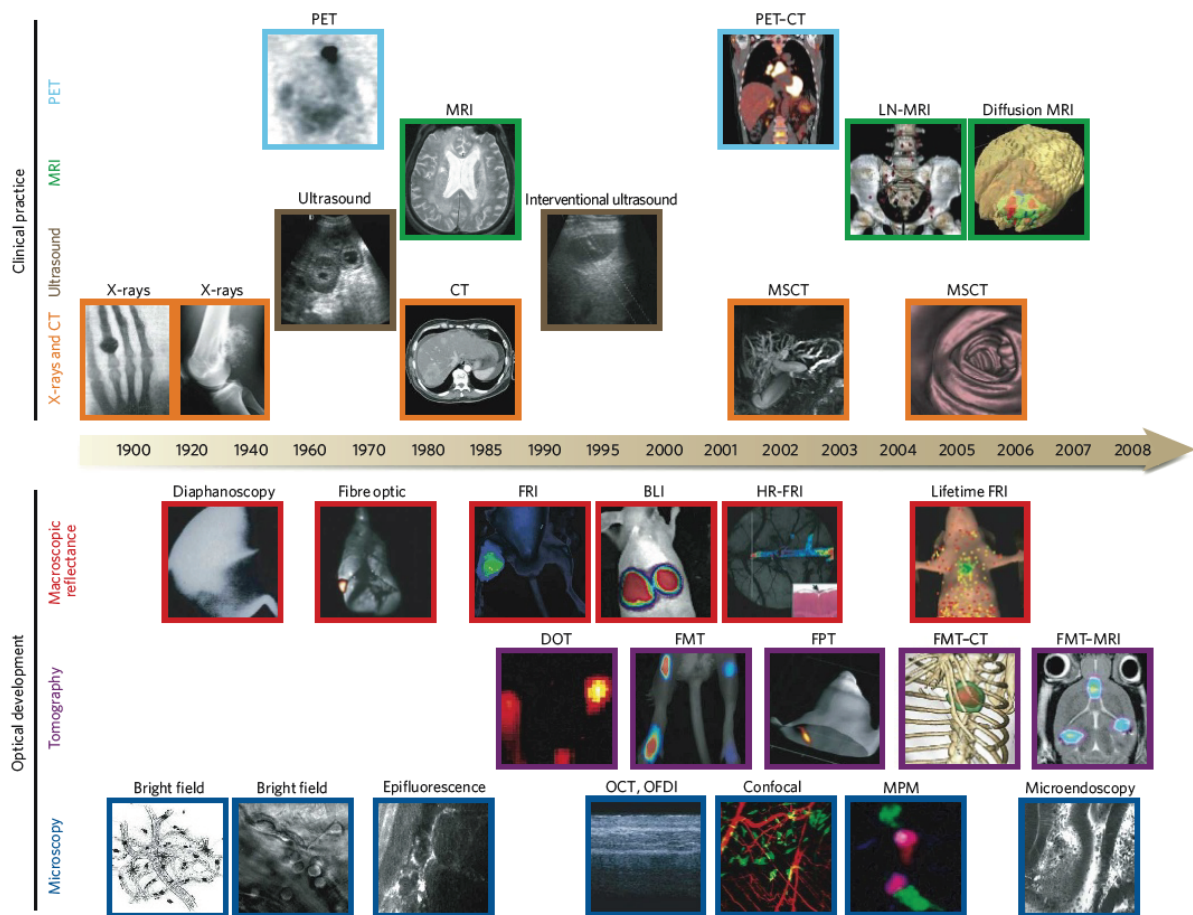


**Figure 1.11:** The development of biological imaging methods<sup>[120]</sup>. Reprinted by permission from Springer Nature Customer Service Centre GmbH: Springer Nature, Nature, “Imaging in the era of molecular oncology” Ralph Weissleder, Mikael J. Pittet, Copyright 2008.

Each of the three techniques are briefly introduced in this section and some typical labels are identified.

### 1.2.1 Optical fluorescence imaging

This technique works in tandem with the administration of a photoactive label (fluorophore) in the body or biological media. Once the fluorophore is in the environment, the imaging equipment can apply light of a specific wavelength required to excite the molecule and cause it to emit photons of a longer wavelength, which are detected by the equipment. The signal can be used to map the environment in the vicinity of the fluorophores, providing information on biological structures and processes. The use of optical fluorescence imaging on the microscale is well established. Multiphoton microscopy imaging systems have been developed with multiple channels available to achieve three-dimensional images constructed from light emitted

at different wavelengths from different fluorophores. Resolution down to the millimetre scale is possible with this technique and the time required to generate an image is short at seconds to minutes<sup>[121]</sup>.

### Labels

Fluorophores that are applied for imaging *in vitro* and *in vivo* should have a  $\lambda_{\text{max}}$  emission that occurs within, or at least close to, a defined region in order to achieve optimal imaging capabilities. This is known as the near-infrared (NIR) window, the position of which in the visible – NIR spectrum is shown in figure 1.12 below.

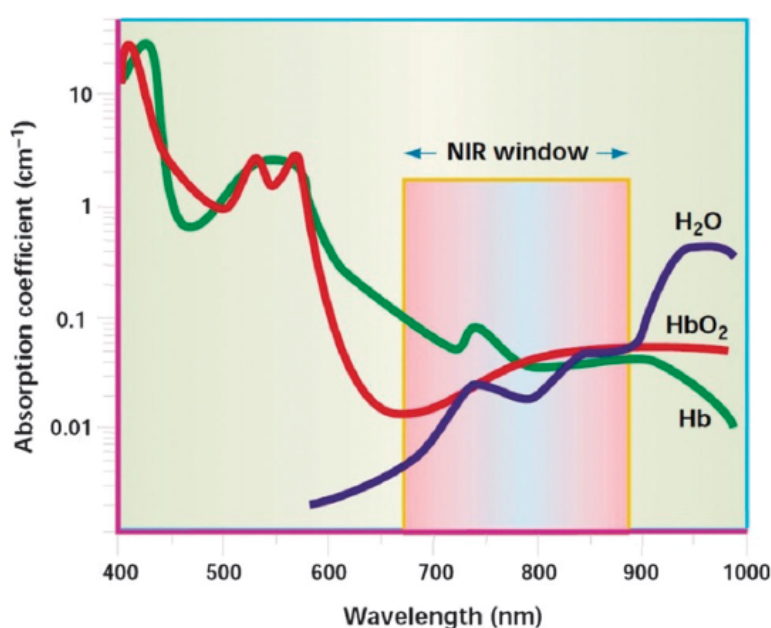


**Figure 1.12:** The position of the near-infrared window for optimal imaging using fluorescent probes<sup>[122]</sup>. Reprinted by permission from Springer Nature Customer Service Centre GmbH: Springer Nature, Nature, “A clearer vision for *in vivo* imaging” Ralph Weissleder, Copyright 2001.

The window is positioned in between points of significant absorption by haemoglobin (<650 nm) and water (>900 nm) both present with high abundance in the body. This represents the ideal region of emission for fluorophores as their emission will be the least quenched. Wavelengths within this window are also to penetrate and be visible at up to 1 cm through bodily tissues.

Many labels of red and NIR emission are commercially available and have seen plenty of use, with one of the most noted being indocyanine green, which has also had positive applications in the clinic<sup>[123]</sup>.

### 1.2.2 Magnetic Resonance Imaging (MRI)

MRI is a widely used macroscopic imaging technique employed in the clinic. While laying down on a bed that enters a large magnetic coil, the patient is in the middle of a strong magnetic field, which can interact with the protons of lipids and water molecules in tissues. The hydrogen nucleus possesses a spin quantum number of  $I = \frac{1}{2}$ , which is utilised in the core principle of the MRI process. The nuclei are able to respond to the external magnetic field and split their spins into two states ( $2I + 1$  states), with the energy between these two states being proportional to the strength of the magnetic field. An external radio frequency pulse is applied simultaneously, with the specific energy of the pulse absorbed by the split-state nuclei. This changes their spin orientation from the  $+1/2$  state to the  $-1/2$  state in a phenomenon known as resonance. When the pulse is discontinued, the excited nuclei relax and return to the ground state with the spin quantum number returned to  $I = \frac{1}{2}$ . Radiofrequency signals from this relaxation process are recorded by the RF detector coils, which converts the data into a molecular resonance image<sup>[124], [59]</sup>.

MRI provides a high resolution between 10 –100  $\mu\text{m}$  and no limit on the detection depth. However, the low sensitivity (milli- to micromolar), long time to generate information (up to hours) and high cost are still the drawbacks of this technique

### 1.2.3 Positron Emission Tomography (PET)

PET is another broadly used medical imaging method in the clinic. The patient is administered radiopharmaceutical and lays on a bed that enters the chamber of circular detector. Here, high energy  $\gamma$ -rays generated by radioactive species in the administered radiopharmaceutical can be detected. Commonly used positron emitting radioisotopes are  $^{15}\text{O}$ ,  $^{13}\text{N}$ ,  $^{11}\text{C}$  and  $^{18}\text{F}$ , but heavier elements also see use including  $^{64}\text{Cu}$ . Using  $^{64}\text{Cu}$  as an example, it stabilises by transforming a proton into a neutron and in the process, emits a positron. The positron loses energy until annihilating with an electron, in an event that produces two  $\gamma$ -photons with identical energies emitted in opposite directions. These are picked up by the detector, which can position the source of the emission and after collecting a sufficient number of measurements from events, reconstruct an image showing the distribution of the emitting molecules<sup>[125]</sup>. Sensitivity of the technique is very high (picomolar range) and there is no limit to the depth of detection. However, the generation of information can take hours and it is a high cost process<sup>[121]</sup>.



### 1.3 Electrochemiluminescence (ECL)

The first Electrochemiluminescence (ECL) studies were performed by Hercules in the 1960s<sup>[126]</sup>. It was shown that a bright luminescence can be observed when applying a voltage through a platinum electrode into a solution containing aromatic hydrocarbons such as anthracene, pyrene, perylene etc. Since these small-scale, experimental beginnings, ECL has become a versatile analytical technique that appears in applications from immunoassays through to water quality testing. Its defining feature is the high sensitivity, which allows for the detection of various desired analytes at very low concentrations<sup>[127]</sup>. Luminescence during the process is triggered by applying a voltage to a solution containing a luminophore instead of through the use of an external light source. The lack of need for incident light means the Raman band belonging to the solvent and the later second-order diffraction band do not appear in data collected using the method, which greatly enhances the signal-to-noise ratio.

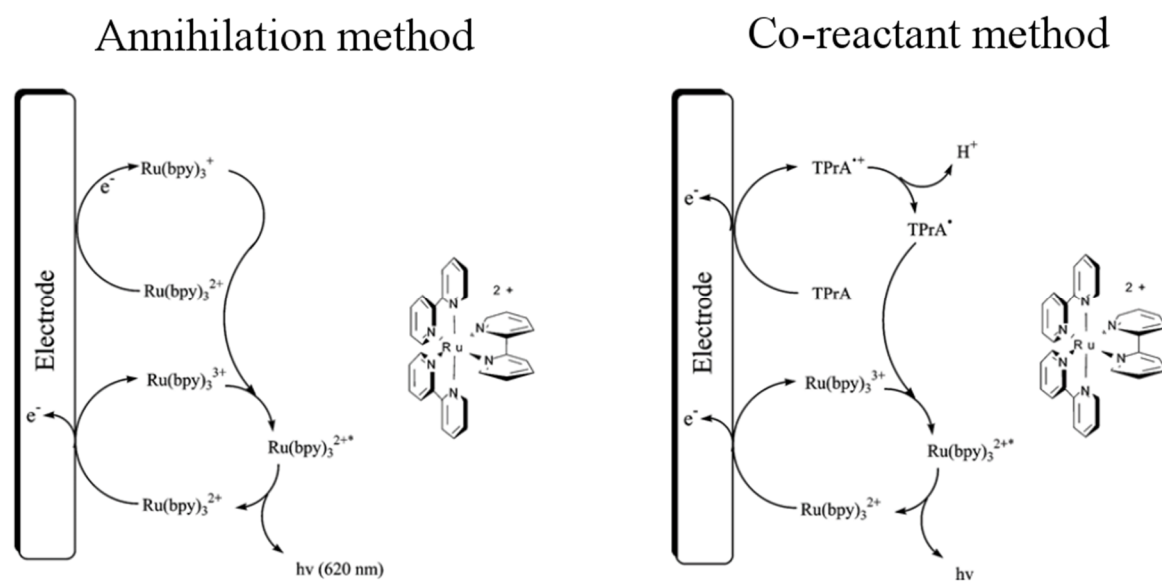


**Figure 1.13:** Schematic of the mechanisms of ECL through the annihilation and co-reactant methods<sup>[127]</sup>. Reprinted with permission from Chem. Rev. 2004, 104, 3003-3036 Copyright (2004) American Chemical Society.

ECL has two main pathways of generation: the annihilation method and the co-reactant method. As shown by Figure 1.13 above<sup>[127]</sup>, in the annihilation method, both the reduced and oxidized forms of [Ru(bpy)<sub>3</sub>]<sup>2+</sup> are generated at the electrodes when the applied voltage is swept from oxidation to reduction potentials of [Ru(bpy)<sub>3</sub>]<sup>2+</sup>. These radical cations and anions are

annihilated to generate the excited-state species, which naturally emits light. In the co-reactant method, the excited state luminophore is generated by the co-reactant at a fixed applied voltage. Using tripropylamine (TPrA), a widely employed co-reactant as an example, once the oxidation potential of TPrA is reached, a TPrA<sup>•</sup> radical is formed (following the removal of one proton from the TPrA<sup>•+</sup> radical cation), which will then transfer one electron to the oxidized [Ru(bpy)<sub>3</sub>]<sup>3+</sup> emitter, forming the excited state species that emits light. There are a few advantages of this method over annihilation. The use of emitters that are stable only in the R<sup>•+</sup> (oxidized) or R<sup>•-</sup> (reduced) form and that only have a reversible electrochemical reduction or oxidation is possible, and it also permits the use of solvents that possess narrow potential windows<sup>[128]</sup>.

The “gold standard” system in ECL identified by the literature to date is based on the ruthenium trisbipyridine complex, [Ru(bpy)<sub>3</sub>]<sup>2+</sup>, and its derivatives. The complex has been established in commercial use for bio-and immunoassays that are based on the co-reactant method<sup>[129]</sup> such as in DNA sequence detection<sup>[130]</sup>, Aptamer and DNA/enzyme biosensors<sup>[131],[132]</sup>, and metal cation detection<sup>[133],[134]</sup>. However, due to the increasing demand for ever increasing accuracy in diagnostics, ECL assays possessing even greater sensitivities and with the added possibility of different emission colours to suit different applications, has become desirable.

### 1.3.1 Nanoparticles in ECL

The use of nanomaterials in ECL has become an interesting prospect in the further development of the field. Initial ECL studies of semiconductors were reported in 2002. Silicon nanoparticles at sizes of 2 to 4 nm displayed an ECL emission signal at 640 nm with use of both the annihilation and co-reactant methods<sup>[136]</sup>. This work inspired the study of other semiconductor materials, including Ge, CdSe and CdTe quantum dots etc., which have seen their ECL properties tested<sup>[137]-[139]</sup>. Their ECL emission is red-shifted in relation to their photoluminescence, which strongly indicates the presence of different emission states. As identified previously, the photoluminescence of QDs is, at least in part, via excitation and emission from the core of the nanoparticles, while the ECL can be said to be mainly influenced by the surface chemistry and the presence of the surface states<sup>[140]</sup>. An example of ECL exhibited by CdSe/ZnSe nanoparticles is detailed in work by Myung *et al.*<sup>[141]</sup> The ECL emission profile identifies two emission peaks: one identical to the emission spectrum of the quantum dots and the other with a 200 nm red-shifted emission band which is said to originate

from the surface states of the QDs. An illustration of the mechanism is shown below in figure 1.14<sup>[142]</sup>

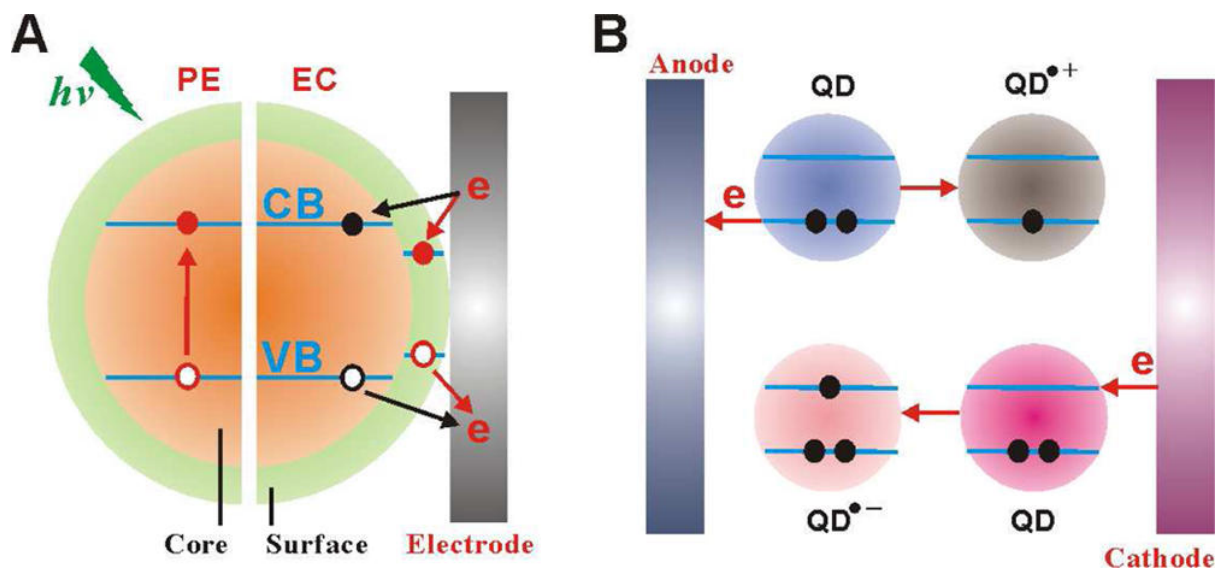


**Figure 1.14:** Schematic representation of the photoluminescence (PE) and ECL (EC and diagram B) processes in semiconductor nanocrystals<sup>[142]</sup>. Reprinted with permission from *Anal. Chem.*, 87, 9520–9531 Copyright (2015) American Chemical Society.

The development of nanoparticle based probes in ECL is an emerging topic that is garnering interest. An approach identified for building highly sensitive ECL assays is the combination of nanomaterials with metal complexes in a nanohybrid system. One direction is encapsulating ECL active molecules into a nanoparticle matrix, which would grant protection from the surrounding solvent and a high proportion of light, while possibly increasing photostability and enhancing the ECL signal due to an increase of active molecules directly on or in close proximity to the electrode. However it could also lead to a decreased rate of the electrochemical processes as well as most likely lead to much slower diffusion of the analytes and reaction intermediates through the encapsulating material. In addition to this, the leaking of the key molecules from the material has been identified as an issue in some cases<sup>[143]-[145]</sup>. A way of getting around this issue is the grafting of the metal complexes onto the surface of the nanoparticles. This has been demonstrated successfully in recent work by our group where carbon dots were covalently linked to  $[\text{Ru}(\text{bpy})_3]^{2+}$  complexes and the resulting hybrid showed a higher ECL efficiency than the free complex or a simple mixture of the two components

alone<sup>[146]</sup>. Building on this result, it would be interesting to see where the use of Si NPs will bring the efficiency of the system.

## 1.4 Scope of the Thesis

Nanomaterials, and specifically nanoparticles, hold great potential in medical imaging and wider diagnostic applications and should be exploited to further improve the diagnosis of diseases and reduce mortality rates. In this thesis, different systems based on Si NPs that function as imaging probes and that can be built upon to work in diagnostic ECL applications, have been developed.

Chapter 2 covers the synthesis of amine-terminated Si NPs through different routes (microemulsion and hydrothermal) and details the extensive characterisation to compare differences and attempt to identify the true chemical nature of the core material.

Chapter 3 focuses on the Si NPs synthesised through the hydrothermal method, for which the large amount of silica present in the structure was central to an investigation into the true structure on the core material.

In Chapter 4, the results of biological imaging investigations using the hydrothermal and microemulsion Si NPs are reported. With the material in hand, the surface amine groups were used to couple different functional molecules to the surface of the Si NPs. The first system sees the Si NPs coupled to a PET radiotracer, with their biodistribution, tumor and wider body imaging efficiency, and subsequent clearance all assessed. This success of this is built upon in the second system, where a fluorescent label is added in order to determine if the creation of a multimodal probe will have any major effect on the activity, and to use the second functionality for further assessments. The third system concerns the creation of a targeted probe functionalised with a sugar and a fluorescent label for studying the uptake and imaging efficiency of the Si NPs across the blood-brain-barrier. As the intrinsic emission of the Si NPs falls outside of the NIR window, it is necessary to use a dye with a emission maximum within the window in order to distinguish the Si NPs from the autofluorescence present in biological environments.

Chapter 5 covers the creation of hybrid nanosystems composed of novel metal complexes of ruthenium and iridium coupled to Si NPs for use in diagnostic bioassays. Full photophysical characterisation of the hybrid systems was performed and their ECL efficiency was evaluated with respect to  $[\text{Ru}(\text{bpy})_3]^{2+}$  as a standard. This particular project was conducted in collaboration with Roche Diagnostics (F. Hoffmann-La Roche Ltd), who provided the metal

complexes and ProCell for the ECL experiments, and due to confidentiality agreements, the content of this chapter remains confidential at the time of writing.

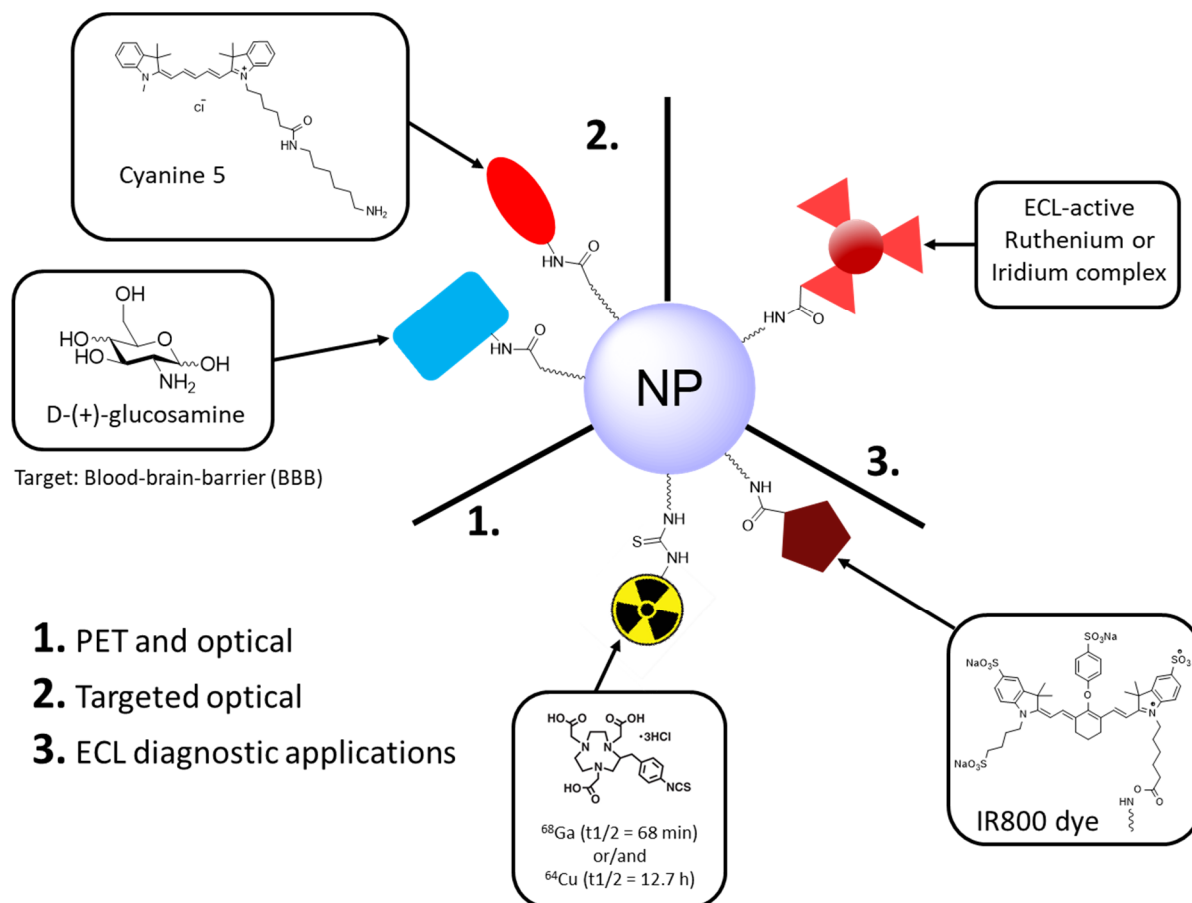


**Figure 1.15:** Schematic representation of the different hybrid Si NP systems investigated in this thesis following Si NP synthesis and characterisation.

## 1.5 References

- [1] H. Goesmann, C. Feldmann, *Angew. Chem. Int. Ed.* **2010**, *49*, 1362–1395.
- [2] J. Estelrich, M. Quesada-Pérez, J. Forcada, J. Callejas-Fernández, in *Nanosci. Nanotechnol. Ser.* (Eds.: J. Callejas-Fernández, J. Estelrich, M. Quesada-Pérez, J. Forcada), Royal Society Of Chemistry, Cambridge, **2014**, pp. 1–18.
- [3] M. Faraday, **n.d.**, 38.
- [4] B. Pelaz, S. Jaber, D. J. de Aberasturi, V. Wulf, T. Aida, J. M. de la Fuente, J. Feldmann, H. E. Gaub, L. Josephson, C. R. Kagan, et al., *ACS Nano* **2012**, *6*, 8468–8483.
- [5] S. Marchesan, M. Prato, *ACS Med. Chem. Lett.* **2013**, *4*, 147–149.
- [6] T. Jamshaid, M. Eissa, N. Zine, A. E. El-Salhi, N. M. Ahmad, A. Elaissari, in *Soft Nanoparticles Biomed. Appl.*, **2014**, pp. 312–341.
- [7] O. S. Wolfbeis, *Chem. Soc. Rev.* **2015**, *44*, 4743–4768.
- [8] S. Kunjachan, J. Ehling, G. Storm, F. Kiessling, T. Lammers, *Chem. Rev.* **2015**, *115*, 10907–10937.
- [9] H.-C. Huang, S. Barua, G. Sharma, S. K. Dey, K. Rege, *J. Controlled Release* **2011**, *155*, 344–357.
- [10] J. Liu, C. Detrembleur, S. Mornet, C. Jérôme, E. Duguet, *J. Mater. Chem. B* **2015**, *3*, 6117–6147.
- [11] J. Rauch, W. Kolch, S. Laurent, M. Mahmoudi, *Chem. Rev.* **2013**, *113*, 3391–3406.
- [12] M. Montalti, A. Cantelli, G. Battistelli, *Chem. Soc. Rev.* **2015**, *44*, 4853–4921.
- [13] P. K. Jain, X. Huang, I. H. El-Sayed, M. A. El-Sayed, *Acc. Chem. Res.* **2008**, *41*, 1578–1586.
- [14] A. K. Gupta, M. Gupta, *Biomaterials* **2005**, *26*, 3995–4021.
- [15] X. Gao, Y. Cui, R. M. Levenson, L. W. K. Chung, S. Nie, *Nat. Biotechnol.* **2004**, *22*, 969–976.
- [16] J. Z. Zhang, C. Noguez, *Plasmonics* **2008**, *3*, 127–150.
- [17] J. E. Millstone, S. J. Hurst, G. S. Métraux, J. I. Cutler, C. A. Mirkin, *Small* **2009**, *5*, 646–664.
- [18] L. Dykman, N. Khlebtsov, *Chem. Soc. Rev.* **2012**, *41*, 2256–2282.
- [19] V. D. Bunin, O. V. Ignatov, O. I. Gulii, A. G. Voloshin, L. A. Dykman, D. O’Neil, D. Ivnitiskii, *Biofizika* **2005**, *50*, 316–321.
- [20] G. Naja, S. Hrapovic, K. Male, P. Bouvrette, J. H. T. Luong, *Microsc. Res. Tech.* **2008**, *71*, 742–748.

- [21] R. L. Phillips, O. R. Miranda, C.-C. You, V. M. Rotello, U. H. F. Bunz, *Angew. Chem. Int. Ed.* **2008**, *47*, 2590–2594.
- [22] G. Wang, A. S. Stender, W. Sun, N. Fang, *Analyst* **2010**, *135*, 215–221.
- [23] S. Klein, S. Petersen, U. Taylor, D. Rath, S. Barcikowski, *J. Biomed. Opt.* **2010**, *15*, 036015.
- [24] N. J. Durr, T. Larson, D. K. Smith, B. A. Korgel, K. Sokolov, A. Ben-Yakar, *Nano Lett.* **2007**, *7*, 941–945.
- [25] G. Maiorano, S. Sabella, B. Sorce, V. Brunetti, M. A. Malvindi, R. Cingolani, P. P. Pompa, *ACS Nano* **2010**, *4*, 7481–7491.
- [26] L. A. Dykman, N. G. Khlebtsov, *Acta Naturae* **2011**, *3*, 34–55.
- [27] I. H. El-Sayed, X. Huang, M. A. El-Sayed, *Nano Lett.* **2005**, *5*, 829–834.
- [28] C. Li, L. V. Wang, *Phys. Med. Biol.* **2009**, *54*, R59-97.
- [29] Q. Zhang, N. Iwakuma, P. Sharma, B. M. Moudgil, C. Wu, J. McNeill, H. Jiang, S. R. Grobmyer, *Nanotechnology* **2009**, *20*, 395102.
- [30] J. A. Copland, M. Eghtedari, V. L. Popov, N. Kotov, N. Mamedova, M. Motamedi, A. A. Oraevsky, *Mol. Imaging Biol.* **2004**, *6*, 341–349.
- [31] P. Sharma, S. C. Brown, N. Bengtsson, Q. Zhang, G. A. Walter, S. R. Grobmyer, S. Santra, H. Jiang, E. W. Scott, B. M. Moudgil, *Chem. Mater.* **2008**, *20*, 6087–6094.
- [32] G. Frens, *Nat. Phys. Sci.* **1973**, *241*, 20–22.
- [33] H. Wang, N. J. Halas, *Adv. Mater.* **2008**, *20*, 820–825.
- [34] H. Masuda, H. Tanaka, N. Baba, *Chem. Lett.* **1990**, *19*, 621–622.
- [35] B. V. Enustun, J. Turkevich, *J. Am. Chem. Soc.* **1963**, *85*, 3317–3328.
- [36] G. Schmid, R. Pfeil, R. Boese, F. Bandermann, S. Meyer, G. H. M. Calis, J. W. A. van der Velden, *Chem. Ber.* **1981**, *114*, 3634–3642.
- [37] W. W. Weare, S. M. Reed, M. G. Warner, J. E. Hutchison, *J. Am. Chem. Soc.* **2000**, *122*, 12890–12891.
- [38] M. Brust, M. Walker, D. Bethell, D. J. Schiffrin, R. Whyman, *J. Chem. Soc. Chem. Commun.* **1994**, *0*, 801–802.
- [39] E. C. Dreaden, A. M. Alkilany, X. Huang, C. J. Murphy, M. A. El-Sayed, *Chem. Soc. Rev.* **2012**, *41*, 2740–2779.
- [40] Y. Pan, S. Neuss, A. Leifert, M. Fischler, F. Wen, U. Simon, G. Schmid, W. Brandau, W. Jahnen-Dechent, *Small* **2007**, *3*, 1941–1949.
- [41] T. K. Sau, C. J. Murphy, *Langmuir* **2004**, *20*, 6414–6420.



- [42] S. J. Oldenburg, R. D. Averitt, S. L. Westcott, N. J. Halas, *Chem. Phys. Lett.* **1998**, 288, 243–247.
- [43] X. Lu, L. Au, J. McLellan, Z.-Y. Li, M. Marquez, Y. Xia, *Nano Lett.* **2007**, 7, 1764–1769.
- [44] F. Kim, S. Connor, H. Song, T. Kuykendall, P. Yang, *Angew. Chem. Int. Ed.* **2004**, 43, 3673–3677.
- [45] C. D. Bain, E. B. Troughton, Y. T. Tao, J. Evall, G. M. Whitesides, R. G. Nuzzo, *J. Am. Chem. Soc.* **1989**, 111, 321–335.
- [46] M.-C. Daniel, D. Astruc, *Chem. Rev.* **2004**, 104, 293–346.
- [47] C. K. Yee, A. Ulman, J. D. Ruiz, A. Parikh, H. White, M. Rafailovich, *Langmuir* **2003**, 19, 9450–9458.
- [48] B. R. Martin, D. J. Dermody, B. D. Reiss, M. Fang, L. A. Lyon, M. J. Natan, T. E. Mallouk, *Adv. Mater.* **1999**, 11, 1021–1025.
- [49] M. Walter, J. Akola, O. Lopez-Acevedo, P. D. Jadzinsky, G. Calero, C. J. Ackerson, R. L. Whetten, H. Grönbeck, H. Häkkinen, *Proc. Natl. Acad. Sci.* **2008**, 105, 9157–9162.
- [50] A. M. Alkilany, C. J. Murphy, *J. Nanoparticle Res.* **2010**, 12, 2313–2333.
- [51] S. D. Conner, S. L. Schmid, *Nature* **2003**, 422, 37–44.
- [52] H. Hess, Y. Tseng, *ACS Nano* **2007**, 1, 390–392.
- [53] J. J. Li, D. Hartono, C.-N. Ong, B.-H. Bay, L.-Y. L. Yung, *Biomaterials* **2010**, 31, 5996–6003.
- [54] Y. Pan, A. Leifert, D. Ruau, S. Neuss, J. Bornemann, G. Schmid, W. Brandau, U. Simon, W. Jahnen-Dechent, *Small* **2009**, 5, 2067–2076.
- [55] J. P. Wilcoxon, J. E. Martin, F. Parsapour, B. Wiedenman, D. F. Kelley, *J. Chem. Phys.* **1998**, 108, 9137–9143.
- [56] Y. Jiang, N. N. Horimoto, K. Imura, H. Okamoto, K. Matsui, R. Shigemoto, *Adv. Mater.* **2009**, 21, 2309–2313.
- [57] L. Vigderman, E. R. Zubarev, *Adv. Drug Deliv. Rev.* **2013**, 65, 663–676.
- [58] R. Hong, G. Han, J. M. Fernández, B. Kim, N. S. Forbes, V. M. Rotello, *J. Am. Chem. Soc.* **2006**, 128, 1078–1079.
- [59] J. Cheon, J.-H. Lee, *Acc. Chem. Res.* **2008**, 41, 1630–1640.
- [60] S. Laurent, D. Forge, M. Port, A. Roch, C. Robic, L. Vander Elst, R. N. Muller, *Chem. Rev.* **2008**, 108, 2064–2110.
- [61] M. Swierczewska, S. Lee, X. Chen, *Mol. Imaging* **2011**, 10, 3–16.
- [62] J. Drbohlavova, R. Hrdy, V. Adam, R. Kizek, O. Schneeweiss, J. Hubalek, *Sensors* **2009**, 9, 2352–2362.

- [63] H. A. JENG, J. SWANSON, *J. Environ. Sci. Health Part A* **2006**, *41*, 2699–2711.
- [64] S. Puntarulo, *Mol. Aspects Med.* **2005**, *26*, 299–312.
- [65] J. Kim, H. S. Kim, N. Lee, T. Kim, H. Kim, T. Yu, I. C. Song, W. K. Moon, T. Hyeon, *Angew. Chem. Int. Ed.* **2008**, *47*, 8438–8441.
- [66] P. Sharma, S. Brown, G. Walter, S. Santra, B. Moudgil, *Adv. Colloid Interface Sci.* **2006**, *123–126*, 471–485.
- [67] A. Sukhanova, I. Nabiev, *Crit. Rev. Oncol. Hematol.* **2008**, *68*, 39–59.
- [68] C. de M. Donegá, *Chem. Soc. Rev.* **2011**, *40*, 1512–1546.
- [69] M. Bruchez, M. Moronne, P. Gin, S. Weiss, A. P. Alivisatos, *Science* **1998**, *281*, 2013–2016.
- [70] W. C. W. Chan, S. Nie, *Science* **1998**, *281*, 2016–2018.
- [71] X. Wu, H. Liu, J. Liu, K. N. Haley, J. A. Treadway, J. P. Larson, N. Ge, F. Peale, M. P. Bruchez, *Nat. Biotechnol.* **2003**, *21*, 41–46.
- [72] Y. Chen, T. Ji, Z. Rosenzweig, *Nano Lett.* **2003**, *3*, 581–584.
- [73] R. Bilan, F. Fleury, I. Nabiev, A. Sukhanova, *Bioconjug. Chem.* **2015**, *26*, 609–624.
- [74] Y. A. Yang, H. Wu, K. R. Williams, Y. C. Cao, *Angew. Chem. Int. Ed.* **2005**, *44*, 6712–6715.
- [75] C. Kirchner, T. Liedl, S. Kudera, T. Pellegrino, A. Muñoz Javier, H. E. Gaub, S. Stölzle, N. Fertig, W. J. Parak, *Nano Lett.* **2005**, *5*, 331–338.
- [76] J. Liu, F. Erogbogbo, K.-T. Yong, L. Ye, J. Liu, R. Hu, H. Chen, Y. Hu, Y. Yang, J. Yang, et al., *ACS Nano* **2013**, *7*, 7303–7310.
- [77] W. C. O'Mara, R. B. Herring, L. P. Hunt, *Handbook of Semiconductor Silicon Technology*, Noyes Publications, **1990**.
- [78] J. D. Cressler, *Silicon Earth: Introduction to the Microelectronics and Nanotechnology Revolution*, Cambridge University Press, **2009**.
- [79] D. Kovalev, H. Heckler, G. Polisski, F. Koch, *Phys. Status Solidi B* **1999**, *215*, 871–932.
- [80] J. D. Holmes, K. J. Ziegler, R. C. Doty, L. E. Pell, K. P. Johnston, B. A. Korgel, *J. Am. Chem. Soc.* **2001**, *123*, 3743–3748.
- [81] L. Pavesi, L. Dal Negro, C. Mazzoleni, G. Franzò, F. Priolo, *Nature* **2000**, *408*, 440–444.
- [82] M. Fujita, *Nat. Photonics* **2013**, *7*, 264–265.
- [83] T. Takagahara, K. Takeda, *Phys. Rev. B* **1992**, *46*, 15578–15581.
- [84] V. Kocevski, O. Eriksson, J. Rusz, *Phys. Rev. B* **2013**, *87*, 245401.
- [85] H. Sugimoto, M. Fujii, K. Imakita, S. Hayashi, K. Akamatsu, *J. Phys. Chem. C* **2013**, *117*, 11850–11857.

- [86] M. Dasog, Z. Yang, S. Regli, T. M. Atkins, A. Faramus, M. P. Singh, E. Muthuswamy, S. M. Kauzlarich, R. D. Tilley, J. G. C. Veinot, *ACS Nano* **2013**, *7*, 2676–2685.
- [87] J. J. Romero, M. J. Llansola-Portolés, M. L. Dell’Arciprete, H. B. Rodríguez, A. L. Moore, M. C. Gonzalez, *Chem. Mater.* **2013**, *25*, 3488–3498.
- [88] A. S. Heintz, M. J. Fink, B. S. Mitchell, *Adv. Mater.* **2007**, *19*, 3984–3988.
- [89] A. S. Heintz, M. J. Fink, B. S. Mitchell, *Appl. Organomet. Chem.* **2010**, *24*, 236–240.
- [90] Z. Kang, Y. Liu, C. H. A. Tsang, D. D. D. Ma, X. Fan, N.-B. Wong, S.-T. Lee, *Adv. Mater.* **2009**, *21*, 661–664.
- [91] Y. Yamada, T. Orii, I. Umez, S. Takeyama, T. Yoshida, *Jpn. J. Appl. Phys.* **1996**, *35*, 1361.
- [92] X. Li, Y. He, S. S. Talukdar, M. T. Swihart, *Langmuir* **2003**, *19*, 8490–8496.
- [93] Q. Liu, S. M. Kauzlarich, *Mater. Sci. Eng. B* **2002**, *96*, 72–75.
- [94] K. A. Pettigrew, Q. Liu, P. P. Power, S. M. Kauzlarich, *Chem. Mater.* **2003**, *15*, 4005–4011.
- [95] D. Neiner, H. W. Chiu, S. M. Kauzlarich, *J. Am. Chem. Soc.* **2006**, *128*, 11016–11017.
- [96] B. M. Nolan, T. Henneberger, M. Waibel, T. F. Fässler, S. M. Kauzlarich, *Inorg. Chem.* **2015**, *54*, 396–401.
- [97] J. R. Heath, *Science* **1992**, *258*, 1131–1133.
- [98] J. P. Wilcoxon, G. A. Samara, P. N. Provencio, *Phys. Rev. B* **1999**, *60*, 2704–2714.
- [99] J. H. Warner, A. Hoshino, K. Yamamoto, R. D. Tilley, *Angew. Chem. Int. Ed.* **2005**, *44*, 4550–4554.
- [100] A. Shiohara, S. Prabakar, A. Faramus, C.-Y. Hsu, P.-S. Lai, P. T. Northcote, R. D. Tilley, **2011**, *5*.
- [101] K. Linehan, H. Doyle, *Small* **2014**, *10*, 584–590.
- [102] R. K. Baldwin, K. A. Pettigrew, E. Ratai, M. P. Augustine, S. M. Kauzlarich, *Chem. Commun.* **2002**, *0*, 1822–1823.
- [103] R. A. Bley, S. M. Kauzlarich, *J. Am. Chem. Soc.* **1996**, *118*, 12461–12462.
- [104] R. K. Baldwin, K. A. Pettigrew, J. C. Garno, P. P. Power, G. Liu, S. M. Kauzlarich, *J. Am. Chem. Soc.* **2002**, *124*, 1150–1151.
- [105] C.-S. Yang, R. A. Bley, S. M. Kauzlarich, H. W. H. Lee, G. R. Delgado, *J. Am. Chem. Soc.* **1999**, *121*, 5191–5195.
- [106] Y. Zhong, F. Peng, F. Bao, S. Wang, X. Ji, L. Yang, Y. Su, S.-T. Lee, Y. He, *J. Am. Chem. Soc.* **2013**, *135*, 8350–8356.
- [107] C. M. Hessel, E. J. Henderson, J. G. C. Veinot, *Chem. Mater.* **2006**, *18*, 6139–6146.

- [108] E. J. Henderson, J. A. Kelly, J. G. C. Veinot, *Chem. Mater.* **2009**, *21*, 5426–5434.
- [109] J. A. Kelly, A. M. Shukaliak, M. D. Fleischauer, J. G. C. Veinot, *J. Am. Chem. Soc.* **2011**, *133*, 9564–9571.
- [110] M. L. Mastronardi, F. Hennrich, E. J. Henderson, F. Maier-Flaig, C. Blum, J. Reichenbach, U. Lemmer, C. Kübel, D. Wang, M. M. Kappes, et al., *J. Am. Chem. Soc.* **2011**, *133*, 11928–11931.
- [111] H. Sugimoto, M. Fujii, K. Imakita, S. Hayashi, K. Akamatsu, *J. Phys. Chem. C* **2013**, *117*, 11850–11857.
- [112] H. Sugimoto, M. Fujii, K. Imakita, S. Hayashi, K. Akamatsu, *J. Phys. Chem. C* **2012**, *116*, 17969–17974.
- [113] N. Licciardello, S. Hunoldt, R. Bergmann, G. Singh, C. Mamat, A. Faramus, J. L. Z. Ddungu, S. Silvestrini, M. Maggini, L. De Cola, et al., *Nanoscale* **2018**, *10*, 9880–9891.
- [114] Z. F. Li, E. Ruckenstein, *Nano Lett.* **2004**, *4*, 1463–1467.
- [115] M. Rosso-Vasic, E. Spruijt, Z. Popović, K. Overgaag, B. van Lagen, B. Grandidier, D. Vanmaekelbergh, D. Domínguez-Gutiérrez, L. D. Cola, H. Zuilhof, *J. Mater. Chem.* **2009**, *19*, 5926–5933.
- [116] Y. Zhong, X. Sun, S. Wang, F. Peng, F. Bao, Y. Su, Y. Li, S.-T. Lee, Y. He, *ACS Nano* **2015**, *9*, 5958–5967.
- [117] S. Ohta, P. Shen, S. Inasawa, Y. Yamaguchi, *J. Mater. Chem.* **2012**, *22*, 10631–10638.
- [118] J.-H. Park, L. Gu, G. von Maltzahn, E. Ruoslahti, S. N. Bhatia, M. J. Sailor, *Nat. Mater.* **2009**, *8*, 331–336.
- [119] C. Tu, X. Ma, A. House, S. M. Kauzlarich, A. Y. Louie, *ACS Med. Chem. Lett.* **2011**, *2*, 285–288.
- [120] R. Weissleder, M. J. Pittet, *Nature* **2008**, *452*, 580–589.
- [121] M. Rudin, R. Weissleder, *Nat. Rev. Drug Discov.* **2003**, *2*, 123–131.
- [122] R. Weissleder, *Nat. Biotechnol.* **2001**, *19*, 316–317.
- [123] M. Hope-Ross, L. A. Yannuzzi, E. S. Gragoudas, D. R. Guyer, J. S. Slakter, J. A. Sorenson, S. Krupsky, D. A. Orlock, C. A. Puliafito, *Ophthalmology* **1994**, *101*, 529–533.
- [124] D. W. McRobbie, *MRI from Picture to Proton*, Cambridge University Press, Cambridge, UK; New York, **2006**.
- [125] S. S. Gambhir, *Nat. Rev. Cancer* **2002**, *2*, 683–693.
- [126] D. M. Hercules, *Science* **1964**, *145*, 808–809.
- [127] M. M. Richter, *Chem. Rev.* **2004**, *104*, 3003–3036.
- [128] W. Miao, *Chem. Rev.* **2008**, *108*, 2506–2553.

- [129] M.-J. Li, P. Jiao, M. Lin, W. He, G.-N. Chen, X. Chen, *The Analyst* **2011**, *136*, 205–210.
- [130] C. Li, J. Lin, Y. Guo, S. Zhang, *Chem. Commun.* **2011**, *47*, 4442–4444.
- [131] M. Famulok, J. S. Hartig, G. Mayer, *Chem. Rev.* **2007**, *107*, 3715–3743.
- [132] J. Liu, Z. Cao, Y. Lu, *Chem. Rev.* **2009**, *109*, 1948–1998.
- [133] H. Lin, M. E. Cinar, M. Schmittel, *Dalton Trans.* **2010**, *39*, 5130–5138.
- [134] M. Schmittel, H. Lin, *Inorg. Chem.* **2007**, *46*, 9139–9145.
- [135] K. K.-W. Lo, J. S.-W. Chan, L.-H. Lui, C.-K. Chung, *Organometallics* **2004**, *23*, 3108–3116.
- [136] Z. Ding, B. M. Quinn, S. K. Haram, L. E. Pell, B. A. Korgel, A. J. Bard, *Science* **2002**, *296*, 1293–1297.
- [137] Y. Bae, N. Myung, A. J. Bard, *Nano Lett.* **2004**, *4*, 1153–1161.
- [138] D. P. Puzzo, E. J. Henderson, M. G. Helander, Z. Wang, G. A. Ozin, Z. Lu, *Nano Lett.* **2011**, *11*, 1585–1590.
- [139] N. Myung, Z. Ding, A. J. Bard, *Nano Lett.* **2002**, *2*, 1315–1319.
- [140] X. Peng, D. M. P. Mingos, *Semiconductor Nanocrystals and Silicate Nanoparticles*, Springer Science & Business Media, **2005**.
- [141] N. Myung, Y. Bae, A. J. Bard, *Nano Lett.* **2003**, *3*, 1053–1055.
- [142] W.-W. Zhao, J. Wang, Y.-C. Zhu, J.-J. Xu, H.-Y. Chen, *Anal. Chem.* **2015**, *87*, 9520–9531.
- [143] P. Bertoncello, R. J. Forster, *Biosens. Bioelectron.* **2009**, *24*, 3191–3200.
- [144] X. Hun, Z. Zhang, *Electroanalysis* **2008**, *20*, 874–880.
- [145] S. Zanarini, E. Rampazzo, L. D. Ciana, M. Marcaccio, E. Marzocchi, M. Montalti, F. Paolucci, L. Prodi, *J. Am. Chem. Soc.* **2009**, *131*, 2260–2267.
- [146] S. Carrara, F. Arcudi, M. Prato, L. De Cola, *Angew. Chem. Int. Ed.* **2017**, *56*, 4757–4761.

# Chapter 2

## Synthesis and characterisation of Silicon-based nanoparticles

### Abstract

The chemistry and properties silicon are exploited in various industries, ranging from electronic and semiconductors through to medicine. Upon transition from the bulk silicon material to small nanoparticles, interesting properties are presented including luminescence, surfaces with tuneable functional groups and biocompatibility, all of which provide a strong platform for entry into the bio- and nanomedicine fields. This chapter focuses on the preparation of small water-soluble silicon nanoparticles via two different bottom-up wet chemistry methods. The nanoparticles are characterised both in terms of their physical and chemical morphology as well as photophysical properties. The differences and similarities in size, core composition and photoluminescence properties are identified to give a basis for their use in further applications.

### 2.1 Introduction

Over the years, silicon-based materials have become established in a position that sees them widely used in a variety of applications from electronic devices through to medical probes and drug delivery systems<sup>[1]-[6]</sup>. At the nanoscale level, silicon-based nanoparticles (Si NPs) have been proposed as a suitable derivative for the full range of applications, owing to their chemical, optical and electronic properties<sup>[7]-[12]</sup>. Moving the focus towards their usage in biological systems, the ability to tune the size and terminal surface functional groups of the nanoparticles is a key aspect of their inherent biocompatibility and non-toxicity<sup>[13],[14]</sup>. This also affords the possibility to further functionalise the surface covalently with different molecules (e.g. labels or targeting agents) through the surface functional groups, allowing the nanoparticles to be used for *in vitro* and *in vivo* imaging<sup>[1],[2]</sup>.

Within the work of this thesis, Si NPs possessing the amine functional group (-NH<sub>2</sub>) as the base surface termination have formed the basis of all investigations. The use of Ω-aminoalkyl chains

as a surface termination on nanoparticles has been very popular in the development of new solutions for theranostic applications, as they give access to biologically-friendly amide chemistry when further functionalisation's are made, while allowing the nanoparticles to remain water soluble<sup>[15]</sup>.

In order to obtain Si NPs of the target small size (< 5 nm), there are different methods reported in the literature. So-called top-down approaches include mechanical processes (high energy ball milling)<sup>[16]</sup> electrochemical etching of silicon wafers<sup>[17],[18]</sup> and high temperature decomposition of large molecular silicon precursors<sup>[19]</sup>, while bottom-up approaches include the laser pyrolysis of molecular silicon precursors<sup>[20]</sup> and solution based wet chemistry methods such as the reduction of small molecular silicon precursors in micelles<sup>[2],[21]</sup> and the hydrothermal and microwave treatment of silanes with citric acid used as a reducing agent<sup>[22]</sup>.

In this chapter, we focus on two of the wet chemistry synthetic methods, which are the so-called microemulsion reduction and hydrothermal syntheses. Both methods have been explored and optimised to achieve small (< 5 nm) amine-terminated Si NPs. The nanoparticles themselves are characterised using a number of analytical techniques, including transmission electron microscopy (TEM), attenuated total reflectance infrared spectroscopy (ATR-FTIR), X-ray photoelectron spectroscopy (XPS) and photophysical measurements, all of which are discussed in this chapter.

## 2.2 Synthesis of amine-terminated Si NPs via microemulsion method

### 2.2.1 Synthesis route

Using a modification of a reported method<sup>[2]</sup>, Si NPs were prepared through the microemulsion synthesis, also known as “reduction in reverse micelles”. Specifically, SiCl<sub>4</sub> is reduced by LiAlH<sub>4</sub> within “nano-reactor” micelles of the tetraoctylammonium bromide (TOAB) surfactant, which allows a controlled growth of the resulting hydride-terminated Si NPs. This is followed by a hydrosilylation of the NPs with allylamine as a capping agent in the presence of catalytic H<sub>2</sub>PtCl<sub>6</sub>. It is also possible to use irradiation with UV light as an alternative to H<sub>2</sub>PtCl<sub>6</sub> in order to catalyse the hydrosilylation with allylamine<sup>[2]</sup>. All reactions were carried

out under an inert atmosphere using dry solvents in order to prevent any oxidation of the NPs. A scheme for the microemulsion method is shown below in figure 2.1.

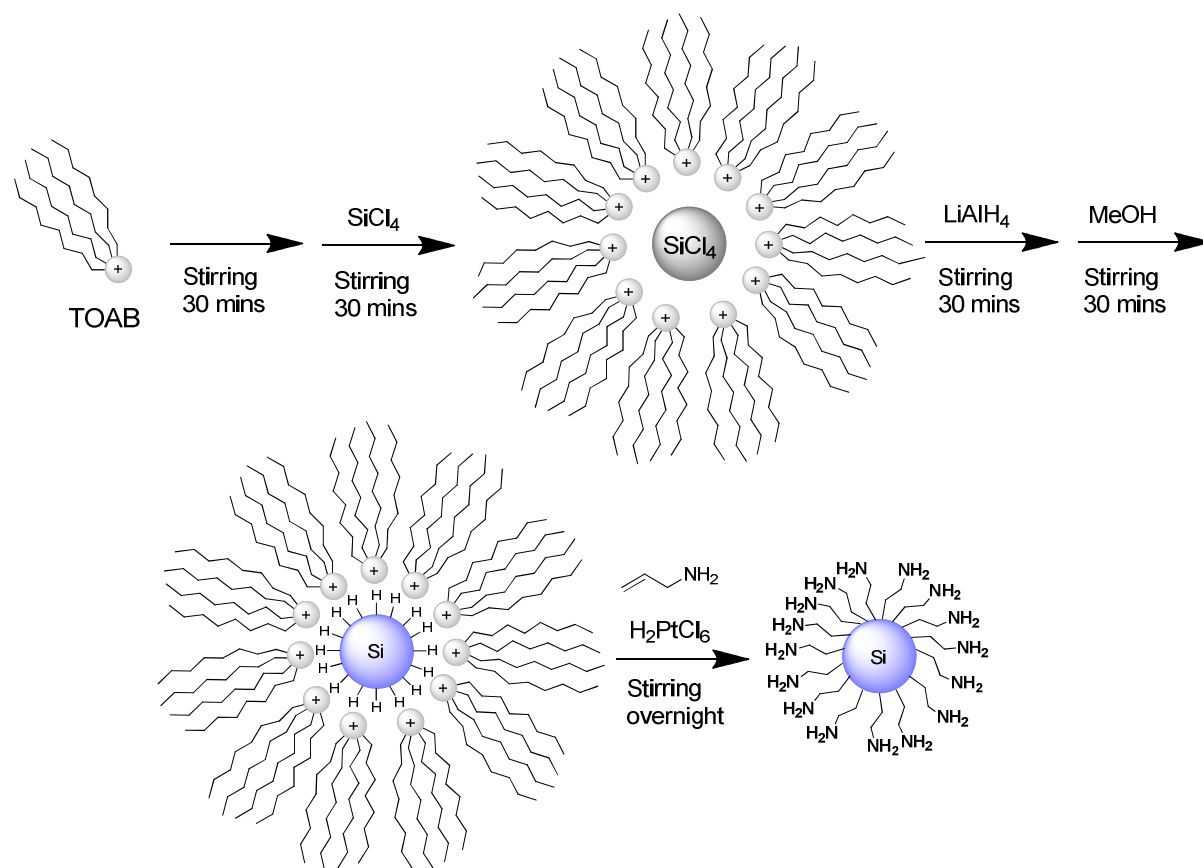


**Figure 2.1:** Reaction scheme for the synthesis of amine-terminated Si NPs through the microemulsion method

Purification of the nanoparticles after the synthesis is a crucial step, especially with regards to the isolation of small ( $< 5$  nm) Si NPs with a narrow size distribution and removing the excess surfactant and allylamine. The classic methods of dialysis and centrifugation were explored as purification procedures, however both proved to be unsuitable for these particular Si NPs. The small size of the Si NPs is the main reason for this, as they are able to pass through the membrane pores of even the smallest available molecular weight cut off (MWCO) dialysis membranes, leading to a large loss of material, and the very low density of the Si NPs renders isolation and separation by centrifugation techniques ineffective. Excess allylamine and surfactant also remain in the sample following the treatments, meaning that a satisfactory purification is not achieved.



To the best of our knowledge, the most effective purification technique for Si NPs synthesised through this method is size exclusion chromatography (Sephadex LH-20 with methanol as eluent), which is indeed used in the literature<sup>[2]</sup>. By repeating the column several times on the reaction product, it is possible to remove excess capping agent and surfactant (evidenced by thin-layer chromatography and NMR) as well as isolate small Si NPs with a narrow size distribution (evidenced by TEM analysis).

### 2.2.2 Characterisation

A broad characterisation of the Si NPs was carried out following their purification in order to define their size, photoluminescence (PL) properties, structure and degree of surface functionalisation.

#### *TEM imaging*

The synthesised nanoparticles were observed through TEM imaging, with typically obtained images shown below (Figure 2.2). The high resolution TEM (HR-TEM) image shows that the particles are crystalline, with an observed distance of 0.2 nm between the fringes, characteristic of the lattice spacing of the (220) planes found in crystalline silicon. The broad view TEM image demonstrates the low polydispersity of the Si NPs as well as a relatively narrow size distribution, which is centred on an average of  $2.7 \pm 0.9$  nm.

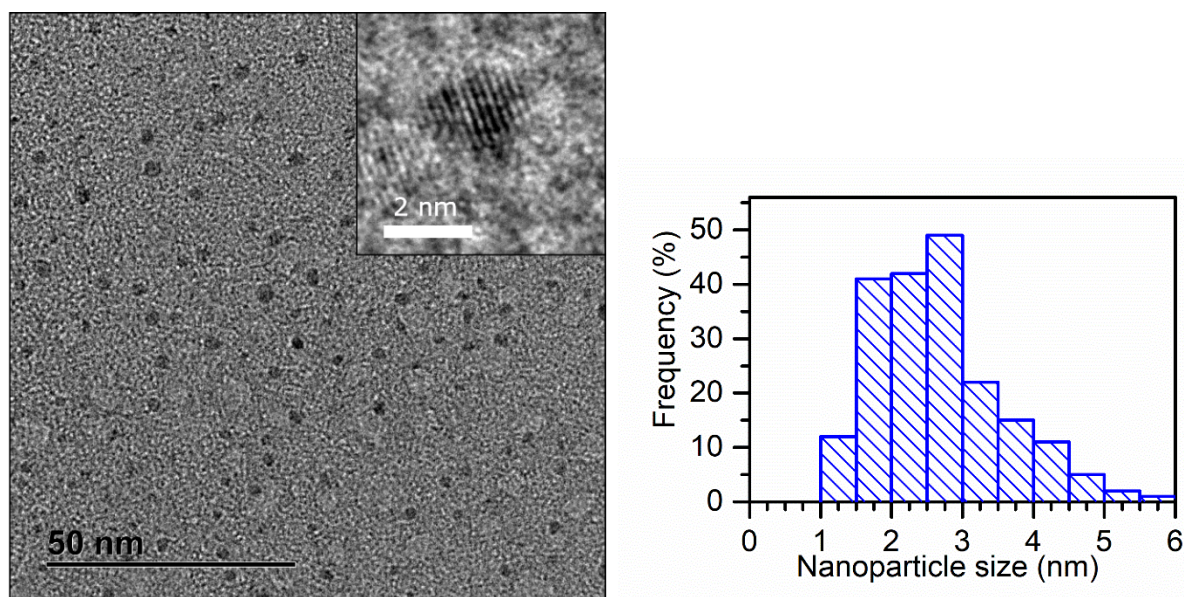


**Figure 2.2:** (Left) TEM images of amine terminated Si NPs obtained through the microemulsion method, in the inset HR-TEM image, crystal fringes belonging to the Si NPs are clearly visible. (Right) Associated size distribution histogram (average size  $2.7 \pm 0.9$  nm)

In order to gain information on the composition of the observed nanoparticles, Energy Dispersive X-ray spectroscopy (EDX) was also performed on the same TEM instrument, with a typical spectrum reported in figure 2.3 below. The analysis shows the characteristic peak of silicon  $K\alpha$  radiation originating from the nanoparticles and does not show the presence of major impurities, such as the Pt catalyst. The intense signals corresponding to copper, oxygen, carbon and chlorine are mainly due to the carbon-coated copper grid used as a substrate for analysing the sample.

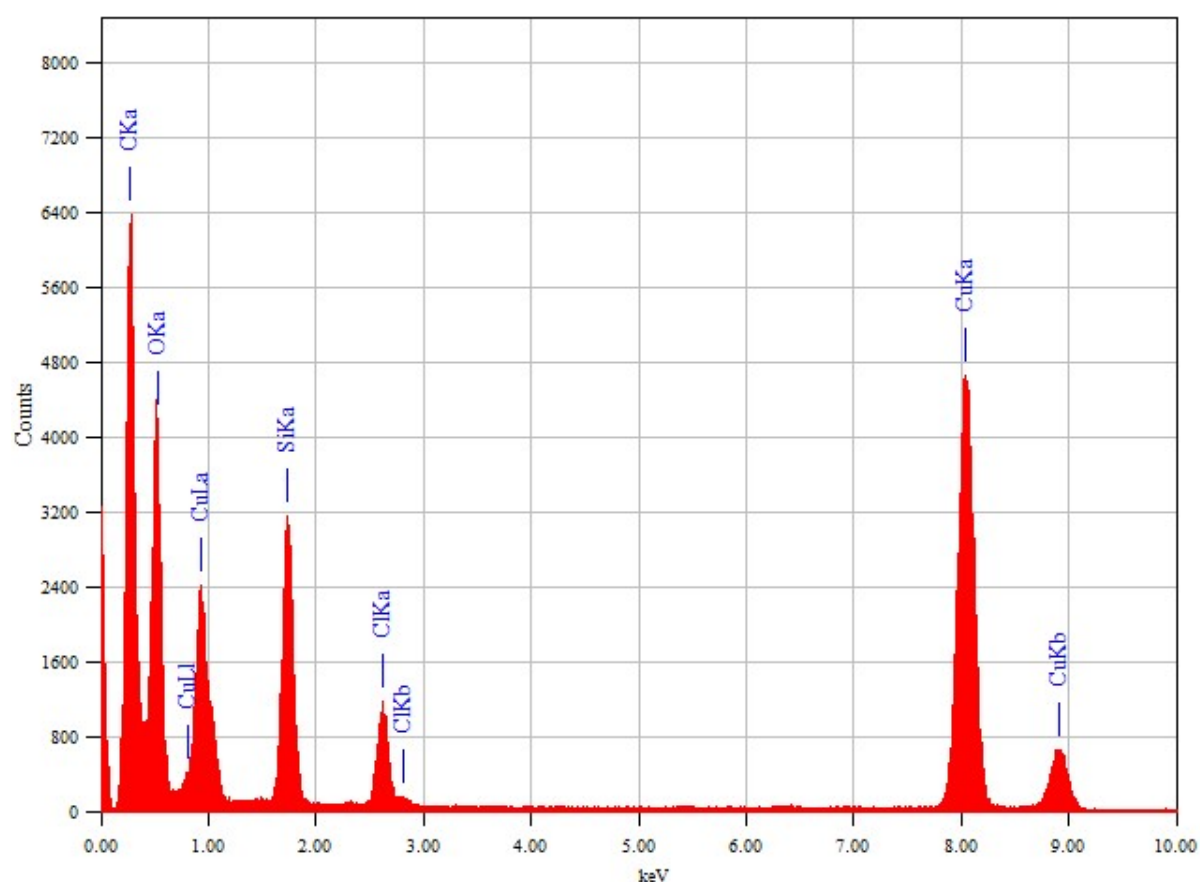


**Figure 2.3:** EDX spectrum of amine-terminated silicon nanoparticles prepared through the microemulsion method

### *Photophysical properties*

A variety of analytical methods were employed to gain an in-depth characterisation of the photophysical properties that the Si NPs possess, including UV-visible absorption spectrometry, Photoluminescence emission and excitation spectroscopy, time resolved excited

state lifetime measurements and quantum yield measurements. All measurements were carried out in water at room temperature.

The UV-visible absorption spectrum of the microemulsion synthesised Si NPs is shown below in figure 2.4. The spectrum was recorded in water with a Si NPs concentration of 0.05 mg/mL. An overall broad and continuous profile is observed with the exception of absorption bands at 270 and 300 nm, which are consistent with the direct L-L band transition in bulk silicon<sup>[23]</sup>.

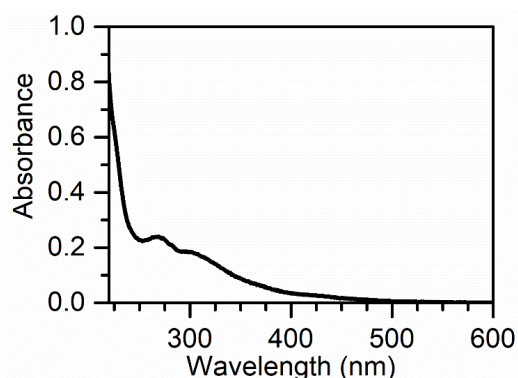


**Figure 2.4:** UV-Vis absorption spectrum of amine-terminated silicon nanoparticles prepared through the microemulsion method

The Si NPs are present in a pale yellow, transparent solution under ambient conditions, which shows an intense light blue emission under UV irradiation, a phenomenon attributed to size effects or surface functionalisation effects<sup>[24],[25]</sup>. This is echoed in the emission spectrum of the Si NPs, which shows a maximum centred at 445 nm when exciting at 360 nm. However, as is shown in figure 2.5 below, the emission maximum does not maintain a constant value and changes depending on the excitation wavelength, with longer wavelengths inducing a red shift in the maximum. This occurrence is said to be related to either the size distribution of the Si NPs or the presence of the Si-C bonds on the surface, which induce surface states that exhibit direct bandgap-like behaviour<sup>[26]</sup>. With the most intense emission being observed at an excitation wavelength of 360 nm, it can be said that either the largest population of Si NPs is of the size giving rise to this band or that the surface state contributing the most to the emission possesses a stronger absorption in this region.

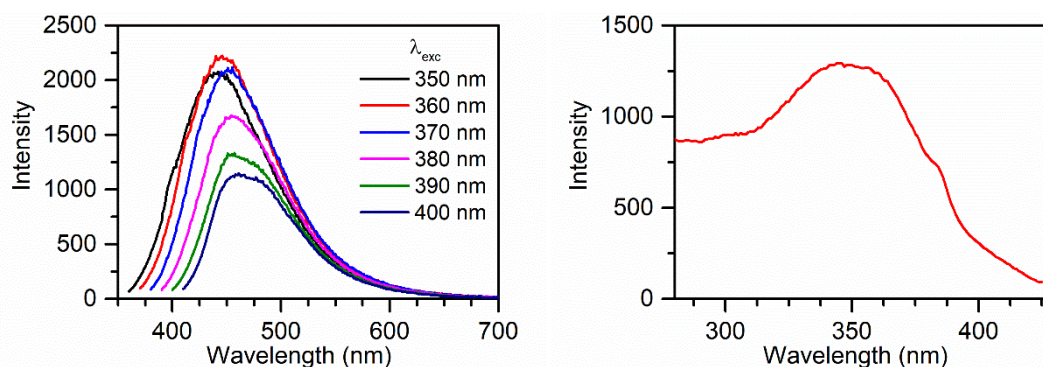


**Figure 2.5:** Emission spectra (left) and excitation spectrum at 445 nm (right) of amine-terminated silicon nanoparticles prepared through the microemulsion method

The excitation spectrum of the Si NPs displays a single significant band centred at 350 nm, which when compared with bulk silicon, is consistent with the direct  $\Gamma$ - $\Gamma$  transition of silicon<sup>[21],[23],[27]</sup>. The excited state lifetime of the Si NPs can be fitted to a bi-exponential decay as shown in table 2.1, which also suggests the presence of defect sites and different surface states and is consistent with reports on similar nanoparticle systems<sup>[28],[29]</sup>. The photoluminescence quantum yield (PLQY) of the Si NPs, measured using an integrating sphere, was found to be 3% across multiple excitation wavelengths in water.

	Emission (nm) <sup>a</sup>	Excitation (nm) <sup>b</sup>	Lifetime (ns) <sup>a</sup>	Q.Y. (%) <sup>c</sup>
Microemulsion Si NPs	445	350	$\tau_1$ : 2.76 (74.3%) $\tau_2$ : 11.04 (25.7%)	3

**Table 2.1:** Photophysical data for amine-terminated silicon nanoparticles prepared through the microemulsion method. (a.  $\lambda_{exc} = 370$  nm b.  $\lambda_{em} = 445$  nm c. Measurement performed using integrating sphere)

### FT-IR spectroscopy

Analysis by Fourier transformed-infra red (FT-IR) spectroscopy in attenuated total reflection (ATR) mode was used to give further confirmation of the surface structure of the Si NPs. At high wavenumbers, N—H asymmetric stretching ( $3380\text{ cm}^{-1}$ ) of the  $\text{NH}_2$  bond and  $\text{sp}^2\text{C—H}$  stretching ( $2922$  and  $2858\text{ cm}^{-1}$ ) of the protecting aminopropyl chain are observed. The peak at  $1638\text{ cm}^{-1}$  originates from the bending of the  $\text{NH}_2$  bond. The peak at  $1462\text{ cm}^{-1}$  can be linked to a deformation mode of H-bonded amine groups (which has been reported<sup>[30]</sup> in similar systems) due to interactions with the shells of adjacent NPs. The peak at  $941\text{ cm}^{-1}$  confirms the successful attachment of the allylamine with the vibration of the Si—C band, for which bands are also reported to occur in the range of  $650\text{--}690\text{ cm}^{-1}$  where they are obscured by background

noise and residual Si—H bands<sup>[31]</sup>. A peak is present at 1117 cm<sup>-1</sup>, which indicates a Si-O bond vibration and the presence of silica on the Si NPs, however, the low intensity, especially when compared to the alkyl chain vibrations means that the amount of silica is negligible. A typical spectrum is shown below in figure 2.6, with assignment of the peaks given in table 2.2.

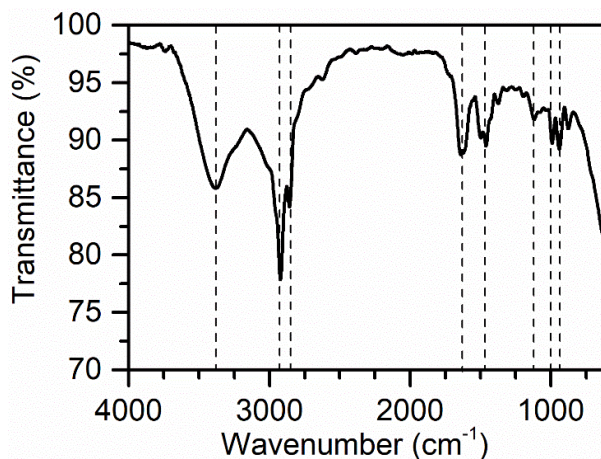


**Figure 2.6:** FT-IR spectra of amine-terminated silicon nanoparticles prepared through the microemulsion method

Signal	Wavenumber (cm <sup>-1</sup> )
N—H	3380
C—H	2922
C—H	2858
N—H	1638
N—H (H-bonded)	1462
Si—O	1117
Si—O	991
Si—C	941

**Table 2.2:** FT-IR spectra data of amine-terminated silicon nanoparticles prepared through the microemulsion method

### *XPS analysis*

X-ray photoelectron spectroscopy (XPS) measurements were performed to study the elemental composition of Si NPs and all the signals were calibrated with the binding energy of C1s at 284.80 eV. High resolution scans of N, C and Si elements are shown in Figure 2.7. The high resolution N1s scan features three components, the one at lower binding energy is assigned to free amine groups, and the higher binding energy component is associated with protonated

amines. The middle signal (green) is attributed to H-bonded amines. Deconvolution of the C1s scan reveals three components; 284.8, 286.2 and 287.6 eV, which correspond to C—C, C=O and C—O bonded carbon, the latter two potentially originating from adventitious carbon and adsorbed carbon dioxide on the substrate. The Si2p scan can be resolved as one band at ~103.0 eV, corresponding to Si—C bonded silicon species originating from the surface grafting of allylamine<sup>[32]</sup> No notable intensity is shown by an elemental silicon component, which would be expected around 99.9 eV for small NPs<sup>[33],[34]</sup>. Although the signal for Si<sup>0</sup> is normally only reported in the case of larger particles possessing a lower ration of surface to bulk silicon atoms<sup>[24]</sup>.

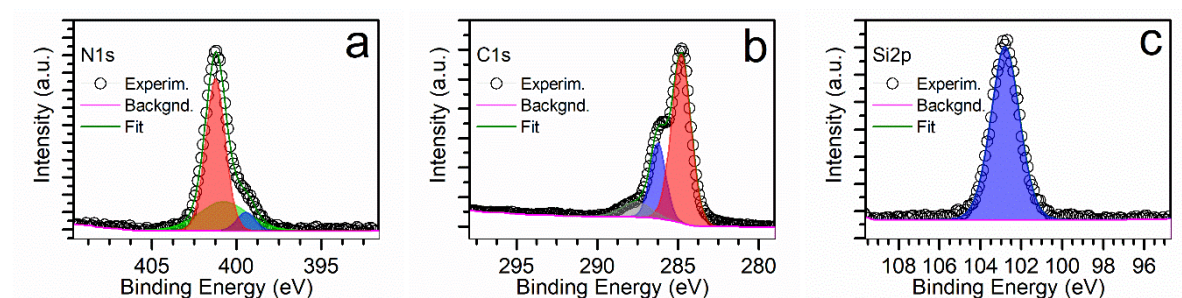


**Figure 2.7:** XPS high resolution scans of amine-terminated silicon nanoparticles prepared through the microemulsion method **a)** Nitrogen N1s scan **b)** Carbon C1s scan **c)** Silicon Si2p scan

### Quantification of amine groups

It is possible to gain information on the degree of surface functionalisation by using a Kaiser Test to calculate the concentration of amine groups for a particular mass of the Si NPs. In this experiment, different known masses of Si NPs are heated with Kaiser Test kit reagents (phenol, potassium cyanide and ninhydrin) in ethanolic solutions. Ninhydrin is able to react with the primary amine groups terminating the surface of the Si NPs and form Ruhemann's purple, which creates coloured solutions of varying intensities depending on the amount of amine initially present.

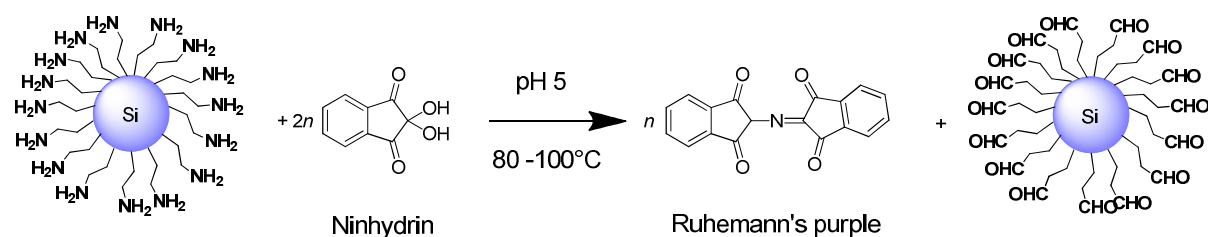


**Figure 2.8:** Reaction of amine terminated Si NPs with ninhydrin to form Ruhemann's purple and aldehyde terminated Si NPs in the Kaiser Test

The absorbance of each of the solutions was measured and the values at  $\lambda = 570$  nm were recorded. As shown in figure 2.9 below, a linear relationship exists between the masses of Si NPs and the absorption at 570 nm in four test solutions, meaning the data has a high degree of reliability.

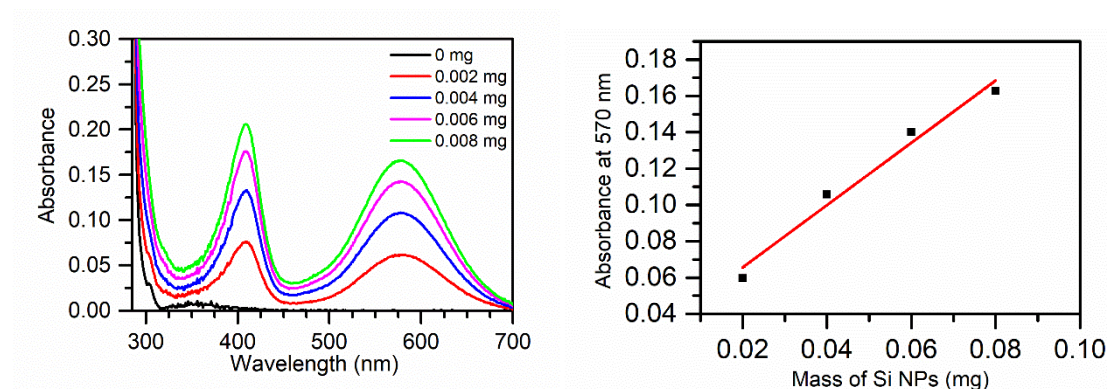


**Figure 2.9:** (Left) UV-Vis absorption spectra of Kaiser Test solutions containing different masses of Si NPs. (Right) Linear fitting of absorbance values against mass of Si NPs. Spectra measured in ethanol.

Using a modification of the Beer-Lambert Law and the data acquired before and after the test, the concentration of amines per mass of Si NPs can be estimated. Input and resulting data are displayed in table 2.3 below.

Mass Si NPs (mg)	Absorbance ( $\lambda = 570$ nm)	Volume of test solution (ml)	$\epsilon$ ( $\text{dm}^3 \text{mol}^{-1} \text{cm}^{-1}$ )	Concentration of amine groups ( $\mu\text{mol}/\text{mg}$ )
0.002	0.0598	0.0025	15000	4.983
0.004	0.10559	0.0025	15000	4.399
0.006	0.14009	0.0025	15000	3.891
0.008	0.16266	0.0025	15000	3.388

**Table 2.3:** Data from the Kaiser Test to evaluate the concentration of amine groups on microemulsion Si NPs (value of  $\epsilon$  calculated from earlier calibration curve with ninhydrin)

$$\text{conc. amine groups} = \frac{(\text{Abs at } \lambda = 570 \text{ nm}) \times \text{Vol} \times 10^6}{\epsilon \times \text{mass Si NPs}}$$

**Equation 2.1:** Calculation for the concentration of amine groups ( $10^6$  used to account for dilution of the test solution when measuring the absorbance)

An average concentration of  $4.17 \mu\text{mol NH}_2$  per mg Si NPs was estimated using the data from the test. Using this method with the different batches of microemulsion Si NPs produced proved useful for determining conditions for functionalisation reactions.

## 2.3 Synthesis of amine-terminated Si NPs via hydrothermal method

### 2.3.1 Synthesis route

The hydrothermal synthesis of Si NPs follows a modification of a reported method<sup>[22]</sup>, where Si NPs are prepared through the microwave treatment of an aqueous solution of (3-Aminopropyl)trimethoxysilane and trisodium citrate. By using a longer reaction time of 5 hours, the hydrothermal method allows for preparation of Si NPs in a conventional oven inside Teflon pressure resistant vessels. The convenience of the apparatus means the synthesis can be easily scaled up to an industrial level. A general synthetic scheme for the hydrothermal method is depicted in Figure 2.10.

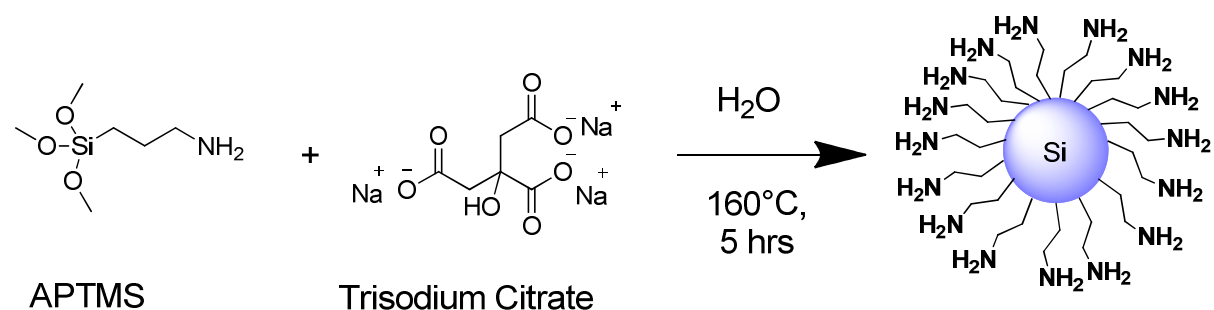


**Figure 2.10:** Reaction scheme for the synthesis of amine-terminated Si NPs through the hydrothermal method [APTMS = (3-aminopropyl) trimethoxysilane; citrate = Trisodium 2-hydroxypropane-1,2,3-tricarboxylate]

The use of only two reagents synthesis and water as the reaction medium makes this synthesis of Si NPs much cleaner than the previously covered microemulsion method and the slightly larger size of the Si NPs produced eases the purification process with the use of dialysis becoming affordable. However, as is shown in the following characterisations, Si NPs made by this method contain a much more notable oxidised component.

### 2.3.2 Characterisation

As with the microemulsion synthesis, broad characterisation of the Si NPs was carried out following their purification in order to define their size, photoluminescence (PL) properties, structure and degree of surface functionalisation.



### TEM imaging

The synthesised nanoparticles were observed through TEM imaging, with typically obtained images shown below (Figure 2.11). The HR-TEM image shows that the particles are crystalline, with an observed distance of 0.2 nm between the fringes, characteristic of the lattice spacing of the (220) planes found in crystalline silicon. The broad view TEM demonstrates the low polydispersity of the Si NPs as well as a relatively narrow size distribution, which is centred on an average of  $3.8 \pm 1.3$  nm.

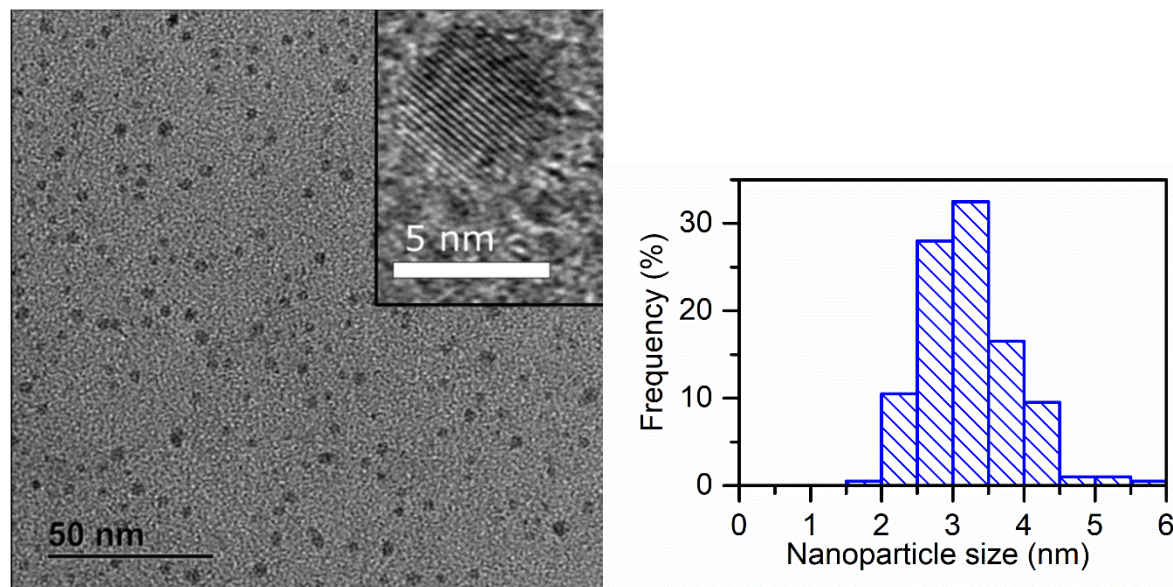


**Figure 2.11:** (Left) TEM images of amine terminated Si NPs obtained through the hydrothermal method, in the inset HR-TEM image, crystal fringes belonging to the Si NPs are clearly visible. (Right) Associated size distribution graph (average size  $3.8 \pm 1.3$  nm)

In order to gain information on the composition of the observed nanoparticles, Energy Dispersive X-ray spectroscopy (EDX) was also performed on the same TEM instrument, with a typical spectrum reported in figure 2.12 below. The analysis shows the characteristic peak of silicon  $K\alpha$  radiation originating from the nanoparticles and does not reveal the presence of major impurities, such as the Pt catalyst. The signals corresponding to copper, oxygen and carbon are once again mainly due to the carbon-coated copper grid used as a substrate for analysing the sample.

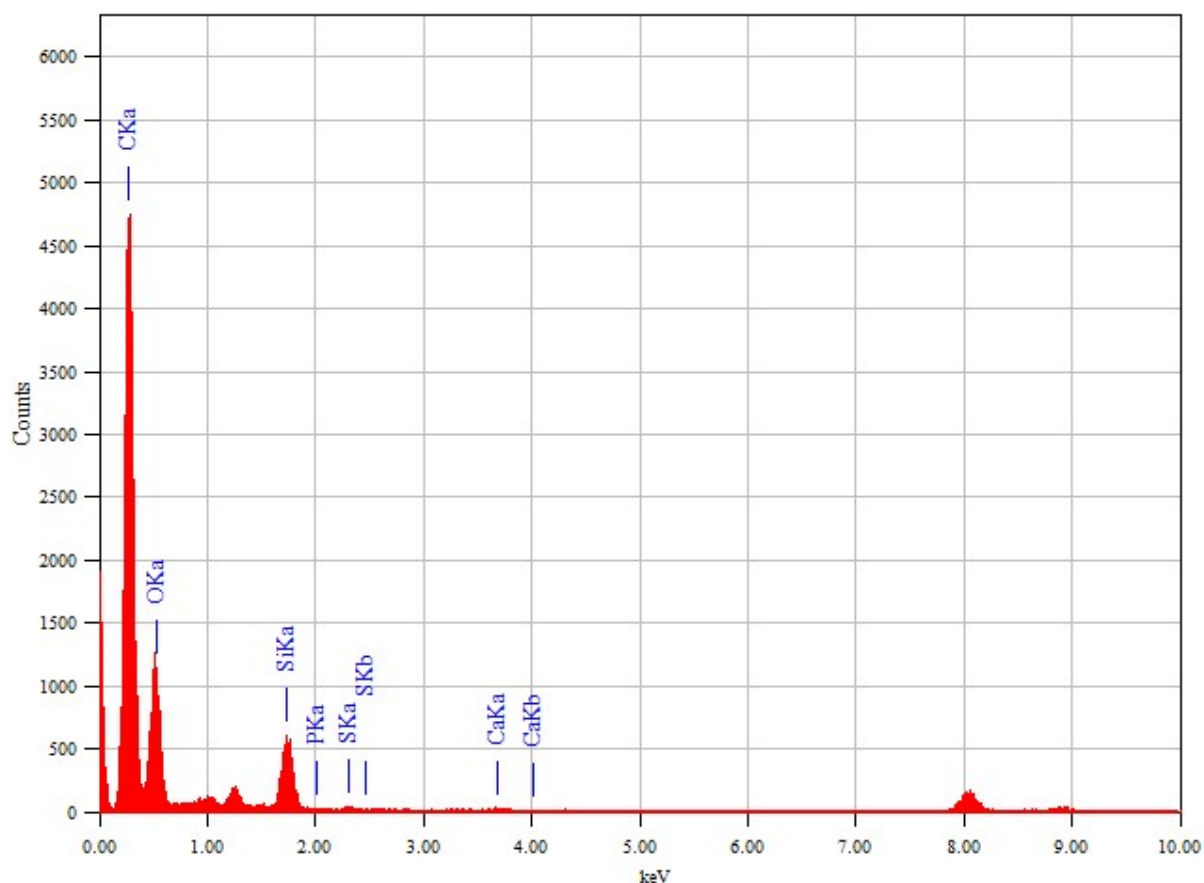


**Figure 2.12:** EDX spectrum of amine-terminated silicon nanoparticles prepared through the hydrothermal method

### *Photophysical properties*

A variety of analytical methods were employed to gain an in-depth characterisation of the photophysical properties that the Si NPs possess, including UV-visible absorption spectrometry, Photoluminescence emission and excitation spectroscopy, time resolved excited state lifetime measurements and quantum yield measurements. All measurements were carried out in water at room temperature.

The UV-visible absorption spectrum of the microemulsion synthesised Si NPs is shown below in figure 2.13. The spectrum was recorded in water with a Si NPs concentration of 0.05 mg/mL. The dominant absorption band is observed at 340 nm and a shoulder-like band is present at ~ 250 nm. According to literature, the former can be attributed to trapping of the surface state<sup>[35], [36]</sup>, which is a reason for the high absorption. The latter band can be associated with a  $\pi$ - $\pi^*$  transition of the C=C bond<sup>[37]</sup>, which is thought to be present in the particle structure from reacted citric acid.

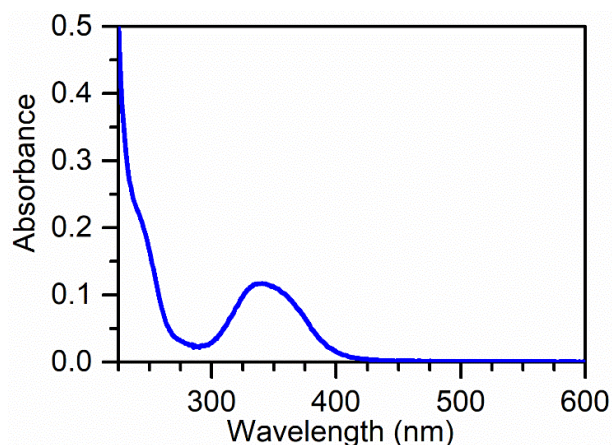


**Figure 2.13:** UV-Vis absorption spectrum of amine-terminated silicon nanoparticles prepared through the hydrothermal method

The Si NPs are present in a colourless, transparent solution under ambient conditions, which shows an intense light blue emission under UV irradiation, a phenomenon also attributed to size effects or surface functionalisation effects as with the Si NPs produced by the microemulsion method<sup>[23]</sup>. This is echoed in the emission spectrum of the Si NPs, which shows a maximum centred at 445 nm when exciting at 360 nm. However, unlike the microemulsion Si NPs, it is shown in figure 2.14 below that the emission maximum remains at a near constant value with little to no shift upon changing the excitation wavelength. Interestingly, this behaviour is not so typical of semi-conductor based quantum dot/ nanoparticles and is actually more similar to that of polymeric carbon dots<sup>[38],[39]</sup>. With the most intense emission being observed at an excitation wavelength of 360 nm, it can be said that either the largest population of Si NPs is of the size giving rise to this band or that the surface state contributing the most to the emission possesses a stronger absorption in this region.

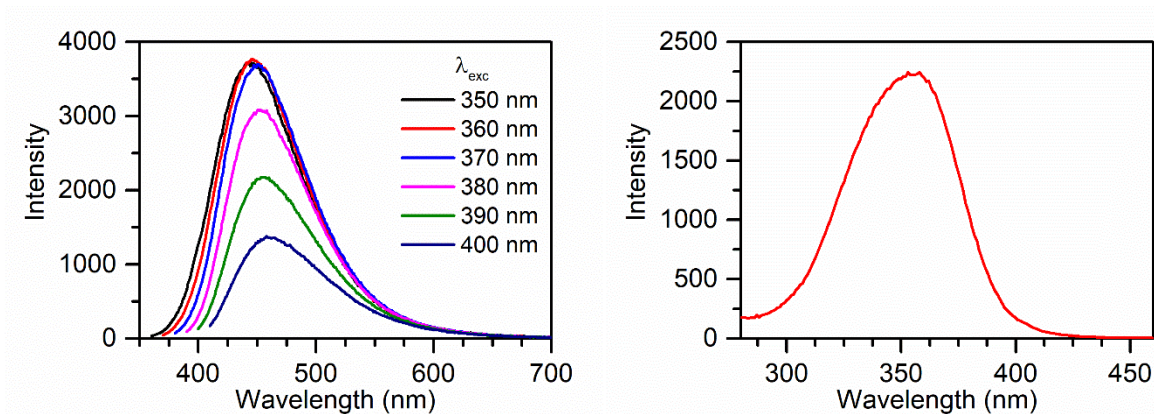


**Figure 2.14:** Emission spectra (left) and excitation spectrum at 470 nm (right) of amine-terminated silicon nanoparticles prepared through the hydrothermal method

The excitation spectrum of the Si NPs displays a single significant band with a maximum at 360 nm, which when compared with bulk silicon, is consistent with the direct  $\Gamma$ - $\Gamma$  transition of silicon<sup>[21],[23],[27]</sup>. This band is identical to that found in the absorption spectrum. The excited state lifetime of the Si NPs can be fitted to a bi-exponential decay as shown in table 2.4, which also suggests the presence of defect sites along with different surface states and is supported by reports on similar nanoparticle systems<sup>[28],[29]</sup>. The photoluminescence quantum yield (PLQY) of the Si NPs, measured using an integrating sphere, was found to be 13% at an excitation wavelength of 360 nm and was seen to range between 8% and 13% when exciting from 320 nm to 390 nm in water.

	Emission (nm) <sup>a</sup>	Excitation (nm) <sup>b</sup>	Lifetime (ns) <sup>b</sup>	Q.Y. (%) <sup>c</sup>
Hydrothermal Si NPs	446	360	$\tau_1$ : 13.84 (48.3%) $\tau_2$ : 4.17 (51.7%)	13

**Table 2.4:** Photophysical data for amine-terminated silicon nanoparticles prepared through the hydrothermal method. (a.  $\lambda_{exc}$  = 370 nm b.  $\lambda_{em}$  = 445 nm c. Measurement performed using integrating sphere)

### *FT-IR spectroscopy*

Analysis by Fourier transformed-infrared (FT-IR) spectroscopy in attenuated total reflection (ATR) mode was used to give further confirmation of the surface structure of the hydrothermal Si NPs. At high wavenumbers, N-H asymmetric stretching ( $3030\text{ cm}^{-1}$ ) of the  $\text{NH}_2$  bond and C—H stretching ( $2917\text{ cm}^{-1}$ ) of the protecting aminopropyl chain are observed. The peak at  $1618\text{ cm}^{-1}$  is associated to the bending of the  $\text{NH}_2$  bond. The peaks at  $1541$  and  $1390\text{ cm}^{-1}$  are

believed to originate from symmetric and asymmetric vibrations of the C=O carbonyl bond, which is present in the structure on the Si NPs through the reacted citric acid. The peak  $1226\text{ cm}^{-1}$  is related to the vibrational modes of the C—O bond. A peak is present at  $1110\text{ cm}^{-1}$ , which indicates a Si—O bond vibration and the presence of silica on the Si NPs, and its intensity, along with that of the peak at  $1018\text{ cm}^{-1}$ , indicates a significant amount. A typical spectrum is shown below in figure 2.15, with assignment of the peaks given in table 2.5.

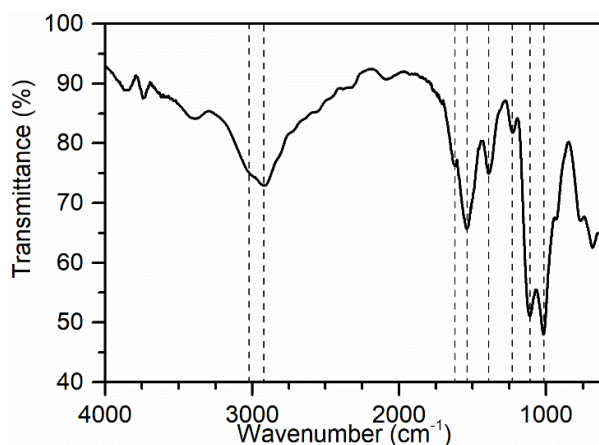


**Figure 2.15:** FT-IR spectra of amine-terminated silicon nanoparticles prepared through the hydrothermal method

Signal	Wavenumber ( $\text{cm}^{-1}$ )
N—H	3030
C—H	2917
N—H	1618
C=O	1541
C=O	1390
C—O	1226
Si—O	1110
Si—O	1018

**Table 2.5:** FT-IR spectra data of amine-terminated silicon nanoparticles prepared through the hydrothermal method

### *XPS analysis*

X-ray photoelectron spectroscopy (XPS) measurements were performed to study the elemental composition of Si NPs and all the signals were calibrated with the binding energy of C1s at

284.80 eV. High resolution scans of N, C and Si elements are shown in Figure 2.16. The high resolution N1s scan features two components, the one at lower binding energy being assigned to free amine moieties, while the higher binding energy one is compatible with protonated amino groups. Interestingly, deconvolution of the C1s scan shows a component with BE close to 284.0 eV, indicating the presence of  $sp^2$ -hybridized carbon double bonds, typically observed in carbon quantum dots. Deconvolution of the Si2p scan firstly shows two components centred in the 101.5–103.0 eV region, compatible with the presence of silicon species bearing organic groups such as alkyl chains. In addition to these, a third, weaker peak at higher binding energy, usually recorded for  $SiO_2$ , was also observed.

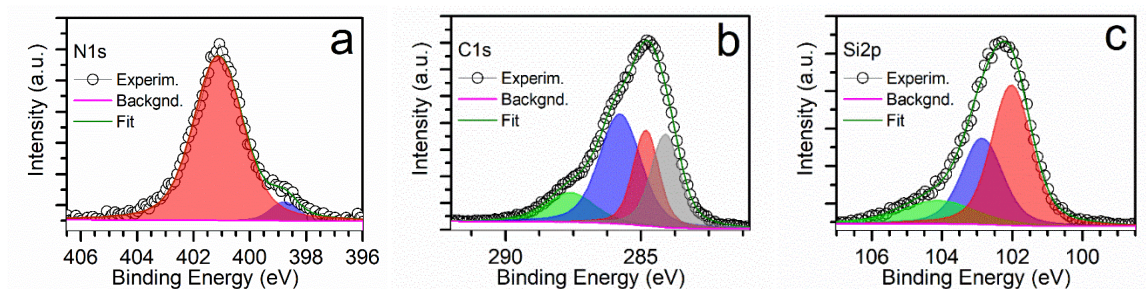


**Figure 2.16:** XPS high resolution scans of amine-terminated silicon nanoparticles prepared through the microemulsion method **a)** Nitrogen N1s scan **b)** Carbon C1s scan **c)** Silicon Si2p scan **d)** Oxygen O1s scan

### Quantification of amine groups

The Kaiser Test was also used to calculate the concentration of amine groups for a particular mass of the HT Si NPs. The procedure was the same as that used for the microemulsion Si NPs.

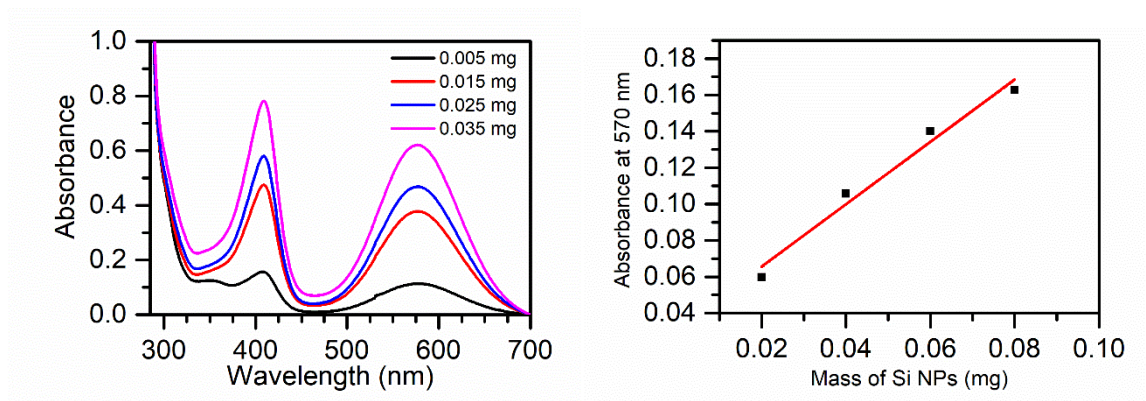


**Figure 2.17:** (Left) UV-Vis absorption spectra of Kaiser Test solutions containing different masses of Si NPs. (Right) Linear fitting of absorbance values against mass of Si NPs

Mass Si NPs (mg)	Absorbance ( $\lambda = 570$ nm)	Volume of test solution (ml)	$\epsilon$ ( $\text{dm}^3 \text{mol}^{-1} \text{cm}^{-1}$ )	Concentration of amine groups ( $\mu\text{mol}/\text{mg}$ )
0.005	0.11164	0.003	15000	4.465
0.015	0.37249	0.003	15000	4.966
0.025	0.46234	0.003	15000	3.698
0.035	0.61334	0.003	15000	3.504

**Table 2.6:** Data from the Kaiser Test to evaluate the concentration of amine groups on HT Si NPs

An average concentration of 4.16  $\mu\text{mol NH}_2$  per mg Si NPs was estimated using the data from the test. Again, this proved useful for determining conditions for functionalisation reactions.

## 2.4 Conclusions

Amine-terminated Si NPs have been synthesised through two different, optimised methods. Identical through characterisation of both products in terms of morphology, chemical composition and photophysics has been carried out, which allows both Si NPs to be compared and evaluated.

The microemulsion method produces smaller Si NPs with a lower content of oxidised species compared to Si NPs from the hydrothermal method (2.8 nm vs. 3.7 nm on average). On the other hand, the hydrothermal method is less complex in terms of the required reagents and purification procedure and can be scaled up as desired due to the absence of produced silane gas as is found for the microemulsion method. While HT Si NPs possess a less tunable emission wavelength, their initial photoluminescence QY values are higher than those of the microemulsion Si NPs (up to 13% compared to 3%)

Both small, water-soluble amine-terminated NPs are suitable for further functionalization to be used in the projected diagnostic applications. Depending on the requirements of the application, it may be more beneficial to use one type of Si NP over the other.

## 2.5 Experimental Section

### 2.5.1 General information

#### *Materials*

All solvents and reagents were purchased from Sigma-Aldrich, Fisher Scientific or Alfa Aesar and used without further purification unless stated. Toluene (Alfa Aesar) was purified and dried

using a Pure Solv PS-MD-5 solvent purification system (Innovative Technology, USA). Sephadex LH-20 was purchased from GE Healthcare Europe GmbH. DI water was prepared using a Milli-Q system by Millipore. The air and water sensitive microemulsion syntheses were carried out in a custom made 250 ml schlenk flask under an inert argon atmosphere using schlenk line techniques. For the hydrothermal synthesis, Teflon vessels resistant to high pressure were used for the reaction inside a Memmert 200 oven (Mettler GmbH) in order to treat reaction mixtures at high temperature.

### *TEM*

Samples for HR-TEM and EDX were prepared by dispersing the aqueous suspensions of the samples onto holey-carbon-on-copper grids (Quantifoil, GmbH) with the excess solvent evaporated. The analysis were performed using both a FEI Titan 80-300 transmission electron microscope operated at 300 KV and Jeol 2100F electron microscope operated at 200 kV.

### *Photophysical measurements*

Steady-state emission spectra were recorded on a HORIBA Jobin-Yvon IBH FL-322 Fluorolog 3 spectrometer equipped with a 450 W xenon arc lamp as the excitation source, double-grating excitation and emission monochromators ( $2.1 \text{ nm mm}^{-1}$  of dispersion;  $1200 \text{ grooves mm}^{-1}$ ), and a TBX-04 single-photon-counting device as the detector. Emission and excitation spectra were corrected for source intensity (lamp and grating) and emission spectral response (detector and grating) by standard correction curves. Time-resolved measurements were performed using the Time-Correlated Single Photon Counting (TCSPC) on the FT-300 (PicoQuant), where a polarized laser source 375 nm used for exciting the samples. The excitation sources were mounted directly on the sample chamber at  $90^\circ$  to a Czerny-Turner type emission monochromator ( $2.7 \text{ nm mm}^{-1}$  of dispersion;  $1200 \text{ grooves mm}^{-1}$ ) and collected by a PMA-C 192M single-photon-counting detector. Signals were collected using EasyTau software, and data analysis was performed using FluoFit software (PicoQuant). The quality of the fit was assessed by minimizing the reduced  $\chi^2$  function and by visual inspection of the weighted residuals. Luminescence quantum yield was performed with integrating sphere (Hamamatsu, C11347-11).



### *FT-IR Spectroscopy*

FTIR spectra were recorded on a Shimadzu IRAffinity-1 spectrometer used in attenuated total reflectance (ATR) mode. Samples from the microemulsion synthesis were drop-cast onto the ATR crystal and the excess solvent was evaporated. Samples from the hydrothermal synthesis were prepared by lyophilisation, with the resulting solids ground with an agate mortar and laid on the ATR crystal. Spectra cumulated 64 scans at a resolution of  $4\text{ cm}^{-1}$ .

### *XPS analysis*

XPS measurements were performed using a Thermo Scientific K-Alpha X-Ray Photoelectron Spectrometer using monochromatic  $\text{AlK}\alpha$  radiation (1486.6 eV). High resolution scans were performed with a 50 eV analyser pass energy and 0.1 eV step size. Binding energies of each element were referenced to carbon C1s peak at 284.8 eV. Samples were prepared by dispersing the aqueous suspensions of the samples onto gold coated glass slides with the excess solvent evaporated.

## 2.5.2 Synthetic procedures

### *Microemulsion synthesis*

This procedure follows a slight modification of a reported method<sup>[2]</sup>. Tetraoctylammonium bromide (500 mg) was added to a 250 ml Schlenk flask, which was then sealed and evacuated and purged with  $\text{N}_2$  gas three times over. Dry toluene (50ml) was added and the solution was stirred for 30 mins. Silicon tetrachloride (0.3 ml) was added and the solution was stirred for a further 30 mins, followed by the addition of Lithium Aluminium Hydride solution (4 0.ml, 1M in THF) with another 30 mins stirring thereafter in order to form hydrogen-terminated Si NPs. Anhydrous methanol (4 ml) was then added to quench the mixture, which was stirred for a further 30 mins. A freshly prepared catalytic solution of Hydrogen Hexachloroplatinate(IV) Hexahydrate in methanol (0.1 ml 0.007M) was administered to the mixture followed by allylamine (2 ml) in order to obtain the final amine-terminated Si NPs. After stirring the reaction overnight, the crude mixture was filtered through paper, the solvent removed in vacuo and Si NPs modified with 3-aminopropyl groups were extracted with water. The precipitated surfactant was removed by filtering the aqueous solution through syringe membrane filters (Millex, Millipore, PVDF,  $0.45\ \mu\text{m}$ ). The resulting Si NPs were then purified by size exclusion chromatography (Sephadex LH-20) with MeOH as eluent. Fractions exhibiting bright blue

luminescence were combined and the solvent was removed in vacuo. The purification was repeated two times over and the solvent removed to obtain Si NPs as a yellow wax.

#### *Hydrothermal synthesis*

This procedure is taken and adapted from previous the report by He and coworkers<sup>[21]</sup>. A precursor solution was prepared by adding 10 mL of (3- aminopropyl)trimethoxysilane to 40 mL Argon-saturated aqueous solution dispersed with 1.66 g of trisodium citrate dihydrate. The mixture was stirred for 10 min. The solution was transferred into a pressure-sealable teflon vessel and heated at 160°C for 5 hours. The sample was removed when the temperature cooled to < 30 °C naturally and was then neutralized to pH 7 with conc. HCl. The residual reagents were removed by dialysis (1 kDa) leaving Si NPs dispersed in a transparent, colourless solution.

## 2.6 References

- [1] F. Erogbogbo, K.-T. Yong, I. Roy, R. Hu, W.-C. Law, W. Zhao, H. Ding, F. Wu, R. Kumar, M. T. Swihart, et al., *ACS Nano* **2011**, *5*, 413–423.
- [2] J. H. Warner, A. Hoshino, K. Yamamoto, R. D. Tilley, *Angew. Chem. Int. Ed.* **2005**, *44*, 4550–4554.
- [3] F. Erogbogbo, K.-T. Yong, R. Hu, W.-C. Law, H. Ding, C.-W. Chang, P. N. Prasad, M. T. Swihart, *ACS Nano* **2010**, *4*, 5131–5138.
- [4] F. Erogbogbo, C.-A. Tien, C.-W. Chang, K.-T. Yong, W.-C. Law, H. Ding, I. Roy, M. T. Swihart, P. N. Prasad, *Bioconjug. Chem.* **2011**, *22*, 1081–1088.
- [5] M. L. Mastronardi, E. J. Henderson, D. P. Puzzo, Y. Chang, Z. B. Wang, M. G. Helander, J. Jeong, N. P. Kherani, Z. Lu, G. A. Ozin, *Small* **2012**, *8*, 3647–3654.
- [6] D. P. Puzzo, E. J. Henderson, M. G. Helander, Z. Wang, G. A. Ozin, Z. Lu, *Nano Lett.* **2011**, *11*, 1585–1590.
- [7] D. S. English, L. E. Pell, Z. Yu, P. F. Barbara, B. A. Korgel, *Nano Lett.* **2002**, *2*, 681–685.
- [8] F. Hua, M. T. Swihart, E. Ruckenstein, *Langmuir* **2005**, *21*, 6054–6062.
- [9] S. Sato, M. T. Swihart, *Chem. Mater.* **2006**, *18*, 4083–4088.
- [10] R. D. Tilley, K. Yamamoto, *Adv. Mater.* **2006**, *18*, 2053–2056.
- [11] X. Zhang, D. Neiner, S. Wang, A. Y. Louie, S. M. Kauzlarich, *Nanotechnology* **2007**, *18*, 095601.
- [12] R. A. Bley, S. M. Kauzlarich, *J. Am. Chem. Soc.* **1996**, *118*, 12461–12462.
- [13] F. Peng, Y. Su, Y. Zhong, C. Fan, S.-T. Lee, Y. He, *Acc. Chem. Res.* **2014**, *47*, 612–623.
- [14] J.-H. Park, L. Gu, G. von Maltzahn, E. Ruoslahti, S. N. Bhatia, M. J. Sailor, *Nat. Mater.* **2009**, *8*, 331–336.
- [15] N. Licciardello, S. Hunoldt, R. Bergmann, G. Singh, C. Mamat, A. Faramus, J. L. Z. Ddungu, S. Silvestrini, M. Maggini, L. De Cola, et al., *Nanoscale* **2018**, *10*, 9880–9891.
- [16] A. S. Heintz, M. J. Fink, B. S. Mitchell, *Adv. Mater.* **2007**, *19*, 3984–3988.
- [17] J. P. Proot, C. Delerue, G. Allan, *Appl. Phys. Lett.* **1992**, *61*, 1948–1950.
- [18] J. L. Heinrich, C. L. Curtis, G. M. Credo, M. J. Sailor, K. L. Kavanagh, *Science* **1992**, *255*, 66–68.
- [19] Y. Yu, C. A. Bosoy, C. M. Hessel, D.-M. Smilgies, B. A. Korgel, *ChemPhysChem* **2013**, *14*, 84–87.

- [20] T. Yoshida, S. Takeyama, Y. Yamada, K. Mutoh, *Appl. Phys. Lett.* **1996**, *68*, 1772–1774.
- [21] J. P. Wilcoxon, G. A. Samara, *Appl. Phys. Lett.* **1999**, *74*, 3164–3166.
- [22] Y. Zhong, F. Peng, F. Bao, S. Wang, X. Ji, L. Yang, Y. Su, S.-T. Lee, Y. He, *J. Am. Chem. Soc.* **2013**, *135*, 8350–8356.
- [23] J. D. Holmes, K. J. Ziegler, R. C. Doty, L. E. Pell, K. P. Johnston, B. A. Korgel, *J. Am. Chem. Soc.* **2001**, *123*, 3743–3748.
- [24] M. Dasog, Z. Yang, S. Regli, T. M. Atkins, A. Faramus, M. P. Singh, E. Muthuswamy, S. M. Kauzlarich, R. D. Tilley, J. G. C. Veinot, *ACS Nano* **2013**, *7*, 2676–2685.
- [25] J. J. Romero, M. J. Llansola-Portolés, M. L. Dell’Arciprete, H. B. Rodríguez, A. L. Moore, M. C. Gonzalez, *Chem. Mater.* **2013**, *25*, 3488–3498.
- [26] K. Dohnalová, A. N. Poddubny, A. A. Prokofiev, W. D. de Boer, C. P. Umesh, J. M. Paulusse, H. Zuilhof, T. Gregorkiewicz, *Light Sci. Appl.* **2013**, *2*, e47–e47.
- [27] K. A. Littau, P. J. Szajowski, A. J. Muller, A. R. Kortan, L. E. Brus, *J. Phys. Chem.* **1993**, *97*, 1224–1230.
- [28] M. Rosso-Vasic, E. Spruijt, Z. Popović, K. Overgaag, B. van Lagen, B. Grandidier, D. Vanmaekelbergh, D. Domínguez-Gutiérrez, L. D. Cola, H. Zuilhof, *J. Mater. Chem.* **2009**, *19*, 5926–5933.
- [29] J. R. Siekierzycka, M. Rosso-Vasic, H. Zuilhof, A. M. Brouwer, *J. Phys. Chem. C* **2011**, *115*, 20888–20895.
- [30] C. Weigel, R. Kellner, *Fresenius Z. Für Anal. Chem.* **1989**, *335*, 663–668.
- [31] C. A. Canaria, I. N. Lees, A. W. Wun, G. M. Miskelly, M. J. Sailor, *Inorg. Chem. Commun.* **2002**, *5*, 560–564.
- [32] G. F. Cerofolini, C. Galati, S. Reina, L. Renna, G. G. Condorelli, I. L. Fragalà, G. Giorgi, A. Sgamellotti, N. Re, *Appl. Surf. Sci.* **2005**, *246*, 52–67.
- [33] M. L. Mastronardi, F. Maier-Flaig, D. Faulkner, E. J. Henderson, C. Kübel, U. Lemmer, G. A. Ozin, *Nano Lett.* **2012**, *12*, 337–342.
- [34] K. Sato, T. Izumi, M. Iwase, Y. Show, H. Morisaki, T. Yaguchi, T. Kamino, *Appl. Surf. Sci.* **2003**, *216*, 376–381.
- [35] X. Wang, L. Cao, S.-T. Yang, F. Lu, M. J. Meziani, L. Tian, K. W. Sun, M. A. Bloodgood, Y.-P. Sun, *Angew. Chem.* **2010**, *122*, 5438–5442.
- [36] Y. Han, Y. Chen, J. Feng, J. Liu, S. Ma, X. Chen, *Anal. Chem.* **2017**, *89*, 3001–3008.
- [37] Y. Jiang, B. Wang, F. Meng, Y. Cheng, C. Zhu, *J. Colloid Interface Sci.* **2015**, *452*, 199–202.

- [38] S. Zhu, Q. Meng, L. Wang, J. Zhang, Y. Song, H. Jin, K. Zhang, H. Sun, H. Wang, B. Yang, *Angew. Chem. Int. Ed.* **2013**, *52*, 3953–3957.
- [39] S. Zhu, Y. Song, X. Zhao, J. Shao, J. Zhang, B. Yang, *Nano Res.* **2015**, *8*, 355–381.

# Chapter 3

## Silicon or Silica? An in depth analysis and comparison of silicon-based nanoparticles produced via the hydrothermal and microwave methods

### Abstract

The hydrothermal synthesis of amine-terminated Si NPs detailed in the previous chapter was adapted from a procedure that utilises microwave irradiation as the heat source instead of heat from a conventional oven. The microwave process has been reported to yield silicon quantum dots, however, thorough characterization and comparison of the products from both reactions led us to question this notion. In this chapter, by highlighting the main issues linked to the proper characterization of these materials, we put forward our case that the nanoparticles produced under both microwave and hydrothermal conditions, are actually a mixture of silica and carbon quantum dots.

### 3.1 Introduction

As reported in the previous chapter, Silicon nanoparticles (SiNPs) can be produced in different ways, which include top-down and bottom-up approaches<sup>[1]-[4]</sup>. The typical products bear surface Si-H groups that can undergo further functionalization<sup>[5]</sup> to yield particles with diverse surface groups.  $\Omega$ -aminoalkyl chains, for example, are very popular in the development of new solutions for theranostic applications, since they give a surface access to biologically-friendly amide chemistry<sup>[6]</sup>.

A particularly attractive method for the preparation of SiNPs bearing 3-aminopropyl chains on their surfaces has been reported by Y. He and coworkers<sup>[7]</sup>. The method makes use of 3-aminopropyl trimethoxysilane (APTMS) as a silicon source, to ensure the presence of amino groups on the surface of the resulting crystalline NPs. The conversion of the silane into nanoparticles is carried out in water, using microwave (MW) irradiation to drive the reaction and trisodium citrate as a reducing agent.

In their paper, He and co-workers state that reduction of APTMS by citrate yields the formation of nuclei that grow to yield fully-fledged nanocrystals via Ostwald ripening. The paper does not focus on the reduction mechanism, or the fate of the excess 3-aminopropyl chains that must be eliminated in the Ostwald ripening process in order to decrease the specific surface of the nanoparticles while providing a purely silicon core. The material cited on the topic deals with MW growth (rather than nucleation) of CdTe-type quantum dots in a process where citrate is not involved and which, again, does not specifically address reaction mechanism. Finally, it should be noted that an APTMS-to-Citrate molar ratio of 10:1 is reported by the authors for the reaction, while the same reducing agent is typically employed in large excess in the preparation of metal nanoparticles.

Citrates are well-known reducing agents for the preparation of metal nanoparticles, often doubling as capping agents to suppress excessive particles growth<sup>[8]</sup>. The mechanism of reduction by citrates has been studied in detail and, in the case of tetrachloroauric salts, goes through a ligand substitution by carboxylate, which attacks the metal and displaces a chloride anion yielding the transition state that can evolve towards the products<sup>[9]</sup>. In the case of APTMS, it is hard to envisage a mechanism where methanoate is displaced by a better leaving group such as a carboxylate. On the other hand, this step may be possible by prior hydrolysis of the alkoxy silane by a hydroxyl group, followed by its substitution. At any rate, the Si-C bond is much less polarized than Si-O, with the 3-aminopropyl chain serving as an even worse leaving group than methanoate, so its reduction by citrate may be more problematic. This is an important aspect since, by considering spherical monocrystalline silicon nanoparticles with radii between 2.0 and 2.5 nm, we can evaluate the number of surface Si atoms as roughly 50-60% of the total number of Si atoms in the particle, meaning that about half of the Si-C bonds in starting APTES molecules need to be substituted by Si-Si ones, if a crystalline particle is to be formed.

The characterization of the chemical nature of the nanoparticles reported by He and co-workers includes high resolution TEM, X-ray powder diffractometry, FT-IR and energy-dispersive X-ray spectroscopy. The latter technique does highlight the presence of silicon atoms, but cannot discriminate between oxidised or reduced states and prove the presence of Si<sup>0</sup> in the sample. Moreover, the FT-IR spectrum highlights a strong C-O vibration that is not discussed, but hardly fits in the chemical scenario proposed by the authors. Finally, the XRD pattern reported by He shows two reflections typical of the diamond structure of crystalline silicon, the (111) and (220), with the (311) being mentioned but not discernible from the background noise.

According to the Scherrer equation<sup>[10]</sup>, the FWHM – or  $\Delta(2\theta)$  – for the diffraction peaks recorded for a 2.2 nm isotropic crystalline silicon nanoparticle, should be around 3.7° for the (111) reflection and 3.9° for the (220) one, considering an ideal instrument that does not contribute to further line broadening, operating with monochromatic CuK $\alpha$  radiation. Many authors have shown that the Scherrer equation can be used to calculate the mean crystallite size for SiNPs, with results closely matching the particles sizes measured by high-resolution TEM<sup>[11], [12]</sup>. While the quality of the data reported by He and co-workers does not allow for a quantitative measurement of the FWHM of the diffraction peak, it is undoubtedly much smaller than 3°, apparently contradicting the DLS and HR-TEM data reported in the same article.

Two observations are apparent from He's protocol: i) the conditions of the synthesis, namely the presence of water and an electrolyte, along with the final basic pH, which may well prompt for an hydrolysis-condensation process on the alkoxy silanes (as in a Stöber-like process<sup>[13]</sup>, or the synthesis of oligomeric silsesquioxanes<sup>[14]</sup>) thus yielding silica (SiO<sub>2</sub>) rather than silicon (Si<sup>0</sup>); ii) that both the hydrothermal treatment of citrate and its microwave-assisted pyrolysis have been reported to yield large macromolecules, graphene oxide or carbon quantum dots with peculiar fluorescent properties and, in some cases, quantum yields exceeding 20%<sup>[15]-[18]</sup>.

Here, we report our findings on the MW-assisted preparation of silicon-based nanoparticles starting from aqueous mixtures of APTMS and sodium citrate, as well as the hydrothermal (HT) variant, where the mixture is thermally treated in a conventional oven for an extended period of time, as reported in the previous chapter. Other authors report the preparation of carbon quantum dots from mixtures of 3-aminopropyl trialkoxysilanes and citric acid<sup>[19]</sup> under hydrothermal conditions, identifying the products as Si-doped CQDs, but a final proof of the inclusion of silicon into the carbon core of the quantum dot is never presented. Therefore, a set of experiments were designed to characterise the materials prepared, in order to elucidate their chemical nature. Syntheses were carried out by mixing the starting materials (APTMS and trisodium citrate) in water and providing either MW irradiation or oven based thermal treatment. Reactions in absence of the reducing agent or the silicon source were also performed to evaluate the roles of the reagents. The chemical structure of the samples was assayed by means of infrared and X-ray photoelectron spectroscopies, while their morphology and crystallinity were evaluated by electron microscopy and X-ray powder diffraction. Finally, UV-Vis spectroscopy and photoluminescence measurements allowed a complete photophysical characterization of the materials.



## 3.2 Synthesis and characterisation of silicon-based nanoparticles

Aqueous mixtures of trisodium citrate and APTMS were treated either in a microwave reactor, as reported by He and coworkers<sup>[7]</sup> (MW-series samples) or under hydrothermal conditions, in a static oven within tightly sealed Teflon containers (HT-series samples). General schemes for both reactions are shown below in figure 3.1.

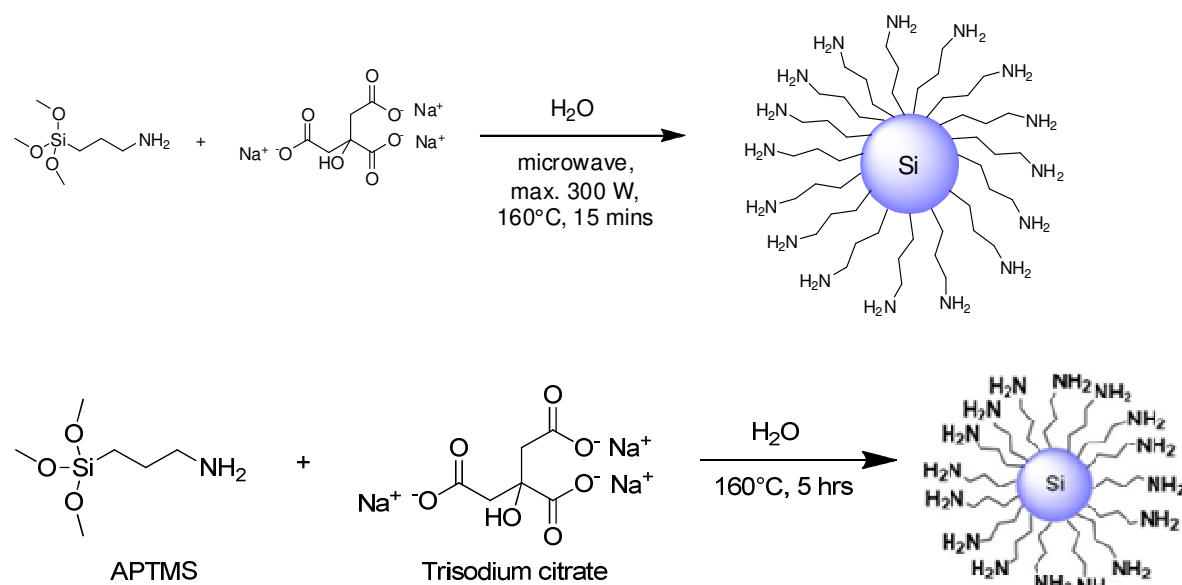


**Figure 3.1:** Reaction schemes for the synthesis of MW Si NPs (top) and HT Si NPs (bottom).

Table 1 summarises the composition of the starting mixtures for the different tests, with -C samples being prepared without the addition of the silicon source in the reaction medium and -CS samples containing both reagents. All mixtures gave crude products with a basic pH, between 8.0 and 9.5, and samples MW-CS, HT-CS and HT-C displayed intense blue emission upon UV irradiation at 365 nm. Sample MW-C was only weakly luminescent after 15 min MW treatment, but prolonging the irradiation time led to increasingly emitting crude samples.

Sample name	[Citrate] (M)	APTMS (M)	Heating	Time (min)
MW-CS	0.126	1.11	MW	15
MW-C	0.126	0	MW	15
HT-CS	0.126	1.11	HT	300
HT-C	0.126	0	HT	300

**Table 3.1:** Samples and experimental conditions

The complete characterization of these samples was carried out after purification of the crudes by dialysis against water through a 1kDa membrane (corresponding to pore diameter below 1.5 nm).

Figure 3.2 compares the FT-IR spectra (collected using an ATR attachment) of trisodium citrate and those of the products of its treatment in water, MW-C and HT-C, highlighting the dominance of the symmetric and asymmetric stretching of the carbonyl groups at 1586 and 1396  $\text{cm}^{-1}$  respectively (for the starting material). Both signals, the former in particular, are slightly shifted to lower wavenumbers for the treated samples, together with a general broadening of the weaker peaks.

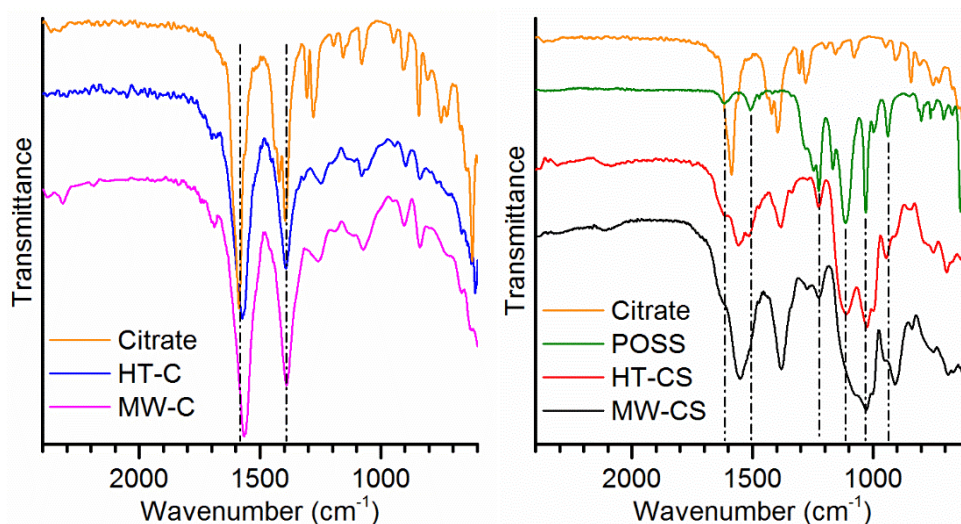


**Figure 3.2:** (Left) FT-IR spectra of the samples MW-C, HT-C and Trisodium citrate. (Right) Comparison of FT-IR spectra of samples MW-CS and HT-CS with trisodium citrate and octa-amino T8-polyhedral oligomeric silsesquioxane (POSS)

Signal	Wavenumbers (cm <sup>-1</sup> )			
	MW-CS	HT-CS	POSS	Citrate
Carbonyl (sym)	1548	1559	-	1586
Carbonyl (asym)	1379	1382	-	1396
N—H bending	1625 (sh)	1619 (sh)	1616	-
C—N	1506 (sh)	1515	1508	-
Si—C	1225	1223	1225	-
Si—O—Si (ring-asym)	1117 (sh)	1110	1114	-
Si—O—Si (ring-sym)	1028	1026	1030	-

**Table 3.2:** Peak assignments for the samples in comparison with pure references (“sh” = shoulder)

The trend for the carboxylic group’s signals is confirmed for MW-CD and HT-CS. To better comprehend the features brought about in the FT-IR spectra by the addition of APTMS in the reaction mixture, we compared the data (table 3.2) with those recorded for a pure sample of the trifluoromethanesulfonic acid salt of octa(3-aminopropyl)silsesquioxane (POSS, green trace), prepared as reported elsewhere<sup>[20]</sup>. All the features of the FT-IR traces, aside from those described for the carboxylates, can be tracked back to the green spectrum. N—H bendings and C—N stretches appear as shoulders for the stronger carbonyl peak, while the signal for the Si—C is more isolated and clear. In polyhedral silsesquioxanes, the asymmetrical (1114 cm<sup>-1</sup>) and symmetrical (1030 cm<sup>-1</sup>) stretches of Si—O—Si units are very sharp due to the well-defined, symmetric geometry of the molecular system<sup>[21]</sup>. The same two peaks typically collapse into a single broad band for amorphous silica. Interestingly, symmetric and asymmetric stretches are clearly recognizable in the trace of HT-CS, while the asymmetric stretching appears as a mere shoulder on MW-CS, indicating a more disordered structure for the latter sample.

High resolution Si2p and C1s XPS scans of MW-CS and HT-CS are reported in Figure 3.3. Si2p lines did not show well-defined spin-orbit components, therefore Si2p<sub>1/2</sub> and Si2p<sub>3/2</sub> contributions have not been separated in the analysis. Clear separation of these components ( $\Delta = 0.63\text{eV}$ ) is typical for bulk silicon only. No signal for elemental silicon was observed, expected at 99.4 eV for bulk silicon or as high as 99.9 eV for small NPs<sup>[11],[12]</sup>. The elemental peak for silicon has previously been reported to gradually disappear as the diameter of SiNPs decreases since most of the silicon atoms are on the surface, but it is possible to be realised for particles above 1 nm in diameter<sup>[11]</sup>. In this case, the samples display very similar profiles, with

two components centred in the 101.5–103.0 eV region, compatible with the presence of silicon species bearing organic groups such as alkyl chains.

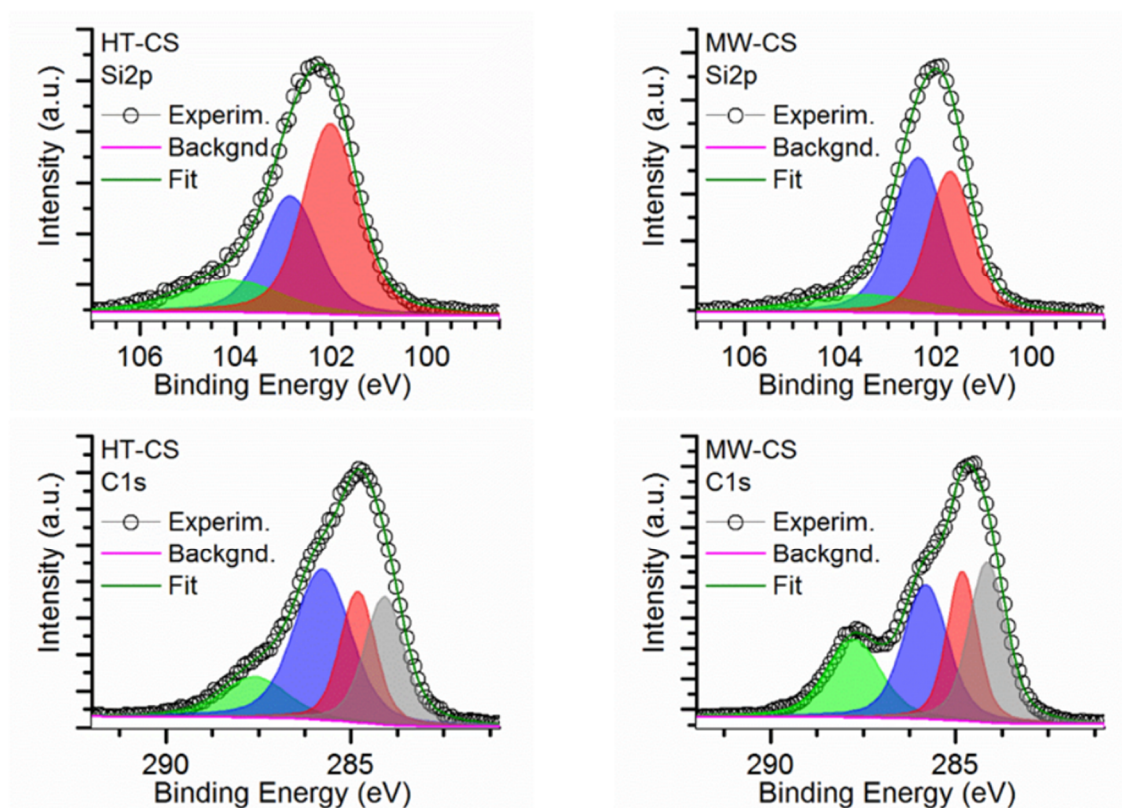


**Figure 3.3:** XPS high resolution scans of the Si2p (top) and C1s (bottom) lines of samples HT-CS (left) and MW-CS (right)

A third, weaker peak at higher binding energy, usually recorded for SiO<sub>2</sub>, was also observed. Elemental compositions, in particular Silicon-to-Nitrogen atomic ratios are in both cases close to 1 (see table 3.3), suggesting that the 3-Aminopropyl chains of the silane starting material have survived the treatment. Interestingly, deconvolution of the C1s scan shows a component with BE close to 284.0 eV, indicating the presence of sp<sup>2</sup>-hybridized carbon double bonds, typically observed in carbon quantum dots.

	MW-CS	HT-CS
Si	12.7 %	10.1 %
O	26.3 %	31.0 %
N	10.5 %	9.1 %
C	50.5 %	49.8 %

**Table 3.3:** Atomic composition of the samples probed by XPS

Transmission electron microscopy (TEM) imaging of the samples was performed to assay the morphology of the various materials and the presence of crystalline domains. This data is typically reported by most authors to provide visual evidence of the presence of nanoparticles and can further support other analytical techniques such as X-Ray powder diffraction. As shown in figure 3.3, recorded for sample HT-CS, the samples are made of particles displaying slightly irregular round shapes. The size distributions recorded for HT-CS and MW-CS are reported in figure 3.4.

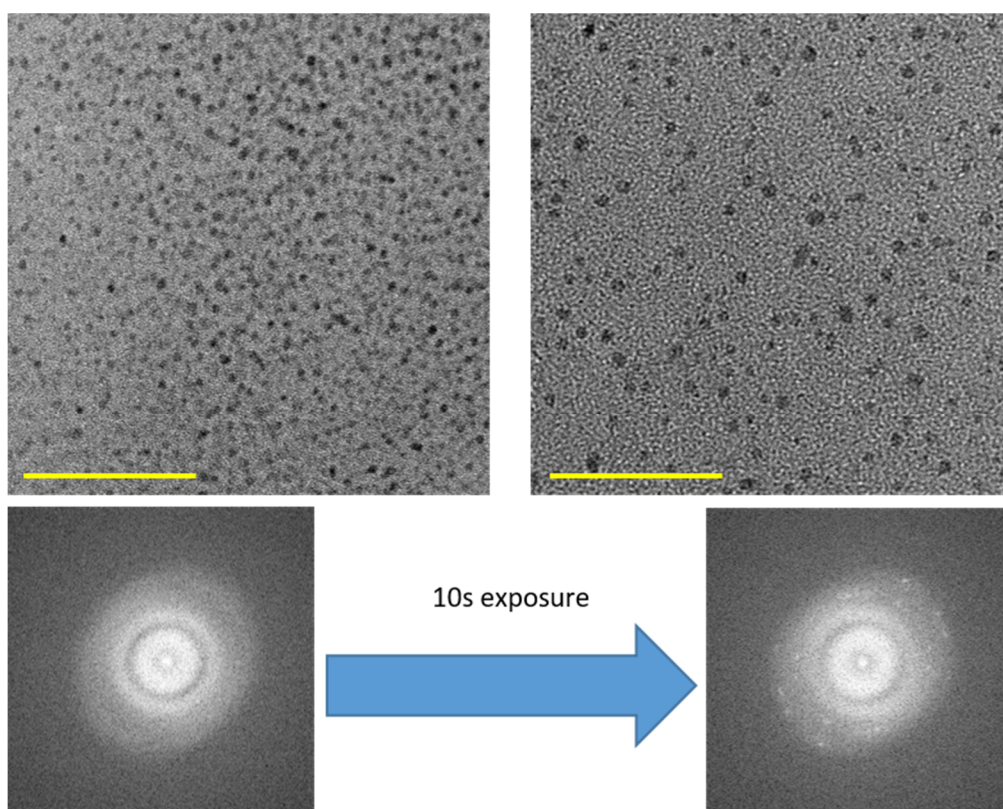


**Figure 3.4:** (Top) representative TEM images for sample HT-CS (left) and MW-CS (right) (scale bars = 50 nm). (Bottom) observed evolution of the live FFT for one particle over time

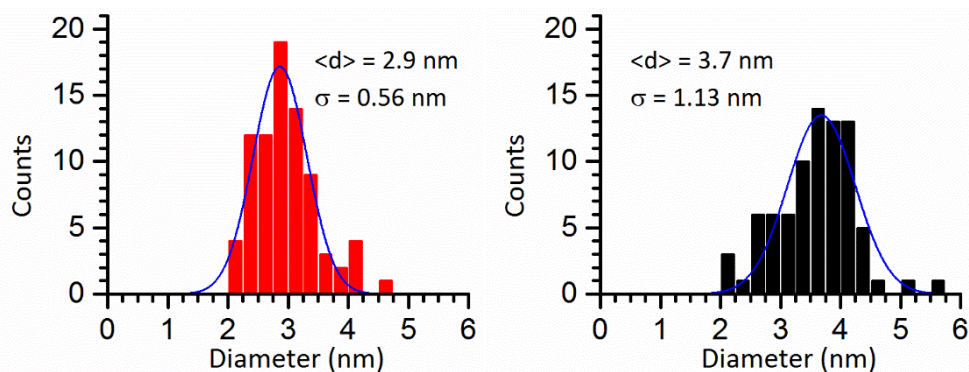


**Figure 3.5:** Size distributions of the particles observed by TEM (histograms) and Gaussian size distribution function (blue line), for samples HT-CS (left) and MW-CS (right)

One important finding is that, upon high resolution imaging, there was a fast phase transition in the particles subjected to the electron beam, that went from amorphous to crystalline as shown by the fourier transforms at the bottom of figure 3.4. This may be due to the heating provided by the electron beam, combined with the high vacuum conditions typical of the analysis chamber. For this kind of sample, crystallinity would be better probed by means of X-Ray diffraction, rather than selected area diffraction experiments on TEM equipment, that should only confirm X-Ray diffraction findings.

Indeed, X-Ray powder diffraction traces (figure 3.6) show amorphous phases with no discernible peaks. Crystalline SiNPs should display three diffraction peaks characteristic of (111), (220) and (311) reflections of the diamond structure, with a full width at half maximum compatible with the mean crystallite size according to the Scherrer equation<sup>[10]</sup>. Both diffractograms are characterised by two broad peaks. The one at ca. 22° can be attributed to silica while the other at ca 11° results from a second amorphous phase<sup>[21]</sup> – most probably amorphous carbon

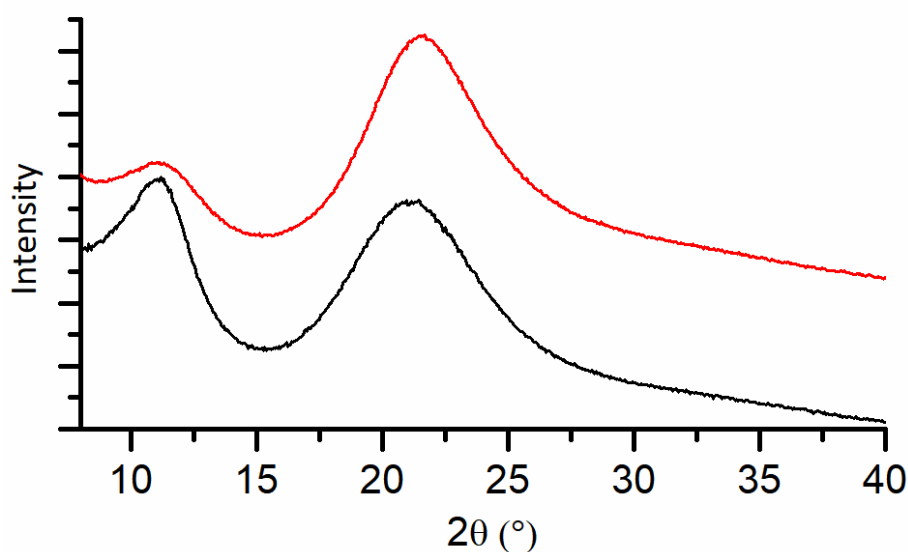


**Figure 3.6:** X-Ray powder diffractograms for samples MW-CS (black) and HT-CS (red).

Figure 3.7 shows the normalized emission spectra recorded for MW-CS and HT-CS upon excitation at 340 nm, comparing them with the emission spectra of sample HT-C and MW-C, prepared without a silicon source. There is a good superimposition between the normalized spectra for all the samples, with a slight shift to lower wavelengths for MW-C and a somewhat broader emission spectrum for HT-CS. The similarities between the spectra prepared with and without a silicon source suggest that the emission may be due to the presence of carbon-based species, rather than silicon nanoparticles. Figure 3.8 highlights the shift of the emission maxima as a function of the excitation wavelength. This is a well-known characteristic of carbon quantum dots and the limited shift under UV irradiation below 400 nm has been described as a consequence of the passivation of the carbon surface<sup>[15]</sup>. MW-C was the only sample in the series that displayed a pronounced shift for the emission maxima below the 400 nm threshold, but it was deemed necessary to assign a large error bar to the data recorded using long excitation wavelengths (380 and 400 nm). Such measurements were marred by the high intensity of the water Raman band relative to the signal given by the sample, due to the low concentration of MW-C resulting from the scarce yield of the process.

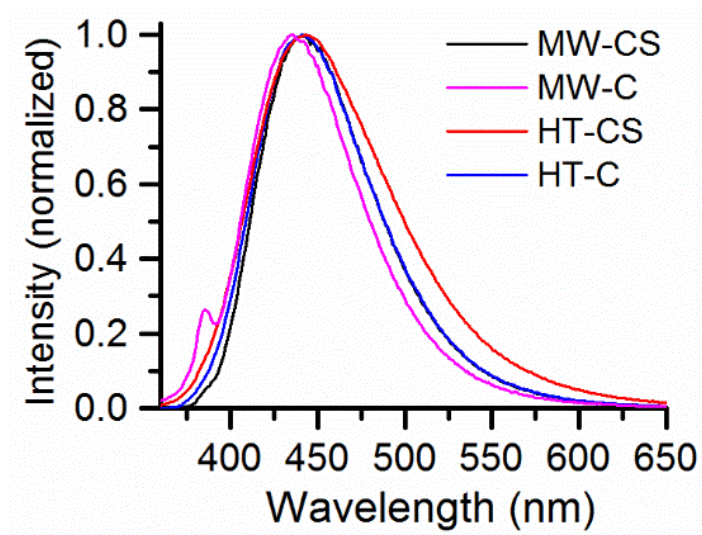


**Figure 3.7:** Normalized emission spectra (in water,  $\lambda_{exc} = 340$  nm)

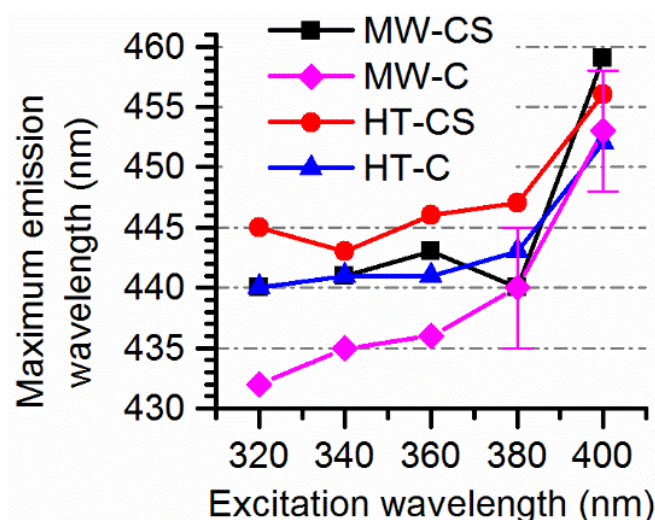


**Figure 3.8:** Position of the maxima in PL emission spectra upon excitation at different wavelengths

To further prove that the photoluminescence recorded for MW-CS is not associated to the presence of silicon quantum dots, aliquots of the sample were treated with either hydrofluoric or hydrochloric acids. The former was employed to dissolve any silicon or silica particles in suspension, the latter to provide an acidic pH without compromising the suspended materials. Figure 3.9 shows the photoluminescence emission spectra at  $\lambda_{exc} = 340$  nm of the acid-treated aliquots. While the signal recorded for the HF-treated sample is lower in intensity than the pristine one, this quenching effect is caused by the acidic pH, as proven by the spectra recorded employing hydrochloric acid. This behaviour was previously reported for carbon quantum dots and further suggests their presence<sup>[23]</sup>.



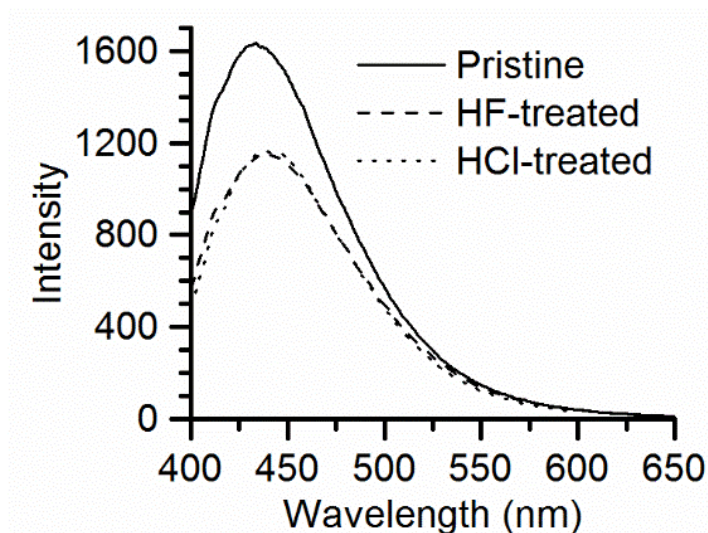


**Figure 3.9:** Emission spectra (in water,  $\lambda_{exc} = 340$  nm) of MW-CS treated with different acids

### 3.3 Conclusion

In this chapter, the process proposed by Y. He and coworkers for the preparation of silicon nanoparticles with 3-aminopropyl surface modification<sup>[7]</sup> has been critically analysed. Comparison of ATR-FTIR spectra with those of the reagents and pure reference compounds, high resolution XPS analyses and powder X-Ray diffraction data suggest that the nanoparticles produced by heating mixtures of sodium citrate and (3-aminopropyl)triethoxysilane in water are not crystalline Si<sup>0</sup>. Rather, they are silica nanoparticles with 3-aminopropyl-decorated surfaces mixed with the thermal degradation products of citrates (carbon quantum dots) that are well-known to display photoluminescence properties very similar to those we observed for our samples.

This highlights a number of critical issues that material scientists should be aware of when approaching the preparation of silicon nanoparticles. In particular, we prove that high resolution transmission electron microscopy should not be used alone to assay the crystallinity of the nanoparticles, since (i) the material may evolve under the electron beam and (ii) both interplanar distances and mean crystallite sizes should be related to powder X-Ray diffraction data. Moreover, we give examples of the reason why photoluminescence properties should not be considered as a proof for the presence of silicon nanoparticles.

## 3.4 Experimental Section

### 2.5.1 General information

#### *Materials*

All solvents and reagents were purchased from Sigma-Aldrich, Fisher Scientific or Alfa Aesar and were used without additional purification. All solutions were prepared using DI water (Milli-Q system by Millipore) as the solvent. A Memmert 200 oven (Memmert GbmH) was used for hydrothermal treatments, while microwave processing was carried out with a Discover model CEM focused microwave synthesis system.

#### *TEM*

Samples for HR-TEM and EDX were prepared by dispersing the aqueous suspensions of the samples onto holey-carbon-on-copper grids (Quantifoil, GmbH) with the excess solvent evaporated. TEM/HRTEM overview images were recorded using a Jeol 2100F electron microscope equipped with Cs-corrected condenser, imaging filter, biprism and 2 CCD cameras, operated at 200 kV.

#### *Photophysical measurements*

Steady-state emission spectra were recorded on a HORIBA Jobin-Yvon IBH FL-322 Fluorolog 3 spectrometer equipped with a 450 W xenon arc lamp as the excitation source, double-grating excitation and emission monochromators ( $2.1 \text{ nm mm}^{-1}$  of dispersion;  $1200 \text{ grooves mm}^{-1}$ ), and a TBX-04 single-photon-counting device as the detector. Emission and excitation spectra were corrected for source intensity (lamp and grating) and emission spectral response (detector and grating) by standard correction curves. Time-resolved measurements were performed using the Time-Correlated Single Photon Counting (TCSPC) on the FT-300 (PicoQuant), where a polarized laser source 375 nm used for exciting the samples. The excitation sources were mounted directly on the sample chamber at  $90^\circ$  to a Czerny-Turner type emission monochromator ( $2.7 \text{ nm mm}^{-1}$  of dispersion;  $1200 \text{ grooves mm}^{-1}$ ) and collected by a PMA-C 192M single-photon-counting detector. Signals were collected using EasyTau software, and data analysis was performed using FluoFit software (PicoQuant). The quality of the fit was assessed by minimizing the reduced  $\chi^2$  function and by visual inspection of the weighted

residuals. Luminescence quantum yield was performed with integrating sphere (Hamamatsu, C11347-11).

#### *FT-IR Spectroscopy*

FTIR spectra were recorded on a Shimadzu IRAffinity-1 spectrometer used in attenuated total reflectance (ATR) mode. Samples were prepared by lyophilisation, with the resulting solids ground with an agate mortar and laid on the ATR crystal. Spectra cumulated 64 scans at a resolution of  $4\text{ cm}^{-1}$ .

#### *XPS analysis*

XPS measurements were performed using a Thermo Scientific K-Alpha X-Ray Photoelectron Spectrometer using monochromatic  $\text{AlK}\alpha$  radiation (1486.6 eV). High resolution scans were performed with a 50 eV analyser pass energy and 0.1 eV step size. Binding energies of each element were referenced to carbon C1s peak at 284.8 eV. Samples were prepared by dispersing the aqueous suspensions of the samples onto gold coated glass slides with the excess solvent.

#### *XRD analysis*

Powder X-ray diffraction (XRD) spectra were recorded on a Bruker D2 PHASER diffractometer operating in  $\theta - 2\theta$  mode with  $\text{CuK}\alpha$  (8.04 keV) radiation passed through a graphite monochromator, scanning between  $8$  and  $40^\circ$  with  $0.05^\circ$  step angle and a 100s dwell time to suppress noise.

### 2.5.2 Synthetic procedures

These procedures are taken and adapted from previous the report by He and coworkers<sup>[7]</sup>. A precursor solution was prepared by adding 10 mL of (3- aminopropyl)trimethoxysilane to 40 mL Argon-saturated aqueous solution dispersed with 1.66 g of trisodium citrate dihydrate. The mixture was stirred for 10 min. The solution was transferred into the appropriate reaction vessels (pressure-sealable teflon vessels for the hydrothermal assisted synthesis or sealable glass tubes for the microwave assisted synthesis). Teflon vessels containing the reaction solution were heated at  $160^\circ\text{C}$  for 5 hours, while glass tubes containing the same solution were irradiated in a microwave reactor for 15 minutes with the temperature set to  $160^\circ\text{C}$ . In both cases, samples were removed when the temperature cooled to  $< 30^\circ\text{C}$  naturally and were then

neutralized to pH 7 with conc. HCl. Residual reagents were removed by dialysis (MWCO = 1 kDa) using Spectra/Por 7 standard regenerated cellulose pre-treated dialysis tubing.

## 3.5 References

- [1] Z. Kang, Y. Liu, S.-T. Lee, *Nanoscale* **2011**, *3*, 777–791.
- [2] J. Zou, R. K. Baldwin, K. A. Pettigrew, S. M. Kauzlarich, *Nano Lett.* **2004**, *4*, 1181–1186.
- [3] T. Yoshida, S. Takeyama, Y. Yamada, K. Mutoh, *Appl. Phys. Lett.* **1996**, *68*, 1772–1774.
- [4] J. P. Proot, C. Delerue, G. Allan, *Appl. Phys. Lett.* **1992**, *61*, 1948–1950.
- [5] A. B. Sieval, A. L. Demirel, J. W. M. Nissink, M. R. Linford, J. H. van der Maas, W. H. de Jeu, H. Zuilhof, E. J. R. Sudhölter, *Langmuir* **1998**, *14*, 1759–1768.
- [6] N. Licciardello, S. Hunoldt, R. Bergmann, G. Singh, C. Mamat, A. Faramus, J. L. Z. Ddungu, S. Silvestrini, M. Maggini, L. De Cola, et al., *Nanoscale* **2018**, *10*, 9880–9891.
- [7] Y. Zhong, F. Peng, F. Bao, S. Wang, X. Ji, L. Yang, Y. Su, S.-T. Lee, Y. He, *J. Am. Chem. Soc.* **2013**, *135*, 8350–8356.
- [8] J. Turkevich, P. Cooper Stevenson, J. Hillier, *Discuss. Faraday Soc.* **1951**, *11*, 55–75.
- [9] I. Ojea-Jiménez, J. M. Campanera, *J. Phys. Chem. C* **2012**, *116*, 23682–23691.
- [10] A. L. Patterson, *Phys. Rev.* **1939**, *56*, 978–982.
- [11] M. L. Mastronardi, F. Maier-Flaig, D. Faulkner, E. J. Henderson, C. Kübel, U. Lemmer, G. A. Ozin, *Nano Lett.* **2012**, *12*, 337–342.
- [12] K. Sato, T. Izumi, M. Iwase, Y. Show, H. Morisaki, T. Yaguchi, T. Kamino, *Appl. Surf. Sci.* **2003**, *216*, 376–381.
- [13] W. Stöber, A. Fink, E. Bohn, *J. Colloid Interface Sci.* **1968**, *26*, 62–69.
- [14] D. B. Cordes, P. D. Lickiss, F. Rataboul, *Chem. Rev.* **2010**, *110*, 2081–2173.
- [15] X. Zhai, P. Zhang, C. Liu, T. Bai, W. Li, L. Dai, W. Liu, *Chem. Commun.* **2012**, *48*, 7955–7957.
- [16] Y. Guo, Z. Wang, H. Shao, X. Jiang, *Carbon* **2013**, *52*, 583–589.
- [17] M. Xu, G. He, Z. Li, F. He, F. Gao, Y. Su, L. Zhang, Z. Yang, Y. Zhang, *Nanoscale* **2014**, *6*, 10307–10315.
- [18] W. H. Green, K. P. Le, J. Grey, T. T. Au, M. J. Sailor, *Science* **1997**, *276*, 1826–1828.
- [19] J. Chen, W. Liu, L.-H. Mao, Y.-J. Yin, C.-F. Wang, S. Chen, *J. Mater. Sci.* **2014**, *49*, 7391–7398.
- [20] M. Janeta, Ł. John, J. Ejfler, S. Szafert, *Chem. – Eur. J.* **2014**, *20*, 15966–15974.
- [21] E. S. Park, H. W. Ro, C. V. Nguyen, R. L. Jaffe, D. Y. Yoon, *Chem. Mater.* **2008**, *20*, 1548–1554.

- [22] P. Riello, M. Munarin, S. Silvestrini, E. Moretti, L. Storaro, *J. Appl. Crystallogr.* **2008**, *41*, 985–990.
- [23] N. Dhenadhayalan, K.-C. Lin, R. Suresh, P. Ramamurthy, *J. Phys. Chem. C* **2016**, *120*, 1252–1261.



# Chapter 4

## Silicon-based nanoparticles for Bio-imaging

### Abstract

Silicon based nanoparticles (Si NPs) have a proven biocompatibility, are non-toxic, and have a well-understood chemistry in terms of synthesis and surface functionalisation, all while still possessing the strong, tuneable photophysical properties associated with the traditional quantum dots. This gives them great potential for application as bio-imaging probes. The ability to covalently link different relevant functional molecules to the surface without disturbing the overall structure of the particles also opens up a variety of further bio-imaging possibilities for Si NPs, including multimodal imaging. This chapter reports on the use of our Si NPs prepared through the hydrothermal and microemulsion methods in *in vitro* and *in vivo* imaging applications. The amine terminated surfaces are modified with molecular dyes and/or radiolabels to facilitate imaging of the particles by optical fluorescence or positron emission tomography. Cytotoxicity, imaging efficiency and biodistribution are evaluated, in addition to *in vivo* clearance. One study here focuses on the use of the microemulsion Si NPs for brain imaging, to which end the particles are functionalised with a molecular dye and glucose in order to promote passage across the blood-brain-barrier (BBB).

### 4.1 Introduction

Semiconductor based quantum dots have by virtue of their high quantum yield of fluorescence, tunable emission wavelength, high photo bleaching threshold and high electro- and chemical stability, been preferred over fluorescent dyes for biological imaging applications<sup>[1],[2]</sup>. However, the complications associated with them regarding surface chemistry, biocompatibility and inherent toxicity of the heavy metal core material has led to restrictions on their further development<sup>[3]</sup>.

Over time, silicon-based nanoparticles (Si NPs) have been developed as an alternative for the same purpose. Si NPs overcome most, if not all of the barriers faced by quantum dots in bio-



imaging, while still possessing the beneficial quantum dot characteristics<sup>[4]</sup>. They have already shown promising results in bio-imaging experiments

Cytotoxicity studies of the particles themselves *in vitro* have already been reported in the literature by our group and others<sup>[5]-[8]</sup> and as mentioned have shown results that give a positive impetus for our *in vivo* studies.

In the following studies, Si NPs produced through both the hydrothermal and microemulsion methods are grafted with different functional molecules to enable *in vivo* imaging through positron emission tomography (PET) and optical fluorescence. PET offers extremely high sensitivity and no limit on detection penetration, while optical fluorescence imaging can function at low cost and offer information in a short amount of time<sup>[9]</sup>. One of our systems sees both the microemulsion and HT Si NPs coupled exclusively with a PET radiotracer (<sup>[64Cu]</sup>Cu-NOTA) in order to generate highly detailed images of the Si NPs *in vivo* bio distribution. The second system builds on the work of the first and sees the HT Si NPs coupled to both the radiotracer and a near-infrared (NIR) fluorescent dye (IR800) in hopes of combining information acquired through the two techniques to gain further details on the bio distribution of the functionalised Si NPs. Our third system focuses on the microemulsion Si NPs and the functionalisation of the surface with a sugar molecule (D-(+)-glucosamine) and a red emissive dye (Cyanine 5). The smaller size of these Si NPs compared to the HT Si NPs along with the added presence of the sugar is intended to provide an improved ability to cross the blood-brain-barrier (BBB) and achieve subsequent optical fluorescence imaging of brain tissue and Si NP bio-distribution.

## 4.2 Si NPs for Positron Emission Tomography (PET)

### 4.2.1 Surface functionalisation

Creation of both microemulsion and HT Si NPs based PET tracers proceeds through an identical synthetic route. First, the Si NPs are coupled to S-2-(4-isothiocyanatobenzyl)-1,4,7-triazacylonane-1,4,7-triacetic acid, a chelating ligand for the <sup>[64Cu]</sup> radionuclide. The reaction proceeds as shown below in figure 4.1.

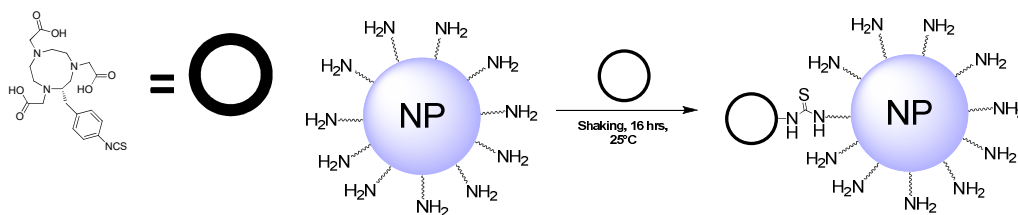


**Figure 4.1:** Reaction scheme for the coupling of Si NPs with p-SCN-Bn-NOTA

Following the reaction, the system is purified of unreacted ligand by dialysis against water. At this point, the toxicity of the particles was assessed with their exposure to human embryonic kidney cells (HEK293) using a standard MTS (3-(4,5-dimethylthiazol-2-yl)-5-(3-carboxymethoxyphenyl)-2-(4-sulfophenyl)-2H-tetrazolium) assay. A kidney cell line was the preferred choice as the preferred excretion pathway for these Si NPs is renal. The results of incubations of the cells over different time periods with 1 to 100  $\mu\text{g mL}^{-1}$  Si NPs-NOTA (0.1  $\mu\text{mol}$  NOTA per mg Si NPs) are shown below in figure 4.2.

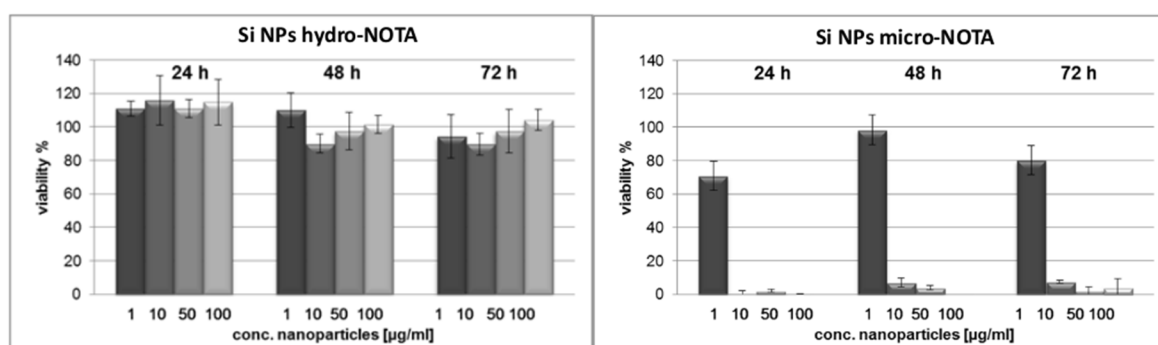


**Figure 4.2:** Effect of HT Si NPs-NOTA and microemulsion Si NPs-NOTA on the viability of HEK293 cells. Viability recorded as % of control. [N. Licciardello, S. Hunoldt, R. Bergmann, G. Singh, C. Mamat, A. Faramus, J. L. Z. Ddungu, S. Silvestrini, M. Maggini, L. De Cola, et al., *Nanoscale* **2018**, *10*, 9880–9891]-Reproduced by permission of The Royal Society of Chemistry

Si NPs hydro-NOTA (HT Si NPs coupled to NOTA) showed little effect on metabolic activity in line with previous literature results<sup>[10]</sup>. On the other hand, Si NPs micro-NOTA (microemulsion Si NPs coupled to NOTA) caused a notable decrease in the viability even at low concentrations. This was hypothesised to be due to the possible presence of residual traces of TOAB surfactant (removable with more washing) and the high density on terminal amino groups on the surface. It has been reported that bare amine terminated Si NPs possess some cytotoxicity<sup>[11]</sup> and in this case, because the surface was functionalised with such a small amount of NOTA, there will be many free amine groups remaining on the surface.

#### 4.2.2 In vivo bio-distribution studies

Next, a solution containing  $[^{64}\text{Cu}]\text{CuCl}_2$  in MES/NaOH buffer (pH 6) was mixed with the particles at room temperature for 30 minutes to complex the surface-attached NOTA chelator with the  $[^{64}\text{Cu}]$  radionuclide. Confirmation of the successful complexation and the absence of free  $^{64}\text{Cu}^{\text{II}}$  was evaluated by radio instant thin layer chromatography, where only signals for the complete systems were observed, which stayed at the baseline due to the mass of the particles. A representation of the complete system in both cases is shown below in figure 4.3.

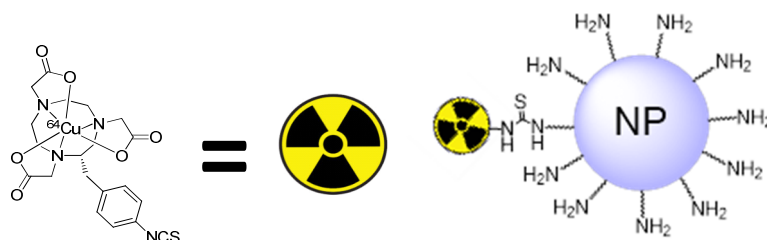


**Figure 4.3:** Schematic representation of the completed systems of both microemulsion Si NPs and HT Si NPs coupled to the final radiotracer.

Biodistribution profiles of the radiotracer coupled Si NPs were evaluated by dynamic PET experiments in female NMRI nu/nu mice, bearing epidermoid carcinoma (A431) xenografts on the right hind leg. After intravenous injection of the radiotracer Si NPs, dynamic PET was recorded at different time points. As shown in figure 4.4 below, images A-D showing the maximum PET activity show a fast localisation of the particles in the kidneys and bladder, indicating a rapid clearance from the body via the renal pathway. Also shown, this time by images E-H, is the rapid distribution of the radiotracer Si NPs in the tumour, allowing clear visualisation at 5 minutes post injection. With regards to the imaging of the tumour, the labelled HT Si NPs showed the best results, however, the activity in the tumour was short lived in both cases as the particles were “washed out” towards the bladder, which is expected with particles of such small sizes<sup>[12]</sup>. Nonetheless, these results provided a solid basis for the further functionalisation of the HT Si NPs in particular for in vivo imaging using this strategy, as is shown in the next section.

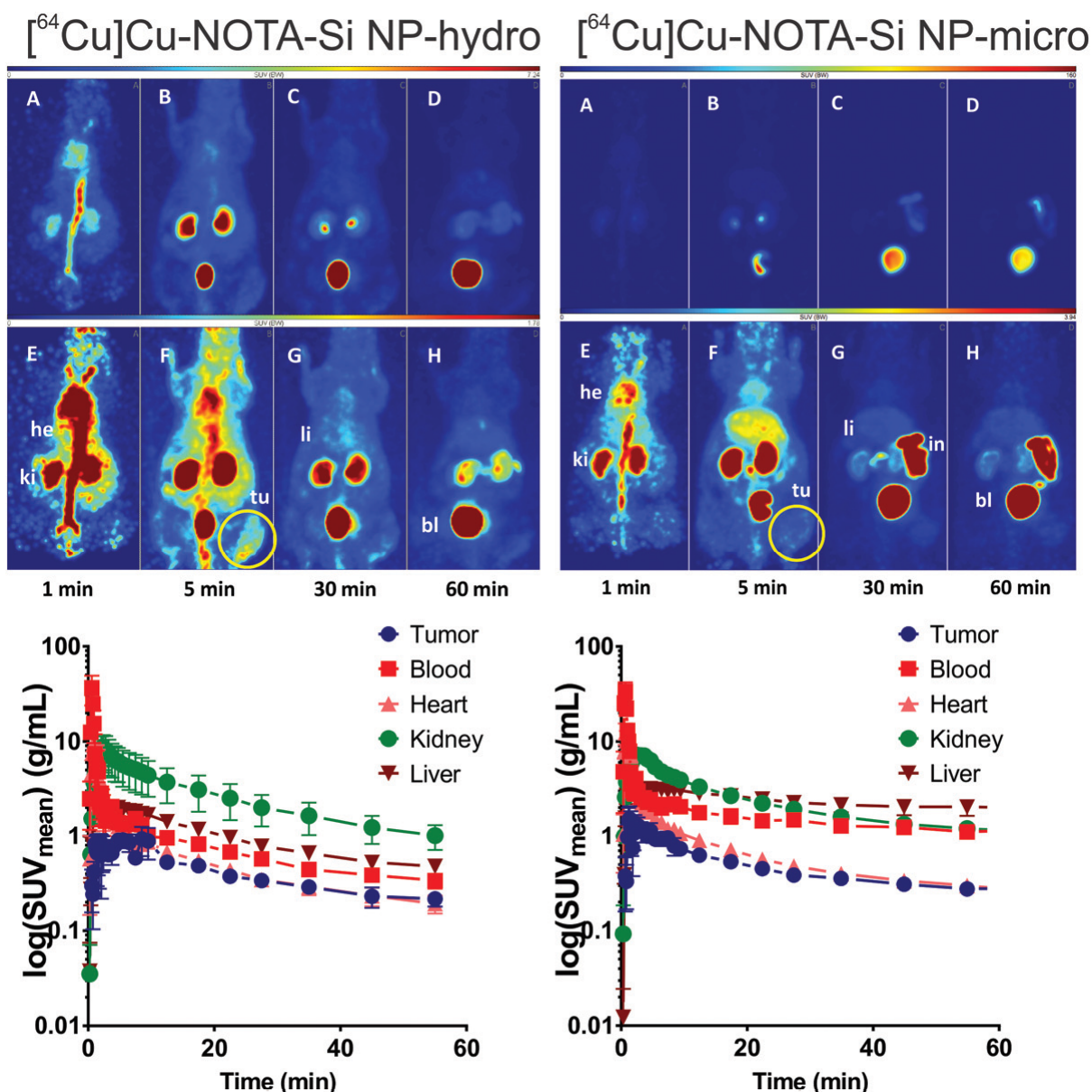


**Figure 4.4:** Maximum intensity projections obtained from a PET study after a single intravenous injection of  $[^{64}\text{Cu}]\text{Cu-NOTA-Si NPs-hydro}$  ( $n = 2$ ) and  $[^{64}\text{Cu}]\text{Cu-NOTA-Si NPs-micro}$  ( $n = 2$ ) in A431 tumour-bearing mice after 1 min (A, E), 5 min (B, F), 30 min (C, G), and 60 min (D, H) after injection. Images A–D were scaled to the maximum activity and images E–H were rescaled to visualize the tumour (above). Abbreviations: bl = bladder, he = heart, in = intestine, ki = kidney, li = liver, tu = tumour. [N. Licciardello, S. Hunoldt, R. Bergmann, G. Singh, C. Mamat, A. Faramus, J. L. Z. Ddungu, S. Silvestrini, M. Maggini, L. De Cola, et al., *Nanoscale* **2018**, *10*, 9880–9891]—Reproduced by permission of The Royal Society of Chemistry

## 4.3 Si NPs for PET and optical fluorescence imaging

### 4.3.1 Surface functionalisation

Creation of the dual labelled HT Si NP based system proceeds by taking advantage of the convenient amine chemistry available on the surface of the particles, as was done for the first probe. HT Si NPs are first coupled to an N-hydroxysuccinimide (NHS) ester functionalised derivative of the IR800 dye by mixing the two components in an aqueous, basic (~pH 9) solution overnight. Any remaining uncoupled dye is then removed from the system by dialysis against water. Following this, attachment of the NOTA chelator and subsequent complexation of the [ $^{64}\text{Cu}$ ] radionuclide is realised with an identical procedure to the previous mono labelled system. A schematic representation of the completed system is shown below in figure 4.5.

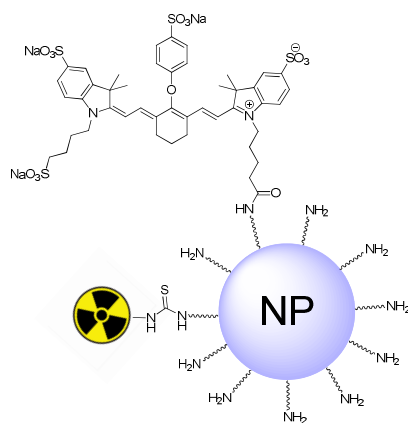


**Figure 4.5:** Schematic representation of the completed system of HT Si NPs coupled to both the IR800 dye and the final radiotracer.

### 4.3.2 In vivo bio-distribution studies

The biodistribution of the dual labelled [ $^{64}\text{Cu}$ ]Cu-Si NP-IR800-NOTA was studied in NMRI nu/nu healthy mice at 5 minutes, 1 hour and 24 hour time points. The standardized uptake value ( $\text{SUV}_{\text{BD}}$ ) and the percent injected dose ( $\% \text{ID}$ ) were used to evaluate the preferred mode of elimination of the particles from the body and the accumulation of these particles in different tissues and organs. The data is also used to compare the biodistribution of the dual labelled imaging agent to that of previous monolabelled system.

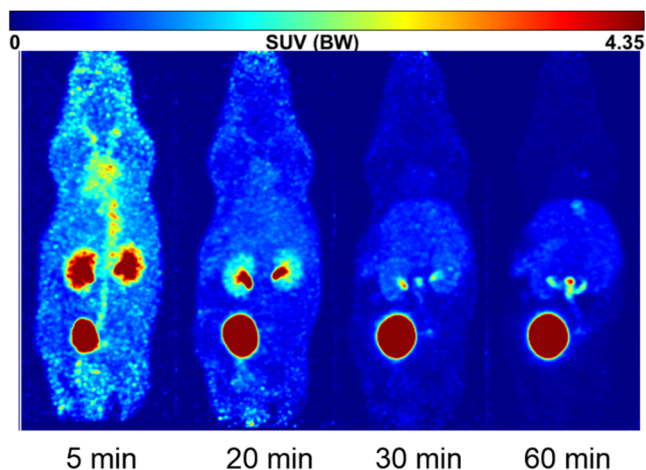


**Figure 4.6:** Maximum intensity projections obtained from a PET study after a single intravenous injection of  $[^{64}\text{Cu}]\text{Cu-Si NP-IR800-NOTA}$  in NMRI nu/nu healthy mice at 5 mins, 20 mins, 30 mins and 60 mins post-injection.

Urine samples from the experimental mice were collected and the radioactivity was examined using radio instant thin layer chromatography. The Si  $[^{64}\text{Cu}]\text{Cu-Si NP-IR800-NOTA}$  remains at the origin ( $R_f = 0$ ) on the iTLC and the free radionuclide  $[^{64}\text{Cu}]\text{CuCl}_2$  moves towards the front line ( $R_f = 0.8$ ). A comparative TLC of the sample injected and the urine collected after 5 minutes and 1 hour post injection is displayed in figure 4.7. No significant differences are observed between the three samples, confirming the stability of the nanoconjugates in the physiological system of the mice. The imaging modality (radiotracer) remains intact and there is no loss of the radionuclide or chelator within the biological system. This therefore proves the covalent attachment of the complete radiotracer to the HT Si NPs.

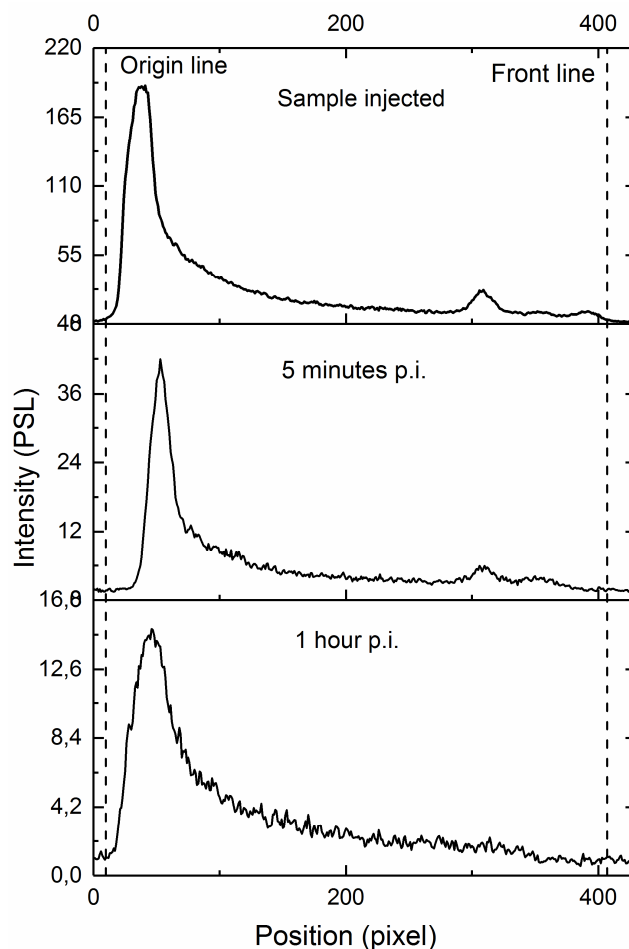


**Figure 4.7:** Radio instant thin layer chromatograms of urine samples collected from the experimental mice at different time points.

For ex vivo imaging and autoradiography studies, mice were excised at 5 mins, 1 hour and 24 hour post injection and comparative data based on %ID and SUV values was obtained.

The widest spread of radioactivity was observed in organs that were excised and measured by autoradiography at 5 minutes post-injection. About 40% of activity was in the urine, with the kidneys, liver and intestine constituting around 5%, 5% and 3% respectively. At 1 hour, the radioactive content in the urine rose to 85%, while falling to less than 5% in the kidneys, liver and intestine. The rest of the organs showed negligible amounts of activity, once again confirming the extremely fast renal clearance of the labelled HT Si NPs from the system within 1 hour. The 24 hour study showed the presence of 99% activity in the urine with 1% in the kidney and liver.

The SUV data analysis at 5 minutes post-injection showed the highest activity concentration in the urine (4) whereas all the other organs showed values between 0.5 – 2, which refers to a

smooth, whole body biodistribution pattern. In 1 hour, the values in the kidney, liver and spleen were observed to be around 1.5, 0.7 and 0.3. The values in other organs were substantially lower.

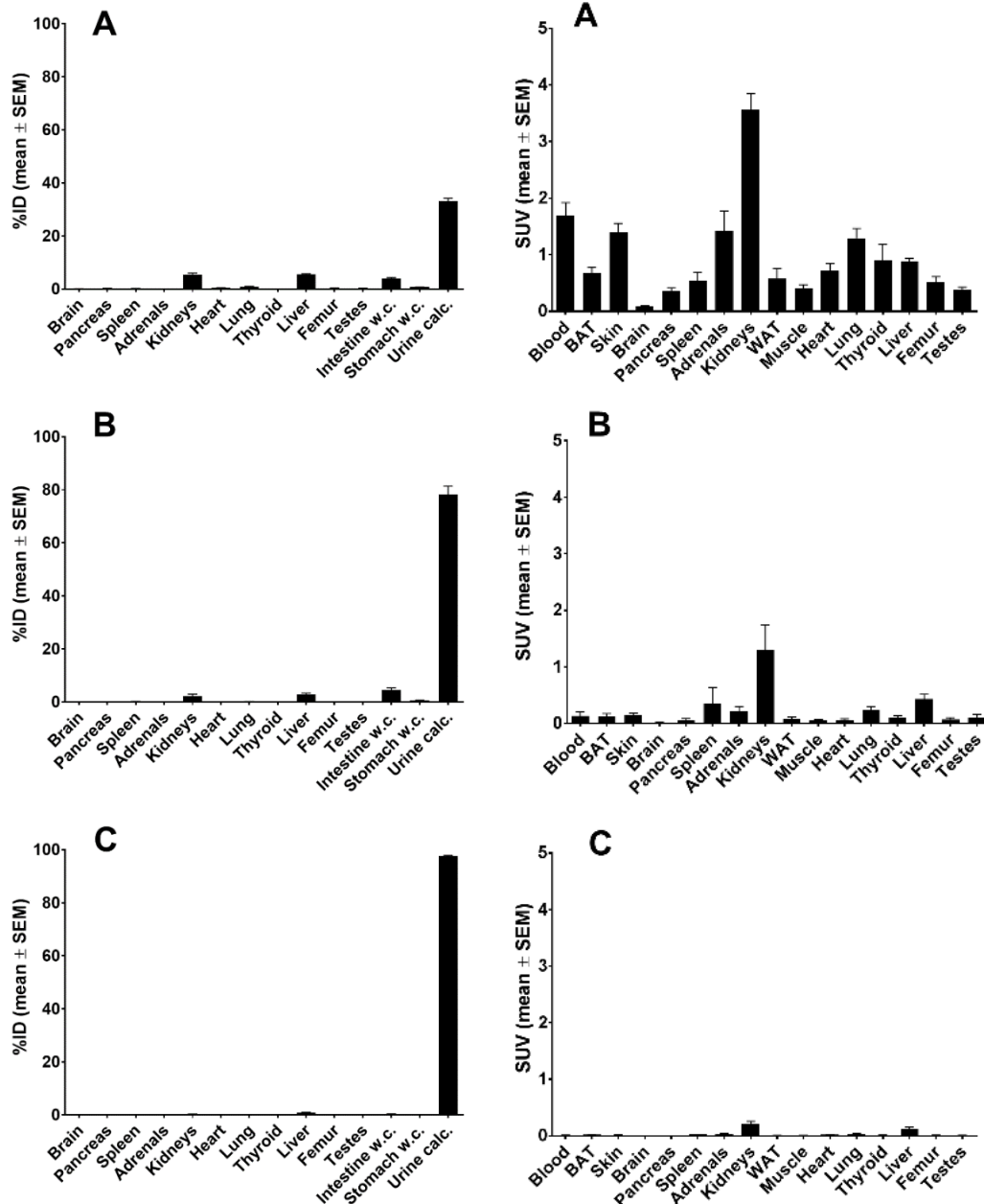


**Figure 4.8:** *Ex vivo* biodistribution and autoradiography studies of  $[^{64}\text{Cu}]\text{Cu-Si NP-IR800-NOTA}$ . Left: %ID values-based analysis. Right: SUV-based analysis

To evaluate the mode of elimination of the particles, we compared the the %ID and SUV values of the kidneys (to check renal excretion) and the liver (to check hepatobiliary mode of



elimination). The values clearly show that the most plausible mode of elimination is renal. The particles show no sign of sticking in the medulla and easily pass through the glomerular pores in as short as 1 hour time.

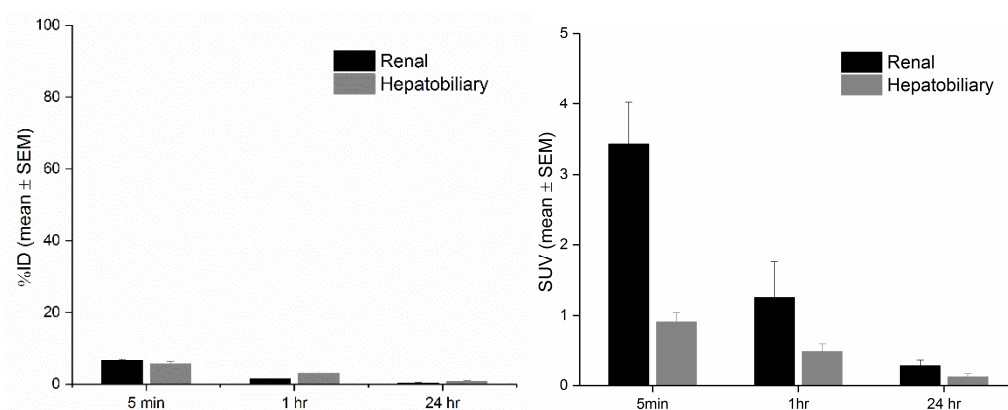


**Figure 4.9:** Comparison of renal vs hepatobiliary elimination

Finally, the attached IR800 dye was used in an ex vivo fluorescence imaging experiment. The data was analysed by fluorescence maximum intensity projections. This was necessary as after the elimination of the majority of the injected sample through the urine, only traces of fluorescence was detectable in the organs. Figure 4.10 below shows the organs of the excised mice at 5 minutes, 1 hour and 24 hour post injection. In the first 5 minutes, the fluorescence is observed almost uniformly distributed in the whole body and also actively filtered through the kidneys, which shows prominent signals for the urine sample. In 1 hour, the activity has fallen rather low and the major signals are observed in the urine and intestine. For 24 hour post injection excision samples, traces of fluorescence are detected in the stomach, intestine and urine.

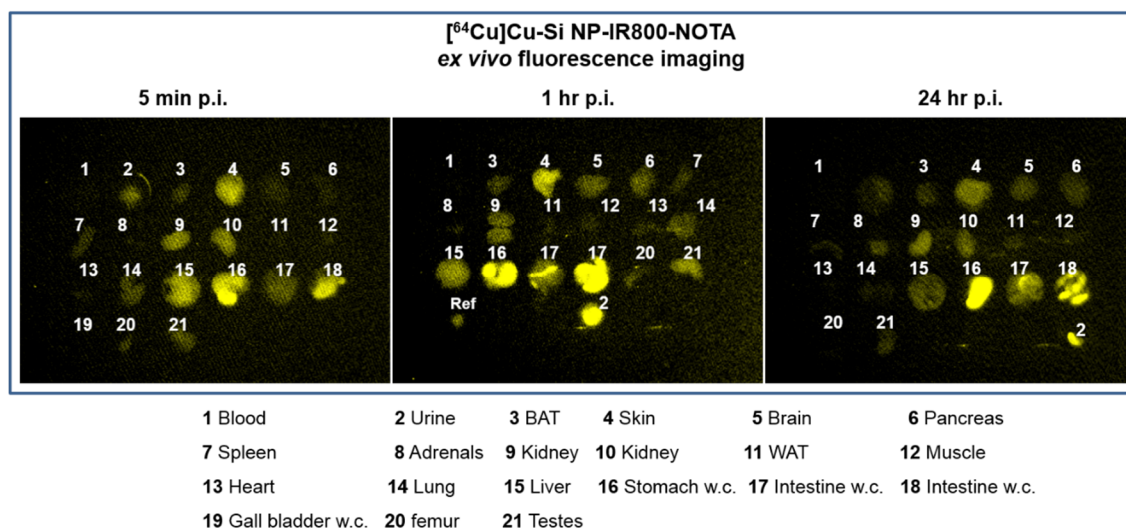


**Figure 4.10:** Optical imaging *ex vivo* biodistribution studies of [<sup>64</sup>Cu]Cu-Si NP-IR800-NOTA. (w.c. = with content)

### 4.3 Si NPs for optical fluorescence imaging across the blood brain barrier (BBB)

Bio-imaging of cancers and other complications in the brain has somewhat remained a challenge in the pharmaceutical industry for a long time. The main obstacle to achieving a reliable system for this is the natural shield of the brain in the form of the blood-brain-barrier (BBB). The main component of this is constructed by cerebral capillary endothelial cells, in between which are “tight junctions” formed of specialised proteins. Endothelial cells prevent the passage of larger hydrophilic molecules and toxic agents, while the tight junctions prevent molecules diffusing from the blood into the brain through the spaces between the endothelial cells<sup>[13], [14]</sup>. The soundness of this barrier construction, coupled with the limited pinocytotic activity of the endothelial cells<sup>[15], [14]</sup> means that many drugs and biomolecules intended for treatment of different brain-based diseases are excluded from entry to the brain<sup>[16], [17]</sup>

A number of molecules that are essential to the brain function do however have pathways to be transported across the barrier. This is illustrated in figure 4.11 below<sup>[13]</sup>

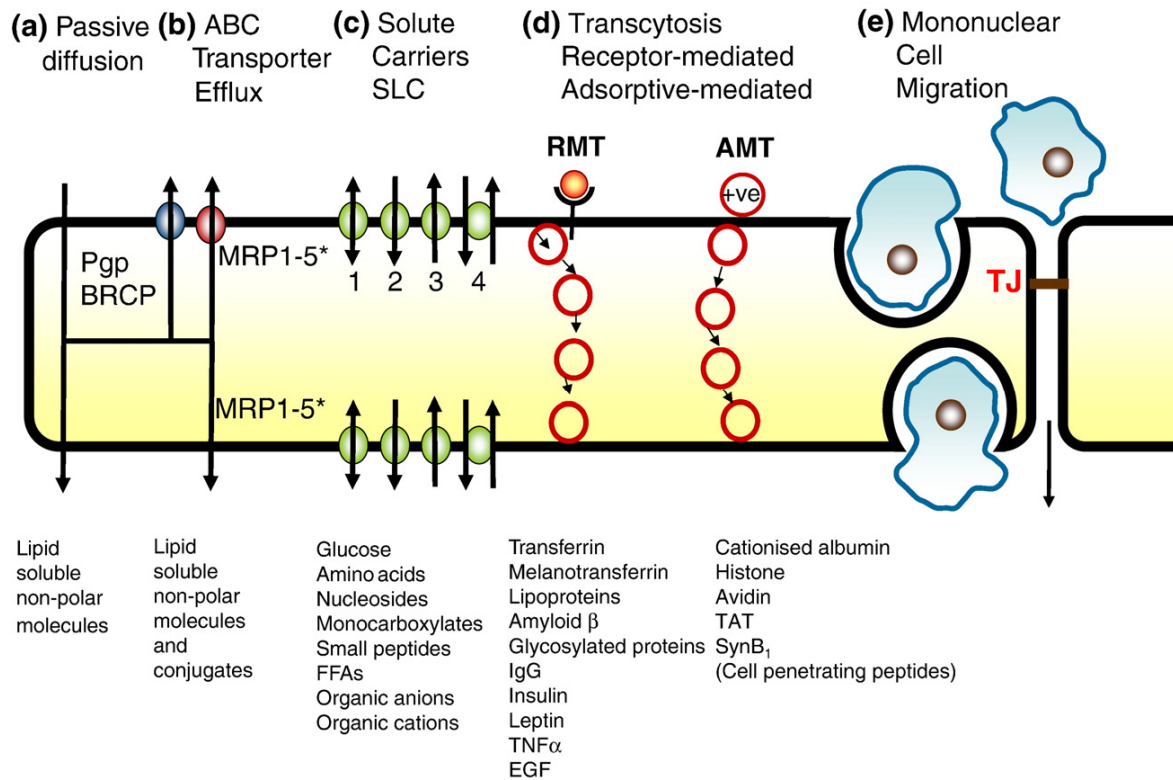


**Figure 4.11:** Modes of transport across the BBB. Reprinted from *Neurobiology of Disease*, 37, N. J. Abbott, A. A. K. Patabendige, D. E. M. Dolman, S. R. Yusof, D. J. Begley, “Structure and function of the blood–brain barrier”, 13–25, Copyright (2010), with permission from Elsevier

Of particular interest is the carrier-mediated influx transport mechanism utilising solute carriers (SLCs). This allows the transport of numerous essential, small, polar molecules such as glucose, amino acids and nucleosides across the barrier through a passive or secondarily active mechanism. Net transport of the molecules can be determined by a concentration gradient, a unidirectional movement, exchange of one substrate for another or by ionic and electrochemical gradients.

In order to facilitate the delivery of objects into the brain that are otherwise blocked by the barrier, it is possible to take advantage of the SLC mechanism by coupling the desired object with a transportable molecule. This strategy has already been used with success in an *in vitro* study to transport glucose-coated gold NPs across human brain endothelial cells via the glucose transporter<sup>[14]</sup> and an *in vivo* study where nanoparticles based on an emulsifying wax were coated with thiamine via the thiamine transporter<sup>[18]</sup>. Despite these positive results for transporting nanoparticles across the BBB, studies on the topic remain limited and few, if any, show the transport of nanoparticles for imaging applications.

### 4.3.1 Surface functionalisation

Glucose was chosen as the sugar to conjugate to the microemulsion Si NPs owing to its known transportation across the BBB<sup>[13]</sup> and use in earlier nanoparticle studies<sup>[14]</sup>. However, grafting of the D-(+)-glucosamine itself to the as synthesised Si NPs was not possible via the amine termination. In order to realise the coupling, either the D-(+)-glucosamine would need to be modified with a functionality that allowed for amine coupling or the amine groups on the surface of the Si NPs would need to be changed in order to facilitate coupling to the amine moiety of the sugar. In the end, to avoid the complex sugar modification chemistry that would need to be navigated in order to modify the D-(+)-glucosamine, we chose to take the approach of modifying the amine groups on the surface of the Si NPs instead.

It is possible to react the amine group of the glucosamine with an activated carboxylic acid in order to create an amide bond and achieve the desired coupling. A COOH termination is also known to reduce the cytotoxicity of the Si NPs compared to their amine terminated analogues<sup>[11]</sup>. As such, the synthesis of Si NPs bearing terminal COOH groups was explored. First, we carried out the oxidation of Mg<sub>2</sub>Si with bromine to form Br-terminated Si NPs followed by reaction with 3-butenylmagnesium bromide to achieve butylene-terminated Si NPs<sup>[19]</sup>. Following this, the alkene was cleaved in a catalysed reaction with sodium periodate to yield COOH terminated Si NPs<sup>[20]</sup>. A scheme for the reaction is shown in figure 4.12.

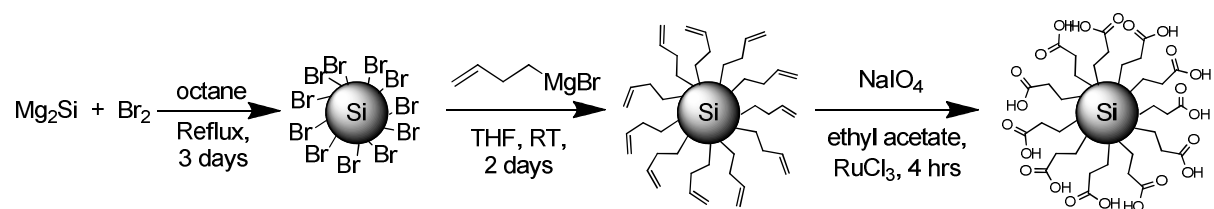


**Figure 4.12:** Synthesis of COOH terminated Si NPs from the oxidation of Mg<sub>2</sub>Si

There were issues found with the product however. Firstly the water-solubility of the Si NPs was limited, which was assumed to be due to the occurrence of side reactions in the butylene termination process. These can cause the Si NPs to be un-homogeneously terminated with alkyl groups at this stage, which persist to the final product and prevent its water solubility. Another problem was observed upon TEM inspection. The Si NPs themselves had a diameter in the region of 10 nm, where an ideal size would be at least half of this to allow optimal transport across the BBB.

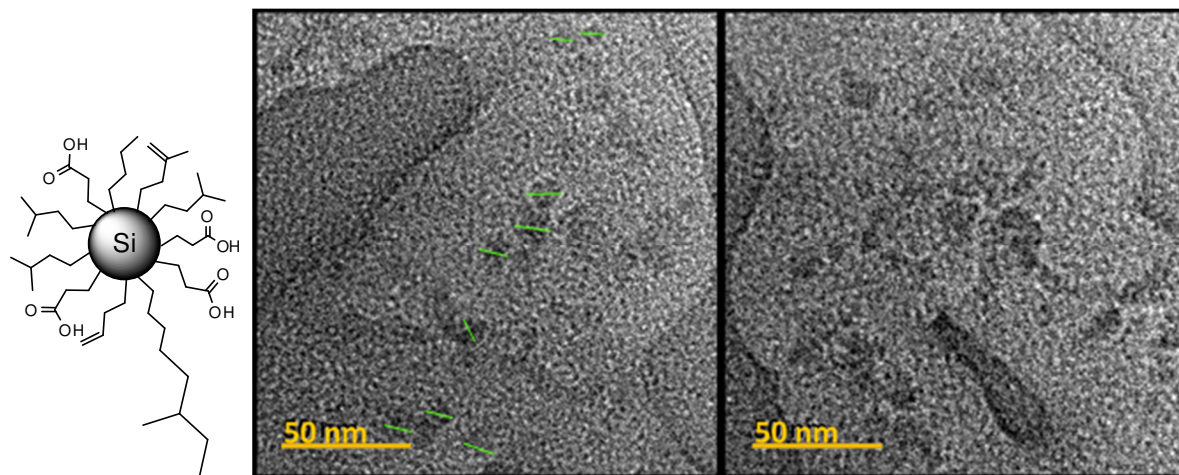


**Figure 4.13:** Representation of a Si NP after several possible side reactions and TEM micrographs obtained for the COOH terminated Si NPs from the oxidation of  $\text{Mg}_2\text{Si}$ . The diameter of individual particles ( $\sim 10$  nm) are shown by green lines on the left micrograph

Following this, a different synthetic route to obtain the desired COOH-terminated Si NPs. As size control to the smallest possible size and retention of water solubility was a priority, it was decided to use the Si NPs synthesised through the microemulsion method and modify the amine groups thereafter.

In fact, this method was reported by Kimura et al. who converted the amine termination of microemulsion Si NPs to COOH groups by way of succinic anhydride and attached glucosamine thereafter to assess the in vitro imaging capabilities of the system<sup>[21]</sup>. Although no characterisation was provided on the success of the functional group conversion, the nature of the reaction suggests it should work.

Following the same reported method, a modification was made with the addition of *N,N*-Diisopropylethylamine (DIPEA) in order to raise the pH of the system to  $\sim$  pH 9 and ensure that the amine groups were deprotonated for the greatest possible conversion. Succinic anhydride was added in large excess compared to the calculated molar amount of  $\text{NH}_2$  groups for the mass of Si NPs used to also push the reaction to maximum yield.

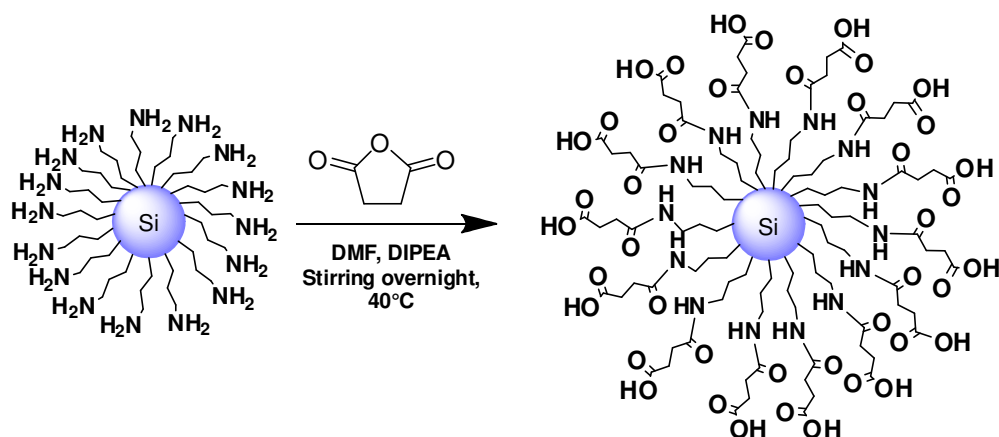


**Figure 4.14:** Reaction scheme for the conversion of amine-terminated Si NPs to COOH terminated Si NPs

Following the reaction, the product was purified by size exclusion chromatography (Sephadex LH-20) in methanol. It was clear to observe the separation of the Si NP-COOH from the excess succinic anhydride (now mostly succinic acid) after the methanol in each fraction evaporated. Early fractions yielded the blue emissive pale yellow wax that was the Si NPs, while the later fractions contained progressively larger amounts of white solid. This observation was used as a means to obtain a close separation and acquire as much of the product Si NPs as possible.

Assessment of the reaction completion was conducted qualitatively by means of the Kaiser test. Identical concentrations (mass/volume) of Si NPs before and after the reaction were reacted with ninhydrin reagent and observed. No visible colour change occurred in the Si NPs-COOH sample indicating that there was a complete conversion of the amine groups. To investigate further, UV-vis studies of the samples were conducted, which serve to confirm the essentially complete conversion of the groups. A very slight absorbance was observed at  $\lambda = 580$  nm, however, with a difference of  $< 0.003$  to the blank and a reading of  $< 0.01$  itself, it is negligible and cannot be used reliably in a quantifying calculation.

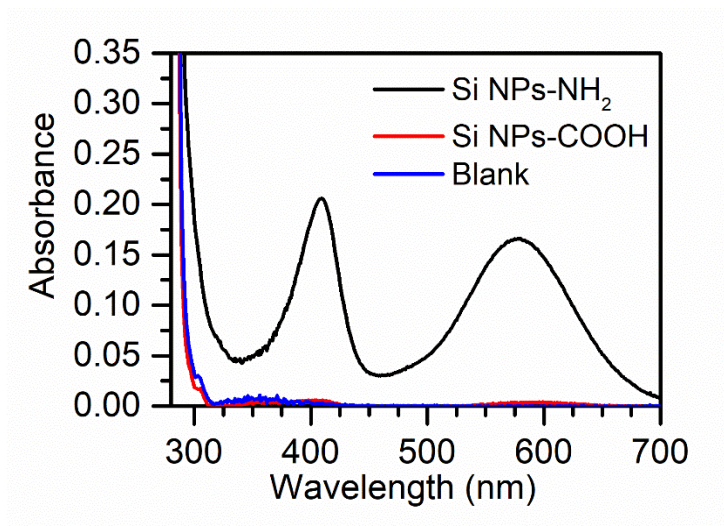


**Figure 4.15:** Results of Kaiser Tests in ethanolic solutions reacting the same quantity of Si NPs before and after the COOH termination reaction. (Blank = Kaiser Test reagents (phenol, potassium cyanide and ninhydrin) in ethanol also heated for an identical time).

XPS measurements were performed to assess the presence of different elements in the system.

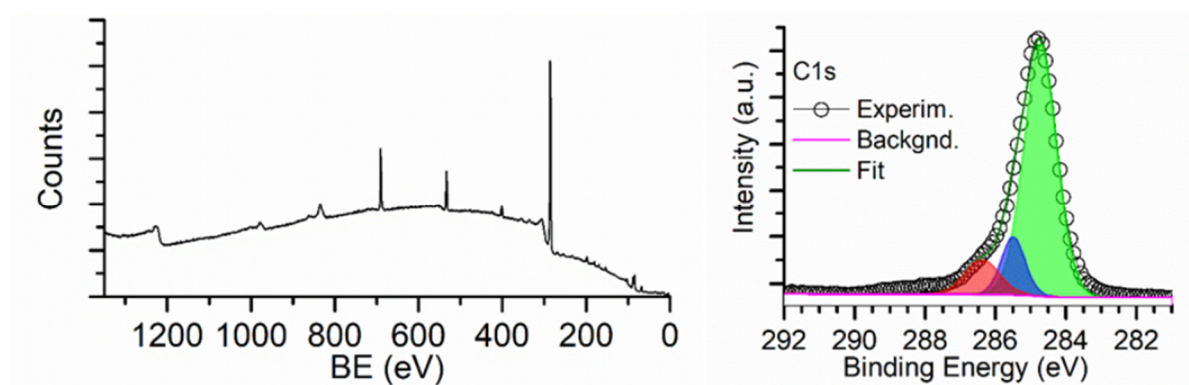


**Figure 4.16:** XPS survey (left) and C1s (right) scans of Si NPs-COOH

As shown in figure 4.16 and listed in table 4.1 the Si NPs-COOH contain the elements C, O, N and Si with the remaining peaks being trace elements of negligible amounts. The successful COOH termination and the coupling are evidenced by deconvolution of the high resolution C1s scan, which reveals the presence of three peaks (table 4.2). Notable are the two peaks at higher binding energy, which indicate presence of carboxylic acid and the formation of amide bonds.

Name	Peak BE	FWHM eV	Area (P) CPS.eV	Atomic %
C1s	285.24	2.58	1425153	88.96
O1s	532.87	2.59	90141.72	2.33
N1s	402.12	2.59	79868.37	3.22
Si2p	102.82	2.58	25166.48	1.56

**Table 4.1:** XPS survey data for Si NPs-COOH

Name	Peak BE	Height CPS	Height Ratio	Area CPS.eV	Area Ratio
C-C	284.73	108503.6	1	127554.1	1
C-O	285.5	24897.72	0.23	21273.34	0.17
C=O	286.38	14795.59	0.14	18579.23	0.15

**Table 4.2:** XPS data for Si NPs-COOH C1s scan

With COOH functionalisation of the surface established, coupling of the required functional molecules could proceed. Cyanine 5 (Cy5) with an amine functionality was chosen to label the particles in order to facilitate attachment to the COOH groups and provide an in vivo visible emission within the NIR window ( $\lambda_{\text{max}}$  emission = 662 nm). To investigate if the glucose coating would indeed have a major enhancement effect on the transport of these small particles across the BBB, two samples were prepared; one with Si NPs-COOH coupled only to the fluorescent dye and the other with the particles coupled to both glucose and the dye. In all cases, the couplings proceed through reaction of the activated COOH groups (activated using a 1-Ethyl-3-(3-dimethylaminopropyl)carbodiimide hydrochloride (EDC) and *N*-Hydroxysuccinimide (NHS) mixture) with the deprotonated amine groups on the label molecules (deprotonated through addition of DIPEA). Essential in each of the reactions is a small volume of solvent and an excess of the EDC and NHS activating reagents in order to drive the heterogeneous reactions to completion. Purification after each reaction was done by size exclusion chromatography (Sephadex LH-20) in methanol.



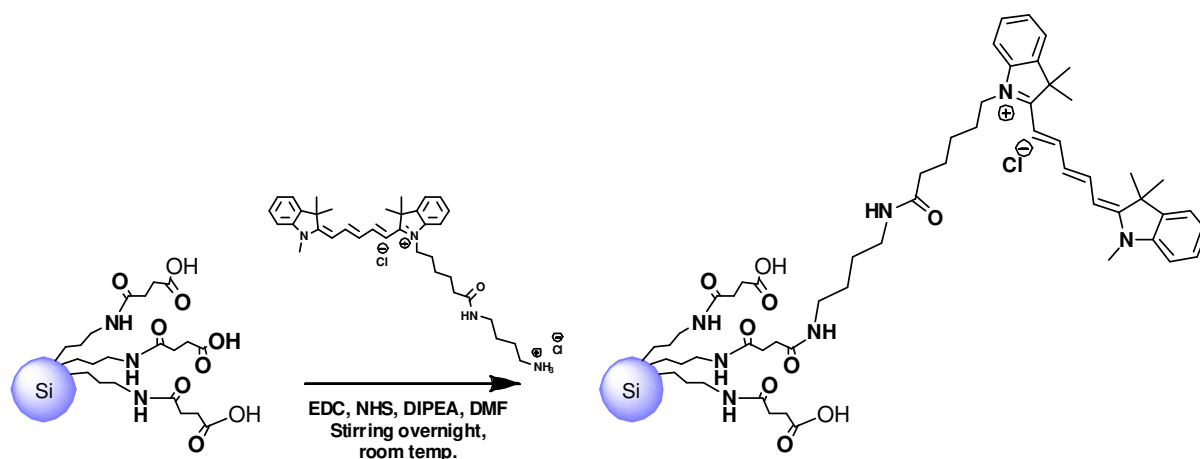


**Figure 4.17:** Coupling of Si NPs-COOH to Cy5 (Si NPs-Cy5)

The dye-exclusive probe (Si NPs-Cy5) was characterised by photophysical analyses to assess the detection properties of the dye on the particles and for initial confirmation of the coupling success. As shown by both the absorption and emission spectra, the dominant photophysical characteristic of the red emissive Cy5 dye. Signs of the Si NPs can still be observed however, with the increased absorption below 300 nm and the emission band centred at  $\lambda = 500$  nm in the emission spectrum, which provides a useful indication that the particles are still present in the system. An indication of coupling between the dye and particles is given by a comparative measurement in the UV-vis absorption spectrum. When the complete, coupled system is compared to a simple mixture of the particles with an identical concentration of Cy5 dye (calculated as shown below in equation), a red shift in the  $\lambda_{\text{max}}$  absorption as well as an overall increased absorption is seen, which is possibly indicative of a slight increase in scattering due to the coupled Si NPs having an increased interaction with the incident light as a single unit.

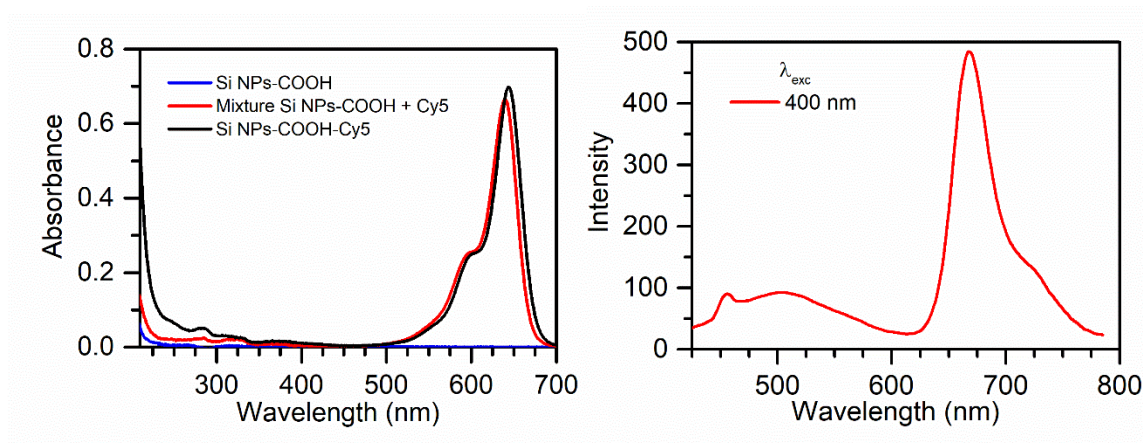


**Figure 4.18:** (Left) UV-Vis absorption spectra of Si NPs-COOH, simple mixture of the system and Si NPs-Cy5. (Right) Emission spectrum of Si NPs-Cy5

The remaining photophysical data of excited state lifetime and quantum yield of the system are displayed in table 4.3.

	Lifetime (ns) <sup>a,b</sup>	Lifetime (ns) <sup>a,c</sup>	Q.Y. (%) <sup>d</sup>
Si NPs-Cy5	$\tau_1$ : 13.97 (79.3%) $\tau_2$ : 4.73 (20.7%)	1.0 (100%)	20 (Cy5) 4 (Si NPs)

**Table 4.3:** Photophysical data for Si NPs-Cy5. (a.  $\lambda_{exc}$  = 375 nm b.  $\lambda_{em}$  = 450 nm c.  $\lambda_{em}$  = 668 nm d. Measurement performed using integrating sphere)

FT-IR spectroscopy was used to provide further information on the structure of the Si NPs-Cy5 in terms of the chemical bonds present. The spectrum was measured via an ATR attachment, onto which the Si NPs-Cy5 were drop cast from methanol, with the solvent evaporated before analysis. Notable are the broad signal at 3314  $\text{cm}^{-1}$  and the signal at 1411  $\text{cm}^{-1}$  both corresponding to the  $-\text{OH}$  of the carboxylate termination and the signal at 1624  $\text{cm}^{-1}$  corresponding to the amide  $\text{C}=\text{O}$  bond, all of which give evidence of the successful COOH termination and coupling.

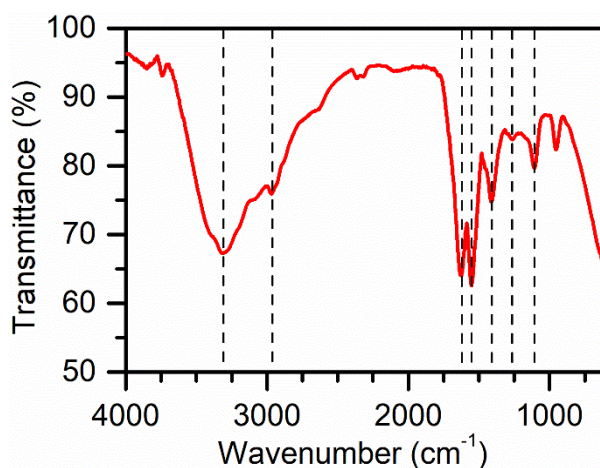


**Figure 4.19:** FT-IR spectrum of Si NPs-Cy5

Signal	Wavenumber (cm <sup>-1</sup> )
O—H (carboxylic acid)	3314
C—H	2970
C=O (amide)	1624
C—H	1553
O—H (carboxylic acid)	1411
C—O	1263
C—N	1107

**Table 4.4:** FT-IR spectral data of Si NPs-Cy5

The final size and monodispersity of the functionalised Si NPs were assessed by means of TEM. As shown in figure 4.20 below, the Si NPs-Cy5 retain a circular shape and appear to be monodisperse, with an average size of  $3.8 \pm 0.7$  nm. High resolution TEM (HRTEM) reveals that the crystalline nature of the silicon core is still maintained by the particles, showing that the core structure of the Si NPs has not been modified by the coupling, despite changes seen in, for example, the absorption and emission spectra.

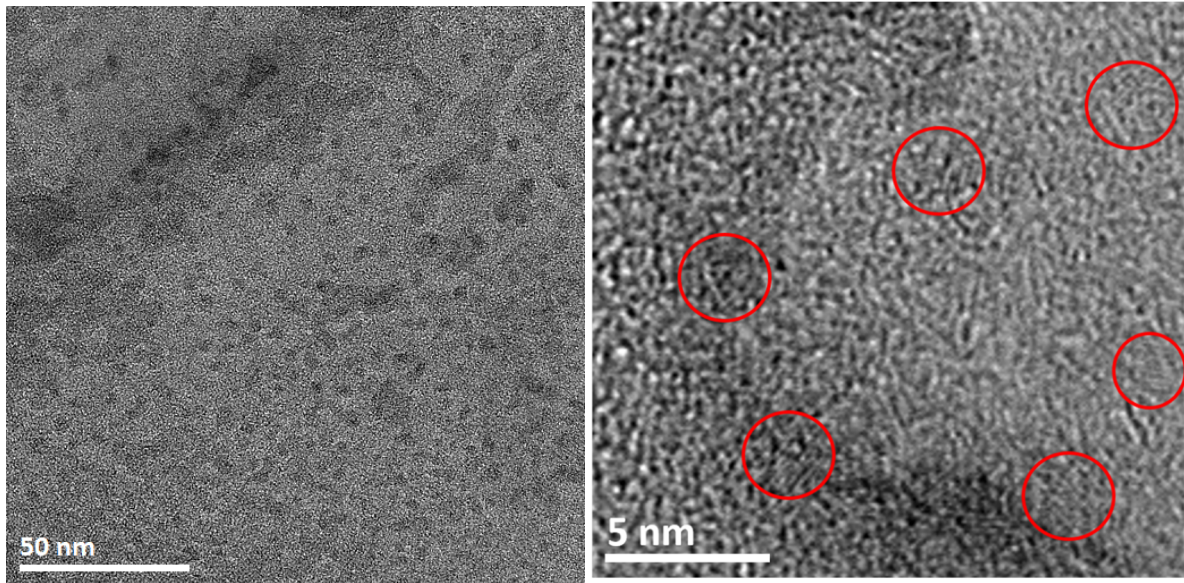


**Figure 4.20:** TEM micrographs of Si NPs-Cy5 (right: HRTEM micrographs with examples of individual particles circled)

Taking data from the UV-vis absorption spectrum of the sample and the average size of the particles found through TEM analysis allows an estimate for the number of dye molecules per particle to be calculated. Using ratiometric absorbance and the workings of the equation below, a value for the number of dye molecules can be calculated.

*Cy5 grafting*

*Mol mass (minus  $H^+$ ,  $Cl^-$ ) = 617.34 g/mol*

*$\epsilon = 250000 \text{ dm}^3 \text{ mol}^{-1} \text{ cm}^{-1}$*

*For SiNPs grafted with Cy5, max abs. at 642 nm =  $A = 0.70$*

*Therefore:  $c = A / \epsilon l = 0.70 / (250000 \times 1) = 2.8 \times 10^{-6} \text{ mol} / \text{dm}^3$*

*So  $n = cv ((2.8 \times 10^{-6}) \times (3 \times 10^{-3})) = 8.4 \times 10^{-9} \text{ mol in 3 mL (used for UV-vis comparison)}$*

*(Measured solution approx. 0.11 mg of SiNPs Cy5 in 3mL water)*

*Mass =  $n \times \text{Mol mass} = (8.4 \times 10^{-9}) \times 617.34 = 5.19 \times 10^{-6} \text{ g} = 5.19 \times 10^{-3} \text{ mg dye in 3 mL}$*

*(So in 0.11 mg of SiNPs Cy5 in 3 mL water)*

*So mass Cy 5 per mL =  $5.19 \times 10^{-3} / 3 = 1.73 \times 10^{-3} \text{ mg/mL} = M_{\text{dye}}$*

*Mass of SiNPs:*

*One SiNP:*

*Diameter = 3.8 nm*

$$\text{Vol (V)} = (4/3) \pi (1.9 \times 10^{-9})^3 = 2.87 \times 10^{-26} \text{ m}^3 = 2.87 \times 10^{-20} \text{ cm}^3$$

$$\text{Density (D)} = 2.33 \text{ g/cm}^3 \text{ (silicon)}$$

$$\text{Mass of one NP (M = V x D)} = 6.7 \times 10^{-20} \text{ g} = 6.7 \times 10^{-17} \text{ mg} = M_{\text{SiNP}}$$

*No. of SiNPs*

$$\text{Total conc. of SiNPs-Cy5 in measured solution} = 0.037 \text{ mg/mL (0.11 mg in 3 ml soln.)}$$

$$\text{Mass per mL soln.} = M_{\text{total}} - M_{\text{dye}} = 0.037 - (1.72 \times 10^{-3}) = 0.035 \text{ mg} = M_{\text{SiNPs}}$$

$$\text{So No. of particles per mL soln.} = M_{\text{SiNPs}} / M_{\text{SiNP}} = 5.22 \times 10^{14}$$

*No. of dye molecules:*

$$M_{\text{dye}} = 1.73 \times 10^{-6} \text{ g/mL}$$

$$\text{So: } n = \text{mass} / \text{Mol. mass} = (1.73 \times 10^{-6}) / 617.34 = 2.8 \times 10^{-9}$$

$$\text{No. dye molecules in 1 mL} = n \times N_A = (2.8 \times 10^{-9}) \times (6.022 \times 10^{23}) = 1.68 \times 10^{15}$$

Number of dye molecules per particle:

$$5.22 \times 10^{14} \text{ particles per mL}$$

$$1.68 \times 10^{15} \text{ dye molecules per mL}$$

*So molecules per particle*

$$= \text{molecules per mL} / \text{particles per mL}$$

$$= 3 \text{ dye molecules per particle}$$

**Equation 4.1:** Calculation of the number of Cy5 dye molecules per Si NP

### Si NPs-Cy5-sugar

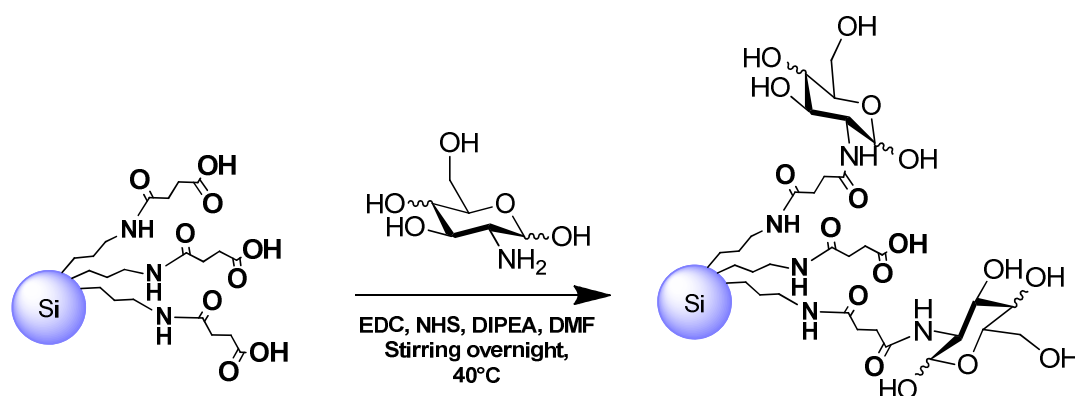


**Figure 4.21:** Coupling of Si NPs-COOH with D-(+)-glucosamine (Si NPs-sugar)

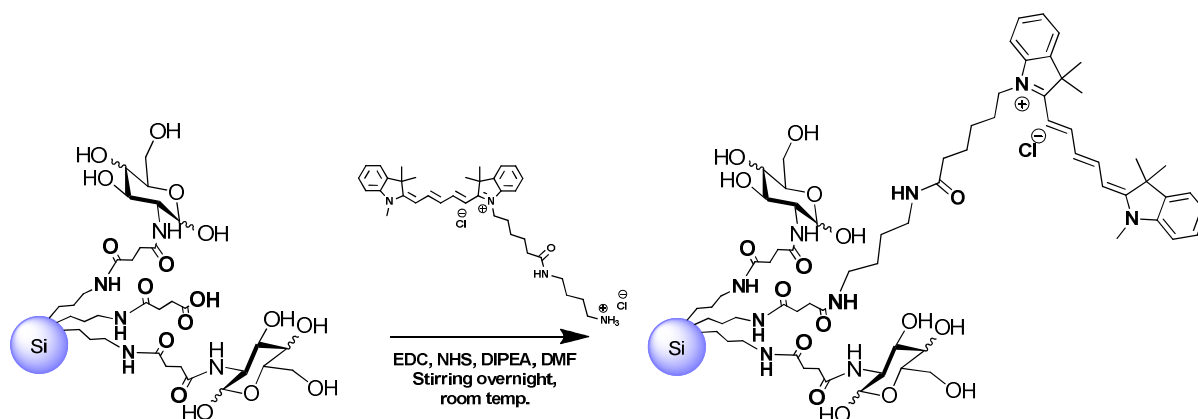


**Figure 4.22:** Coupling of Si NPs-sugar with Cy5 (Si NPs-Cy5-sugar)

The dual functionalised probe (Si NPs-Cy5-sugar) was characterised by the same techniques as the Si NPs-Cy5. The absorption and emission spectra again show that the dominant photophysical characteristic of the system becomes the red emissive Cy5 dye. The photoactive Si NPs can once again still be observed with the absorption band below 300 nm and the relatively weak emission band centred at  $\lambda = 500$  nm in the emission spectrum, showing that the particles are in the system with the dye.

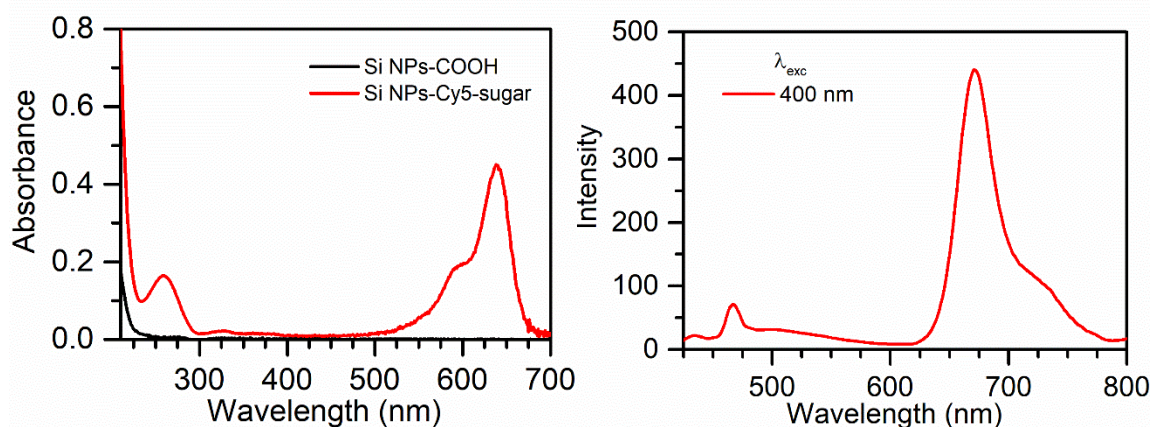


**Figure 4.23:** (Left) UV-Vis absorption spectra of Si NPs-COOH and Si NPs-Cy5-sugar. (Right) Emission spectrum of Si NPs-Cy5-sugar

The remaining photophysical data of excited state lifetime and quantum yield of the system are displayed in table 4.5.

	Lifetime (ns) <sup>a,b</sup>	Lifetime (ns) <sup>a,c</sup>	Q.Y. (%) <sup>d</sup>
Si NPs-Cy5	8.7 (100%)	0.94 (100%)	18 (Cy5) 2 (Si NPs)

**Table 4.5:** Photophysical data for Si NPs-Cy5-sugar. (a.  $\lambda_{exc} = 375$  nm b.  $\lambda_{em} = 450$  nm c.  $\lambda_{em} = 668$  nm d. Measurement performed using integrating sphere)

Information regarding the chemical bonds present was gathered by FT-IR spectroscopy. The spectrum was measured via an ATR attachment, using the same preparation method as Si NPs-Cy5. Similar signals are present when comparing to the former spectrum. The broad signal at  $3314\text{ cm}^{-1}$  is weaker than that for Si NPs-Cy5 and also broader at the peak due to the presence of the O-H bonds on the attached glucose molecules, which could also be responsible for the signal. A similar evaluation could be made of the signal at  $1454\text{ cm}^{-1}$ .

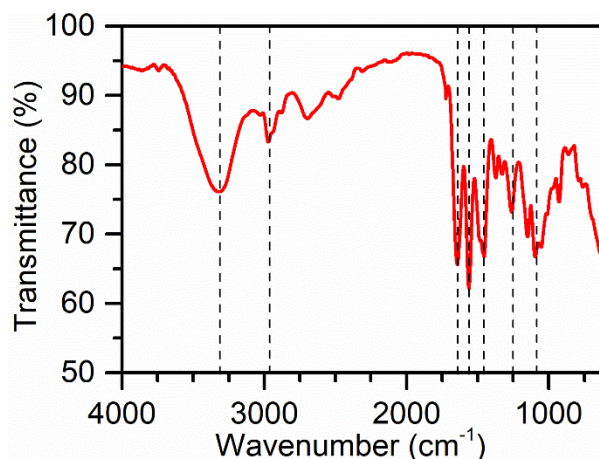


**Figure 4.24:** FT-IR spectrum of Si NPs-Cy5-sugar

Signal	Wavenumber (cm <sup>-1</sup> )
O—H (carboxylic acid)	3314
C—H	2971
C=O (amide)	1643
C—H	1560
O—H (carboxylic acid)	1454
C—O	1259
C—N	1096

**Table 4.6:** FT-IR spectral data of Si NPs-Cy5-sugar

Size and monodispersity of the functionalised Si NPs were assessed by means of TEM as shown in figure 4.25 below. The presence of a larger amount of organic material on the surface of the Si NPs in the form of the attached sugar in addition to the dye meant that only lower resolution images could be obtained where the particles could be visualised, due to the deposition of advantageous carbon at higher magnifications. A relatively monodisperse system could be observed however, with the average size of  $3.8 \pm 0.7$  nm retained. The Si NPs used to synthesise both samples were from the same batch, so at least a similar size could be expected.



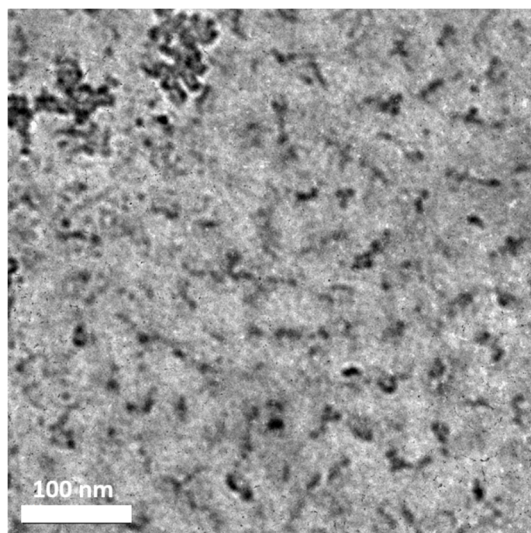


**Figure 4.25:** TEM micrograph of Si NPs-Cy5-sugar

The estimative quantification of coupled molecules was carried out using the same method as the previous sample. However, because the glucose is not photoactive, it had to be quantified in a different way. A recent paper from our group reported a method for quantifying the amount of attached long-chain sugar molecules to Si NPs by using  $^1\text{H}$  NMR<sup>[22]</sup>. Here, a known amount of particles are measured together with a known amount of chloroform ( $\text{CHCl}_3$ ) added as a standard. Taking data from the UV-vis absorption spectrum of the sample and the average size of the particles found through TEM analysis allows an estimate for the number of dye molecules per particle to be calculated. Using ratiometric absorbance and the workings of the equation below, a value for the number of dye molecules can be calculated. The integral of the lone proton in  $\text{CHCl}_3$  can be compared with the integral of the peak corresponding to the proton on the C1 position of the glucose can be used to calculate the number of moles and thereafter, the mass of glucose molecules in the amount of sample measured. This can then be used to make the estimative calculation.

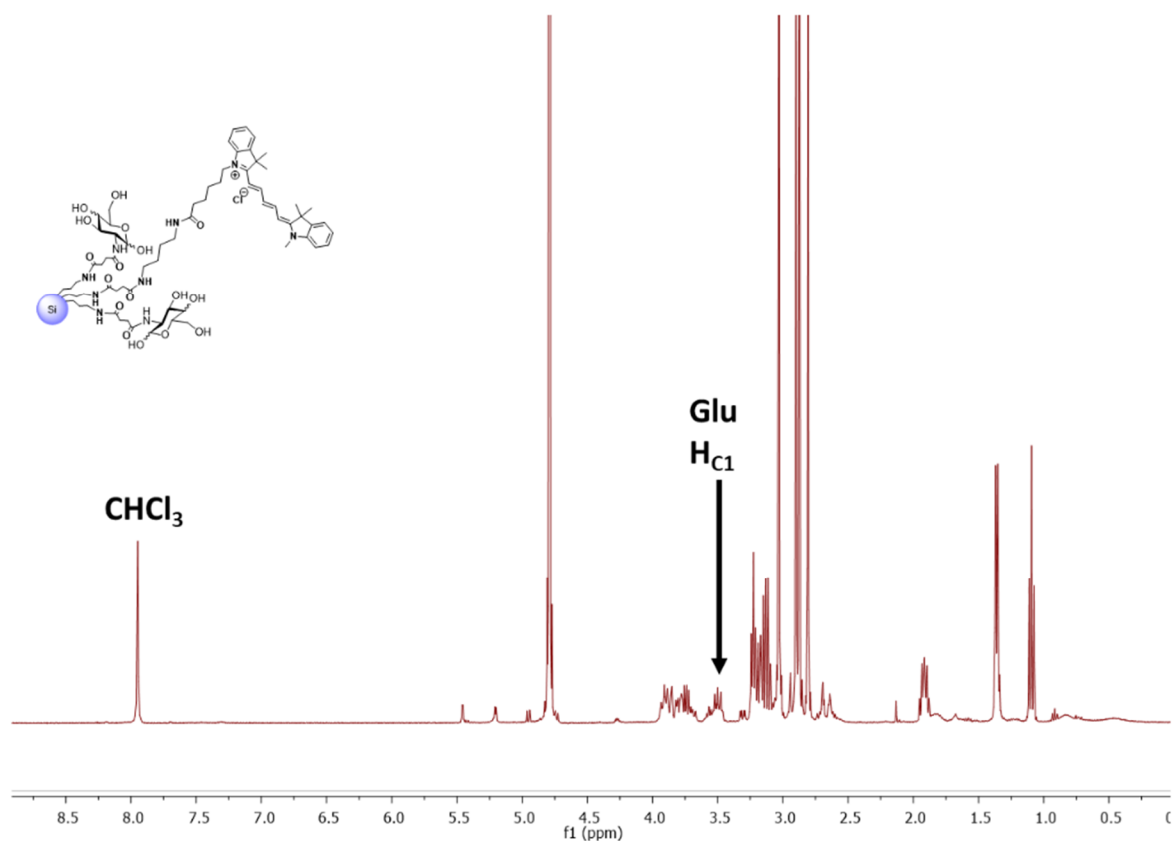


**Figure 4.26:**  $^1\text{H}$  NMR spectrum of Si NPs-Cy5-sugar indicating positions of peaks for chloroform and the proton on the C1 carbon of the attached glucose

### *Cy5 & glucose grafting*

*Mol mass (minus  $\text{H}^+$ ,  $\text{Cl}^-$ ) = 617.34 g/mol*

*$\epsilon = 250000 \text{ dm}^3 \text{ mol}^{-1} \text{ cm}^{-1}$*

*For SiNPs grafted with Glc and Cy5, max abs. at 638 nm =  $A = 0.45$*

*Therefore:  $c = A / \epsilon l = 0.45 / (250000 \times 1) = 1.8 \times 10^{-6} \text{ mol} / \text{dm}^3$*

*So  $n = cv ((1.8 \times 10^{-6}) \times (3 \times 10^{-3})) = 5.4 \times 10^{-9} \text{ mol in 3 mL}$*

*(Measured solution approx. 0.25 mg of SiNPs Glc Cy5)*

*Mass =  $n \times \text{Mol mass} = (5.4 \times 10^{-9}) \times 617.34 = 3.33 \times 10^{-6} \text{ g} = 3.33 \times 10^{-3} \text{ mg dye in 3 mL}$*

*(So in 0.25 mg of SiNPs-Cy5-sugar  $\rightarrow$  from 35.5  $\mu\text{l}$  of stock sample in 3 mL water)*

*So mass S-Cy 5 per mL =  $3.33 \times 10^{-3} / 3 = 1.11 \times 10^{-3} \text{ g/mL} = M_{\text{dye}}$*

*Mass of SiNPs:*

*One SiNP:*

*Diameter = 3.8 nm*

*Vol (V) = (4/3) π (1.9 × 10<sup>-9</sup>)<sup>3</sup> = 2.87 × 10<sup>-26</sup> m<sup>3</sup> = 2.87 × 10<sup>-20</sup> cm<sup>3</sup>*

*Density (D) = 2.33 g/cm<sup>3</sup> (silicon)*

*Mass of one NP (M = V × D) = 6.7 × 10<sup>-20</sup> g = 6.7 × 10<sup>-17</sup> mg = M<sub>SiNP</sub>*

*No. of SiNPs*

*Total conc. of SiNPs-Cy5-sugar in measured solution = 0.0833 mg/mL (0.25 mg in 3 ml soln.)*

*Mass Glc (calc from <sup>1</sup>H NMR) = 0.06 mg / 4 = 0.015 mg (in 0.25 mg sample)*

*0.015 / 3 = 5 × 10<sup>-3</sup> mg (mass per ml of measured sample) = M<sub>Glc</sub>*

*Mass per mL soln. = M<sub>total</sub> - (M<sub>dye</sub> + M<sub>Glc</sub>) = 0.083 - ((1.11 × 10<sup>-3</sup>) + (5 × 10<sup>-3</sup>)) = 0.077 mg = M<sub>SiNPs</sub>*

*So no. of particles per mL soln. = M<sub>SiNPs</sub> / M<sub>SiNP</sub> = 1.153 × 10<sup>15</sup>*

*No. of dye molecules:*

*M<sub>dye</sub> = 1.11 × 10<sup>-6</sup> g/mL*

*So: n = mass / Mol. mass = (1.11 × 10<sup>-6</sup>) / 617.34 = 1.8 × 10<sup>-9</sup>*

*No. dye molecules in 1 mL = n × N<sub>A</sub> = (1.8 × 10<sup>-9</sup>) × (6.022 × 10<sup>23</sup>) = 1.083 × 10<sup>15</sup>*

*No. of Glucose molecules:*

*M<sub>Glc</sub> = 0.015 × 10<sup>-3</sup> g/mL*

*So: n = mass / Mol. mass = (0.015 × 10<sup>-3</sup>) / 215.63 = 6.956 × 10<sup>-8</sup>*

*No. dye molecules in 1 mL = n × N<sub>A</sub> = (6.956 × 10<sup>-8</sup>) × (6.022 × 10<sup>23</sup>) = 4.189 × 10<sup>16</sup>*

*Number of dye and glucose molecules per particle:*

*1.153 × 10<sup>15</sup> particles per mL*

*1.083 × 10<sup>15</sup> dye molecules per mL*

*4.189 × 10<sup>16</sup> Glc molecules per mL*

*So molecules per particle*

*= molecules per mL / particles per mL*

*= 1 dye molecule per particle*

*= 36 Glc molecules per particle*

**Equation 4.2:** Calculation of the number of Cy5 and glucose molecules per Si NP

### 4.3.2 In vivo bio-distribution studies

Firstly, the radiant efficiencies of both formulations of Si NP were evaluated as shown in figure 4.27 below.

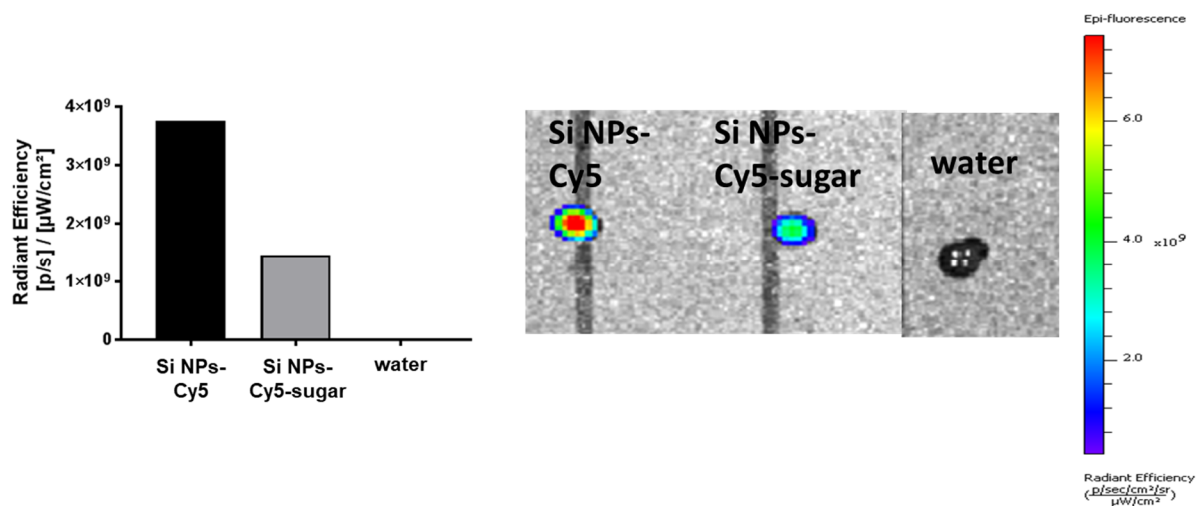


**Figure 4.26:** Fluorescence signals associated with Si NPs-Cy5 and Si NPs-Cy5-sugar from drops of suspensions (0.7 mg/ml, 4 μl/drop). Water was used as control.

The Si NPs-Cy5 had a higher fluorescence signal than the Si NPs-Cy5-sugar by virtue of the higher grafting of Cy5 (calculated in the previous section). Since the intensity is different, all values for the tests were normalised according to the Si NPs-Cy5 fluorescent intensity (i.e, the ratio between the two is 2.7 times, therefore the values for the Si NPs-Cy5-sugar were multiplied by 2.7) and then compared to non-treated (set as NT= 1). This correction has been applied in all of the following quantification measurements to the same extent.

Mice were administered an intravenous injection of Si NPs with a dose of 7 mg/kg. *In vivo* analysis was conducted at 1 and 4 hours post injection. After 4 hours, the mice were sacrificed and organs were collected for *ex vivo* analysis.

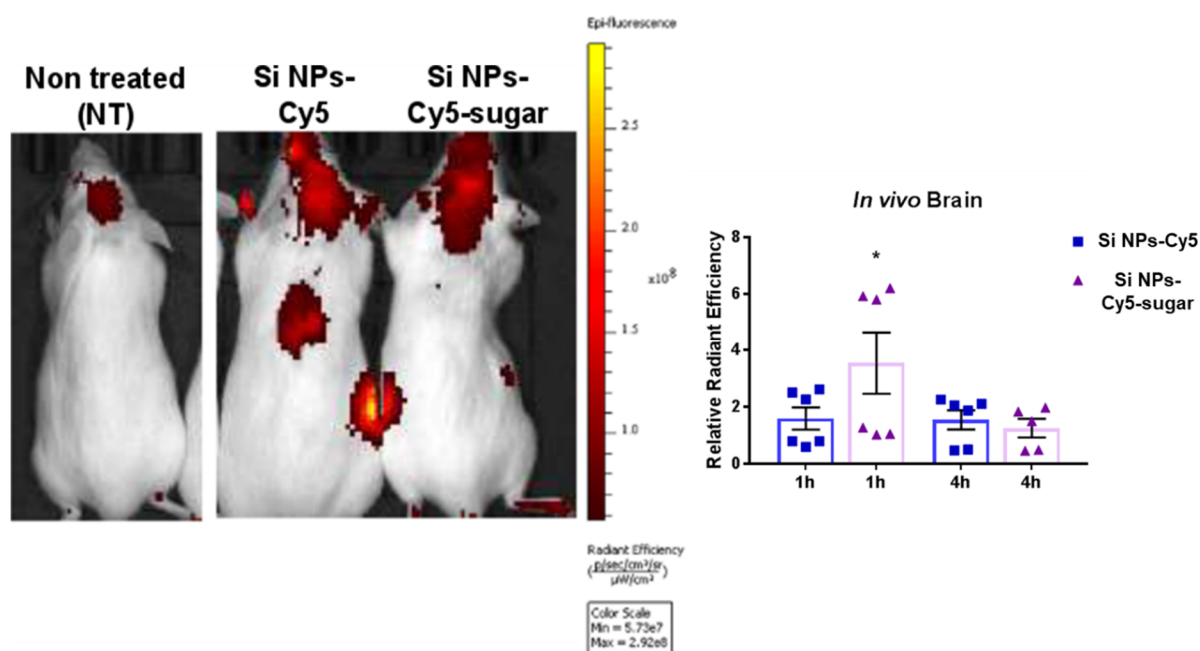


**Figure 4.27:** (Left) Fluorescence images of non-treated and treated mice at 1 hr post injection. (Right) Quantification of *in vivo* optical imaging signals related to the brain region of Si NPs-Cy5 and Si NPs-Cy5-sugar treated mice. Data are reported as mean  $\pm$  standard error (SE). The analysis was performed by One-way ANOVA and Bonferroni post hoc test (\* $p < 0.05$  vs. NT). Each value is normalised to non-treated mice (NT = 1)

A slight increase of the fluorescence signal related to the Cy5 on NPs was observed for both formulations. In particular, a significant increase of the signal related to the Si NPs-Cy5-sugar was observed at 1h post injection compared to control group. This could be suggestive of the Si NPs-Cy5-sugar having a greater uptake through the BBB and an efficient clearance at 4 hrs, both facilitated via the glucose solute carriers in the BBB. However, there is a high variability between the mice, with an equal number showing a low fluorescence signal, so this cannot be concluded.

In order to better elucidate the BBB passage of the Si NPs, *ex vivo* analysis using IVIS Lumina and ICP-AES were also carried out. *Ex vivo* imaging and the ICP-AES were performed on brain tissue at the last time point (4h post injection).

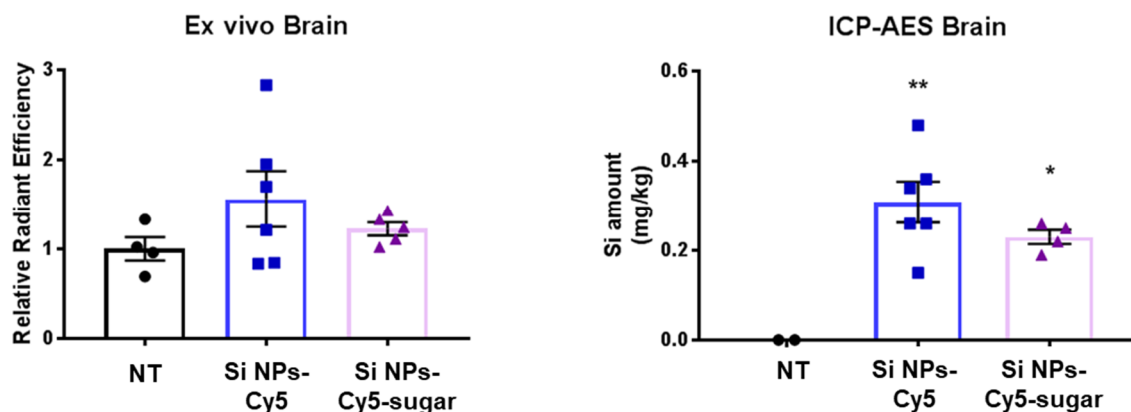


**Figure 4.28:** (Left) Quantification of *ex vivo* optical imaging signals related to the brain of Si NPs-Cy5 and Si NPs-Cy5-sugar treated mice. Data are reported as mean  $\pm$  SE. Values to NT =1. (Right) Quantification of Si amount in brain of 5nm and 5 nm sugar treated mice. Data are reported as mean  $\pm$  SE. Analysis performed by One-way ANOVA and Bonferroni post hoc test (\* $p$ <0.05, \*\* $p$ <0.005 vs. NT). Values normalised to NT =1.

The quantity of silicon in the brain of Si NPs-Cy5 and Si NPs-Cy5-sugar treated mice was measured by ICP-AES. As shown, both formulations are able to cross the BBB, but a higher accumulation of Si was measured in Si NPs-Cy5 treated mice than Si NPs-Cy5-sugar treated mice. It can be said that the sugar decoration on the Si NP therefore does not strongly influence the passage across the BBB. This data is in accordance with *ex vivo* analysis on brain, where the same pattern was observed.

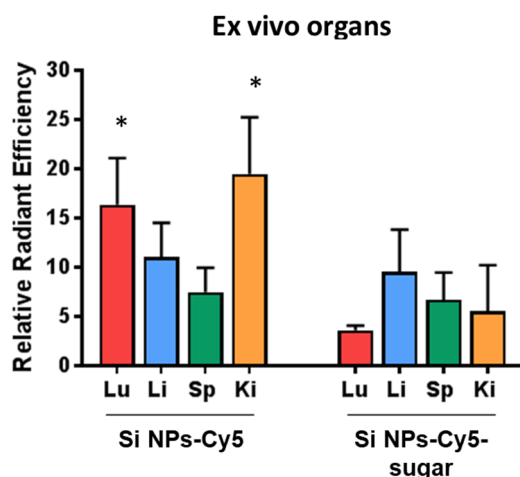


**Figure 4.29:** Quantification of *ex vivo* optical imaging signals of excised organs (Lu: lung, Li: liver, Sp: spleen, Ki: kidney) from mice sacrificed 4 hours after treatment. Data are reported as mean  $\pm$  SE. The analysis was performed by One-way ANOVA and Bonferroni post hoc test (\* $p$ <0.05, vs. NT). Values normalised to NT =1

As shown in figure 4.29, both formulations of Si NPs accumulate in the collected organs. However, Si NPs-Cy5 show a higher fluorescence signal than Si NPs-Cy5-sugar in the lungs and kidneys. Taking account of previous studies also, it can be said that Si NPs have a significant tropism and accumulation into these organs without the sugar coating.

## 4.4 Conclusions

Si NPs produced through both the microemulsion and hydrothermal methods have been successfully functionalised to create different systems that have been tested *in vivo* to identify their behaviour and imaging capabilities. Microemulsion Si NPs with amine terminations were shown to not be extremely toxic to cells at low concentrations, while HT Si NPs retained a high cell viability even at high concentrations.

Through the coupling of the Si NPs to a [<sup>64</sup>Cu]Cu-NOTA complex for *in vivo* PET, it is shown that the Si NPs obtain a whole body distribution in mice at 5 minutes post-administration. Near complete localization of the particles into the bladder and intestines is observed at 1 hr post administration, from where the Si NPs can be excreted via the renal pathway. This observation is supported by *ex vivo* fluorescence imaging of organs, which also show a high signal in the urine after 1 hr.

Compared to current benchmark radiopharmaceutical used for routine PET evaluation in the clinic, [<sup>18</sup>F]-labeled 2-fluorodeoxyglucose (FDG)<sup>[23]</sup>, the radiolabeled Si NPs do have some performance issues that present a barrier to them achieving a similar standing for application. Firstly, the larger size of the Si NPs compared to the molecular FDG leads to differences in physiological activity, particularly with regards to circulation and metabolism following intravenous injection. With its glucose basis, FDG is readily circulated to all organs of the body after administration<sup>[24]</sup>, similar to the Si NPs. However, interactions with cells that are exclusive to glucose allow the activity levels of [<sup>18</sup>F] to steadily increase in essential organs, including the brain, after administration, with the peak said to occur at about 90 mins post administration<sup>[25]</sup>. This is more practical, as it provides ample time between the administration of the molecule and the imaging process for setting up the patient in the scanner, in contrast to the developed Si NP model, where after the same time period, activity is only present in the excretory organs. Another advantage of FDG is the shorter half-life of the [<sup>18</sup>F] ion at 1.8 hours<sup>[26]</sup> compared to that of [<sup>64</sup>Cu]<sup>[23]</sup> and its subsequent decay into lighter isotopes. With these

points in mind, while the Si NPs may struggle to find use as PET radiopharmaceuticals in the clinic, this study has provided a detailed insight into the nature of their circulation, localisation and clearance. These findings could prove useful in the further development of Si NPs for different multimodal proposes, for example as theranostic materials<sup>[27]</sup>.

Studies of Si NPs both with and without a coupled sugar moiety have shown that the same, whole body distribution of the particles is maintained regardless of the surface coating. In addition to this, contrary to the initial hypothesis, it seems that a sugar functionality does not have a significant effect on the passage of the Si NPs through the BBB. The Si NPs due to their size, are more than likely transported across the endothelial cells via a passive mechanism, with the possible function of the P-glycoproteins in the endothelial layer<sup>[28]</sup> causing an efflux transport of the more readily recognised glucose coupled Si NPs from the inside of the barrier. This could be an explanation for the notable drop in the signal of the glucose coupled Si NPs from 1hr to 4 hrs.

## 4.5 Experimental Section

### 4.5.1 General information

#### *Publication*

My personal contribution to the published work covered in section 4.2 was the synthesis and characterisation of the Si NPs used in the study. Typical data regarding this can be found in chapters 2 and 3.

#### *Materials*

All solvents and reagents were purchased from Sigma-Aldrich, Fisher Scientific or Alfa Aesar and used without further purification unless stated. Sephadex LH-20 was purchased from GE Healthcare Europe GmbH. DI water was prepared using a Milli-Q system by Millipore.

### 4.5.2 Synthetic procedures

#### *Coupling of SCN-Bn-NOTA to HT Si NPs and microemulsion SiNPs*

Coupling reactions were carried out by dispersing 1 mg of amine-terminated Si NPs (microemulsion Si NPs or HT Si NPs) in 150  $\mu$ l of deionized water and placing the solution in a 1.5 ml low protein binding Eppendorf-tube. A specific amount of SCN-Bn- NOTA (0.1, 0.2, 0.4, and 0.8  $\mu$ mol per mg of nanoparticles) was dissolved in 100  $\mu$ L of deionized water and added to the dispersion of NPs. The final dispersion was then shaken on a thermo-mixer



(Eppendorf) at 750 rpm for 16 hrs at room temperature. All samples prepared for in vivo experiments were purified by dialysis against deionized water (MWCO 0.5–1 kDa, Spectra Por Float-A-Lyzer G2, 1 mL). [N. Licciardello, S. Hunoldt, R. Bergmann, G. Singh, C. Mamat, A. Faramus, J. L. Z. Ddungu, S. Silvestrini, M. Maggini, L. De Cola, et al., *Nanoscale* **2018**, *10*, 9880–9891]-Reproduced by permission of The Royal Society of Chemistry

#### *Butylene terminated Si NPs*

This procedure follows that reported in<sup>[19]</sup>. To a suspension of Mg<sub>2</sub>Si (0.6g, 7.9 mmol) in distilled octane (200 mL) bromine (2.0 mL, 77 mmol) was added via syringe. The suspension was stirred for 2 h at room temperature, during which the red-brown colour of the bromine disappeared completely. The suspension was heated to reflux for 72 h, with additional 1 mL (39 mmol) portions of bromine being added after 24 h, 36 h and 48 h. The suspension was kept under argon, while the solvent and bromooctane were removed by distillation. To the flask, dry THF (50 mL) was added, and the suspension was cooled on ice. To Mg curls (1.24 g, 52 mmol) under argon atmosphere, a solution of 4-bromo-1-butene (4 mL, 40 mmol) in freshly distilled THF (30 mL) was added dropwise over 15 minutes. An short burst of light heat was used to initiate the reaction. After addition of the 4-bromo-1-butene, the mixture was stirred for an additional 3 h. The solution of 3-butenylmagnesium bromide was added slowly via a cannula to the bromine-terminated Si NPs. The reaction mixture was then removed from the ice and stirred overnight. NH<sub>4</sub>Cl (10 mL) was added dropwise to quench the excess of 3-butenylmagnesium bromide. The mixture was stirred for 1 h, then filtered and the filtrate was subsequently extracted with ethyl acetate (3x), aqueous HCl (2M) (3x) and distilled water until the pH of the solution reached 7 (16x). The organic layer was dried over MgSO<sub>4</sub> and the solvent then removed *in vacuo* to yield 208 mg SiNPs as an orange-brown oil.

#### *Carboxyl-terminated Si NPs*

Butylene-terminated SiNPs (208 mg from prior synthesis) were dissolved in ethyl acetate (6 mL). Acetonitrile (6 mL) was then added to the mixture with stirring, which formed a yellow precipitate. Sodium periodate (877 mg, 4.1 mmol) dissolved in distilled water (9 mL) was then added to the reaction mixture and a brown precipitate was formed. Ruthenium trichloride (5 mg, 0.02 mmol) was stirred into the mixture and the flask was sealed, with the reaction left for 3½ h. Water (15 mL) was then added to dissolve the yellow precipitate and the mixture was extracted with ethyl acetate (6x) and water (2x). The combined organic phases were dried over Na<sub>2</sub>SO<sub>4</sub> and the solvent then removed *in vacuo*. The yellow-orange residue of SiNPs was dissolved in MeOH and further purified by elution onto a Sephadex column with methanol as

the eluting solvent three times. UV-emissive fractions were combined and concentrated *in vacuo* to yield 88 mg carboxyl-terminated SiNPs as a yellow solid.

#### *Si NPs-COOH from microemulsion Si NPs*

This procedure follows a slight modification of a reported method<sup>[21]</sup>. To a 10 ml flask was added microemulsion Si NPs (15 mg, 121.5  $\mu\text{mol}$   $\text{NH}_2$  in 2 ml dry DMF) under Ar. *N,N*-diisopropylethanamine (10  $\mu\text{l}$ ) was then added with stirring to increase the pH of the solution to 9. Succinic anhydride (243 mg, 2.42 mmol) was dissolved in 3 ml dry DMF and slowly added to the stirring solution in the flask. The solution was then stirred in the dark at 40°C under Ar for 16 hrs. After concentrating the solution in *vacuo*, the crude product was re-dispersed in methanol and purified by size-exclusion chromatography (Sephadex LH-20). Fractions exhibiting bright blue luminescence were combined and the solvent was removed in *vacuo* to obtain Si NPs-COOH as a yellow wax.

#### *Si NPs-Cy5*

To a 10 ml flask was added Si NPs-COOH (15 mg in 2 ml dry DMF) under Ar. *N,N*-diisopropylethanamine (10  $\mu\text{l}$ ) was then added with stirring to increase the pH of the solution to 9. 1-Ethyl-3-(3-dimethylaminopropyl)carbodiimide hydrochloride (7.3 mg, 38.1  $\mu\text{mol}$ ) and *N*-Hydroxysuccinimide (4.4 mg, 38.2  $\mu\text{mol}$ ) were dissolved in 1 ml dry DMF and added to the stirring solution in the flask. Then cyanine 5 amine (5 mg, 7.65  $\mu\text{mol}$ ) was dissolved in 2 ml dry DMF and slowly added to the stirring solution in the flask. The solution was then stirred in the dark at room temperature under Ar for 16 hrs. After concentrating the solution in *vacuo*, the crude product was re-dispersed in methanol and purified by size-exclusion chromatography (Sephadex LH-20). Molecular impurities and unbound dye were removed in the final fractions as monitored by thin-layer chromatography. Fractions containing the final product were combined, the solvent removed and the blue residue redispersed in water. The final product was a deep blue dispersion of Si NPs-Cy5 in water.

#### *Si NPs-Cy5-sugar*

To a 10 ml flask was added Si NPs-Cy5 (10 mg in 1 ml dry DMF) under Ar. *N,N*-diisopropylethanamine (10  $\mu\text{l}$ ) was then added with stirring to increase the pH of the solution to 9. 1-Ethyl-3-(3-dimethylaminopropyl)carbodiimide hydrochloride (38 mg, 0.2 mmol) and *N*-Hydroxysuccinimide (23 mg, 0.2 mmol) were dissolved in 2 ml dry DMF and added to the stirring solution in the flask. Then D-(+)-glucosamine (21 mg, 0.1 mmol) was dissolved in 2 ml dry DMF and slowly added to the stirring solution in the flask. The solution was then stirred

in the dark at room temperature under Ar for 16 hrs. After concentrating the solution in vacuo, the crude product was re-dispersed in methanol and purified by size-exclusion chromatography (Sephadex LH-20). Molecular impurities were removed in the final fractions as monitored by thin-layer chromatography. Fractions containing the final product were combined, the solvent removed and the blue residue redispersed in water. The final product was a blue dispersion of Si NPs-Cy5-sugar in water.

#### *Radiolabelling experiments*

The production of  $^{64}\text{Cu}$  was performed at a Cyclone® 18/9 (Helmholtz-Zentrum Dresden-Rossendorf). For the  $^{64}\text{Ni}(p,n)^{64}\text{Cu}$  nuclear reaction, 15 MeV protons with a beam current of 12  $\mu\text{A}$  for 150 min were used. The yields of the nuclear reaction  $^{64}\text{Ni}(p,n)^{64}\text{Cu}$  were 3.6–5.2 GBq [at the end of bombardment (EOB)] with molar activities of 150–250 GBq  $\mu\text{mol}^{-1}$  Cu diluted in HCl (10 mM). An aliquot of [ $^{64}\text{Cu}$ ]  $\text{CuCl}_2$  solution (20–100 MBq) was buffered with MES (2-(N-morpholino) ethanesulfonic acid)/NaOH-buffer (0.1 M; pH 6). Typically, a specific amount of nanoparticles, up to 10  $\mu\text{g}$ , was mixed in a 1.5 mL low protein binding Eppendorf-tube with a specific aliquot of [ $^{64}\text{Cu}$ ]  $\text{CuCl}_2$ -solution (varying up to 40 MBq) and addition of MES/NaOH buffer (0.1 M; pH 6) up to a final volume in the range of 150–200  $\mu\text{L}$ . The particles were labelled by means of mechanical shaking for 30 min at 25 °C. The specific activity of the nanoparticles (0.1  $\mu\text{mol}$  NOTA per mg NP) was  $\sim 4$  GBq  $\text{mg}^{-1}$  NPs. To check the full labeling, 2 nmol EDTA was added to a 5  $\mu\text{L}$  aliquot of the solution and the labeling process of the nanoparticles ( $R_f = 0$ ) was monitored by radio-TLC on iTLC-SA plates (instant TLC medium impregnated with salicylic acid, Agilent Technology) using 0.9% NaCl in H<sub>2</sub>O as mobile phase. As control, separate radio-TLC analysis of [ $^{64}\text{Cu}$ ]Cu-EDTA ( $R_f = 0.9$ ) was performed in the same mobile phase. Evaluation of radio-TLC was carried out using a radioactivity thin layer analyzer (Rita Star, Raytest, Germany).  $^{64}\text{Cu}$ -labeled nanoparticles were challenged with a 10.000-fold excess of EDTA and a 1.000-fold TETA (24 h, at 38 °C). Radio-iTLC analysis (see above) was used to monitor the stability of  $^{64}\text{Cu}$ -labeled NPs ( $^{64}\text{Cu}$ -NPs,  $R_f = 0$ ; [ $^{64}\text{Cu}$ ]Cu-EDTA and [ $^{64}\text{Cu}$ ]Cu-TETA,  $R_f = 0.9$ ). 1-Octanol–water distribution coefficients were determined for the  $^{64}\text{Cu}$ -labeled nanoparticles. Aliquots of radiolabeled nanoparticles (50  $\mu\text{L}$  with a concentration of 1  $\mu\text{g}$  NPs  $\text{mL}^{-1}$ ) were added to 450  $\mu\text{L}$  of 0.05 M of HEPES-NaOH buffer at pH 7.4 and then 0.5 mL 1-octanol was added. The distribution experiments were carried out at room temperature in microcentrifuge tubes (2  $\text{cm}^3$ ) with mechanical shaking for 30 min. All samples were centrifuged and the phases then separated. The copper concentration in both phases was determined radiometrically using a  $\gamma$ -radiation gamma counter 1480,

Wizard 3, PerkinElmer. The results are average values of one experiment with repeat determination.

#### 4.5.3 *In vitro* assessment of nanotoxicity

All cell culture reagents were purchased from Biochrom AG and Sigma-Aldrich unless otherwise specified. Cell culture flasks, dishes and plates were supplied by Greiner Bio-One GmbH. The human embryonic kidney cell line HEK293 (DSMZ no.: ACC 305) was cultured as previously reported<sup>[23], [24], [25]</sup>. The cell line was confirmed to be mycoplasma-negative and was tested monthly. To assess cell viability following nanoparticle exposure, HEK293 cells were seeded in 96-well cell culture plates (~5000 cells per 0.1 mL per well) and were grown for 24 h. The cell viability was measured using the CellTiter 96® AQueous One Solution Cell Proliferation Assay (MTS, Promega Corporation) according to the manufacturer's instructions. With this colorimetric assay, the activity of cellular enzymes is determined, since these proteins reduce the tetrazolium compound 3-(4,5-dimethylthiazol-2-yl)-5-(3-carboxymethoxy-phenyl)-2-(4-sulfophenyl)-2H-tetrazolium (MTS) to purple-colored formazan, which can be quantified by recording the absorbance at 490 nm.

#### 4.5.4 Animal experiments

##### *PET biodistribution studies*

Animal experiments were carried out according to the guidelines of the German Regulations for Animal Welfare. The local Ethical Committee for Animal Experiments approved the animal facilities and the protocol according to institutional guidelines and the German animal welfare regulations (reference numbers 24D-9168.11-4/2007-2 and 24-9168.21-4/2004-1). Male Wistar rats (Harlan Winkelmann GmbH, Borchon, Germany) between 7 and 9 weeks of age and female NMRI nu/nu mice (aged 7–14 weeks; Technische Universität Dresden, Oncoray, Germany) were housed in an Animal Biosafety Level 1 (ABSL-1) acclimatized facility with a temperature of  $22 \pm 2$  °C and humidity of  $55 \pm 5\%$ . For PET experiments in tumorbearing mice, about  $2 \times 10^6$  A431 cells (ATCC number: CRL-1555) were injected subcutaneously in the back or right hind leg of NMRI nu/nu mice according to the protocol published elsewhere<sup>[26]</sup>. Animals were kept under a 12 h light cycle in temperature controlled airflow cabinets ( $27 \pm 1$  °C) and had free access to standard pellet feed and water.

Two groups of four rats each (5 and 60 min) were intravenously injected into a lateral tail vein with 0.5–5.0 MBq of <sup>64</sup>Cu-labeled nanoparticles, which were dissolved in 0.5 mL of electrolyte solution E-153 (Serumwerk Bernburg, Germany) at pH 7.2. The molar activity ranged from 5.0 to 30 GBq μmol<sup>-1</sup> at the time of injection. Animals were sacrificed at 5 and 60 min post injection. Blood and major organs were collected, weighed, and counted in a Wallac WIZARD automatic γ-counter (PerkinElmer, Germany). The activity of the tissue samples was decay-corrected and calibrated by comparing the counts in tissue with the counts in aliquots of the injected particles that were measured in the γ-counter at the same time.

The activity amount in the selected tissues and organs was expressed as percent of injected dose (% ID). The activity concentration in the biodistribution measurements were calculated as SUV [SUV = (activity/g tissue)/(injected activity/body weight)] and expressed as means ± standard deviation (mean ± SD) for each group of four animals.

#### *Blood-Brain-Barrier studies*

Female CD1 mice, 5–6 weeks old, were obtained from Harlan Laboratories (Bresso, Italy). Mice were maintained under specific pathogen free condition in the Institute's Animal Care Facilities; they were regularly checked by a certified veterinarian who is responsible for health monitoring, animal welfare supervision, and experimental protocol revision. Procedures involving animals and their care were conducted in conformity with the institutional guidelines at the Institute for Pharmacological Research “Mario Negri” IRCCS in compliance with national (Legislative Decree nr 26, March 4, 2014; Authorization n 19/2008-A issued March 6, 2008 by the Italian Ministry of Health) and international laws and policies (EEC Council Directive 2010/63, August 6, 2013; Standard for the Care and Use of Laboratory Animals, US National Research Council, Statement of Compliance A5023-01, October 28, 2008). This work was reviewed by of research has been reviewed by IRFMN IRCCS Animal Care and Use Committee (IACUC) and then approved by the Italian “Istituto Superiore di Sanità” (code: 699/2015-PR).

As regards biodistribution study, 16 CD1 mice were enrolled. Mice were intravenously treated with 5nm Silicon NPs-Cy5 (n=6) and 5nm sugar silicon NPs-Cy5 (n=6) at the dose of 7 mg/kg body weight. Four mice were not treated and used as controls.

*In vivo* optical imaging was conducted, on animals anesthetized with a continuous flow of 2% isoflurane/oxygen mixture, at 1h (n=6), 4 h (n=6) after treatment. Fluorescence images were acquired using IVIS<sup>®</sup> Lumina III XRMS imaging system (PerkinElmer). The following

acquisition parameters were used: excitation filter 680 to 740 nm, emission filter 790 nm, exposure time: 2 sec, binning factor 4, and f/stop: 2. Fluorescence analysis of single organs was performed 4 h after NP administration. Brain, lung, liver, spleen and kidney were explanted and imaged for ex-vivo imaging with IVIS<sup>®</sup> Lumina III XRMS. Spectral unmixing, image processing, and analysis were performed using Living Image 4.3.1 software (PerkinElmer).

#### 4.5.5 In vivo small animal positron emission tomography (PET)

The procedures are described in detail elsewhere<sup>[27]</sup>. Rats or mice were anesthetized (desflurane in oxygen/air (30%)), positioned and immobilized prone with their medial axis parallel to the axial axis of the scanners (NanoScan PET/CT, Mediso, microPET<sup>®</sup> P4, Siemens preclinical solutions). The radiotracer was administered intravenously as an infusion using a syringe pump over one minute (Harvard Apparatus, flow rate: injection volume as mL min<sup>-1</sup>) through a needle catheter into a lateral tail vein. The standardized uptake values (SUV) were calculated from the ROI as the ratio of activity concentration (Bq mL<sup>-1</sup>) at time t and injected dose (Bq) at the time of injection (t<sub>0</sub>) divided by body weight (g). For the demonstration of the increasing activity uptake, the early (mid-frame time 3 min post injection) images were subtracted from the late image (mid-frame time 50 min post injection).

## 4.6 References

- [1] P. Sharma, S. Brown, G. Walter, S. Santra, B. Moudgil, *Adv. Colloid Interface Sci.* **2006**, *123–126*, 471–485.
- [2] M. Montalti, A. Cantelli, G. Battistelli, *Chem. Soc. Rev.* **2015**, *44*, 4853–4921.
- [3] R. Bilan, F. Fleury, I. Nabiev, A. Sukhanova, *Bioconjug. Chem.* **2015**, *26*, 609–624.
- [4] J. Liu, F. Erogbogbo, K.-T. Yong, L. Ye, J. Liu, R. Hu, H. Chen, Y. Hu, Y. Yang, J. Yang, et al., *ACS Nano* **2013**, *7*, 7303–7310.
- [5] Y. Zhong, F. Peng, F. Bao, S. Wang, X. Ji, L. Yang, Y. Su, S.-T. Lee, Y. He, *J. Am. Chem. Soc.* **2013**, *135*, 8350–8356.
- [6] M. Rosso-Vasic, E. Spruijt, Z. Popović, K. Overgaag, B. van Lagen, B. Grandidier, D. Vanmaekelbergh, D. Domínguez-Gutiérrez, L. D. Cola, H. Zuilhof, *J. Mater. Chem.* **2009**, *19*, 5926–5933.
- [7] L. Ruizendaal, S. Bhattacharjee, K. Pournazari, M. Rosso-Vasic, L. H. J. de Haan, G. M. Alink, A. T. M. Marcelis, H. Zuilhof, *Nanotoxicology* **2009**, *3*, 339–347.
- [8] S. Bhattacharjee, L. H. de Haan, N. M. Evers, X. Jiang, A. T. Marcelis, H. Zuilhof, I. M. Rietjens, G. M. Alink, *Part. Fibre Toxicol.* **2010**, *7*, 25.
- [9] M. Rudin, R. Weissleder, *Nat. Rev. Drug Discov.* **2003**, *2*, 123–131.
- [10] Y. Zhong, F. Peng, F. Bao, S. Wang, X. Ji, L. Yang, Y. Su, S.-T. Lee, Y. He, *J. Am. Chem. Soc.* **2013**, *135*, 8350–8356.
- [11] S. Bhattacharjee, I. M. C. M. Rietjens, M. P. Singh, T. M. Atkins, T. K. Purkait, Z. Xu, S. Regli, A. Shukaliak, R. J. Clark, B. S. Mitchell, et al., *Nanoscale* **2013**, *5*, 4870–4883.
- [12] K. Zarschler, L. Rocks, N. Licciardello, L. Boselli, E. Polo, K. P. Garcia, L. De Cola, H. Stephan, K. A. Dawson, *Nanomedicine Nanotechnol. Biol. Med.* **2016**, *12*, 1663–1701.
- [13] N. J. Abbott, A. A. K. Patabendige, D. E. M. Dolman, S. R. Yusof, D. J. Begley, *Neurobiol. Dis.* **2010**, *37*, 13–25.
- [14] R. Gromnicova, H. A. Davies, P. Sreekanthreddy, I. A. Romero, T. Lund, I. M. Roitt, J. B. Phillips, D. K. Male, *PLoS ONE* **2013**, *8*, e81043.
- [15] V. T. Marchesi, *Invest. Ophthalmol. Vis. Sci.* **1965**, *4*, 1111–1121.
- [16] D. Baker, D. J. R. Hankey, *Gene Ther.* **2003**, *10*, 844–853.
- [17] F. P. Manfredsson, R. J. Mandel, *Discov. Med.* **2010**, *9*, 204–211.
- [18] P. R. Lockman, M. O. Oyewumi, J. M. Koziara, K. E. Roder, R. J. Mumper, D. D. Allen, *J. Controlled Release* **2003**, *93*, 271–282.

- [19] Q. Liu, S. M. Kauzlarich, *Mater. Sci. Eng. B* **2002**, *96*, 72–75.
- [20] S.-W. Lin, D.-H. Chen, *Small* **2009**, *5*, 72–76.
- [21] Y. Nakahara, K. Machiya, T. Sato, N. T. Nwe, T. Furuike, H. Tamura, K. Kimura, *Chem. Lett.* **2013**, *42*, 498–500.
- [22] C.-H. Lai, J. Hütter, C.-W. Hsu, H. Tanaka, S. Varela-Aramburu, L. De Cola, B. Lепенies, P. H. Seeberger, *Nano Lett.* **2016**, *16*, 807–811.
- [23] M. Shokeen, C. J. Anderson, *Acc. Chem. Res.* **2009**, *42*, 832–841.
- [24] **N.d.**
- [25] M. E. Phelps, S. C. Huang, E. J. Hoffman, C. Selin, L. Sokoloff, D. E. Kuhl, *Ann. Neurol.* **1979**, *6*, 371–388.
- [26] **N.d.**
- [27] J.-H. Park, L. Gu, G. von Maltzahn, E. Ruoslahti, S. N. Bhatia, M. J. Sailor, *Nat. Mater.* **2009**, *8*, 331–336.
- [28] M. Demeule, M. Labelle, A. Régina, F. Berthelet, R. Béliveau, *Biochem. Biophys. Res. Commun.* **2001**, *281*, 827–834.
- [29] K. Pombo-García, K. Zarschler, J. A. Barreto, J. Hesse, L. Spiccia, B. Graham, H. Stephan, *RSC Adv.* **2013**, *3*, 22443–22454.
- [30] K. Pombo-García, S. Weiss, K. Zarschler, C.-S. Ang, R. Hübner, J. Pufe, S. Meister, J. Seidel, J. Pietzsch, L. Spiccia, et al., *ChemNanoMat* **2016**, *2*, 959–971.
- [31] K. Zarschler, K. Prapainop, E. Mahon, L. Rocks, M. Bramini, P. M. Kelly, H. Stephan, K. A. Dawson, *Nanoscale* **2014**, *6*, 6046–6056.
- [32] A. Leonidova, C. Foerster, K. Zarschler, M. Schubert, H.-J. Pietzsch, J. Steinbach, R. Bergmann, N. Metzler-Nolte, H. Stephan, G. Gasser, *Chem. Sci.* **2015**, *6*, 5601–5616.
- [33] M. Ullrich, R. Bergmann, M. Peitzsch, E. F. Zenker, M. Cartellieri, M. Bachmann, M. Ehrhart-Bornstein, N. L. Block, A. V. Schally, G. Eisenhofer, et al., *Theranostics* **2016**, *6*, 650–665.





# Chapter 5

## Metal complex + silicon-based nanoparticles hybrid systems for Electrochemiluminescence applications

**\*The contents of this chapter are partially confidential at the time of writing. As such, structures and names of metal complexes have been simplified.**

### Abstract

Electrochemiluminescence (ECL) is an innovative and useful technique for inducing emission in photoactive species without the need of photo-excitation by incident light. The high sensitivity of the technique allows it to be employed in bioassays for the detection of specific analytes at down to very low concentrations.  $[\text{Ru}(\text{bpy})_3]^{2+}$  derivatives and recently, iridium complexes have been the focus of most works in the field due to their high efficiency. While it is believed that using hybrid systems with nanoparticles could further increase the efficiency, work related to this remains limited in the literature. This chapter details the development of Si NPs coupled to metal complexes for use in ECL applications. Efficiencies of the systems are evaluated with respect to  $[\text{Ru}(\text{bpy})_3]^{2+}$  as a standard.

### 5.1 Introduction

Electrochemiluminescence (ECL) is an extremely sensitive assay that can be applied for detection different biomolecules present in a sample at concentrations even below the picomolar scale. The absence of photo excitation by incident light to create the excited state of a labelled analyte is the key source of the high sensitivity, which lowers background noise, and affords the selective excitation of actice labels<sup>[1],[2]</sup>. The ECL technique requires the use of a active luminophore, with  $[\text{Ru}(\text{bpy})_3]^{2+}$  derivatives being the “gold standard” of the species used in today’s applications and studies. In more recent times though, there have been developments and reports of other cyclometalated complexes based on ruthenium and iridium that have

displayed higher ECL efficiency than those in common use<sup>[3]-[5]</sup>. A recent model where metal complexes are encapsulated in silica nanoparticles has shown that ECL is still observed from the luminophores<sup>[6],[7]</sup>. An interesting observation made is that the silica shell effectively shields the water-insoluble metal complexes from the outside solution, which gives them the ability to be applied in biological systems. However, the encapsulated complexes notably showed weaker emission compared to the simple labels normally used in bio-imaging and the large size of the silica particles at around 30 to 50 nm gave the hybrid system some real disadvantages. A possible method to overcome the issue of low ECL efficiency was developed by Li *et al*<sup>[8]</sup>. In their work, they modified a gold electrode with a magnet, to which the magnetic nanoparticles they employed were attracted and attached onto surface where they then exhibited a high ECL efficiency.

Our approach entails using a different strategy in an attempt to solve the main problems. This involves using ultrasmall nanomaterials (< 5 nm) such as silicon nanoparticles, which present interesting electronic properties<sup>[9]-[12]</sup>. Silicon nanoparticles (Si NPs) have received a lot of attention in recent times due to their inherent photoluminescent properties. Though the origin of the emission remains controversial, the two most generally accepted explanations are the quantum confinement effect and surface states<sup>[13]</sup>. Due to the quantum confinement effect, Si NPs display a bright blue luminescence when below 5 nm in size. Emission can also originate from the surface states caused by the surface modifications and the defect sites inside the nanoparticles. In addition to their photoluminescent properties, the biocompatibility, facility of surface functionalisation and photo-/electrochemical stability grant them great potential for application in various fields.

In this chapter, we focus on the development of novel hybrid systems composed of amine-terminated silicon-based nanoparticles coupled with a ruthenium complex, and in another example with an iridium complex. We chose to use Si NPs synthesised through the microemulsion method exclusively for the basis of the core of the system for two main reasons. Firstly, as the Si NPs formed through the hydrothermal method have been evaluated to be more silica in nature than elemental silicon, it would not be possible to take advantage of the ECL enhancing effects that could occur, as has been reported for semiconductor quantum dots<sup>[14],[15]</sup>. Secondly, it is thought that the smaller size of the microemulsion Si NPs will be beneficial towards their diffusion through the media in the ECL experiment, giving them an inherent ECL enhancement property over the HT Si NPs. The particular ruthenium and iridium complexes as

well as the Si NPs themselves are water soluble and thus create water soluble systems, which is a draw towards their potential common application.

## 5.2 Synthesis of ruthenium complex modified Si NPs

### 5.2.1 Synthesis route

Si NPs synthesised through the microemulsion method were used to prepare the hybrid nanosystem. In a basified (pH ~ 9 using *N,N*-Diisopropylethylamine (DIPEA)), air and water free environment, the Si NPs were coupled to the sulfonated Ru complex through the terminal amine groups and the activated *N*-Hydroxysuccinimide (NHS) ester of the metal complex. A simplified reaction schematic is shown below in figure 5.1.

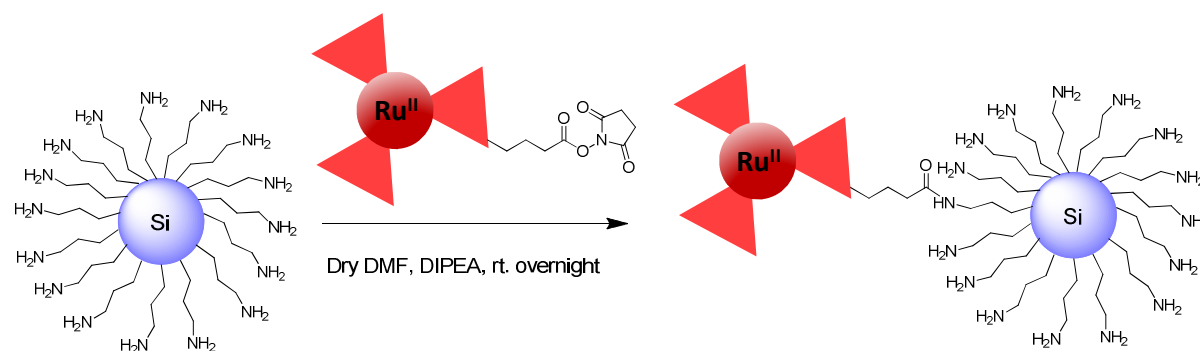


**Figure 5.1:** Reaction scheme for the synthesis of Si NPs-[Ru].

Following the reaction, the product was purified by size exclusion chromatography (Sephadex LH-20) in methanol. Si NPs bound to the [Ru] complex were eluted first and uncoupled free complex eluted last as confirmed by thin layer chromatography. The relevant fractions were combined to isolate the Si NPs-[Ru] product.

## 5.2.2 Characterisation

### *X-ray photoelectron spectroscopy (XPS)*

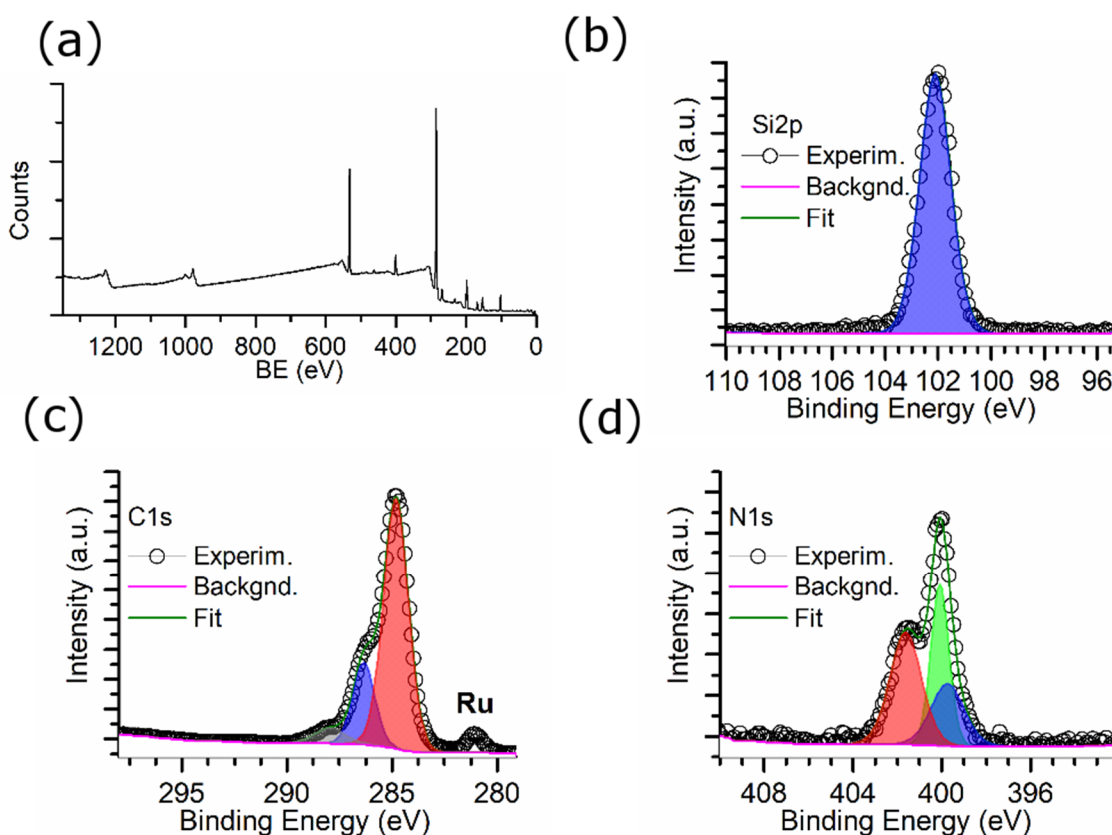


**Figure 5.2:** XPS of Si NPs-[Ru]. (a) Survey scan (b) Si scan (c) C scan (d) N scan

XPS measurements were also performed for Si NPs-[Ru]. As shown in Figure 5.2 a, the NPs contain the elements C, O, N, S, Si and Ru (listed in table 5.1). The bonding energy of Si2p (figure 5.2 b) is at 102.10 eV, corresponding to Si—C bonded silicon species originating from the surface grafting of allylamine. The deconvolution of the N scan was performed as shown in Figure 5.2 d and listed in table 5.2. The Si NPs-[Ru] contain three types of nitrogen: pyridine N is from the Rubpy, amine N is from the remaining terminal amines Si NPs surface and amide N is from the coupling of Si NPs and [Ru] complex which proves the complex is covalently bound on the Si NPs.

Scan	Peak BE	FWHM eV	Area (P) CPS.eV	Atomic %
C1s	284.80	2.90	1412268.68	66.84
O1s	531.81	2.69	725573.89	14.21
N1s	400.42	3.26	175690.1	5.36
S2p	168.06	1.68	65311.32	1.53
Si2p	101.80	2.45	96719.53	4.56
Ru3d	285.16	2.75	1190901.82	3.81

**Table 5.1:** XPS survey data of Si NPs-[Ru].

Name	Peak BE	Height CPS	Height Ratio	Area CPS.eV	Area Ratio, %
N1s (amide N)	401.19	6501.92	0.31	10984.49	0.43
N1s (amine N)	399.44	20872.67	1	25345.15	1
N1s (pyridine N)	398.82	2699.97	0.13	6186.83	0.24

**Table 5.2:** XPS data of Si NPs-[Ru] N1s scan

### *FT-IR Spectroscopy*

In order to provide more information on the structure of the Si NPs-[Ru] system through way of the chemical bonds present, the FT-IR spectrum was recorded (figure 5.3). The spectrum was measured via an ATR attachment, onto which the Si NPs-[Ru] were drop cast from methanol, with the solvent evaporated before analysis. The observed main absorptions correspond to the bonds typically found in the amine terminated Si NPs as summarised in table 5.3. In particular, the C=O amide stretching absorption shows the successful grafting of the complex onto the Si NPs through reaction of the terminal amines and NHS ester.

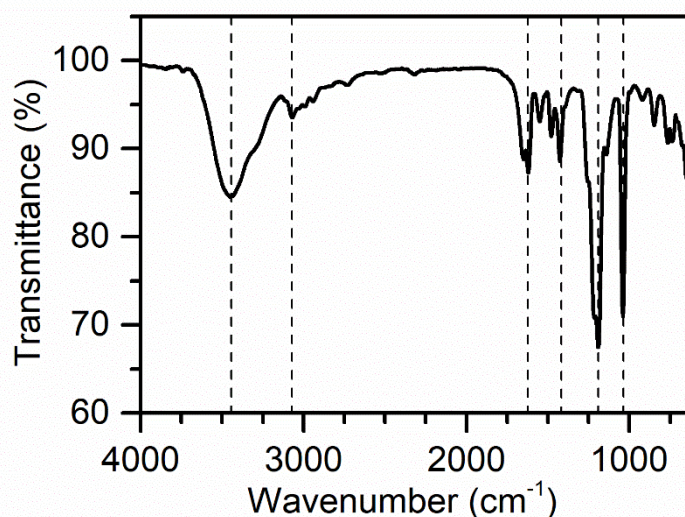


**Figure 5.4:** FT-IR of Si NPs-[Ru]

Signal	Wavenumber (cm <sup>-1</sup> )
N—H	3444
C—H	3072
C=O (amide)	1653
C—H	1423
C—O	1220
C—N	1039

**Table 5.3:** FT-IR spectral data of Si NPs-[Ru]

### *TEM imaging*

TEM imaging analysis of the Si NPs-[Ru] system shows crystalline particles with a circular shape and a size of  $3.1 \pm 0.7$  nm, as shown in figure 5.4.

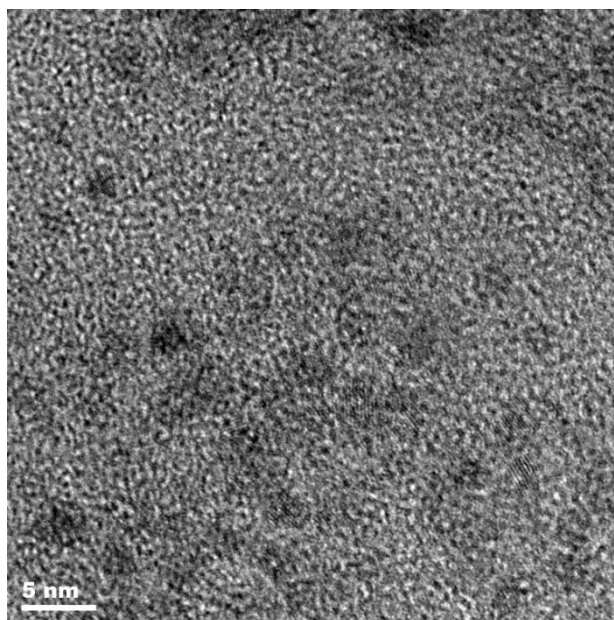


**Figure 5.4:** TEM micrograph of Si NPs-[Ru]

### *Photophysical properties*

A variety of analytical methods were employed to gain an in-depth characterisation of the photophysical properties that the Si NPs possess, including UV-visible absorption spectrometry, Photoluminescence emission and excitation spectroscopy, time resolved excited state lifetime measurements and quantum yield measurements. All measurements were conducted in water.

UV-Vis absorption was performed in order to compare the Si NPs-[Ru] with the [Ru] complex (measured complex soln.  $1.0 \times 10^{-5}$  M in water). As shown in Figure 5.5, the absorption bands of the [Ru] complex are mirrored by the Si NPs-[Ru]. Absorption bands at 249, 257 and 292 nm are assigned to the ligand  $\pi-\pi^*$  transition, the absorption band at 463 nm is assigned to the MLCT. The Si NPs-[Ru] likewise show absorption peaks at the same wavelengths, which are assigned to the attached [Ru] complex. The larger relative increase of absorption intensity below 275 nm is due to the presence of Si NPs.

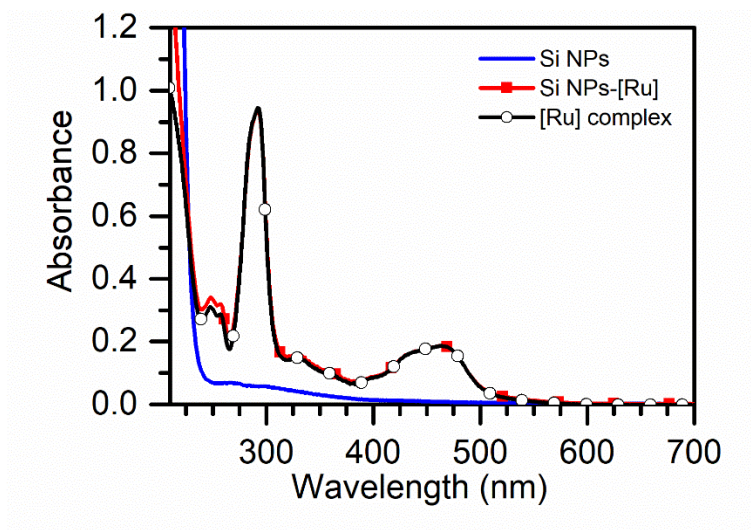


**Figure 5.5:** UV-vis absorption spectra of microemulsion Si NPs, Si NPs-[Ru] and the [Ru] complex in water

The emission spectra of Si NPs-[Ru] and the [Ru] complex were then recorded and are shown in Figure 5.6. A  $\lambda_{\text{max emission}}$  of the Ru complex  $^3\text{MLCT}$  band is observed at 637 nm for  $\lambda_{\text{excitation}}$  of 405 nm. The close overlap of the spectra shows that there is no quenching effect by the Si NPs on the emission of the complex.



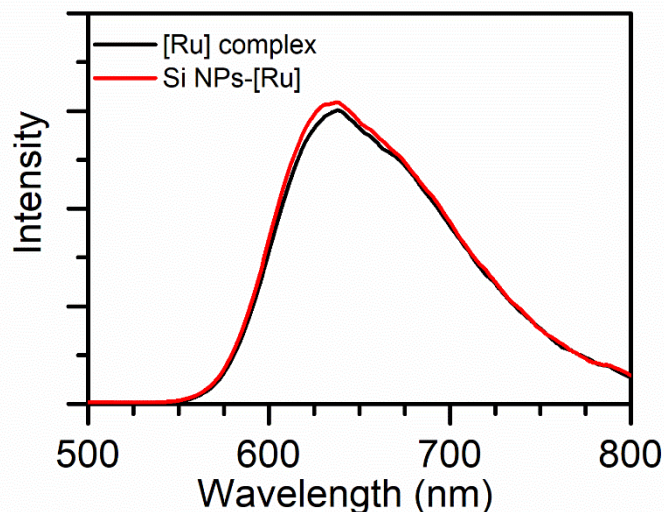


**Figure 5.6:** Emission spectra of Si NPs [Ru] and [Ru] complex in water ( $\lambda_{exc} = 405$  nm).

The excited state lifetimes of the [Ru] complex and Si NPs-[Ru] in water (measured at  $\lambda_{Emission}$  of 637 nm with  $\lambda_{Excitation} = 405$  nm) are comparable at 342 ns for the complex and 358 ns for the Si NPs-[Ru], indicating no emission quenching in the Si NPs-[Ru]. In fact, there is a slight enhancement of the lifetime measured for the Si NPs-[Ru] possibly due to the immobilisation of the complex on the surface of the nanoparticles, reducing quenching by reactive oxygen species in solution.

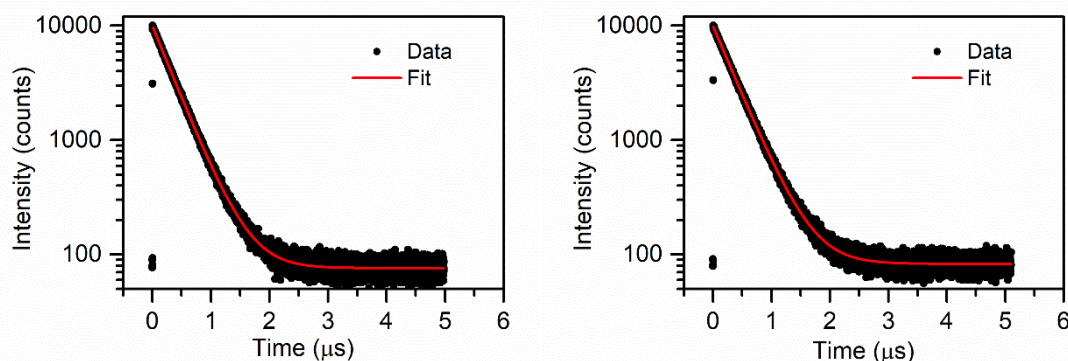


**Figure 5.7:** Time resolved excited state lifetime decay curves for the [Ru] complex (left) and the Si NPs-[Ru] (right) ( $\lambda_{exc} = 405$  nm).

Both the [Ru] complex and Si NPs-[Ru] show an emission quantum yield of 3.7% ( $\lambda_{Excitation} = 405$  nm, measured using integrating sphere).

### *Quantification of complex on Si NPs*

In order to gain an estimate of the number of complexes per particle in the sample, the technique of radiometric absorbance was used by taking data from the UV-vis absorption spectrum of the sample and the average size of the particles found through TEM analysis. Using the workings of the equation below, a value for the number of [Ru] complexes per particle could be estimated.

$$\text{Mol mass ([Ru] complex)} = 1185.1 \text{ g/mol}$$

$$\epsilon = 12871.39 \text{ dm}^3 \text{ mol}^{-1} \text{ cm}^{-1} \text{ (calculated from calibration curve of [Ru] complex)}$$

$$\text{For Si NPs-[Ru], max abs. at 463 nm} = A = 0.1869$$

$$\text{Therefore: } c = A / \epsilon l = 0.1869 / (12871.39 \times 1) = 1.452 \times 10^{-5} \text{ mol/dm}^3$$

$$\text{So } n = cv = (1.452 \times 10^{-5}) \times (3 \times 10^{-3}) = 4.356 \times 10^{-8} \text{ mol in 3 mL}$$

(Used 10  $\mu\text{L}$  of 0.01 mg/ $\mu\text{l}$  mother soln. of sample in 3 mL for UV absorption analysis. So 0.1 mg of sample)

$$\text{Mass} = n \times \text{Mol mass} = (4.356 \times 10^{-8}) \times 1185.1 = 5.16 \times 10^{-5} \text{ g} = 5.16 \times 10^{-2} \text{ mg complex in 3 mL}$$

$$\text{So mass of complex per mL} = (5.16 \times 10^{-2}) \div 3 = \mathbf{0.017 \text{ mg/mL} = M_{\text{complex}}}$$

*Mass of Si NPs:*

*One Si NP:*

$$\text{Diameter} = 3.1 \text{ nm}$$

$$\text{Vol (V)} = (4/3) \pi (1.55 \times 10^{-9})^3 = 1.6 \times 10^{-26} \text{ m}^3 = 1.6 \times 10^{-20} \text{ cm}^3$$

$$\text{Density (D)} = 2.33 \text{ g/cm}^3 \text{ (silicon)}$$

$$\text{Mass of one NP (M = V x D)} = 3.7 \times 10^{-20} \text{ g} = \mathbf{3.7 \times 10^{-17} \text{ mg} = M_{\text{SiNP}}}$$

*No. of Si NPs*

$$\text{Total conc. of Si NPs-[Ru] in measured solution} = 0.033 \text{ mg/mL}$$

$$\text{Mass per mL soln.} = M_{\text{total}} - M_{\text{complex}} = 0.033 - 0.017 = \mathbf{0.016 \text{ mg} = M_{\text{Si NPs}}}$$

$$\text{So No. of particles per mL soln.} = M_{\text{Si NPs}} / M_{\text{SiNP}} = \mathbf{4.3 \times 10^{14}}$$

*No. of complexes:*

$$M_{\text{complex}} = 0.017 \times 10^{-3} \text{ g/mL}$$

$$\text{So: } n = \text{mass} / \text{Mol. mass} = (0.017 \times 10^{-3}) / 1185.1 = 1.434 \times 10^{-8}$$

$$\text{No. complexes in 1 mL} = n \times N_A = (1.434 \times 10^8) \times (6.022 \times 10^{23}) = 8.638 \times 10^{15}$$

Number of complexes per particle:

$4.3 \times 10^{14}$  particles per mL

$8.6 \times 10^{15}$  complexes per mL

So complexes per particle = complexes per mL / particles per mL = **20 complexes per particle**

**Equation 5.1:** Calculation of the number of [Ru] complexes per Si NPs-[Ru]

## 5.3 Synthesis of iridium complex modified Si NPs

### 5.3.1 Synthesis route

Following an identical procedure to the coupling of the ruthenium complex to the Si NPs as detailed above, coupling of the particles to a novel sulfonated iridium complex was also realised. DIPEA was again used to introduce a basic pH to optimise the coupling of the Si NPs to the sulfonated Ir complex through the terminal amine groups and the activated NHS ester of the metal complex. A simplified reaction schematic is shown below in figure 5.1.

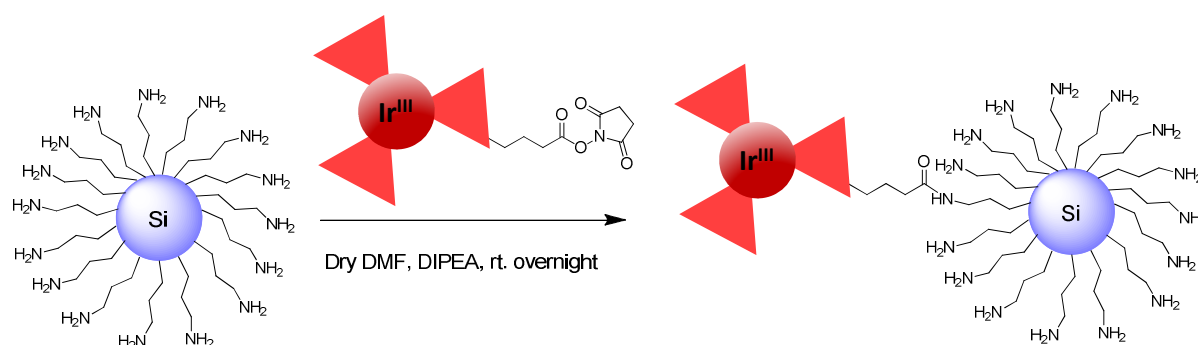


**Figure 5.8:** Reaction scheme for the synthesis of Si NPs-[Ir].

Once again, the product was purified by size exclusion chromatography.

### 5.3.2 Characterisation

#### *X-ray photoelectron spectroscopy (XPS)*

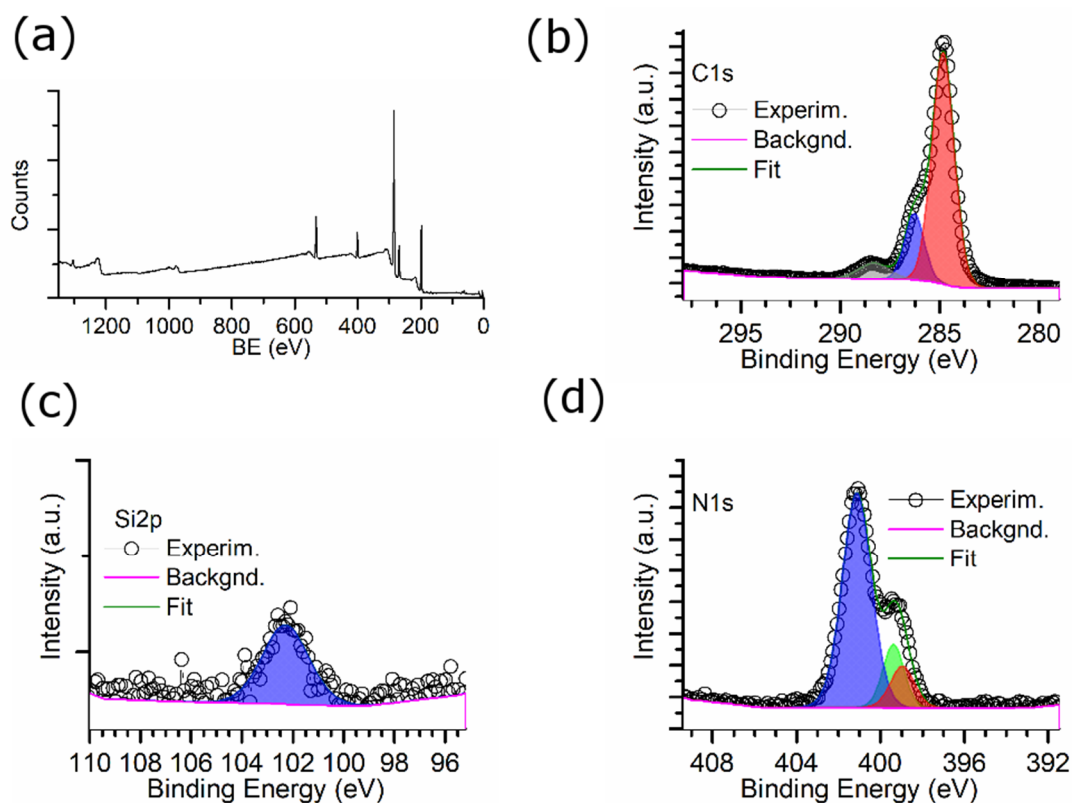


**Figure 5.9:** XPS of Si NPs-[Ir]. (a) Survey scan (b) C scan (c) Si scan (d) N scan (e) Ir scan

Similar XPS measurements were performed for Si NPs-[Ir]. As shown in Figure 5.9 a, the NPs contain the elements C, O, N, S, and Cl (listed in table 5.4). The bonding energy of Si2p (figure 5.9 c) is at 102.27 eV which again suggests partial oxidation of the silicon surface. The deconvolution of the N scan is shown in Figure 5.9 d and listed in table 5.5. The Si NPs-[Ir] contain three types of nitrogen: pyridine N is from the [Ir] complex, amine N is from the remaining terminal amines on the Si NPs surface and amide N is from the coupling between Si NPs and the [Ir] complex which proves the complex is covalently bound on the Si NPs.

Scan	Peak BE	FWHM eV	Area (P) CPS.eV	Atomic %
C1s	284.80	2.76	1326005.00	70.90
Cl2p	198.08	1.88	621626.10	11.49
O1s	531.96	1.94	392253.00	8.68
N1s	401.11	1.91	244758.00	8.44
S2p	168.52	2.99	18772.68	0.50

**Table 5.4:** XPS survey data of Si NPs-[Ir].

Name	Peak BE	Height CPS	Height Ratio	Area CPS.eV	Area Ratio, %
N1s (amide N)	401.12	13610.69	1.00	24232.35	0.21
N1s (amine N)	399.37	4012.95	0.29	5190.50	1.00
N1s (pyridine N)	398.95	2641.38	0.19	3881.38	0.16

**Table 5.5:** XPS data of Si NPs-[Ir] N1s scan

### FT-IR Spectroscopy

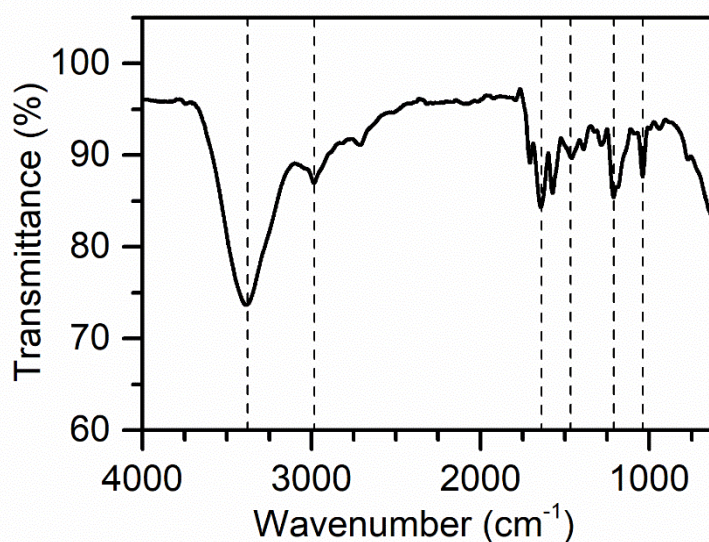


**Figure 5.10:** FT-IR of Si NPs-[Ir]

The FT-IR spectrum of Si NPs-[Ir] was also recorded (figure 5.3), as with the Ru analogue, in order to provide more structural information. The spectrum was measured via an ATR attachment, using the same method as before. The observed main absorptions correspond to the bonds typically found in the amine terminated Si NPs as summarised in table 5.3. In particular, the C=O amide stretching absorption shows the successful grafting of the complex onto the Si NPs through reaction of the terminal amines and NHS ester.

Signal	Wavenumber (cm <sup>-1</sup> )
N—H	3387
C—H	2985
C=O (amide)	1637
C—H	1456
Si—C	1211
C—N	1039

**Table 5.6:** FT-IR spectral data of Si NPs-[Ir]

### *TEM imaging*

TEM imaging analysis of the Si NPs-[Ir] system again shows crystalline particles with a circular shape and a size of  $3.1 \pm 0.7$  nm, as shown in figure 5.11. The Si NPs used to create the Si NPs-[Ru] also came from the same batch, so the same or a similar size is to be expected.

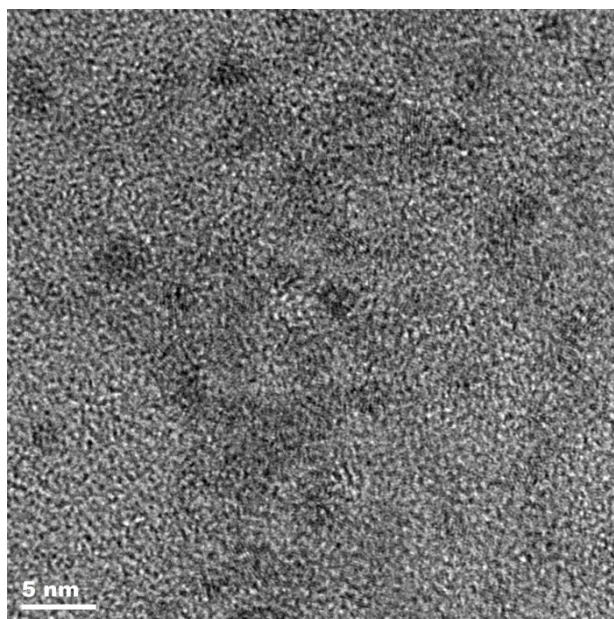


**Figure 5.11:** TEM micrograph of Si NPs-[Ir]

### *Photophysical properties*

Again, UV-visible absorption spectrometry, Photoluminescence emission and excitation spectroscopy, time resolved excited state lifetime measurements and quantum yield measurements were conducted to assess the Si NPs-[Ir] system. All measurements were once again conducted in water.

UV-Vis absorption was performed in order to compare the Si NPs-[Ir] with the [Ir] complex (measured complex soln.  $1.0 \times 10^{-5}$  M in water). As shown in Figure 5.12, the absorption bands of the [Ir] complex are matched by the Si NPs-[Ir]. Absorption bands at 247, 284, 332, 362 and 384 nm are assigned to the ligand  $\pi$ - $\pi^*$  transition, and the absorption band at 417 nm is assigned to the MLCT. The Si NPs-[Ir] likewise show absorption peaks at the same wavelengths, assigned to the attached [Ir] complex. The larger relative increase of absorption intensity below 300 nm is due to the presence of Si NPs.

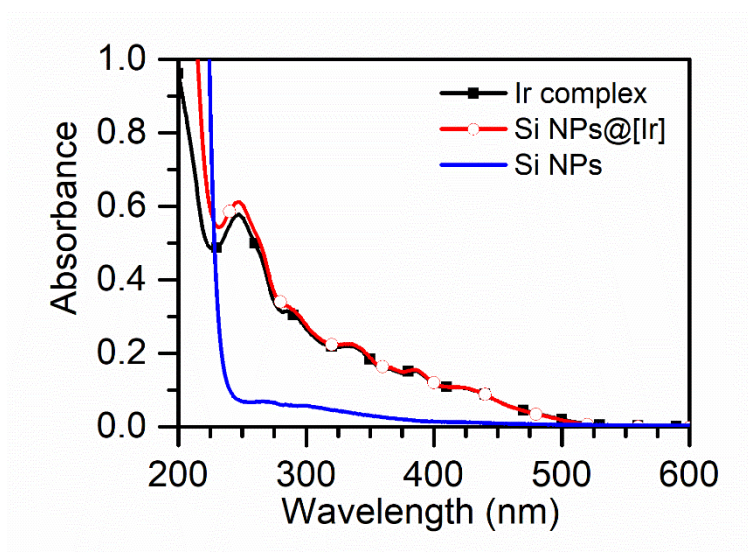


**Figure 5.12:** UV-vis absorption spectra of microemulsion Si NPs, Si NPs-[Ir] and the [Ir] complex in water

The emission spectra of Si NPs-[Ir] and the [Ir] complex are shown in Figure 5.13. A  $\lambda_{\text{max emission}}$  of the Ir complex  $^3\text{MLCT}$  band is observed at 642 nm for  $\lambda_{\text{excitation}}$  of 405 nm. The close overlap of the spectra again shows that there is no quenching effect by the Si NPs on the emission of the complex.

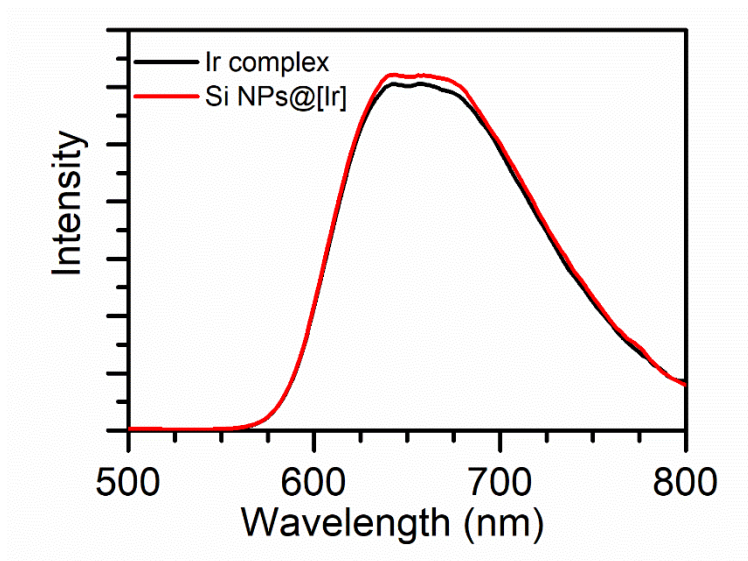


**Figure 5.13:** Emission spectra of Si NPs-[Ir] and [Ir] complex in water ( $\lambda_{exc} = 405$  nm).

The excited state lifetimes of the [Ir] complex and Si NPs-[Ir] in water (measured at  $\lambda_{Emission}$  of 642 nm with  $\lambda_{Excitation} = 405$  nm) can both be fit to the same value of 883 ns. This shows that no emission quenching of the complex on the Si NPs-[Ir] occurs.

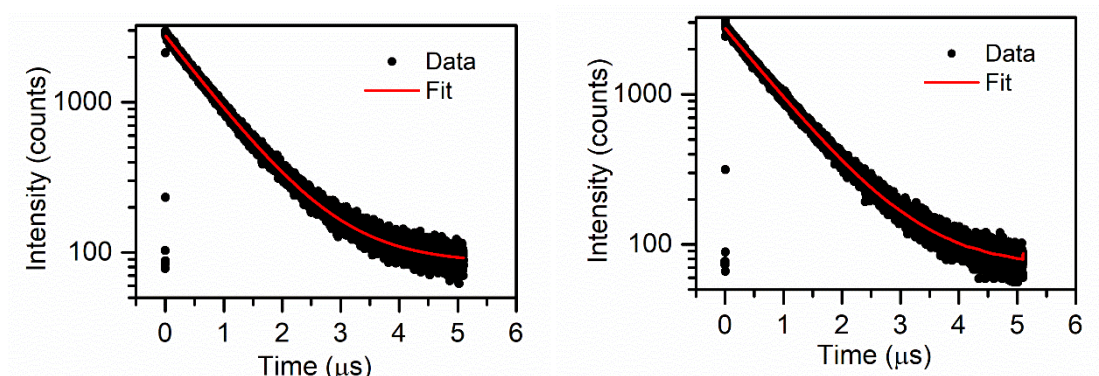


**Figure 5.14:** Time resolved excited state lifetime decay curves for the [Ir] complex (left) and the Si NPs-[Ir] (right) ( $\lambda_{exc} = 405$  nm).

Both the [Ir] complex and Si NPs-[Ir] show an emission quantum yield of 4.8% ( $\lambda_{Excitation} = 405$  nm measured using integrating sphere).

#### *Quantification of complex on Si NPs*

Ratiometric absorbance was again used to estimate the number of [Ir] complexes per Si NP using the relevant data as for the Ru analogue.

$$\text{Mol mass ([Ir] complex)} = 2020.2 \text{ g/mol}$$



$\epsilon = 10060.4547 \text{ dm}^3 \text{ mol}^{-1} \text{ cm}^{-1}$  (calculated from calibration curve of [Ir] complex)

For Si NPs@[Ir], max abs. at 417 nm =  $A = 0.10741$

Therefore:  $c = A / \epsilon l = 0.10741 / (10060.4547 \times 1) = 1.0676 \times 10^{-5} \text{ mol} / \text{dm}^3$

So  $n = cv = (1.0676 \times 10^{-5}) \times (3 \times 10^{-3}) = 3.2028 \times 10^{-8} \text{ mol}$  in 3 mL

(For UV absorption analysis, used 0.15 mg of sample)

Mass =  $n \times \text{Mol mass} = (3.2028 \times 10^{-8}) \times 2020.2 = 6.4703 \times 10^{-5} \text{ g} = 6.4703 \times 10^{-2} \text{ mg}$  complex in 3 mL

So mass of complex per mL =  $(6.4703 \times 10^{-2}) \div 3 = 0.0216 \text{ mg/mL} = M_{\text{complex}}$

Mass of Si NPs:

One Si NP:

Diameter = 3.1 nm

Vol (V) =  $(4/3) \pi (1.55 \times 10^{-9})^3 = 1.6 \times 10^{-26} \text{ m}^3 = 1.6 \times 10^{-20} \text{ cm}^3$

Density (D) = 2.33 g/cm<sup>3</sup> (silicon)

Mass of one NP (M = V x D) =  $3.7 \times 10^{-20} \text{ g} = 3.7 \times 10^{-17} \text{ mg} = M_{\text{SiNP}}$

No. of Si NPs

Total conc. of Si NPs-[Ir] in measured solution = 0.05 mg/mL

Mass per mL soln. =  $M_{\text{total}} - M_{\text{complex}} = 0.05 - 0.0216 = 0.0284 \text{ mg} = M_{\text{Si NPs}}$

So No. of particles per mL soln. =  $M_{\text{Si NPs}} / M_{\text{SiNP}} = 7.676 \times 10^{14}$

No. of complexes:

$M_{\text{complex}} = 0.0216 \times 10^{-3} \text{ g/mL}$

So:  $n = \text{mass} / \text{Mol. mass} = (0.0216 \times 10^{-3}) / 2020.2 = 1.069 \times 10^{-8}$

No. complexes in 1 mL =  $n \times N_A = (1.069 \times 10^{-8}) \times (6.022 \times 10^{23}) = 6.439 \times 10^{15}$

Number of complexes per particle:

$7.676 \times 10^{14}$  particles per mL

$6.439 \times 10^{15}$  complexes per mL

So complexes per particle =  $\text{complexes per mL} / \text{particles per mL} = 8 \text{ complexes per particle}$

**Equation 5.2:** Calculation of the number of [Ir] complexes per Si NPs-[Ir]

## 5.4 ECL performance

The ECL efficiencies were evaluated in comparison to the  $\text{Ru}(\text{bpy})_3$  standard as shown below in figure 5.11. Here, each type of measurement is addressed in turn, with the measurements with the Si NPs-[Ru] detailed first and then those with the Si NPs-[Ir].

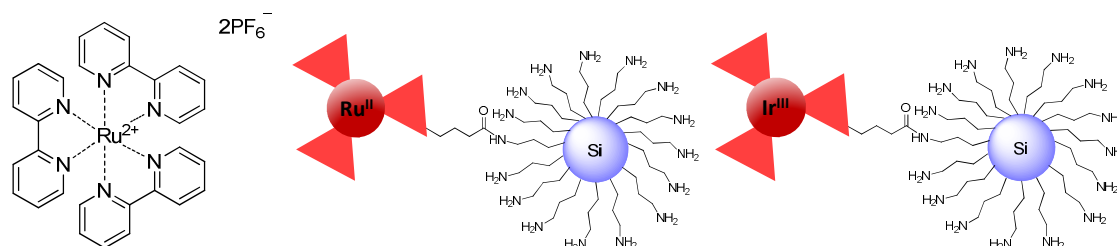


**Figure 5.15:** Representations of the  $[\text{Ru}(\text{bpy})_3]^{2+} 2(\text{PF}_6)^-$  standard and both the Si NPs-[Ru] and Si NPs-[Ir] used in the ECL experiments.

All ECL measurements were performed with samples in ProCell. In order to gain a better examination of the ECL efficiency, it is useful to record the photophysical spectra again in the same media used for the ECL experiments. The same concentrations of samples ( $1.0 \times 10^{-5} \text{ M}$ ) were used in all cases as before. What can be noted in the case of both systems is the increase in the difference between the absorptions and emission intensities of the complexes coupled Si NPs and the free complexes. This is because the coupled Si NPs have a slight tendency to aggregate in ProCell solution due to the presence of tripropylamine (TPrA) and surfactants, which increase the viscosity. This slight aggregation causes some scattering in the absorption and a higher emission intensity. The UV-Vis absorption and emission spectra for both the [Ru] system and the [Ir] complex system in ProCell are shown in figures 5.16 and 5.17 respectively.

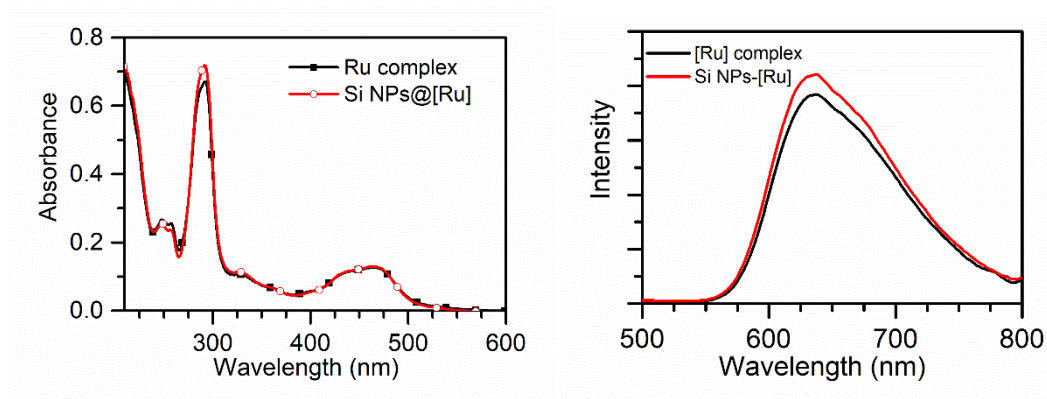


**Figure 5.16:** (Left) UV-Vis absorption spectra of the [Ru] complex and Si NPs-[Ru] in ProCell solution. (Right) Emission spectra of the [Ru] complex and Si NPs-[Ru] in ProCell solution ( $\lambda_{exc} = 405$  nm).

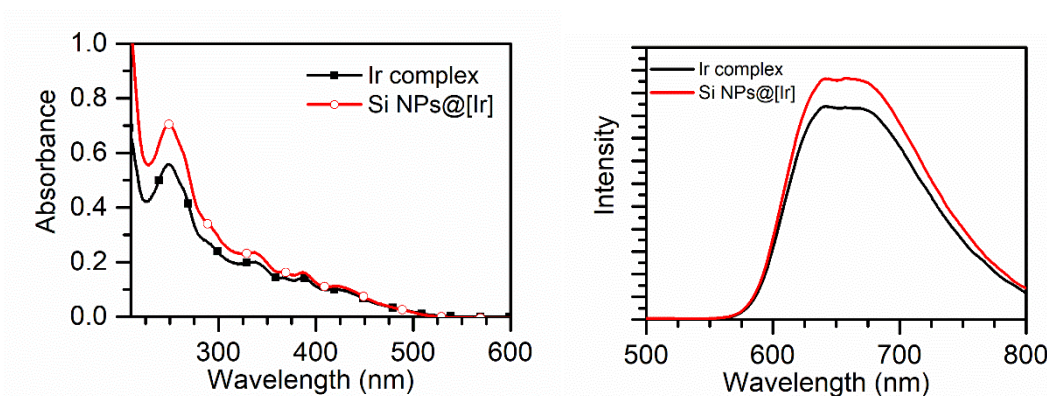


**Figure 5.17:** (Left) UV-Vis absorption spectra of the [Ir] complex and Si NPs-[Ir] in ProCell solution. (Right) Emission spectra of the [Ir] complex and Si NPs-[Ir] in ProCell solution ( $\lambda_{exc} = 405$  nm).

The excited state lifetimes of the [Ru] complex and Si NPs-[Ru] in ProCell (measured at  $\lambda_{Emission}$  of 633 nm with  $\lambda_{Excitation} = 405$  nm) are identical in this case at 389 ns for both, indicating no occurrence of emission quenching or enhancement in the ProCell solution. The [Ir] complex and the Si NPs-[Ir] in ProCell could also be fit to the same lifetime once again, this time being 1.36  $\mu$ s. The enhancement in the lifetime in the case of all samples can be attributed to the lack of quenching from oxygen when in water.

Both the [Ru] complex and Si NPs-[Ru] in ProCell show an emission quantum yield of 3.9%, while the [Ir] complex and Si NPs-[Ir] show a quantum yield of 7.0% ( $\lambda_{Excitation} = 405$  nm, measured using integrating sphere in both cases).

The ECL activity (intensities) of both systems was evaluated as function of voltage applied, time and emission in comparison to a reference solution of  $[Ru(bpy)_3]^{2+} 2(PF_6)^-$  in ProCell. The

ProCell introduces the tripropylamine (TPrA) molecule into the system, which participates in the ECL mechanism. As shown in figure 5.18 below by the black traces, the  $[\text{Ru}(\text{bpy})_3]^{2+} 2(\text{PF}_6)^-$  TPrA system shows two waves at +1.23 V and +1.48 V vs Ag/AgCl (1M KCl), both of which contribute to the generation of the  $[\text{Ru}(\text{bpy})_3]^{2+}$  excited state.

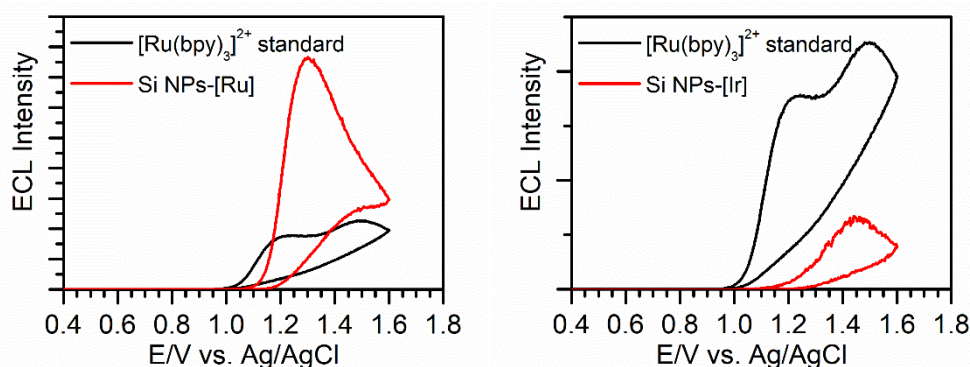
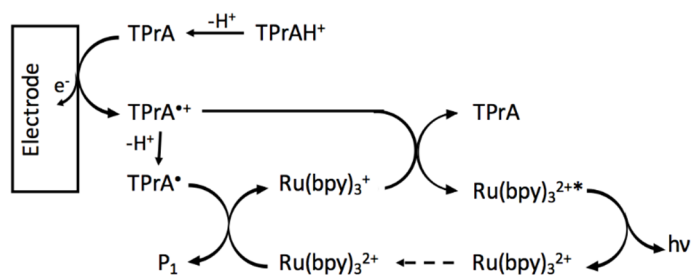


**Figure 5.18:** ECL intensities recorded during cyclic voltammetry at a scan rate of  $0.55 \text{ V s}^{-1}$  of  $10^{-5} \text{ M}$   $[\text{Ru}(\text{bpy})_3]^{2+} 2(\text{PF}_6)^-$  (black) and  $10^{-5} \text{ M}$  Si NPs-metal complexes (red) in Procell.

According to the oxidative-reduction mechanism 1 in figure 5.19<sup>[16]</sup>, the first wave involves the electrochemical oxidation of TPrA to  $\text{TPrA}^{\bullet+}$ , which then oxidises  $[\text{Ru}(\text{bpy})_3]^{2+}$  to  $[\text{Ru}(\text{bpy})_3]^{2+\bullet}$ . The latter species then decays to the ground state with emission of a photon. The second wave is associated with the classic oxidative-reduction mechanism (mechanism 2) that occurs when electrogenerated  $[\text{Ru}(\text{bpy})_3]^{2+}$  reacts with  $\text{TPrA}^{\bullet}$  (Figure 5.19)<sup>[16]</sup>.

### Mechanism 1



### Mechanism 2

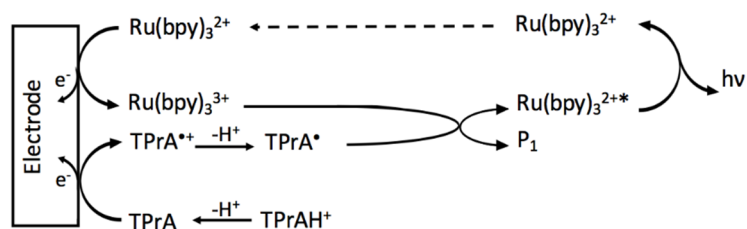


**Figure 5.19:** Mechanisms reported by Bard *et al.* for the system  $[\text{Ru}(\text{bpy})_3]^{2+} 2(\text{PF}_6)^- / \text{TPrA}$  in aqueous solution containing Rubpy in low concentration. Reprinted with permission from J. Am. Chem. Soc., 2002, 124, 14478-14485, Copyright (2004) American Chemical Society.

Performing the same experiment on the Si NPs-metal complexes systems produces different ECL profiles to the reference. Both are characterised by a single broader peak, centred at +1.3 V for Si NPs-[Ru] and +1.4 V for Si NPs-[Ir] (figure 5.18, red traces). In the case of the Si NPs-[Ru], this peak corresponds to mechanism 1 in figure 5.19 and the generation of the excited state of Si NPs-[Ru]\*. The intensity is notably higher, which could be due to the complex coupled Si NPs bringing more of the complex into the diffusion layer of the electrode surface. In the case of the Si NPs-[Ir], the peak is hypothesised to relate to the direct oxidation of the Ir complex. The intensity this time though is much lower than the standard, which is thought to be due to the low ECL efficiency of the complex itself.

Chronoamperometric experiments, shown in Figure 5.20 were used to evaluate the overall ECL efficiencies of the new systems vs the  $[\text{Ru}(\text{bpy})_3]^{2+} 2(\text{PF}_6)^-$  standard. Here, ECL is generated by chronoamperometric pulses at +1.4 V for 1 second. To reduce the standard deviation of the final calculation to < 10%, the experiments were performed in fresh solutions on three different days with three repetitions each day (for a total of 9 experimental runs). The ECL efficiency is calculated from the average of the 9 results. Representative examples of the

chronoamperometry experiments for both Si NPs-[Ru] and Si NPs-[Ir] are shown in figure 5.20.

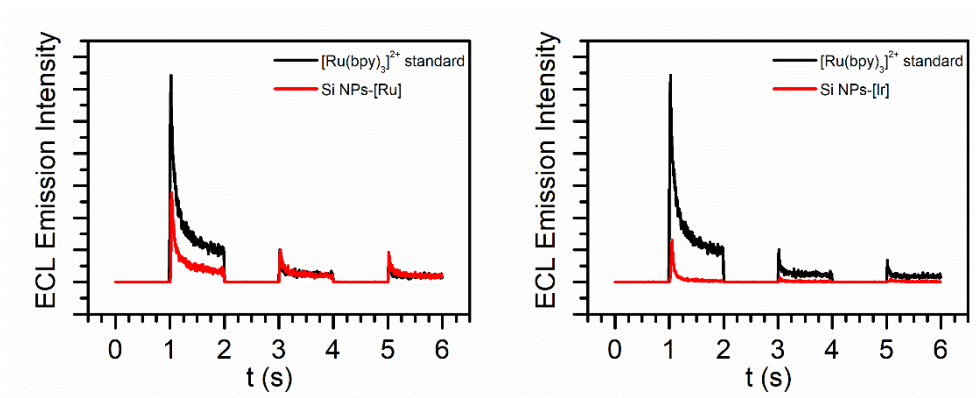


**Figure 5.20:** Chronoamperometric experiments of ECL Intensities over time for  $10^{-5}$  M  $[\text{Ru}(\text{bpy})_3]^{2+} 2(\text{PF}_6)^-$  (black) and  $10^{-5}$  M Si NPs-metal complexes (red) in Procell.

The efficiency of the Si NPs-[Ru] system was found to have 66% compared to the  $[\text{Ru}(\text{bpy})_3]^{2+} 2(\text{PF}_6)^-$  standard (100%), while the Si NPs-[Ir] system resulted in 15% efficiency. Interestingly, the [Ru] complex itself possessed an efficiency of 51%, meaning that the hybrid system with the Si NPs provides an enhancement. The [Ir] complex itself showed an efficiency of 19%, indicating an inherent low efficiency would be exhibited by the system. The lower time-related intensity compared to the  $[\text{Ru}(\text{bpy})_3]^{2+} 2(\text{PF}_6)^-$  standard in both cases could be partially linked to the slow diffusion of the coupled systems towards the electrode surface, but again, for the Si NPs-[Ir] complex also because of the low efficiency of the [Ir] complex.

Finally, the wavelength-resolved ECL spectra of the Si NPs systems were also measured to evaluate the nature of the electro-generated emissive excited states (figure 5.21). In these experiments, the ECL signal was collected during 5 chronoamperometry pulses of 1 s between 0 V and +1.4 V vs Ag/AgCl and the resulting spectra were collected using a cooled EMCCD camera with an accumulation time of 10 s.

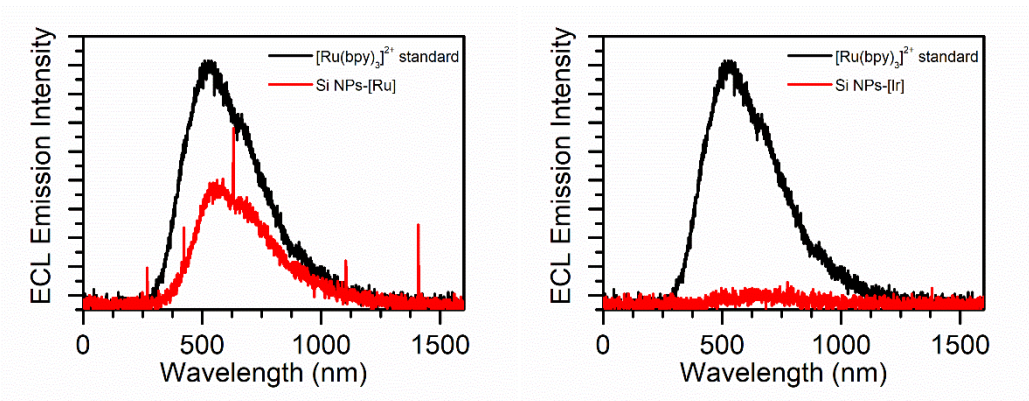


**Figure 5.21:** ECL emission spectra of  $10^{-5}$  M  $[\text{Ru}(\text{bpy})_3]^{2+} 2(\text{PF}_6)^-$  (black) and  $10^{-5}$  M Si NPs-metal complexes (red) in Procell.

As shown in figure 5.21, the ECL emission of Si NPs-[Ru] shows an identical profile upon photoexcitation to that of the  $[\text{Ru}(\text{bpy})_3]^{2+}$  standard, but at a lower intensity. It is, however, slightly more intense than that of the free [Ru] complex (figure 5.22), which is still a promising result for this particular system, as it retains a water solubility, which the standard lacks. The Si NPs-[Ir] show an extremely low intensity compared to the  $[\text{Ru}(\text{bpy})_3]^{2+}$  standard, however, the free [Ir] complex shows an intensity almost equal in intensity to that of the standard. This is most likely due to some form of diffusion effects and suggests that the relation between mass diffusion and ECL efficiency of these systems should also be investigated in following work.

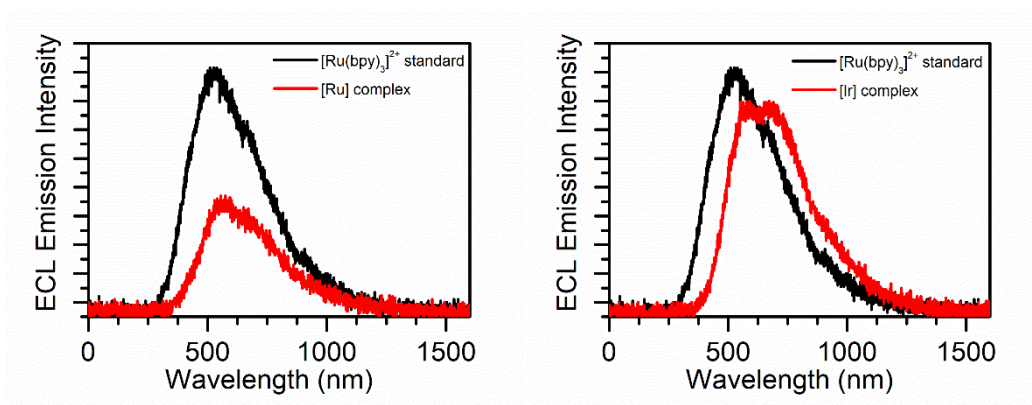


**Figure 5.22:** ECL emission spectra of  $10^{-5}$  M  $[\text{Ru}(\text{bpy})_3]^{2+} 2(\text{PF}_6)^-$  (black) and  $10^{-5}$  M metal complexes (red) in Procell.

## 5.4 Conclusion

The small, silicon-based nanoparticles have been successfully surface functionalised with water soluble ruthenium and iridium complexes, thoroughly characterised thereafter and have been assessed in terms of their ECL efficiency. The novel systems remain completely water-soluble and can be used as imaging and diagnostic tools. The ECL efficiency of the Si NPs-[Ru] system was found to be lower than the  $[\text{Ru}(\text{bpy})_3]^{2+}$  standard, but higher than that of the free novel [Ru] complex, showing that the Si NPs have a beneficial effect on the ECL performance in this case. The Si NPs-[Ir] system on the other hand shows a very low ECL efficiency, which in contrast is lower than that of the free novel [Ir] complex itself. This suggests that diffusion effects may play a role in the ECL performance of the Si NPs systems and that studies should be performed to evaluate this phenomenon. It could also be related to the need to graft more of the [Ir] complex onto the Si NPs in order to achieve a more optimal system as through the estimation calculation, there were only roughly half as many [Ir] complexes on the Si NPs-[Ir] compared to [Ru] complexes on the Si NPs-[Ru]. An alternative reason for the decreased efficiency could be due to the self-quenching of the metal complexes while in such close proximity to each other. A possible method to explore this in the future could be to conduct the same experiments on multi-centred metal complexes themselves to see if a similar reduction in efficiency is observed. Another future study would be to explore the same systems using hydrothermal Si NPs in place of the microemulsion Si NPs. This would give a much clearer insight into the role, if any, played by the silicon-based core in the enhancement or reduction of the ECL efficiency.

## 5.5 Experimental section

### 5.5.1 General information

#### *Materials*

The sulfonated ruthenium and iridium complexes, and ProCell solution were provided by Roche Diagnostics (F. Hoffmann-La Roche Ltd). Microemulsion Si NPs were synthesised as reported in Chapter 2. All other solvents and reagents were purchased from Sigma-Aldrich and used without further purification. Sephadex LH-20 was purchased from GE Healthcare Europe GmbH. DI water was prepared using a Milli-Q system by Millipore.



## *TEM*

Samples for HR-TEM and EDX were prepared by dispersing the aqueous suspensions of the samples onto holey-carbon-on-copper grids (Quantifoil, GmbH) with the excess solvent evaporated. The analysis were performed using a FEI Titan 80-300 transmission electron microscope operated at 300 KV.

## *Photophysical measurements*

Steady-state emission spectra were recorded on a HORIBA Jobin-Yvon IBH FL-322 Fluorolog 3 spectrometer equipped with a 450 W xenon arc lamp as the excitation source, double-grating excitation and emission monochromators ( $2.1 \text{ nm mm}^{-1}$  of dispersion;  $1200 \text{ grooves mm}^{-1}$ ), and a TBX-04 single-photon-counting device as the detector. Emission and excitation spectra were corrected for source intensity (lamp and grating) and emission spectral response (detector and grating) by standard correction curves. Time-resolved measurements were performed using the Time-Correlated Single Photon Counting (TCSPC) on the FT-300 (PicoQuant), where a polarized laser source 405 nm used for exciting the samples. The excitation sources were mounted directly on the sample chamber at  $90^\circ$  to a Czerny-Turner type emission monochromator ( $2.7 \text{ nm mm}^{-1}$  of dispersion;  $1200 \text{ grooves mm}^{-1}$ ) and collected by a PMA-C 192M single-photon-counting detector. Signals were collected using EasyTau software, and data analysis was performed using FluoFit software (PicoQuant). The quality of the fit was assessed by minimizing the reduced  $\chi^2$  function and by visual inspection of the weighted residuals. Luminescence quantum yield was performed with integrating sphere (Hamamatsu, C11347-11).

## *FT-IR Spectroscopy*

FTIR spectra were recorded on a Shimadzu IRAffinity-1 spectrometer used in attenuated total reflectance (ATR) mode. Samples were drop-cast onto the ATR crystal and the excess solvent was evaporated.

## *XPS analysis*

XPS measurements were performed using a Thermo Scientific K-Alpha X-Ray Photoelectron Spectrometer using monochromatic  $\text{AlK}\alpha$  radiation (1486.6 eV). High resolution scans were

performed with a 50 eV analyser pass energy and 0.1 eV step size. Binding energies of each element were referenced to carbon C1s peak at 284.8 eV. Samples were prepared by dispersing the aqueous suspensions of the samples onto gold coated glass slides with the excess solvent evaporated.

### *Electrochemilumescence*

Two different systems were used to record the ECL data. Firstly, a home-made system consisting of an electrochemical cell based on a home-made glassy carbon (Tokai Inc.) disk electrode (3 mm diameter) as the working electrode, which was closely facing the PMT at a distance of a few millimetres. The working electrode was mechanically and electrochemically cleaned for the electrochemical measurements. An Ag/AgCl (1M KCl) electrode from CHI-Instruments, separated from the catholyte by glass frits, was used as the reference electrode. A platinum wire was used as the counter electrode. The system was controlled using an Autolab electrochemical workstation PGSTAT101 (Metrohm, The Netherlands) coupled with a photosensor module with a photomultiplier tube (PMT, Hamamatsu, H10723-01, Japan). The pulsing potential was between 0 and 1.4 V vs Ag/AgCl (1M KCl). The pulse width was 1 second. The photocurrent produced by the PMT was directly converted to a voltage signal through the photosensor module and acquired by the external input channel of the analog-to-digital converter (ADC) of the Autolab. The transients and the faradic currents were managed using the software package “NOVA” provided with the Autolab. The ECL spectra were acquired using a calibrated electron multiplying charge couple device (EM-CCD) camera (A-DU970N-UVB Andor technology, Newton EM-CCD) coupled with a spectrograph (Andor Technology, Shamrock 163).

## 5.5.2 Synthetic procedures

### *Si NPs-[Ru]*

To a 10 mL flask was added microemulsion Si NPs (10 mg in 2 mL dry DMF) under Ar. N,N-diisopropylethylamine (10  $\mu$ l) was then added with stirring to increase the pH of the solution to 9. [Ru] complex NHS ester (25 mg, 21  $\mu$ mol) was dissolved in 3 mL dry DMF and then slowly added to the stirring solution in the flask. The reaction mixture was then stirred in the dark at room temperature under Ar for 16 hrs. After concentrating the solution in vacuo, the crude product was re-dispersed in methanol and purified by size-exclusion chromatography (Sephadex LH-20). After eliminating molecular impurities and unbound complex in the final fractions as monitored by thin-layer chromatography, fractions containing the final product

were combined, the solvent removed and the orange residue redispersed in water. Final product is a deep orange dispersion of Si NPs-[Ru] in water.

#### *Si NPs-[Ir]*

To a 10 mL flask was added microemulsion Si NPs (5 mg in 2 mL dry DMF) under Ar. N,N-diisopropylethanamine (10  $\mu$ l) was then added with stirring to increase the pH of the solution to 9. [Ir] complex NHS ester (10 mg, 5  $\mu$ mol) was dissolved in 3 mL dry DMF and then slowly added to the stirring solution in the flask. The reaction mixture was then stirred in the dark at room temperature under Ar for 16 hrs. After concentrating the solution in vacuo, the crude product was re-dispersed in methanol and purified by size-exclusion chromatography (Sephadex LH-20). After eliminating molecular impurities and unbound complex in the final fractions as monitored by thin-layer chromatography, fractions containing the final product were combined, the solvent removed and the orange residue redispersed in water. Final product is an orange dispersion of Si NPs-[Ir] in water.

## 5.6 References

- [1] L. Hu, G. Xu, *Chem. Soc. Rev.* **2010**, *39*, 3275.
- [2] M. M. Richter, *Chem. Rev.* **2004**, *104*, 3003–3036.
- [3] M.-J. Li, P. Jiao, M. Lin, W. He, G.-N. Chen, X. Chen, *The Analyst* **2011**, *136*, 205–210.
- [4] J. I. Kim, I.-S. Shin, H. Kim, J.-K. Lee, *J. Am. Chem. Soc.* **2005**, *127*, 1614–1615.
- [5] I.-S. Shin, J. I. Kim, T.-H. Kwon, J.-I. Hong, J.-K. Lee, H. Kim, *J. Phys. Chem. C* **2007**, *111*, 2280–2286.
- [6] S. Zanarini, E. Rampazzo, L. D. Ciana, M. Marcaccio, E. Marzocchi, M. Montalti, F. Paolucci, L. Prodi, *J. Am. Chem. Soc.* **2009**, *131*, 2260–2267.
- [7] S. Zanarini, E. Rampazzo, S. Bonacchi, R. Juris, M. Marcaccio, M. Montalti, F. Paolucci, L. Prodi, *J. Am. Chem. Soc.* **2009**, *131*, 14208–14209.
- [8] M.-J. Li, Z. Chen, N. Zhu, V. W.-W. Yam, Y. Zu, *Inorg. Chem.* **2008**, *47*, 1218–1223.
- [9] Y. Wang, A. Hu, *J. Mater. Chem. C* **2014**, *2*, 6921.
- [10] D. P. Puzzo, E. J. Henderson, M. G. Helander, Z. Wang, G. A. Ozin, Z. Lu, *Nano Lett.* **2011**, *11*, 1585–1590.
- [11] M. L. Mastronardi, E. J. Henderson, D. P. Puzzo, Y. Chang, Z. B. Wang, M. G. Helander, J. Jeong, N. P. Kherani, Z. Lu, G. A. Ozin, *Small* **2012**, *8*, 3647–3654.
- [12] A. Gupta, S. Hartner, H. Wiggers, *TechConnect Briefs* **2010**, *1*, 376–378.
- [13] B. Ghosh, N. Shirahata, *Sci. Technol. Adv. Mater.* **2014**, *15*, 014207.
- [14] N. Myung, Y. Bae, A. J. Bard, *Nano Lett.* **2003**, *3*, 1053–1055.
- [15] S. Carrara, F. Arcudi, M. Prato, L. De Cola, *Angew. Chem. Int. Ed.* **2017**, *56*, 4757–4761.
- [16] W. Miao, J.-P. Choi, A. J. Bard, *J. Am. Chem. Soc.* **2002**, *124*, 14478–14485.



# Chapter 6

## Instrumental techniques

### Abstract

This chapter provides a short overview of the instrumental techniques used in the thesis along with their principles. Only the general features of techniques are described, while details of specific experiments and measurements are found in the experimental sections of the previous chapters.

### 6.1 UV-Vis absorption spectroscopy

UV-Vis absorption spectroscopy refers to absorption spectroscopy occurring in the ultra-violet to visible regions of the electromagnetic spectrum. When this light passes through a medium, a quantitative measurement of the light transmitted through, and therefore absorbed by the medium species as a function of wavelength can be made. Transmittance ( $T$ ) at a given wavelength ( $\lambda$ ) is a ratio between the intensity of light that has passed through the medium (transmitted light,  $I_s$ ) and the intensity of incident light before passing through the medium ( $I_0$ ). This is defined by the following equation:

$$T(\lambda) = \frac{I_s}{I_0}$$

Absorbance ( $A_s$ ) can be defined as the negative logarithm of transmittance or the logarithmic ratio between  $I_0$  and  $I_s$  as shown:

$$A_s(\lambda) = -\log T = -\log \frac{I_s}{I_0} = \log \frac{I_0}{I_s}$$

From here, it is possible to define absorbance by the Beer-Lambert law as shown:

$$A_s(\lambda) = \varepsilon(\lambda) \cdot l \cdot c$$

Where  $\varepsilon$  is the molar extinction coefficient ( $\text{L mol}^{-1} \text{cm}^{-1}$ ),  $l$  is the path length of light through the medium (cm) and  $c$  is the concentration ( $\text{mol L}^{-1}$ ). There are limitations to the application

of the Beer-Lambert law in that it cannot be applied to samples that experience scattering or aggregation phenomena and the samples must be of a low enough concentration ( $A_s$  below 1.00) in order to maintain the validity of the linear relationship proposed by the law.

A schematic representation of the most commonly used double beam UV-Vis spectrophotometer is shown below in figure 6.1.

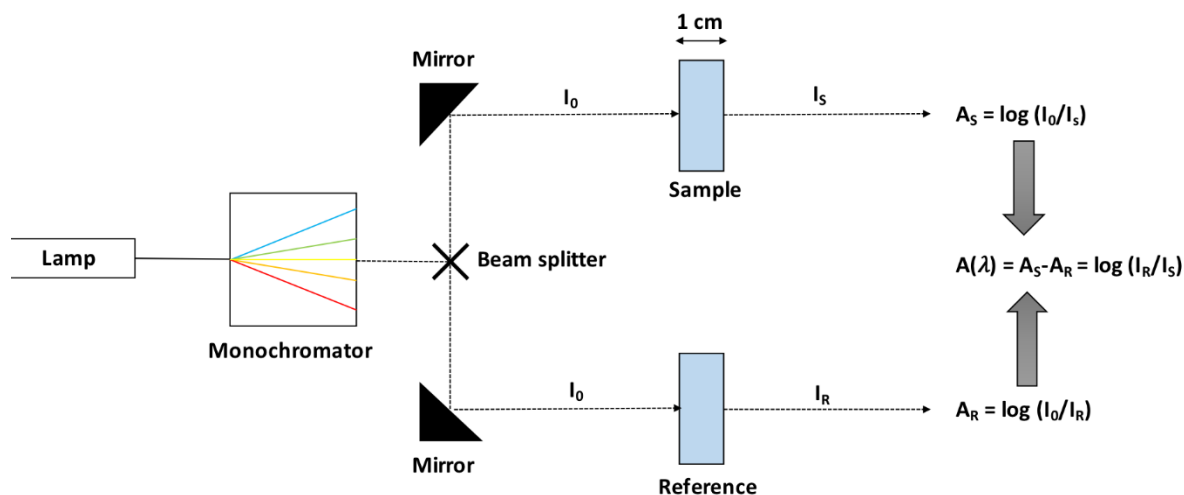


**Figure 6.1:** Schematic representation of the UV-vis absorption spectrometer and the measurement principle<sup>[1]</sup>

Incident light across the UV-visible spectral range is emitted from the lamp and passes through the monochromator, which selects the specific chosen wavelength. The monochromatic light is then split into two beams and directed through each of the two sample holders in the instrument simultaneously. In the case of the illustrated setup where a liquid medium is used, one beam of light passes through a cuvette containing just the pure solvent (reference) and the other passes through a cuvette containing the sample dispersed in the same solvent (sample). The absolute absorbance of the sample is then calculated by subtracting the absorbance of the sample from the absorbance of the reference. Absorption spectra shown in this thesis were recorded on a Shimadzu UV-3600 double-beam UV-VIS-NIR spectrophotometer.

## 6.2 Emission and excitation spectroscopy

Emission spectra show the intensity of light emitted from a sample measured against the emission wavelength at a constant excitation wavelength. On the other side, excitation spectra

show the intensity of excited light measured against the scanned excitation wavelength at a specified emission wavelength<sup>[2]</sup>. A general setup of a spectrofluorometer used to measure emission and excitation spectra is displayed in the schematic representation (figure 6.2) below.

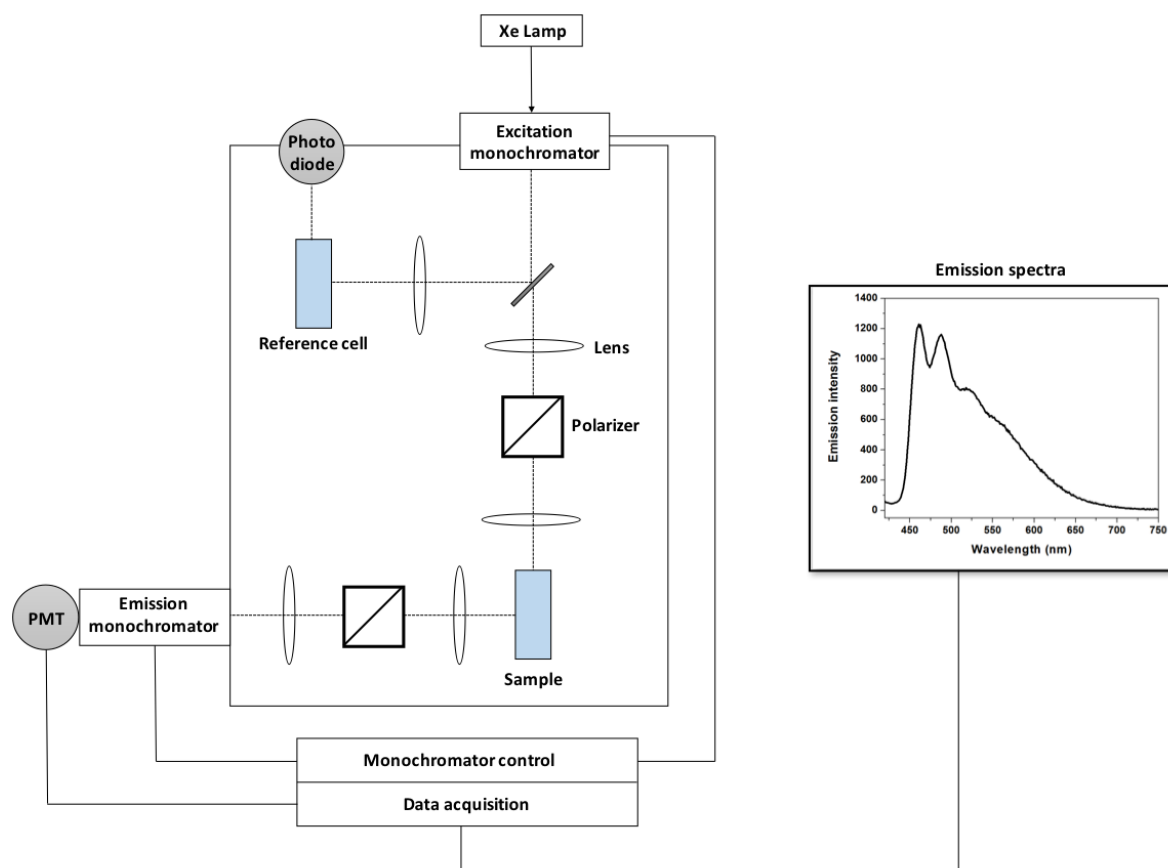


**Figure 6.2:** Schematic representation of the fluorescence spectrophotometer and the setup for steady state measurements<sup>[2]</sup>

The steady-state emission spectra shown in this thesis were recorded using a HORIBA Jobin-Yvon IBH FL-322 Fluorolog 3 spectrometer equipped with a 450 W xenon arc lamp as the excitation source, double-grating excitation and emission monochromators ( $2.1 \text{ nm mm}^{-1}$  of dispersion;  $1200 \text{ grooves mm}^{-1}$ ), and a TBX-04 single-photon-counting device as the detector. Light from the Xe lamp is passed through a monochromator, which selects a specified excitation wavelength, and is then directed onto the sample, with a small amount going to a reference channel. The emission of the sample, collected at  $90^\circ$  relative to the incident light, passes through a second monochromator before reaching the detector. At this point, the reference channel is used to correct the wavelength-intensity dependence of the excitation light.



## 6.3 Photoluminescence quantum yield

Photoluminescence quantum yield defines the efficiency of photon emission by a species. Simply, it is defined as the ratio of photons emitted to photons absorbed.

Quantum yields in this thesis were measured by an absolute method using an integrating sphere<sup>[3]</sup>. The general setup of the apparatus is shown below in figure 6.3

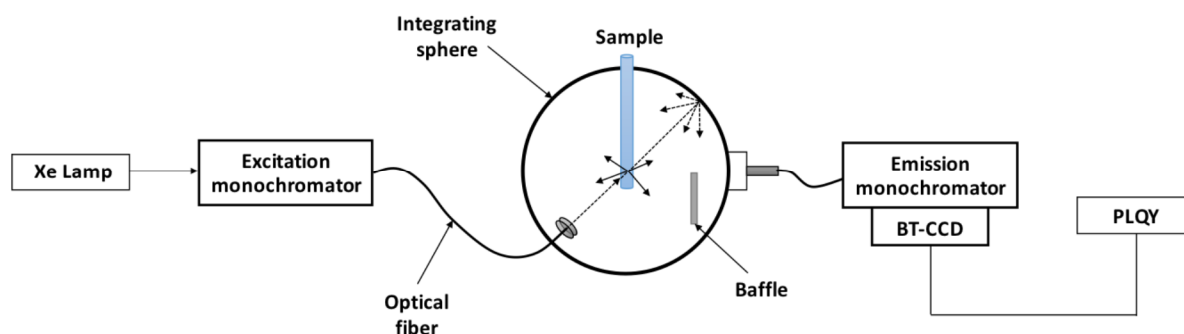


**Figure 6.3:** Schematic representation of an integrating sphere used for absolute quantum yield measurements<sup>[4]</sup>

From the Xe lamp light source, an incident beam is passed through a monochromator to select a specific wavelength. The monochromatic beam passes along an optical fibre and enters the integrating sphere, irradiating the sample. All of the photons emitted by the sample are collected after total reflection in the integrating sphere by a calibrated photodiode and enter an emission monochromator via a second optical fibre, and from there they pass into the detector. A reference is measured prior to the sample and the software uses this to correct the quantum yield of the sample and calculate the absolute photoluminescence quantum yield through the following equation:

$$\Phi = \frac{N_{emission}}{N_{absorption}} = \frac{\int \frac{\lambda}{hc} \{I_{em}^S(\lambda) - I_{em}^R(\lambda)\} d\lambda}{\int \frac{\lambda}{hc} \{I_{ex}^R(\lambda) - I_{ex}^S(\lambda)\} d\lambda}$$

Where:  $N_{absorption}$  is the number of photons absorbed by the sample

$N_{emission}$  is the number of photons emitted by the sample

$I_{em}$  is the intensity of emission

$I_{ex}$  is the intensity of the excitation

$h$  is Plank's constant

$c$  is the velocity of light

$R$  and  $S$  superscripts denote reference and sample respectively.

In this thesis, all quantum yields were measured using a Hamamatsu Photonics absolute PL quantum yield measurement system (C9920-02) equipped with a L9799-01 CW Xenon light source (150 W), a monochromator, a C7473 photonic multichannel analyzer, and an integrating sphere. The data was analysed with U6039-05 PLQY software (Hamamatsu Photonics, Ltd., Shizuoka, Japan).

## 6.4 Time resolved spectroscopy

The principle of time-correlated single photon counting (TCSPC) was used to conduct time resolved spectroscopy measurements and analyse the time dependant behaviour of excited states. A schematic of the setup to achieve this is shown in figure 6.4

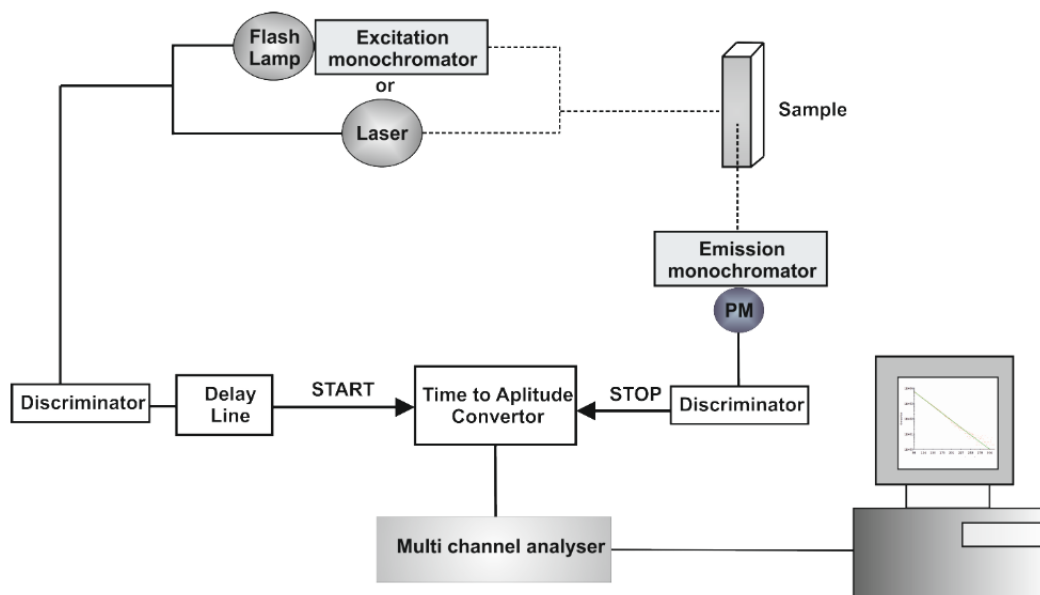


**Figure 6.4:** Schematic representation of the time correlated single photon counting (TCSPC) setup<sup>[2]</sup>

The principle is based on the ability to count individual photons and measure the luminescence decay of a sample. The time resolved profile of the decay is determined by measuring the

difference in time between the sample excitation and the associated photon emission that is detected by the photomultiplier. Using a laser as a source of pulsed light, an electrical signal is created and is directed to START input of the time-to-amplitude (TAC) converter. Following this, an electrical response is generated by the detector in response to a photon emitted through the sample luminescence, which is used as a STOP signal for the TAC. Charging of the capacitor is initiated by the START pulse and is terminated by the STOP pulse. As a result, the final voltage is proportional to the time between the two pulses. Several repetitions of the measurement create a histogram of events, which correspond to the decay curve.

In this thesis, time-resolved measurements were performed using a PicoHarp 300 equipped with a TCSPC system on the Fluro Time 300 (PicoQuant) spectrophotometer. Samples were excited by a laser source, which was mounted directly on the sample chamber at 90° to a Czerny-Turner type emission monochromator (2.7 nm mm<sup>-1</sup> of dispersion; 1200 grooves mm<sup>-1</sup>). Emission signal was collected by a PMA-C 192M single photon counting detector and visualised using EasyTau software. Data analysis was performed using FluoFit software (PicoQuant) and the quality of the fit was assessed through minimisation of the reduced  $\chi^2$  function and by human inspection of weighted residuals.

## 6.5 Transmission Electron Microscopy (TEM)

Transmission Electron Microscopy (TEM) is a powerful microscopy technique used to produce images with down to atomic scale resolution. It is based on the interaction of a sample with a high-energy electron beam of between 100 to 300 keV in a high vacuum chamber. A general schematic of a TEM instrument is shown in figure 6.5.

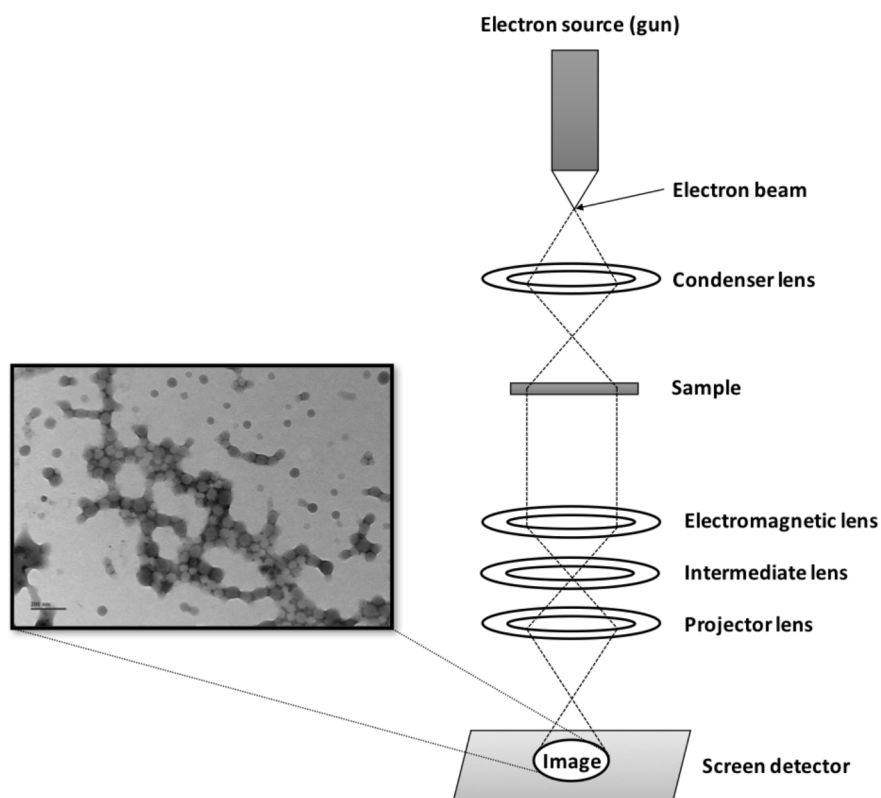


**Figure 6.5:** Schematic representation of a transmission electron microscope<sup>[5]</sup>

The electron gun is the source of the electron beam and emits electrons into the vacuum. Here, the beam of electrons is accelerated and focused towards the sample by passing through the electromagnetic condenser lens. The electrons that are not scattered by the sample and are transmitted through it are focused by the objective lens and directed to the fluorescent screen, where they are detected and processed by the image recording system. The result is generation of a shadow image of the sample, with components displayed in different bright or dark contrasts depending on the density and thickness of the material. The condenser lens allows control of magnification by controlling the diameter of the incident electron beam, where for higher magnifications, the diameter of the beam is reduced and condensed strongly onto the sample.

## 6.6 X-ray Photoelectron Spectroscopy (XPS)

XPS is a powerful analytical technique by virtue of its high sensitivity, which allows a specific atomic signal to be distinguished from the large majority of other atoms present in the sample.

A schematic example of the process occurring during the XPS measurement is shown in figure 6.6.

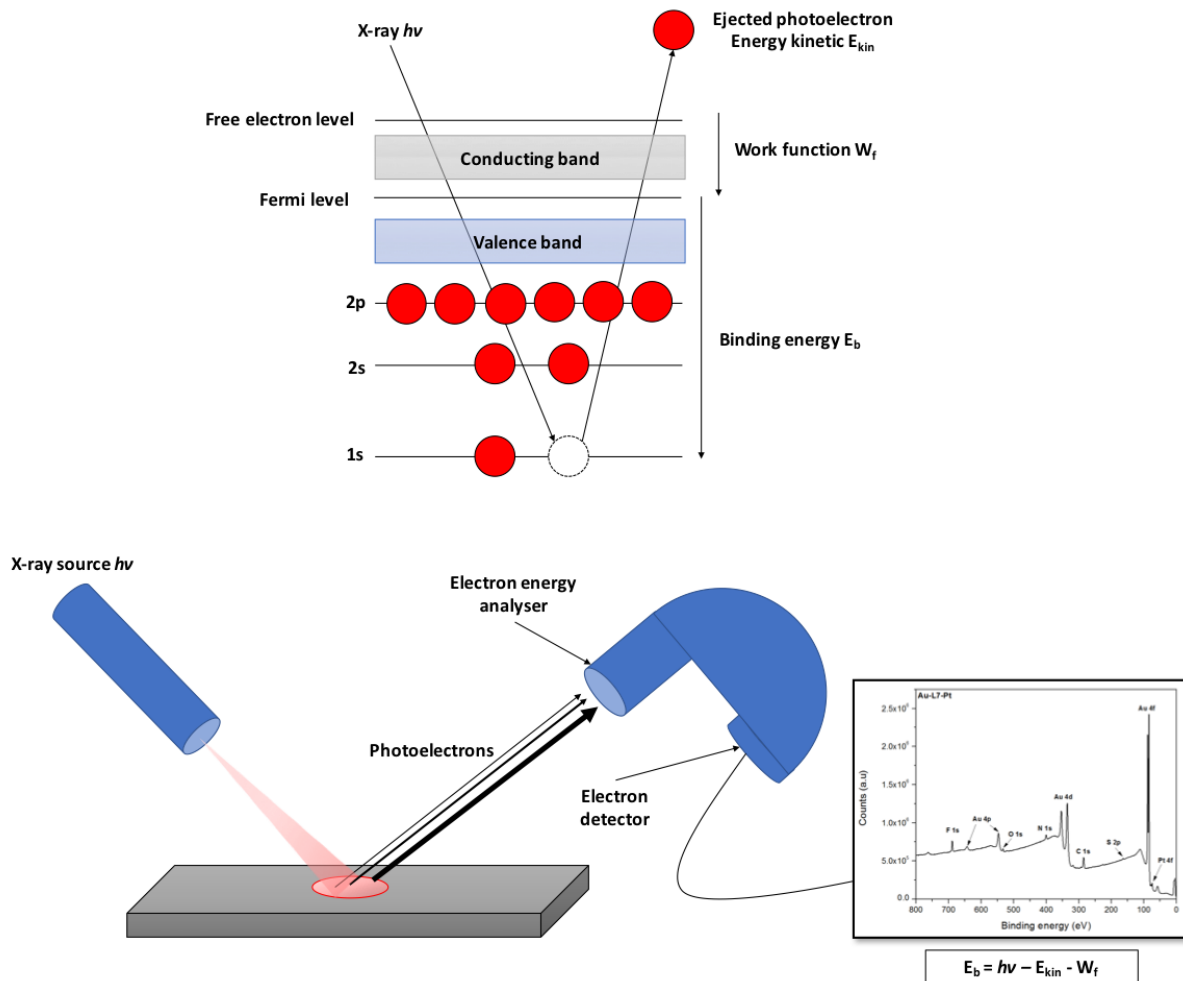


**Figure 6.6:** Schematic representation of the XPS measurement principle<sup>[5]</sup>

An incident ray (200~2000eV) is applied under vacuum onto the sample and an electron in the K shell (1s electron) is ejected from the bombarded atom. The photoelectron is collected by the electron multiplier detector and analysed by the electron spectrometer to acquire the kinetic energy ( $E_k$ ). The binding energy ( $E_B$ ) of the electron is used to identify the electron regarding its parent element and the original atomic energy level. It can be described by the following equation:

$$E_B = h\nu - E_k - W$$

Where:  $h\nu$  is the X-ray energy

$E_k$  is the kinetic energy of the electron

$W$  is the work function of the spectrophotometer

EB can be determined from the three above parameters, which are either known constants or are measurable.

In this thesis, XPS measurements were carried out using a Thermo Scientific K-Alpha X-ray Photoelectron Spectrometer with a monochromatic  $AlK\alpha$  radiation ( $h\nu = 1486.6$  eV;  $\lambda = 8.340113$  Å). Survey measurements were performed with a 200 eV analyzer pass energy and a 1 eV energy step size to calculate the atomic concentrations. Element scans were performed with 50 eV analyzer pass energy and a 0.1 eV energy step size to obtain the chemical state information. All the obtained binding energies were referenced from the carbon 1s peak, originating from the residual  $CO_2$ , at 284.80 eV.

## 6.7 X-ray diffraction

The broad technique of powder diffraction involves the use of radiation for the sensitive structural characterisation of a powder or micro- to nanocrystalline samples. In the case of X-ray diffraction, X-rays are the radiation diffracted on the sample for the analysis. A schematic of the setup and principle of the measurement is shown in figure 6.7.

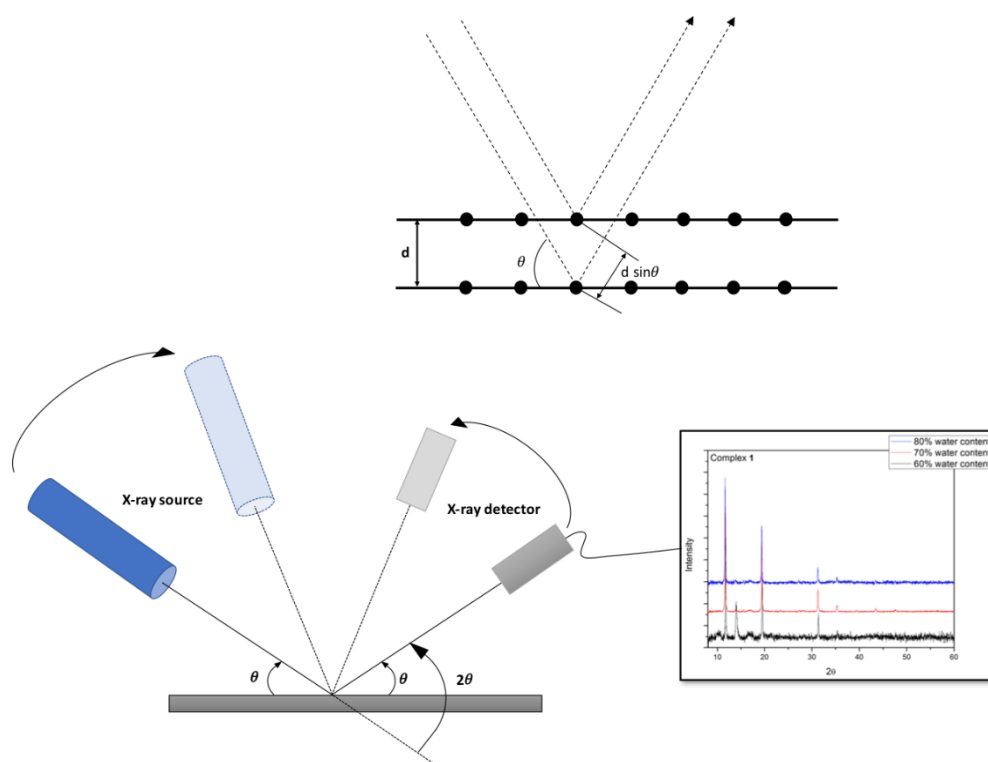


**Figure 6.7:** Schematic representation of the X-ray diffraction measurement principle<sup>[6]</sup>

A monochromatic X-ray is directed onto the sample with a glancing angle  $\theta$ . Each of the crystalline planes of the sample reflects a small fraction of this incident radiation beam. The radiation is scattered by the atoms of the crystalline system and undergoes constructive interference. For a crystalline solid, the incident waves from adjacent planes are separated by an interplanar distance  $d$ . The difference of the optical path is equal to  $2d \sin \theta$  and related to the incident wavelength  $\lambda$  by the Bragg equation:

$$2d \sin \theta = n\lambda$$

Where:  $n$  is the positive integer

$\lambda$  is the wavelength of the incident X-ray beam in nm

$d$  is the distance between adjacent planes of atoms, the d-spacing in nm

$\theta$  is the glancing angle in  $^\circ$

A diffraction pattern can be obtained by measuring the intensity of scattered waves as a function on the scattering angle. High intensity Bragg peaks are observed in the diffraction pattern at points where the scattering angles satisfy the Bragg condition.

In this thesis, powder XRD spectra were recorded on a Bruker D2 PHASER diffractometer operating in  $\theta - 2\theta$  mode with  $\text{CuK}\alpha$  (8.04 keV) radiation passed through a graphite monochromator, scanning between 8 and  $40^\circ$  with  $0.05^\circ$  step angle and a 100s dwell time to suppress noise.

## 6.8 Positron Emission Tomography

Following the administration of a radiotracer to a body, Positron emission tomography (PET) can be used to generate a two- or three-dimensional in vivo image. A general schematic for the process is shown below in figure 6.8<sup>[4]</sup>.

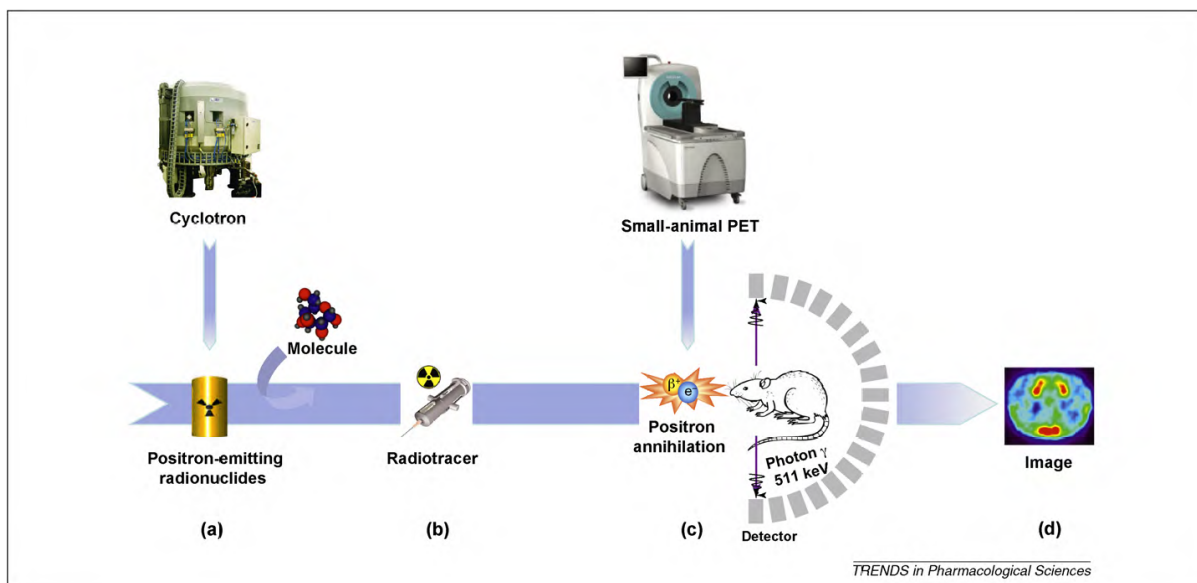


**Figure 6.8:** Schematic representation of the PET diagnosis process in small animals. Reprinted from Trends in Pharmacological Sciences., 31, S. Lancelot, L. Zimmer “Small-animal positron emission tomography as a tool for neuropharmacology”, 411–417., Copyright 2010, with permission from Elsevier.

In this thesis,  $^{64}\text{Cu}$  is used as the radionuclide. As a positron emitter, it stabilises by transforming a proton into a neutron and in the process, emits a positron. The positron loses energy until annihilating with an electron, in an event that produces two  $\gamma$ -photons with identical energies emitted in opposite directions. These are detected by the detector, which can position the source of the emission and after collecting a sufficient number of measurements from events, reconstruct an image showing the distribution of the emitting molecules.

## 6.9 References

- [1] B. Valeur, M. N. Berberan-Santos, *Molecular Fluorescence: Principles and Applications*, John Wiley & Sons, **2013**.
- [2] N. J. Turro, V. Ramamurthy, V. Ramamurthy, J. C. Scaiano, *Principles of Molecular Photochemistry: An Introduction*, University Science Books, **2009**.
- [3] J. C. de Mello, H. F. Wittmann, R. H. Friend, *Adv. Mater.* **1997**, 9, 230–232.
- [4] K. Suzuki, A. Kobayashi, S. Kaneko, K. Takehira, T. Yoshihara, H. Ishida, Y. Shiina, S. Oishi, S. Tobita, *Phys. Chem. Chem. Phys.* **2009**, 11, 9850–9860.
- [5] A. Lanje, S. Sharma, R. Pode, *Functional Nanomaterial Synthesis and Characterization Electrical, Magnetic and Optical*, **2014**.



- [6] I. Iordanova, V. Antonov, C. Sprecher, B. Gueorguiev, **2012**.
- [7] S. Lancelot, L. Zimmer, *Trends Pharmacol. Sci.* **2010**, *31*, 411–417.

## Summary

Nanoparticles have received growing attention over the past decades due to their potential as effective nanoprobes in bio-imaging<sup>[1]</sup>. Indeed, those based on semiconductor materials, such as II-VI or III-V quantum dots (QDs) have shown great potential in the field<sup>[2]</sup>. This is due to their high quantum yield of fluorescence, tunable emission wavelength, high photo bleaching threshold and high electro- and chemical stability, all of which contribute to their preference over organic dyes<sup>[3]</sup>.

Despite these promising properties however, there are some notable drawbacks to QDs that stand to prevent them from becoming established tools in the bio-imaging field<sup>[4]</sup>. For example, the most prominent QDs based on Cd, In, Pb, Hg, Se or Te derived cores with a ZnS shell have complicated surface chemistries that render them water-insoluble and difficult to functionalise with biomolecules. In addition to this, controlling the size of these QDs during synthesis is not so simple, making very small sizes for optimal bio-imaging applications hard to achieve and due the chemical nature of the core materials, they are non-biodegradable and inherently toxic in most cases<sup>[4]</sup>. While bio-imaging using these QDs has been demonstrated, these issues, especially the toxicity at low concentrations, have hindered progress with the materials.

In order to eliminate these problems, a number of actions have been suggested including; removing the heavy metals from the QD formulation, using a single inorganic element to simplify the properties of the material and above all, ensuring that this material is biodegradable, earth-abundant, has a well understood chemical behavior, has demonstrated biological applications and possesses minor biological roles such that it can be metabolised in the body<sup>[5]</sup>. This has led to a growing interest into research of silicon quantum dots or silicon-based nanoparticles (Si NPs). The high natural abundance of silicon and the well understood chemistry of Si NPs has led to a recognition of their broad potential of applications ranging from electronics to medicine<sup>[6]</sup>. Elemental Si making up the core of the Si NPs can be metabolized in the body to silicic acid, which is readily cleared by the kidneys<sup>[7]</sup> and studies have also shown that Si NPs are biodegradable and non-toxic<sup>[8]</sup>. A growing number of studies are demonstrating the use of these nanoparticles for *in vivo* imaging applications, which shows their promise towards the design of an optimal bio-imaging probe<sup>[3] - [9],[10],[11]</sup>.

In order to further improve bio-imaging to the levels required for the very early detection of diseases and for real-time image guided surgery, the simultaneous use of different non-invasive imaging techniques (multimodal imaging) has been explored with different nanoparticle systems<sup>[12]-[15]</sup>. While there are now numerous examples of bio-imaging with Si NPs in the literature<sup>[3] - [11]</sup>, few studies have put a focus on multimodal imaging and those that have regularly achieve the multimodal functionality by combining the Si NPs together with functional molecules in larger structures such as micelles<sup>[6]</sup>. This increases the size of the bio-imaging probe and can result in a limitation in imaging certain areas of the body. The lack of interaction between the Si NPs themselves and the other active molecules can also mean that imaging of exactly the same areas *in vivo* is not achieved once the transport releases the imaging cargo.

In the work of this thesis, titled “Synthesis and characterisation of silicon-based nanoparticles for diagnostic applications” the objective is to firstly explore the synthesis of silicon-based nanoparticles (Si NPs) of very small sizes (< 5 nm) through different synthetic techniques and obtain an in-depth characterisation of the prepared material. From here, we aim to assess the ability of the nanoparticles to work as multimodal imaging probes *in vitro* and *in vivo* through the surface functionalisation of the Si NPs with two different imaging labels that function with two separate imaging techniques. Finally, we aim to explore the application of the Si NPs in electrochemiluminescence (ECL), an emerging diagnostic technique for bioassays.

This thesis has been divided into six chapters. Chapter 1 presents an introduction to the topic of nanoparticles in medicine, with focus placed on their application in bio-imaging. SiNPs are presented as the material of choice and an overview of their preparation methods, properties, functionalisation, *in vitro* and *in vivo* applications is given. The common diagnostic techniques of optical fluorescence imaging, magnetic resonance imaging (MRI) and positron emission tomography (PET) are introduced and the possibility of imaging nanoparticles with two or more of these techniques simultaneously in multimodal imaging is briefly discussed. Different functional labels and molecules required for the imaging techniques and biological application of the nanoparticles are highlighted and with regards to one of these labels, namely transition metal complexes, the technique of electrochemiluminescence and its emerging use in bioassays is briefly covered.

Chapter 2 covers the synthesis of amine-terminated Si NPs through different routes and details the extensive characterisation to compare differences and attempt to identify the true chemical

nature of the core material. The SiNPs were prepared through two different synthetic pathways; the so-called microemulsion and hydrothermal methods, which are illustrated in figure 1.

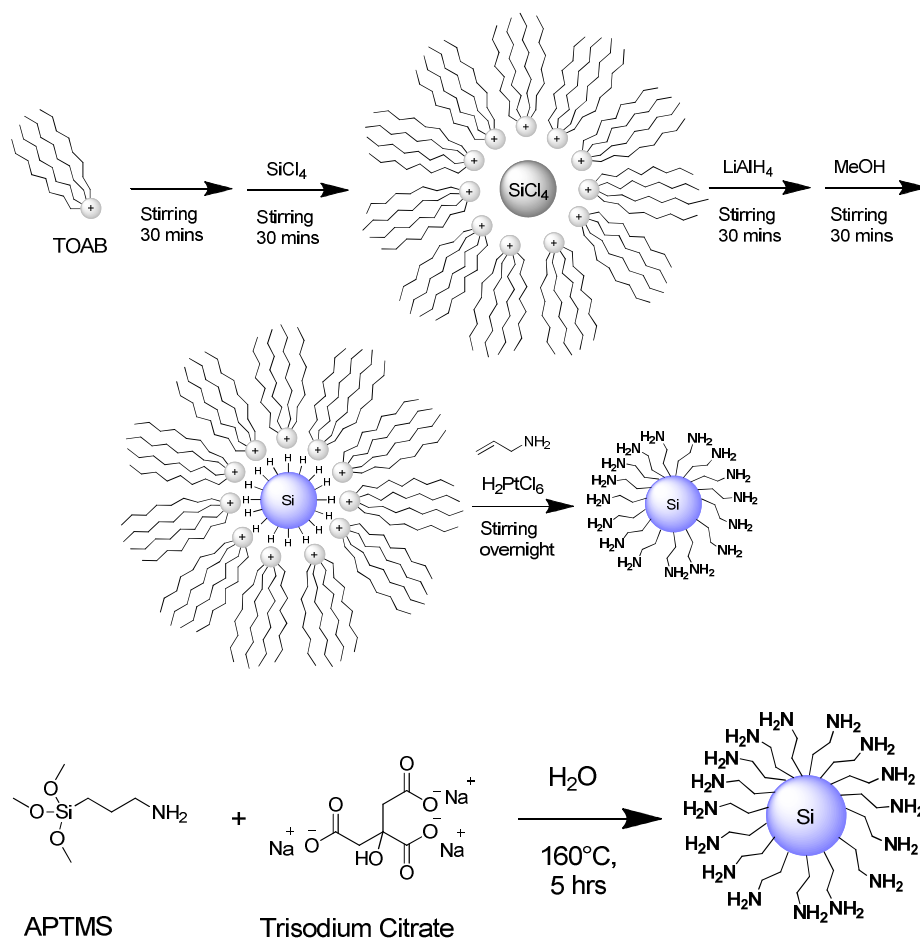


**Figure 2** Schematic representations of the syntheses of SiNPs. (Top) Amine-terminated SiNPs by reduction of  $\text{SiCl}_4$  (microemulsion method – microemulsion Si NPs)<sup>[10]</sup>. (Bottom) Amine-terminated SiNPs by hydrothermal reduction of APTMS (hydrothermal method – HT Si NPs)<sup>[11]</sup>

These bottom-up, wet chemistry methods both progress through the reduction of a silicon source as described. In the microemulsion synthesis, silicon tetrachloride is reduced by lithium aluminum hydride in a micelle formed by tetraoctylammonium bromide in toluene. The resulting hydride terminated Si NPs are then capped with allylamine using hexachloroplatanic acid as a catalyst. In the hydrothermal synthesis, (3-aminopropyl)trimethoxysilane (APTMS) is reduced by citric acid trisodium salt in water at high temperature in a pressure sealed vessel. Transmission electron microscopy (TEM) characterisation of the Si NPs shows the desired ultra-small sizes are achieved through both syntheses;  $2.7 \pm 0.9$  nm for the microemulsion method and  $3.1 \pm 0.8$  nm for the hydrothermal.

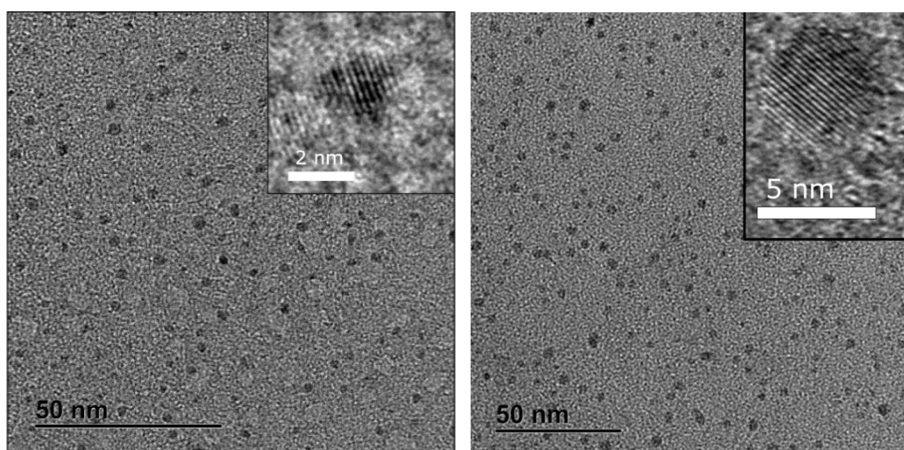


**Figure 2:** TEM images of amine terminated Si NPs obtained through the microemulsion method (left) and hydrothermal method (right). The crystalline lattice fringes of the Si NPs are clearly visible on the inset high-resolution images.

The photophysical properties of the prepared materials have been analysed by UV-vis spectroscopy, steady-state emission and excitation spectroscopy, time resolved luminescence spectroscopy to acquire data on excited state lifetimes and quantum yield measurements. A notable difference between the two Si NPs here is that those from the microemulsion method display an emission maximum that shifts depending on the excitation wavelength, while those from the hydrothermal method show an emission maximum at a constant wavelength regardless of the excitation wavelength. In the case of the microemulsion Si NPs, this behaviour is reported to be typical of elemental silicon nanoparticles, and is attributed to either the size distribution of the Si NPs or the presence of the Si-C bonds on the surface, which induce surface states that exhibit direct bandgap-like behaviour. The spectra acquired from the hydrothermal Si NPs (HT Si NPs) however are actually more similar to that of polymeric carbon dots, giving an initial indication that the structure of the core material could be different.

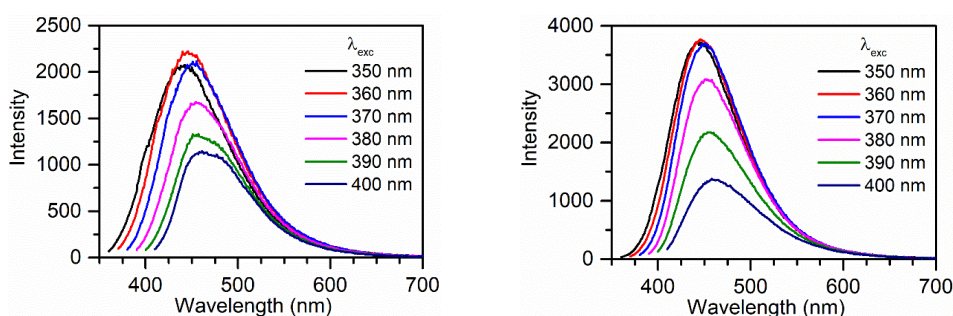


**Figure 3:** Emission spectra of microemulsion Si NPs (left) and HT Si NPs (right) in water

For both materials, the surface aminoalkyl groups can be identified by FT-IR analysis; broad bands centred at  $3380\text{ cm}^{-1}$  and  $2930\text{ cm}^{-1}$  correspond to N-H stretching, bands at  $2850\text{ cm}^{-1}$  corresponding to C-H stretching in the alkyl chains, bands at  $1200\text{ cm}^{-1}$  corresponding to Si-C

vibrations and in the case of HT Si NPs, an intense band at  $1026\text{ cm}^{-1}$  corresponding to Si-O-Si vibrations from the presence of silica in the structure.

X-ray photoelectron spectroscopy (XPS) measurements show the presence of more carbon and oxidised silicon species in the HT Si NPs compared to the microemulsion Si NPs, which is another strong suggestion that the core of the former is closer to silica than elemental silicon in nature and that the emission may indeed originate from a carbon based source.

Chapter 3 focuses on the HT Si NPs, for which the large amount of silica present in the structure was central to an investigation into the true structure on the core material. The experimental procedure for the hydrothermal synthesis was adapted from a reported method<sup>[11]</sup>, where microwave treatment of APTMS and citric acid trisodium salt was used instead of heating in a pressure sealed vessel in a conventional oven. The original paper reports that the obtained material is crystalline nanoparticles of elemental silicon, however, considering the nature of the reaction, it seemed more plausible to us that silica nanoparticles would be formed in the process. In order to test the claim of the original report and our hypothesis, a series of reactions were performed where either the APTMS or citric acid were removed from the reaction mixture before the treatment, with the same characterisation techniques performed thereafter. Notable are the near identical characteristics found between the products of both reactions, particularly with regards to the XPS high resolution silicon Si2p and carbon C1s spectra, which show the same number of peaks corresponding to the same types of bonding environments of the atoms in similar ratios for both products.

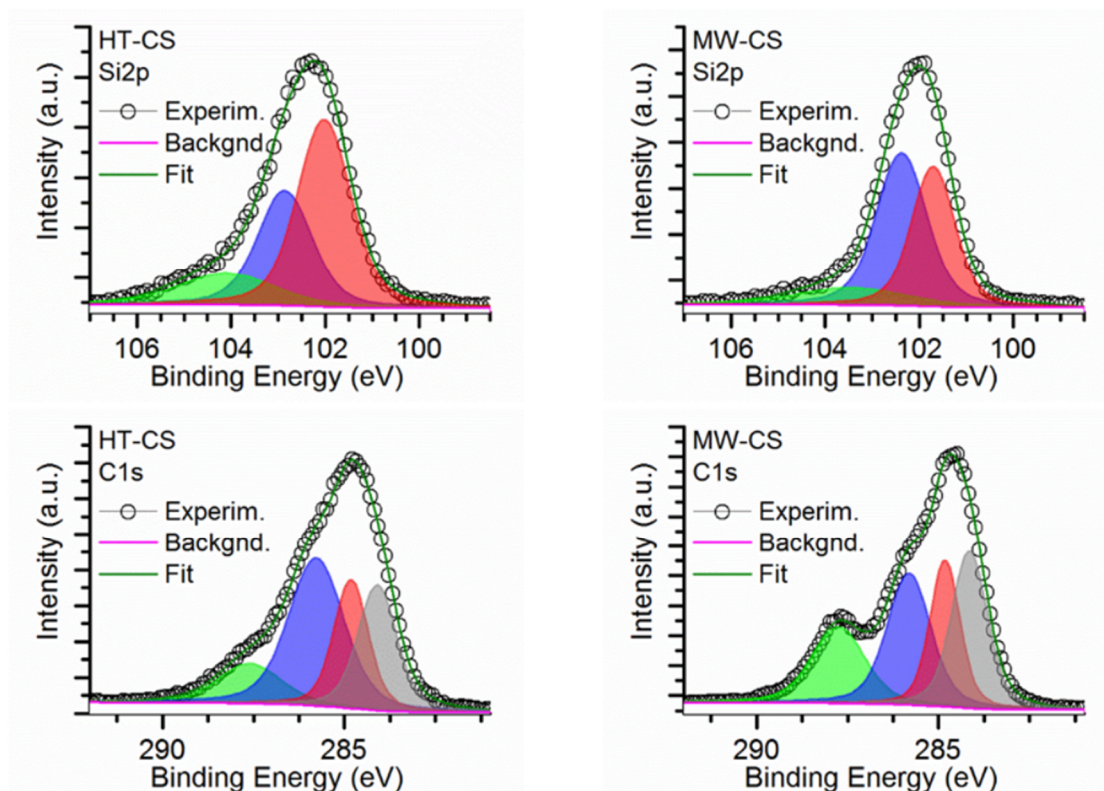


**Figure 4:** XPS high resolution scans of the Si2p (top) and C1s (bottom) lines of hydrothermal (HT-CS (left)) and microwave (MW-CS (right)) samples

Photophysical studies show that the absorption profiles of the Si NPs formed by the reaction of both APTMS and citric acid are identical to that of the citric acid treated alone, indicating that the photo-active component of the particles is related to the formation of a carbon-based product. FT-IR data shows that the particles do indeed have more in common structurally with silica. Symmetric and asymmetric stretches of Si-O-Si units are present in the spectra of both products, which is made very clear when compared to the spectrum for polyhedral silsesquioxane. Crystallographic data also strongly suggests that crystalline silicon is not present in the structures, indicating that elemental Si nanoparticles are not formed in the reaction. Both X-ray crystallography diffractograms for the Si NPs are characterised by two broad peaks. The one at ca.  $22^\circ$  can be ascribed to silica while the other at ca  $11^\circ$  must result from a second amorphous phase – most probably amorphous carbon

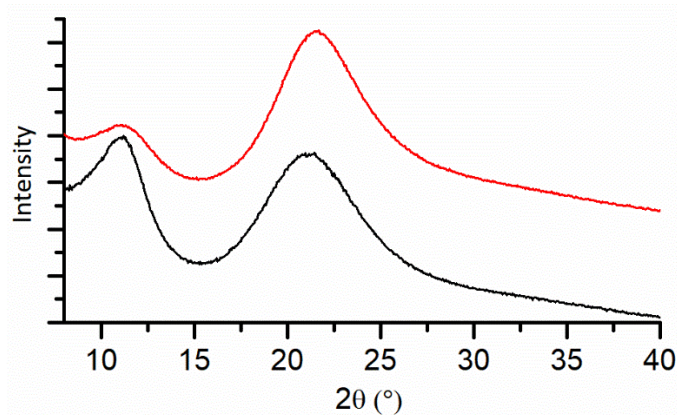


**Figure 5:** (Top) representative TEM images for sample HT-CS (left) and MW-CS (right) (scale bars = 50 nm). (Bottom) observed evolution of the live FFT for one particle over time.

Finally, TEM imaging revealed a fast phase transition in the particles subjected to the electron beam, that went from amorphous to crystalline as shown by the fourier transforms in figure 6. This could be caused by the heating from the electron beam, combined with the high vacuum conditions inside the analysis chamber and is further proof of the hybrid silica-carbon nature of the as synthesised material.

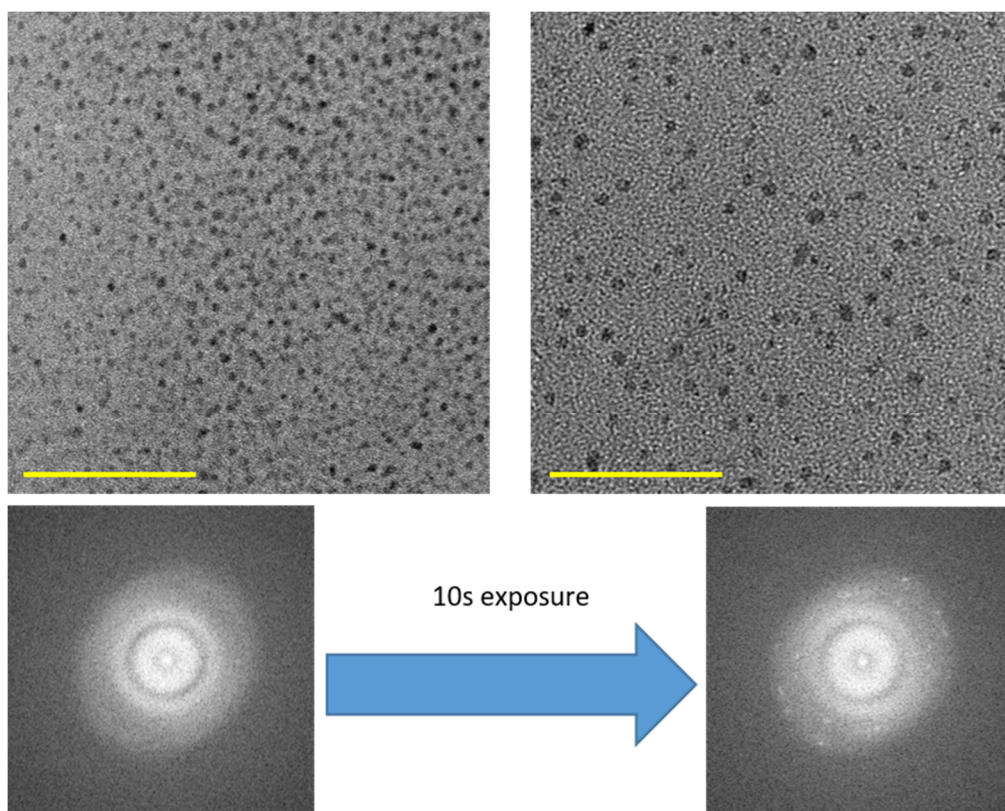


**Figure 6:** (Top) representative TEM images for sample HT-CS (left) and MW-CS (right) (scale bars = 50 nm). (Bottom) observed evolution of the live FFT for one particle over time.



In Chapter 4, the results of biological imaging investigations using the hydrothermal and microemulsion Si NPs are reported. With the material in hand, several biological studies were performed as shown in our recent publication<sup>[16]</sup>. Cell viability tests were used to assess the toxicity of the Si NPs towards healthy cells. Microemulsion Si NPs showed more of a cytotoxicity compared to HT Si NPs, which, if all of the residual surfactant is removed from the sample, can be attributed to the higher concentration of amine groups. Covalent functionalisation of the surface of the Si NPs via the terminal amines was performed in order to facilitate their use for *in vivo* imaging. Sulfo-cyanine5 NHS ester was used to give the Si NPs an *in vivo* visible emission in the red, with the attachment confirmed through photophysical measurements and FT-IR. Optical *in vivo* imaging of the functionalised particles in mice shows whole-body fluorescence at 20 minutes post injection and a concentration of the Si NPs in the bladder at 50 minutes post injection, demonstrating the fast clearance of the particles via the renal pathway. The possibility of using the Si NPs for PET imaging was also demonstrated. After grafting the surface with a <sup>64</sup>Cu-NOTA complex, *in vivo* studies in mice were once again performed, with whole-body imaging and movement to the kidneys and bladder for excretion observed in a similar timeframe<sup>[16]</sup>.

Next, a multimodal imaging probe (<sup>64</sup>Cu]Cu-Si NP-IR800-NOTA) was created by attaching both a fluorescent dye (IR 800) and a radioactive label (<sup>64</sup>Cu-NOTA) to the surface of the SiNPs. These allowed the nanoparticles to be tracked by optical fluorescence imaging and Positron Emission Tomography (PET). The application of the Si NPs in *in vivo* imaging was assessed through imaging and renal clearance in healthy mice.

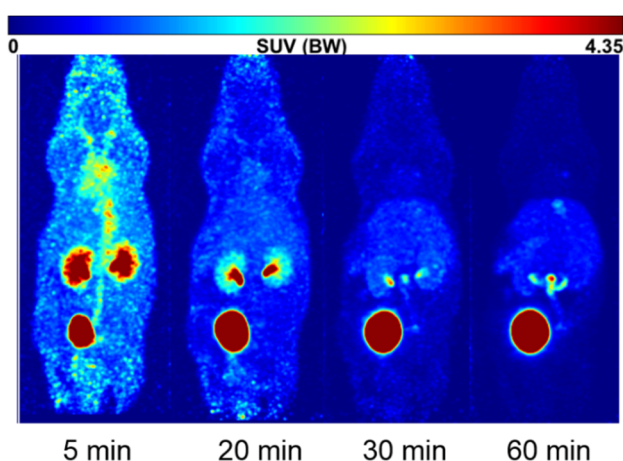


**Figure 7:** *In vivo* PET images of a mouse at different time points post-intravenous injection of [<sup>64</sup>Cu]Cu-Si NP-IR800-NOTA, showing full-body circulation and subsequent fast clearance from the kidneys via the bladder and urine.

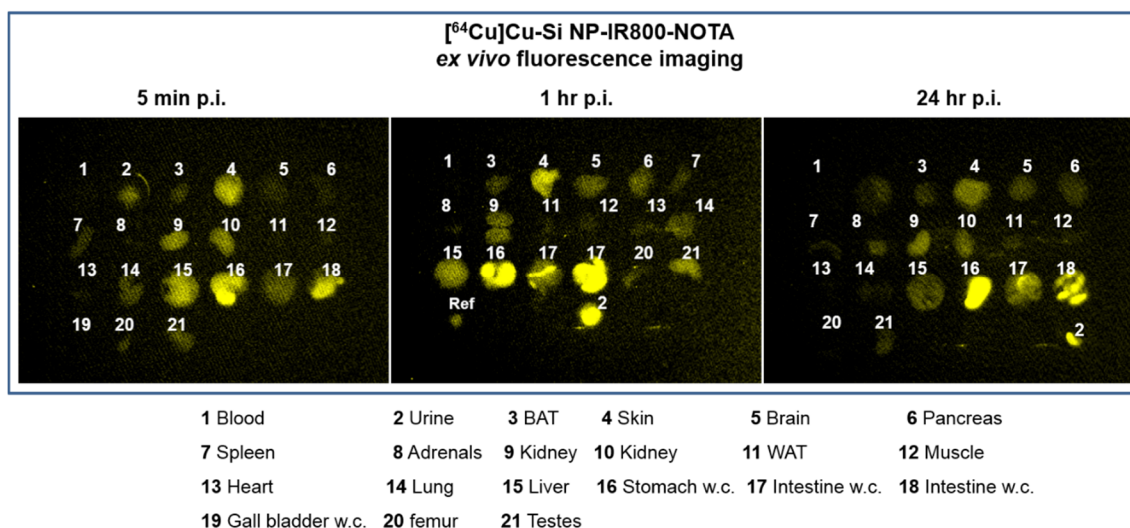


**Figure 8:** *Ex vivo* fluorescence imaging of mice organs at different time points post injection. Uniform distribution is observed in the first 5 mins, while after 1 hr the majority of the fluorescence is seen in the intestine and urine. At 24 hrs, traces of remaining fluorescence can be detected in the stomach, intestine and urine.

In another *in vivo* imaging study, the ability of the Si NPs to cross the blood-brain-barrier (BBB) for the imaging of brain tissues and tumors and their subsequent clearance was assessed. It is possible for glucose in the bloodstream to be transported across the BBB via specific transporter proteins present in the barrier and it has been shown that glucose-coated gold nanoparticles are able to traverse the barrier *in vitro*<sup>[17]</sup>. Applying this to our model, Si NPs were functionalised with Cyanine5 for optical imaging and D-(+)-glucosamine to support transport across the BBB. Uptake, imaging and clearance efficiencies were evaluated in mice using optical fluorescence imaging.

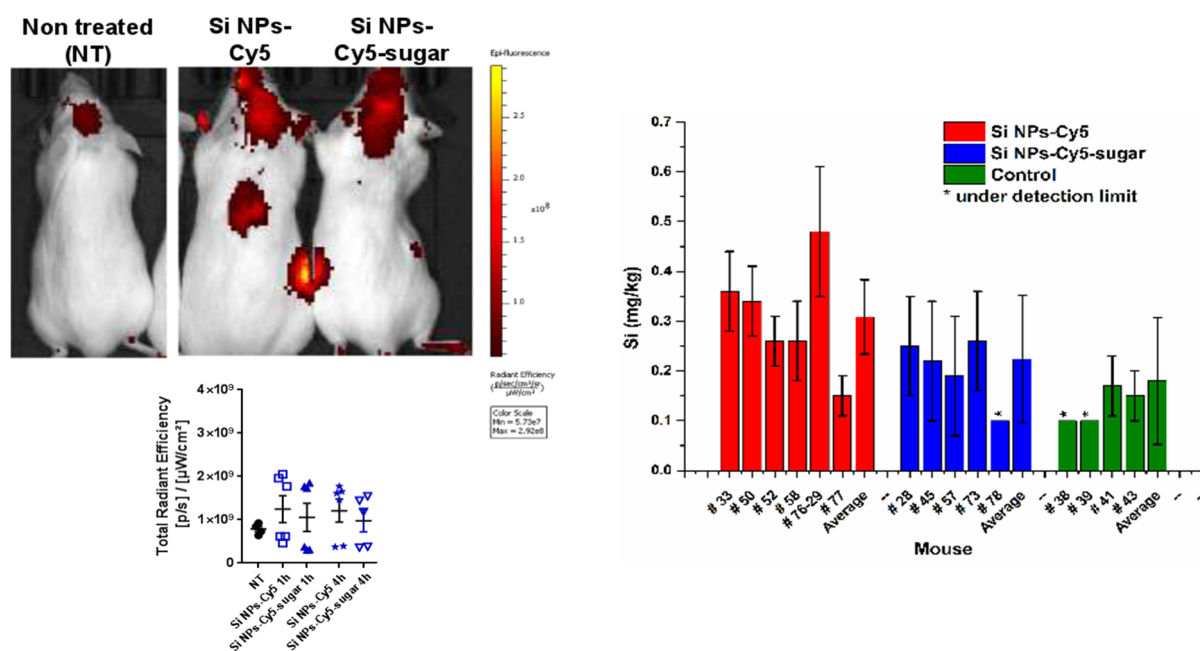


**Figure 9:** (Left) In vivo brain imaging of SI NP conjugates with graph to show radiant efficiency at 1 hr and 4 hrs post-intravenous injection. (Right) ICP-AES results from different mice brains showing quantity of Si found in the brain tissue.

**Some of the contents of Chapter 5 are confidential at the time of writing.**

Chapter 5 covers the creation of hybrid nanosystems composed of metal complexes of ruthenium and iridium coupled to Si NPs for use in diagnostic bioassays. Metal complexes have been well-used in the production of bioassays via the employment of electrochemiluminescence (ECL). Among these, ruthenium(II)tris-bipyridine ( $[\text{Ru}(\text{bpy})_3]^{2+}$ ) complex derivatives have become the “gold standard” after showing higher ECL efficiency than organic luminophores<sup>[18]</sup>. Recent studies have suggested that using metal complexes bearing more than one metal center or mounting complexes on a species that can hold multiple complexes together in close proximity could further increase the ECL efficiency. In order to investigate this further, Si NPs were grafted with a  $[\text{Ru}(\text{bpy})_3]^{2+}$  derivative and the ECL efficiency was tested in addition to the characterisation of the material by the previously used methods. Recently, iridium complexes have been reported to possess a higher ECL efficiency than ruthenium complexes. Therefore, a novel iridium complex was coupled to the microemulsion Si NPs in a system that uses the smallest Si NPs available in an attempt to optimise the diffusion kinetics of the system.

The microemulsion Si NPs were coupled to a novel sulfonated  $[\text{Ru}(\text{bpy})_3]^{2+}$  derivative via the amine surface groups and an active N-hydroxysuccinimide (NHS) ester respectively.

Microemulsion Si NPs were also conjugated to the iridium complex using a similar method. Using UV-vis spectroscopy, the concentrations of the systems were controlled to  $10^{-5}$  M by using the profile of the free complex at the same concentration as a reference. From this data, calculations to estimate the number of complexes bound to individual Si NPs could be made. ECL studies slightly support the initial hypotheses, with the microemulsion Si NPs-[Ru] system boasting a higher ECL efficiency than the novel complex alone, which is assumed to be due to the presence of amino groups on the Si NPs, which are able to function as co-reactants in addition to the TPrA in the solution. The ECL efficiency was lower than that of  $[\text{Ru}(\text{bpy})_3]^{2+}$  however, which was used as a reference, calculated to be 66% of the maximum efficiency of  $[\text{Ru}(\text{bpy})_3]^{2+}$ . Also of note was the low ECL efficiency calculated for the microemulsion Si NPs-[Ir] system, which is thought to be due to a combination of the lower than expected efficiency of the complex itself and the slow diffusion of the Si NPs to the electrode surface.

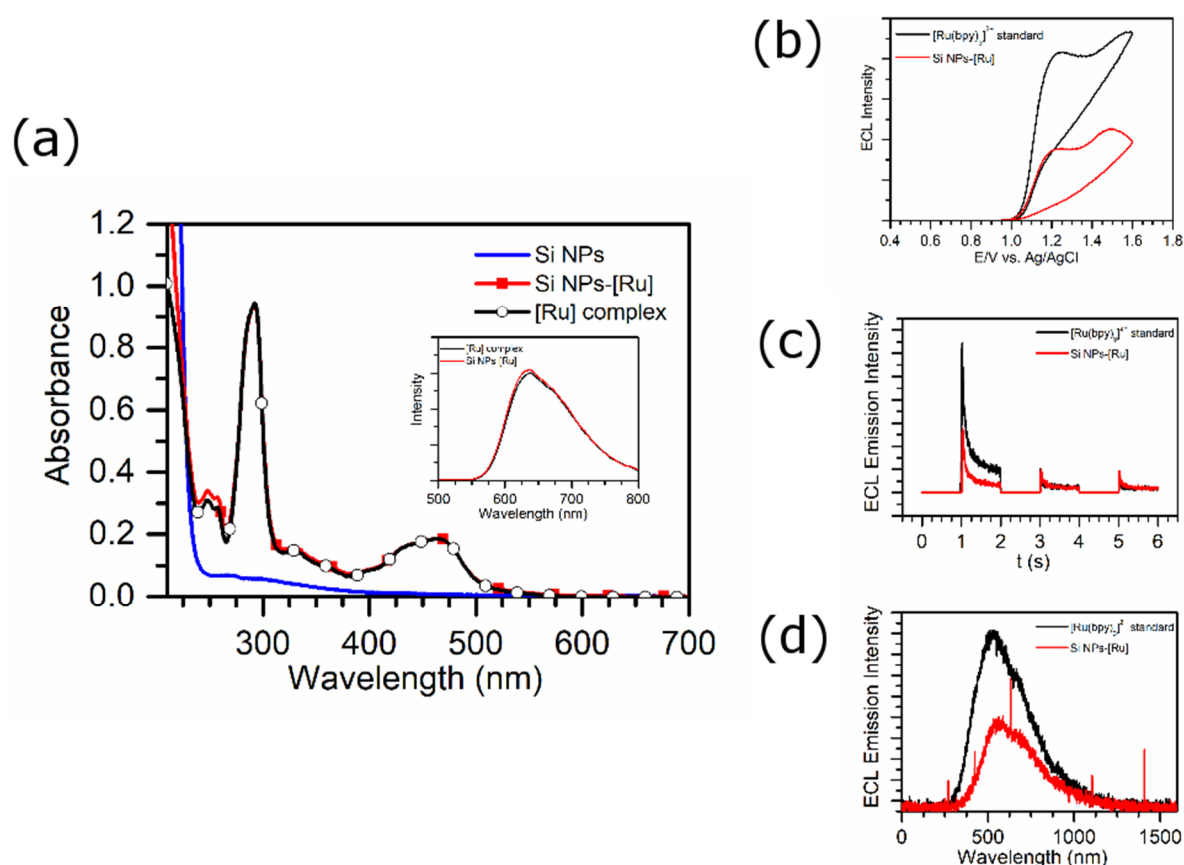


**Figure 10:** a) UV-Visible spectra of microemulsion Si NPs, Si NPs-[Ru] and the novel [Ru] complex in water (inset: emission spectra of the novel [Ru] complex and Si NPs-[Ru] in water). b) Cyclic voltammetry plots of  $[\text{Ru}(\text{bpy})_3]^{2+}$  and Si NPs-[Ru] in Procell. c) Chronoamperometry plots of  $[\text{Ru}(\text{bpy})_3]^{2+}$  and Si NPs-[Ru] in Procell. d) ECL emission spectra of  $[\text{Ru}(\text{bpy})_3]^{2+}$  and Si NPs-[Ru] in Procell.

In Chapter 6, a short overview of the instruments used in the thesis is given, along with brief details of their methods of use and principles.

In conclusion, amine terminated silicon based nanoparticles have been synthesised using two different methods. The structural characteristics of both have been scrutinized through thorough characterisation in order to determine the true natures of the core materials. The biocompatibility and application of various functionalised systems of Si NPs in bio-imaging has been tested with success in different studies. By coupling the smallest Si NPs with novel metal complexes, steps have been made towards the development of an efficient probe for bioassays and a foundation for further optimization has been established.

## Références

- [1] P. Sharma, S. Brown, G. Walter, S. Santra, B. Moudgil, *Adv. Colloid Interface Sci.* **2006**, *123–126*, 471–485.
- [2] M. Bruchez, M. Moronne, P. Gin, S. Weiss, A. P. Alivisatos, *Science* **1998**, *281*, 2013–2016.
- [3] M. Montalti, A. Cantelli, G. Battistelli, *Chem. Soc. Rev.* **2015**, *44*, 4853–4921.
- [4] R. Bilan, F. Fleury, I. Nabiev, A. Sukhanova, *Bioconjug. Chem.* **2015**, *26*, 609–624.
- [5] J. Liu, F. Erogbogbo, K.-T. Yong, L. Ye, J. Liu, R. Hu, H. Chen, Y. Hu, Y. Yang, J. Yang, et al., *ACS Nano* **2013**, *7*, 7303–7310.
- [6] F. Erogbogbo, K.-T. Yong, I. Roy, R. Hu, W.-C. Law, W. Zhao, H. Ding, F. Wu, R. Kumar, M. T. Swihart, et al., *ACS Nano* **2011**, *5*, 413–423.
- [7] L. T. Canham, *Adv. Mater.* **1995**, *7*, 1033–1037.
- [8] J.-H. Park, L. Gu, G. von Maltzahn, E. Ruoslahti, S. N. Bhatia, M. J. Sailor, *Nat. Mater.* **2009**, *8*, 331–336.
- [9] K. Linehan, H. Doyle, *Small* **2014**, *10*, 584–590.
- [10] J. H. Warner, A. Hoshino, K. Yamamoto, R. D. Tilley, *Angew. Chem. Int. Ed.* **2005**, *44*, 4550–4554.
- [11] Y. Zhong, F. Peng, F. Bao, S. Wang, X. Ji, L. Yang, Y. Su, S.-T. Lee, Y. He, *J. Am. Chem. Soc.* **2013**, *135*, 8350–8356.
- [12] M. Swierczewska, S. Lee, X. Chen, *Mol. Imaging* **2011**, *10*, 3–16.
- [13] S. Y. Lee, S. I. Jeon, S. Jung, I. J. Chung, C.-H. Ahn, *Adv. Drug Deliv. Rev.* **2014**, *76*, 60–78.

- [14] D.-E. Lee, H. Koo, I.-C. Sun, J. H. Ryu, K. Kim, I. C. Kwon, *Chem. Soc. Rev.* **2012**, *41*, 2656–2672.
- [15] A. Louie, *Chem. Rev.* **2010**, *110*, 3146–3195.
- [16] N. Licciardello, S. Hunoldt, R. Bergmann, G. Singh, C. Mamat, A. Faramus, J. L. Z. Ddungu, S. Silvestrini, M. Maggini, L. De Cola, et al., *Nanoscale* **2018**, *10*, 9880–9891.
- [17] R. Gromnicova, H. A. Davies, P. Sreekanthreddy, I. A. Romero, T. Lund, I. M. Roitt, J. B. Phillips, D. K. Male, *PLoS ONE* **2013**, *8*, e81043.
- [18] N. Kebede, P. S. Francis, G. J. Barbante, C. F. Hogan, *The Analyst* **2015**, *140*, 7142–7145.



# Acknowledgements

This section is the last, but by no means the least important of my thesis. In fact, by its nature, it holds the upmost importance! More than pages of typed words, it represents my deep thoughts reflecting over my PhD journey over the past few years, thinking of all the experiences I've had, the lessons I've learned and the people I have been so fortunate to meet, who have all had a helping hand in making this stage of my life unforgettable and making me into the person I have become now on the other side of it.

My first acknowledgement and sincere gratitude has to be given to my supervisor, Prof. Luisa De Cola. From the moment you answered my inquisitive email about the possibility of starting a PhD in your group, all the way through to now, you have given me opportunities and guidance that have not only improved my knowledge in chemistry, but have helped me learn how to approach many different situations in my professional and general life. Thank you for welcoming me into your group and for all of the fruitful discussions we have had. You have made me a much better scientist and a much stronger person.

Remaining on my teachings, I would first like to thank the University of Birmingham, the staff at the School of Chemistry, my former course mates and my former colleagues in the Pikramenou lab for giving me the great quality of education during my undergraduate MSci needed to undertake this PhD. I would like to thank the University of Strasbourg for all the opportunities given to me while enrolled on the PhD programme and for the financial support provided. Importantly, I would like to thank the Karlsruhe Institute of Technology (KIT) along with the Helmholtz Virtual Institute "NanoTracking" Project (now within the Nanoscale systems collaborative group at the Helmholtz Zentrum Dresden Rossendorf), and the "French-German Graduate school on Hybrid Organic-Inorganic Nanostructures and Molecular Electronics" for financing the great majority of my PhD work, and making it possible for me to attend various meetings and conferences.

My PhD journey began with me living in Karlsruhe and spending most of my time working at the Institute of Nanotechnology at KIT, so I will now move on to reflect on this chapter. I want to extend a big thank you out to all of the support and administrative staff at the INT for helping me throughout my time there, but there are a few people in this group who I feel deserve a special thanks from me. Heidi Hagel, Antje Hase and Susanne Speck, thank you for helping me with all financial matters and for your patience when I was struggling with the paperwork.



Christine Fischer and Patricia Jäger, thank you for giving me the friendliest welcome to the INT on my first day and for always being so warm thereafter, always being able to listen and offer advice on any issue I came to you with. Thank you, Dr Olaf Fuhr, for helping us out at times when we had puzzling issues in the lab and for ensuring that our safety was ensured. Dr Matthias Hettler, thank you for always being on hand to help me with different equipment and computer issues and for maintaining a great community feeling in the institute.

I would like to thank all of my colleagues throughout the INT, of whom there are again some who deserve special thanks. To everyone in the Electron Microscopy and Spectroscopy Lab, especially Dr Christian Kübel, Dr Di Wang, Dr Xiaoke Mu, Mohammad Saleh Gorji, Dorothee-Vinga Szabo and Sabine Schlabach, thank you for spending so much time with me on both the Tecnai and Titan TEMs to help me get images of my nanoparticles. At times (most times) it took long hours in the room with no results to show for it, but I am very grateful for every moment of your time that you gave to me, through which you helped me to learn a great deal about TEM in general. Dr. Dr. Michael Hirtz and Dr Sylwia Sekula-Neuner, thank you for making my extra-curricular time at the INT more enjoyable, especially with regards to the Christmas party (our quiz was the best!). Thank you to the members of the new Biedermann lab, Amrutha Prabodh, Laura Grimm, Philipp Avon and Matthias Schuster, for making the lab a better place to be in my later time at the INT and for involving me in the group activities. Lastly, I would like to thank my lunch mates, with whom I spent many nice break times with and had some good discussions with over various wild topics. Dr Lutz Greb, Dr Bernhard Schäfer, Dr John Francois-Greich and Dr Romain Danneau, despite the difference in our ages, you made me feel like I had a good group of friends that I could meet every day at the institute.

Next I would like to thank all of my project collaborators. First, all my colleagues and fellow scientists on the former Helmholtz Virtual Institute “NanoTracking” Project, with whom I attended meetings and shared many inspiring scientific discussions, different project collaborations and also some fun activities. Thank you to Dr Holger Stephan for being so inspirational in your ideas for the project and for giving me the opportunity to collaborate with your group in order to see some very interesting application of my nanoparticles. Garima Singh, thank you for all the work you have done in getting the great results of the PET for the nanoparticles. It has been invaluable and I wish you all the best for your upcoming defense too. Thank you very much also to Dr Kritee Pant, Dr Silvia Varela and Dr Robin Vernooij for providing me great inspiration with your work and being great friends to be with at the Nanotracking meetings. You made those days in Trapani and Dresden among the highlights of

my PhD. Thank you very much to Prof. Paolo Bigini and Laura Talamini at the Mario Negri Institute in Milan. Without your kind collaboration, the project of exploring the activity of the Si NPs across the BBB would not have been possible. You have been so brilliant to work with and Laura, I wish you all the best for your defence next year.

After two years of living in Germany, I finally moved to Strasbourg to finish the remainder of my PhD, so now I would like to mention all of the people who have been a part of my experience in Strasbourg, both within and outside the De Cola group, of who there are many. First I would like to thank Dr Corinne Bouillet for your invaluable help with acquiring TEM images of my nanoparticles in the final year of my PhD. Your determination to get the best out of every sample is one of the reasons I have been able to produce this thesis, and I can't thank you enough for that. Within the Institute de Sciences et Ingénierie Supramoléculaires, I would like to thank all of the administrative and support staff, along with my fellow PhD students and scientists all over the building for building such a nice atmosphere and making it an amazing place to come and work every day once I had moved. Some of you I have spent more time with and have gotten to know both in and out of the lab. Matilde, Agostino, Cosimo, Marco, Annet, Yoseline, Oussama, Dr Thomas Hermans, Serena and Michi, thank you for having such great personalities and making times during the PhD more fun.

Outside of the lab, I was lucky enough to meet a great group of people who I feel definitely helped me get the most out of my time in Strasbourg. First, back in Karlsruhe, Thomas and Veró, you have been amazing friends and I am forever grateful to you for finding me over Facebook. Thank you for all the parties and trips we made, which made my time in Karlsruhe so much more enjoyable. Veró, I wish you all the best with completing your thesis. Ramzi and Pilar, thank you for including me in your activities and for making our skiing trip one to remember. Daniela and the now Dr Joel, thank you for bringing your fun-loving personality whenever we met and teaching me the best in Colombian slang. The French people I have met, Dimby, Mustapha, Juline, Laurie, Kate (honorary French), Valentine, Faustine, Laura and Thomas. Thank you very much for making my experience much more authentic and adding your own uniqueness to everything we have done together. Then we have some of the "Italian crew". Lorenzo, Matteoandrea, Flavio, Alessia, Livia, Barbara, Alice and the crazy Masters girls Federica and Giulia. Thank you all for making me feel like I was actually doing my PhD in three different countries rather than two and for involving me in all of your amazing days out and parties. And to you Giulia, thank you for making me learn how to look after my very own fat plant!

There are so many people who I have met and gotten to know during my stay in Strasbourg. For everyone who I haven't listed here, know that you have all brought something to my experience in the city, both during work and play, and that I am forever grateful for meeting you.

Now I reflect on the many people I have been able to work with in the De Cola group. I remember how nervous I was having my interview in front of a group of around 35 of you right at the beginning, and now that I am leaving, as many people have come and gone, there are only around 15 of us. First I would like to thank Claire for all her help with the tricky administration and paperwork that is a natural part of the French system. Thank you for being the essential person in the workplace and a good friend. Thank you to Ines Below-Lutz for keeping the lab running during my first year in the group and for being always interested in how I was doing in Germany.

Everyone that I have shared everyday life in the lab with, I have been extremely lucky and honoured to work with. Some of you have been teachers, some of you fellow students, some of you my own or the students of colleagues, but all of you have been, and are, good friends.

Dr Angelique Faramus, thank you for being the first and most essential teacher I had in the lab and my pseudo supervisor. You helped me become a proper PhD student. Thank you for all your work on the TEM of our particles and for getting some of the brilliant images I have used in my thesis. Thank you for being an amazing taxi driver all of the times we went from Strasbourg to Karlsruhe, for being a great office mate, and a great friend.

Dr Damiano Genovese, thank you for all the great advice you gave me in the early days. You were also one of my awesome taxi drivers and one of my good friends outside the lab in Karlsruhe. Thank you for involving me in football and the other fun activities.

Dr Frank Biedermann, thank you for teaching me a number of tricks to work best in the lab. I know that you will be an amazing Prof. one day and I wish you and your group all the best.

Dr Eko Adi Prasetyanto, thank you for always being there to help us solve problems whenever they came up. I wish you and your family all the best in your new lives in Indonesia. Dr Matteo Mauro and Dr Alessandro Aliprandi, thank you for using your vast knowledge to help me with various things related to photophysics and science in general. Dr Simone Silvestrini, you have also been an essential person in my PhD journey and with regards to this thesis. Thank you for your help in driving our silicon/silica question project to completion and for your assistance

with the range of equipment we have in the institute. Dr Nadia Liccardello and Dr Chien Wei Hsu, thank you both for also being a great silicon teachers in my early days. I hope I have done you proud. Dr Nina Matusovich, thank you for your help with the synthesis of cobalt nanoparticles. Even though the project didn't quite work out, it was great to learn the new chemistry. Dr Leana Travaglini, Dr Brian Di Marco, Dr Sourav Chakraborty, Dr Ingrid Cabrera Puig, Dr Amparo (super tomato) Ruiz Carretero, Dr Valentina Giglio, Dr Elena Longhi, Dr Sarah Laird, Dr Marina Bantzi, Dr Maria del Carmen Ortega Liebana, Dr Luis Guillermo Moreno Alcantar, Dr. Etienne Borré, Loïc Donato, Dr Leti, Dr. Veronika Zajicova, Dr Federica Fiorini, Dr Alessandro Bertucci, Dr Dedy Septiadi and Dr Stephan Sinn, thank you all for being so helpful and for being so nice to be around, both in and out of the lab. Dr Pengkun Chen and Dr Hiroki Ohara, thank you for being great lunch buddies and for your help in the lab. Thanks also, along with Chien Wei, for the great trip we had to Prague.

There have been many visiting students in the lab that I have had the pleasure to meet, all of whom I am very grateful to call my friends. Christof, Simon, Martina, Natalia, Camilla, Qiang, Ligia, Guille, Francesca, Kasia and Cintia, thank you very much for all you help.

We have also had the pleasure of hosting many talented masters and bachelors students, to whom I am thankful for giving me renewed energy to work. I have to particularly mention Alexa (Koala) Carla, Silvia and Lucrezia. Though you made me party at a time when I said I wouldn't, I thank you girls for keeping things so fun and refreshing during my final year. A very special mention to Alessandra, my very own master's student. Thank you for all of your hard work and determination to get the results that we wanted. You have the makngs of a great researcher and I'm sure you'll do extremely well with your PhD.

My fun loving American colleague and now Dr Becky. Thank you for introducing me to skiing and climbing, for keeping me active during this time and for always being happy.

The original "La grande" herself, Dr Serena. Thank you for bringing you amazing personality everywhere with you. Your help both in and out of the lab has been absolutely invaluable. Thank you for being such a generous host to me so many times and providing me a place to stay when I needed it, both in Strasbourg and in Melbourne.

Mon pote, Dr Alberto. Thank you for being the knowledgeable and fun guy that you are. The lab was always buzzing when you were in it. Thanks for also being such a generous host when I needed your help.

Mon frère Dr Youssef. Thank you for your extreme kindness, patience and generosity. To talk about both science and football, you were one of the best. I wish you all the best in your new married life.

Also mon frère, Dr Riccardo. Thank you for bringing you crazy personality with you everywhere. Thank you for all of your support, generosity and friendship.

One of my true best friends, Dr Remi. I spent a lot of time with you, both when I was being hosted countless times in your Strasbourg flat in the early days, when we were office mates at KIT and when we were doing the early morning at late night drives between Strasbourg and Karlsruhe (sorry for sleeping, many times...). Thank you for everything.

My fellow PhD students in the lab; Pierre, Giuseppe, Etienne and Mariel. Thank you for being solid rocks in the lab and so great to be with after work. You guys are great and I know you will go on to finish great theses. Giuseppe, I'm glad to be defending alongside you. A special mention to Matteo, it was great having you with us for a year and I'm happy to see you defending too!

Finally, my latest officemates, Charles and Mike. Thank you guys for making 205 truly the best. Through all of the serious and visionary scientific ideas we shared, to all of the other fun things we did together out of the lab, I couldn't ask for better people to be around so often.

To finish, I would like to thank all of my family and great friends back home for their unconditional support and encouragement. I really do apologise for being so silent in recent times, but I will definitely catch up with you all soon. Mum, Dad and Jonah, thank you for being there with me every step of the way. If it wasn't for you, there is no way I would have made it to this stage or become the person who I am today. Finally, thank you John P, my big brother, for inspiring me to take up chemistry as my field of study in the first place. Though you are no longer with us, I always draw inspiration from the words you gave me all those years ago. I know you would have easily gone on to get a chemistry PhD, so I dedicate this to you too.



# John Lawrence Zachariah Ddungu

**Address:** 2 Rue des Hallebardes,  
67000 Strasbourg, France

**Nationality:** British

**LinkedIn:** <https://www.linkedin.com/in/johnddungu>

**Mobile:** +33767114803

**Email:** johnddungu@gmail.com

**D.O.B:** 14 June 1991

## Education

### **2016-present** *PhD Chemistry*

University of Strasbourg, France

**Research Topic:** Synthesis and characterisation of ultra-small, functional silicon-based nanoparticles for diagnostic applications

### **2010-2014** *MSci (Hons) Chemistry with Study Abroad (Upper-second Class)*

University of Birmingham, UK (Year abroad at Phillips Universität Marburg, Germany)

**Dissertation Project:** "Luminescent nanoparticles in the visible and near IR functionalised with peptides for targeting cancer cells" (First class)

### **2009-2010** *1<sup>st</sup> year of BSc Chemistry*

Aston University, UK

### **2002-2009** *The Ecclesbourne School, UK*

## Research experience

### **May 2015-present** *Karlsruhe Institute of Technology (KIT) & University of Strasbourg*

- Acquisition of the necessary skills and knowledge of techniques for working towards a PhD thesis. These include microscopy techniques, multiple analytical spectrometry and spectroscopy techniques, electrochemistry and the basics of cell imaging.

### **Oct 2013-Apr 2014** *Research training during Masters Research Project*

- Gained a grounding in standard chemical research practises such as risk assessment, lab management, report writing and results communication in addition to the required technical skills and knowledge needed to complete the work for my thesis.

## Key skills *Teamwork:*

- Actively participated in collaborations with colleagues and external international partners in other labs and companies during my research experiences and took a central role in the work, allowing me to drive stages of projects to completion.
- Designed and created a functioning, innovative water control system with a team of fellow students, which won the first year design and build competition in chemical engineering at Aston University and achieved a first class mark.
- Maintained regular communication with fellow members of the Student Mentor team and university site staff, ensuring student support needs were met in different locations across the campus.

### ***Communication:***

- Created and delivered regular coherent presentations during my projects and throughout my degrees in order to communicate work and research to peers and co-workers at group meetings, symposia and international conferences.
- Utilised excellent interpersonal skills during my time working abroad to quickly adapt to the new environment and develop strong contacts with others of different nationalities.
- Applied my language skills to promote study in the UK to German students as a British representative at foreign study fairs in Germany.

### ***Organisation and time management:***

- Produced long term plans, allocating adequate time for lab work and the use of high demand analytical equipment well in advance, allowing the acquisition of a good quantity of highly relevant results within the timeframe of my research projects.
- Planned out academic tutorials and karate classes to include a number of specific sections, which allowed all students to have their differing requirements addressed within the allocated class time.
- Scheduled the delivery of the various equipment needed to build the Valefest festival site in advance of the festival, upholding prior agreements with the site owners and avoiding late arrivals by meeting the deadlines.

### **Academic teaching experience**

***Sept 2014- Private Tutor***

***May 2015***

- Deliver tailored tuition in the Sciences and German to students at all levels of schooling and to adult learners, boosting the progression towards their educational goals.

### **Other work experience**

***Mar 2010-***

***Aug 2012***

***JMK Restaurants Ltd McDonald's Restaurants: Full & Part-time Crew Member***

- Supported and at times led a team of other crew members, contributing to increased productivity levels, high customer satisfaction and the stores good assessments.

***Sept 2011-***

***Jun 2012***

***Guild of Students, University of Birmingham: Student Mentor Welcome Team Member***

- Provided support and advice for new students at the university as part of a team of mentors, streamlining their transition into university life.

***Jul 2007-***

***Sept 2009***

***GKR Karate International: Volunteer Karate Instructor***

- Trained and enthused students of all ages in Karate using creative, self-formulated class plans, leading to their sustained successes in grading assessments and tournaments.

### **Professional Memberships**

***2009-present***

***Affiliate Member of the Royal Society of Chemistry (RSC)***

### **Other Skills**

***IT:*** High competency with Microsoft Office programmes, Origin, CorelDraw, Inkscape, Kaleidagraph, ChemDraw, MestreNova, specialist instrument software packages and different internet browsers, which were used extensively throughout my projects to produce reports, reference databases and presentations.

***Languages:*** English (mother tongue), German (professional working proficiency), French (limited working proficiency), Polish (elementary proficiency)

### **Interests**

- Avid reader of numerous chemical science publications, which I use to keep up to date with developments in chemistry, particularly in inorganic, nanoscale, supramolecular photochemistry and electrochemistry as well as the applications in nanomedicine.
- Training and competing in karate (member of GKR Karate, 2002-present, current black belt).



- Event management (“Valefest” Organising Committee Member, 2011-2014: Contributed to the organisation, promotion (in person and via social media) and running of the UK’s largest student run festival for three editions, raising thousands of pounds for different charities each time).
- Breakdancing (member of the university Breakdance society, 2010-2014: Promoted the society both in person and on social media and advised the president on events and further training opportunities, which led to more memberships and higher attendance at competitions).

### **Contributions to scientific meetings and conferences**

- John Ddungu, Angelique Faramus, Nadia Licciardello, Luisa De Cola., Annual “NanoTracking” Meeting 2015, Lipari, Italy, 23.09.2015 - 25.09.2015 (oral)
- John Ddungu, Angelique Faramus, Luisa De Cola., Multifunctional, Hybrid and Nanomaterials Conference, Lisbon, Portugal, 06.03.2017 - 10.03.2017 (poster)
- John Ddungu, Simone Silvestrini, Angelique Faramus, Luisa De Cola., Journée des doctorants en chimie 2017, Collège Doctoral Européen, Strasbourg, 10.11.2017 (oral)
- John Ddungu, Simone Silvestrini, Angelique Faramus, Luisa De Cola., “Complex molecular systems towards adaptive materials” Minisymposium - ISIS, Uds, Strasbourg, 21.06.2018 (oral)
- John Ddungu, Simone Silvestrini, Luisa De Cola., 7th EuCheMS Chemistry Congress ‘Molecular frontiers and global challenges’, Liverpool, United Kingdom, 26.08.2018 - 30.08.2018 (oral)

### **Scientific publications**

“Biodistribution studies of ultrasmall silicon nanoparticles and carbon dots in experimental rats and tumor mice”  
 N. Licciardello, S. Hunoldt, R. Bergmann, G. Singh, C. Mamat, A. Faramus, J. L. Z. Ddungu, S. Silvestrini, M. Maggini, L. De Cola and H. Stephan, *Nanoscale*, **2018**, 10, 9880-9891 DOI: 10.1039/c8nr01063c

#### **Referees:**

##### **Professor Zoe Pikramenou**

*MSci Project Supervisor*

*Professor of Inorganic Chemistry and Photophysics*

School of Chemistry

University of Birmingham

BIRMINGHAM

B15 2TT

United Kingdom

z.pikramenou@bham.ac.uk

##### **Professor Luisa De Cola**

*PhD Supervisor*

*Chair in Supra-molecular and Biomaterial Chemistry*

Institut de Science et d'Ingénierie Supramoléculaires (ISIS)

Université de Strasbourg

67083 Strasbourg Cedex

France

decola@unistra.fr

**John DDUNGU**  
**Synthesis and  
characterisation of silicon-  
based nanoparticles for  
diagnostic applications**

## Résumé

Dans le cadre de cette thèse intitulée “Synthèse et caractérisation de nanoparticules à base de silicium pour des applications de diagnostic”, nous avons conçu des nanosondes basées sur des systèmes de petites nanoparticules à base de silicium (<5 nm) (NPs) portant différentes molécules fonctionnelles sur leur surface. Les NPs de Si ont été synthétisées, caractérisées et fonctionnalisées pour une utilisation dans les applications d'imagerie *in vivo* et d'électrochimiluminescence (ECL). Pour l'imagerie, une sonde active de tomographie par émission de positrons (TEP) et un colorant émissif ont été utilisés pour montrer les capacités d'imagerie et l'élimination rapide des NP de Si des corps des souris. La fixation d'un sucre sur les NPs de Si a été utilisée pour étudier le passage à travers la barrière hémato-encéphalique (BHE). Enfin, la fixation de complexes de ruthénium et d'iridium a montré que les NP de Si possédaient une bonne efficacité en tant que sondes dans les applications ECL.

## Résumé en anglais

Within the work of this thesis, entitled “Synthesis and characterisation of silicon based nanoparticles for diagnostic applications”, we have designed nanobrobes based on systems of small (< 5 nm) silicon-based nanoparticles (Si NPs) bearing different functional molecules on the surface. Si NPs were synthesised, thoroughly characterised and functionalised for use in *in vivo* imaging and electrochemiluminescence (ECL) applications. For imaging, a positron emission tomography (PET) active probe and an emissive dye have been used to show the effective imaging capabilities and fast clearance of the Si NPs from the bodies of mice. Attachment of a sugar to the Si NPs has been used to study passage through the blood-brain-barrier (BBB). Finally, attachment of ruthenium and iridium complexes has shown that the Si NPs possess some good efficiency as probes in ECL applications.